

DOCTOR OF PHILOSOPHY

Predicting Fatigue Crack Growth Life in Additive Manufactured Titanium Alloy

Wang, Xueyuan

Award date:
2016

Awarding institution:
Coventry University

[Link to publication](#)

General rights

Copyright and moral rights for the publications made accessible in the public portal are retained by the authors and/or other copyright owners and it is a condition of accessing publications that users recognise and abide by the legal requirements associated with these rights.

- Users may download and print one copy of this thesis for personal non-commercial research or study
- This thesis cannot be reproduced or quoted extensively from without first obtaining permission from the copyright holder(s)
- You may not further distribute the material or use it for any profit-making activity or commercial gain
- You may freely distribute the URL identifying the publication in the public portal

Take down policy

If you believe that this document breaches copyright please contact us providing details, and we will remove access to the work immediately and investigate your claim.

Predicting Fatigue Crack Growth Life in Additive Manufactured Titanium Alloy

By

Xueyuan Wang

May 2016



*A thesis submitted in partial fulfilment of the University's
requirements for the Degree of Doctor of Philosophy*

Some materials have been removed from this thesis due to Third Party Copyright. Pages where material has been removed are clearly marked in the electronic version. The unabridged version of the thesis can be viewed at the Lanchester Library, Coventry University.



Certificate of Ethical Approval

Applicant:

Xueyuan Wang

Project Title:

Predicting Fatigue Crack Growth Life in Additively Manufactured Titanium Parts

This is to certify that the above named applicant has completed the Coventry University Ethical Approval process and their project has been confirmed and approved as Low Risk

Date of approval:

18 May 2016

Project Reference Number:

P35963

Abstract

The aim of this PhD project is to investigate the fatigue crack propagation behaviour in an additive manufactured high strength titanium alloy, Ti-6Al-4V. Test specimens were made by the Wire+Arc Additive Manufacture (WAAM) process. The research focus is the fatigue crack behaviour (crack growth rate and trajectory) near interface between WAAM and substrate materials. The challenges are the understanding and assessment of the effects of residual stress, microstructure change and anisotropic material properties as the result of rapid heating and cooling, and rapid solidification cycles in additive manufacturing. This PhD project has focused on numerical modelling and simulation of fatigue crack behaviour. Specimen fabrication and experimental tests were conducted by our collaborators in linked projects.

Finite element method (FEM) was employed to evaluate the influence of anisotropic Young's modulus and yield strength properties on the crack tip stress intensity factor and crack tip plasticity. Residual stress distribution in the compact tension, C(T), specimens were obtained by FEM based on experimentally measured residual stress in a much larger WAAM-substrate wall, from which the C(T) specimens were extracted. Residual stress profile was also established by an analytical approach for another WAAM-substrate wall, from which the fatigue crack growth rates (FCGR) for pure WAAM material were measured. Based on these calculations, fatigue crack growth rate and life were predicted by empirical methods from the Linear Elastic Fracture Mechanics, namely the modified Paris law and the Harter T-method. Residual stress effect is accounted for by the superposition method, via the effective R ratio parameter.

Key findings and main conclusions are: (1) the difference in the stress intensity factor is less than 1% when considering the anisotropic material properties. Therefore, the influence of anisotropic material properties on the crack growth driving force can be neglected. (2) After extracting a C(T) specimen from a larger wall sample, retained residual stress in the C(T) specimen is much reduced; consequently the stress intensity factor due to the residual stress is also small. (3) Residual stress free assumption is not valid for C(T) specimens which provide FCGR data for pure WAAM material. (4) The Harter T-method is better when predicting FCGRs in WAAM material and residual stress effect should not be ignored. (5) Predicted fatigue crack growth life for the specimens containing WAAM-substrate interface have a difference about 25% compared to experiments. Predicted fatigue crack deviation angles for various crack locations and orientations are consistently larger than the experimental measurement, as the crack closure has reduced the effect of mode II stress intensity factor.

Acknowledgements

I would like to thank the China Scholarship Council for sponsorship of this work.

I would like to acknowledge Professor Xiang Zhang, Professor Michael Fitzpatrick, and Dr. Abdul Khadar Syed for supervising this work.

I would like to thank Dr. Sanjooram Paddea at The Open University for their important experimental work on residual stress measurement. Thanks must also go to Dr. Jikui Zhang for his helpful discussions. I would also like to thank the Welding Engineering and Laser Processing Centre at Cranfield University for manufacturing the test specimens and MSc students for conducting part of the experimental work. Finally, the support of my wife has made it possible for me to conduct this 40 month PhD study.

Contents

| | | |
|-----|--|-----|
| 1 | Introduction | 1 |
| 1.1 | Why WAAM Ti-6Al-4V? | 1 |
| 1.2 | Why damage tolerance? | 4 |
| 1.3 | Challenges, research questions and approach | 5 |
| 1.4 | Aim, objectives and scope | 6 |
| 1.5 | Thesis structure | 8 |
| 2 | Literature Review | 9 |
| 2.1 | AM processes | 9 |
| 2.2 | Microstructure in Ti-6Al-4V | 12 |
| 2.3 | Mechanical properties of Ti-6Al-4V | 17 |
| 2.4 | Residual stress measurement techniques | 27 |
| 2.5 | Fatigue crack growth rates of Ti-6Al-4V | 30 |
| 2.6 | Summary of literature survey | 46 |
| 3 | Experiments Used in This Project | 49 |
| 3.1 | Introduction | 49 |
| 3.2 | The WAAM process | 49 |
| 3.3 | Samples made by WAAM | 50 |
| 3.4 | Residual stress measurements | 52 |
| 3.5 | C(T) specimens for FCGR tests | 59 |
| 3.6 | Fatigue crack growth rate tests | 62 |
| 3.7 | Optical microscope (OM) observation | 67 |
| 4 | Residual Stress Analysis | 70 |
| 4.1 | Introduction | 70 |
| 4.2 | Modelling residual stress in Wall-Bi120 | 71 |
| 4.3 | Evaluation of retained residual stress in C(T) specimens | 75 |
| 4.4 | Inputting directly residual stress into C(T) specimen | 82 |
| 4.5 | Evaluation of Residual Stress by Analytical Approach | 84 |
| 4.6 | Measured transverse residual stress | 102 |
| 5 | Calculation of Stress Intensity Factors | 104 |
| 5.1 | Introduction | 104 |
| 5.2 | Isotropic material under applied load | 104 |

| | | |
|-----|---|-----|
| 5.3 | Influence of anisotropic Young's modulus | 111 |
| 5.4 | Influence of bi-material Young's modulus..... | 113 |
| 5.5 | Influence of yield strength on LEFM applicability | 114 |
| 5.6 | Stress intensity factors due to residual stress | 118 |
| 6 | Prediction of Fatigue Crack Growth Life | 125 |
| 6.1 | Introduction | 125 |
| 6.2 | Fatigue crack growth rate model | 125 |
| 6.3 | Fatigue crack growth life in the Type A and C specimens | 134 |
| 6.4 | Crack trajectory in Type B, D and E | 142 |
| 7 | Conclusions and Future Work..... | 146 |
| 7.1 | Conclusions | 146 |
| 7.2 | Future work | 148 |
| | References | 149 |
| | Appendix A Published papers..... | 160 |

List of figures

| | |
|---|----|
| Figure 1-1 Wire and arc additive manufacturing (a) set-up (Martina, 2014 p.28) and (b) WAAM fabricated part (Addison et al., 2015)..... | 3 |
| Figure 1-2 Hybrid manufacturing strategy (a) flap track (Kazanas, 2011) and (b) QTD-series insert drills (Alec, 2015) | 4 |
| Figure 1-3 Crack growth history in response to cyclic loads (FAA, 1993)..... | 5 |
| Figure 1-4 Schematic diagram of research approach | 6 |
| Figure 2-1 Schematic of WAAM process equipment (Martina et al., 2012)..... | 10 |
| Figure 2-2 Schematic of EBM process equipment (Murr et al., 2009) (1) Electron gun assembly; (2) EB focusing lens; (3) EB deflection coils (x-y); (4) powder cassettes; (5) powder (layer) rake; (6) part; (7) build table | 11 |
| Figure 2-3 Schematic of SLM process equipment (Thijs et al., 2010)..... | 11 |
| Figure 2-4 Schematic of SLS process equipment (Gibson et al., 2010 p.104)..... | 12 |
| Figure 2-5 Three types of microstructure in Ti-6Al-4V of wrought products: (a) fully lamellar (Filip et al., 2003), (b) equiaxed (Zhai et al., 2016), (c) bimodal (Boyce and Ritchie, 2001) | 13 |
| Figure 2-6 Anisotropic mechanical properties in Ti-6Al-4V sheet (Zarkades and Larson, 1968): (a) Young's modulus, (b) yield strength, and (c) ultimate tensile strength. | 14 |
| Figure 2-7 Microstructure of WAAM made Ti-6Al-4V: (a) macrostructure showing columnar prior- β grains and white bands (Wang et al., 2011), (b) microstructure on white bands, (c) microstructure between the bands(Wang et al., 2013)..... | 16 |
| Figure 2-8 Pole figures for WAAM made Ti-6Al-4V: (a) reconstructed β texture and (b) α texture (Antonysamy, 2012 p.185). | 16 |
| Figure 2-9 <i>S-N</i> data (test results and best-fit curve) for Ti-6Al-4V of extrusion in MA condition at room temperature, longitudinal direction, unnotched specimens (Rice et al., 2003 p.5-69)..... | 19 |
| Figure 2-10 Stress strain curves of the as-built and polished SLM made Ti-6Al-4V (Formanoir et al., 2016) in X-direction (a) and Z-direction (b)..... | 24 |
| Figure 2-11 Schematic parameters of lamellar microstructure: <i>D</i> : prior- β grain size, <i>d</i> : colony size of the $\alpha + \beta$ lamellar, <i>t</i> : thickness of α lamellae (Sieniawski et al., 2013)..... | 30 |
| Figure 2-12 Effect of stress ratio <i>R</i> on FCGR for wrought Ti-6Al-4V, comparison between bimodal and equiaxed microstructures. Re-plotted from AFGROW | 32 |
| Figure 2-13 Fatigue crack growth rates for Ti-6Al-4V of wrought products in mill annealed condition, a) by Feddersen & Hyler (1971), b) by Shih & Wei (1973)..... | 33 |
| Figure 2-14 Fatigue crack growth rates for Ti-6Al-4V of wrought products in mill annealed condition (Harrington, n. d.)..... | 34 |
| Figure 2-15 Fatigue crack growth rates data for Ti-6Al-4V of wrought products in mill annealed condition showing <i>R</i> ratio effect. ΔK is between 20 to 40 MPa \sqrt{m} . Data are re-plotted from Feddersen & Hyler (1971), Shih & Wei (1973), and Harrington (n. d.)..... | 34 |
| Figure 2-16 Fatigue crack growth rates for Ti-6Al-4V of wrought products in mill annealed condition by Dubey et al. (1997)..... | 35 |
| Figure 2-17 Fatigue crack growth rates for Ti-6Al-4V of wrought products in mill annealed condition by Shademan et al. (2004), the microstructure <i>D</i> is mill annealed condition, (a) <i>R</i> = 0.1, (b) <i>R</i> = 0.25, (c) <i>R</i> = 0.5 and (d) <i>R</i> = 0.8..... | 35 |
| Figure 2-18 Fatigue crack growth rates data for Ti-6Al-4V of wrought products in mill annealed | |

| | |
|--|----|
| condition showing the R ratio effect. ΔK is under $30 \text{ MPa}\sqrt{\text{m}}$. Data are re-plotted from Dubey et al. (1997) and Shademan et al. (2004)..... | 36 |
| Figure 2-19 Fatigue crack growth rates data for mill annealed Ti-6Al-4V of wrought products showing variability (Donachie, 2000 p.109). Data are for 6 heats of plate..... | 37 |
| Figure 2-20 Fatigue crack growth rates data for mill annealed Ti-6Al-4V of wrought products showing variability. Data are re-plotted from Feddersen & Hyler (1971), Harrington (n. d.), Shademan et al. (2004), Shih & Wei (1973), and Dubey et al. (1997). | 37 |
| Figure 2-21 Fatigue crack growth rates for SLM made Ti-6Al-4V tested at $R = 0.1$ by Hooreweder et al. (2012)..... | 40 |
| Figure 2-22 Fatigue crack growth rates for SLM Ti-6Al-4V tested at $R = 0.1$ by Cain et al. (2015) (a) the XY specimen orientation, (b) the XZ specimen orientation, (c) the XZ specimen orientation, (d) the AB condition, (e) the SR condition and (f) the HT condition. (AB: as-built, SR: stress relief treatment, HT: heat treatment)..... | 41 |
| Figure 2-23 Comparison of fatigue crack growth rates data for SLM Ti-6Al-4V tested at $R = 0.1$ in as-built condition. As planes of specimen are parallel to the layers during depositing, this can be regarded as no residual stress. Feddersen & Hyler 1971 is wrought Ti-6Al-4V data. Data are re-plotted from Feddersen & Hyler (1971), Cain et al. (2015) and Van Hooreweder et al. (2012)..... | 42 |
| Figure 2-24 Comparison of fatigue crack growth rates data for SLM made Ti-6Al-4V tested at $R = 0.1$ in as-built condition. Residual stress measurement was not conducted. Feddersen & Hyler 1971 is wrought Ti-6Al-4V data. Data are re-plotted from Feddersen & Hyler (1971), and Cain et al. (2015)..... | 42 |
| Figure 2-25 Comparison of fatigue crack growth rates data for SLM Ti-6Al-4V tested at $R = 0.1$ in heat treated, SR: 650°C for 4 hours, and HT: 890°C for 2 hours. Feddersen & Hyler 1971 is wrought products data. Data are re-plotted from Feddersen & Hyler (1971), and Cain et al. (2015)..... | 43 |
| Figure 2-26 Microstructure of EBM Ti-6Al-4V. (a) layer thickness was $\sim 700 \mu\text{m}$ (Edwards et al., 2013), (b) layer thickness was $\sim 100 \mu\text{m}$ (Murr et al., 2009), (c) layer thickness was $\sim 100 \mu\text{m}$ (Facchini et al., 2009)..... | 44 |
| Figure 2-27 Fatigue crack growth rates for EBM Ti-6Al-4V tested at $R = 0.1$ by Edwards et al. (2013). | 45 |
| Figure 2-28 Fatigue crack growth rates for EBM made Ti-6Al-4V tested at $R = 0.1$ by (a) Greitemeier et al. (2016) and (b) Zhai et al. (2016). (AF: as-fabricated, HT: heat treated, 950°C for 1hour plus $500\text{--}600^{\circ}\text{C}$ for 3–8 hours, HIP: hot isostatic pressing, at 920°C and 1000 bar for 2 hours, annealed: 710°C for 2 hours). | 45 |
| Figure 2-29 Comparison of fatigue crack growth rates data for EBM Ti-6Al-4V tested at $R = 0.1$ in heated treated and as-built. Feddersen & Hyler 1971 is wrought Ti-6Al-4V data. Data are re-plotted from Feddersen & Hyler (1971), Edwards et al. (2013), Greitemeier et al. (2016), and Zhai et al. (2016). | 46 |
| Figure 3-1 Cut planes in Wall-Bi120 for contour measurement, (a) schematic cut plane (unit: mm); (b) photos of Wall-Bi120 and cross section view of cut plane..... | 52 |
| Figure 3-2 Cut plane in Wall-T110 for contour measurement (unit: mm)..... | 53 |
| Figure 3-3 Position of C(T) specimens in Wall-Bi120 and cut planes in C(T) specimens for contour measurement, Type A, B and C specimens in terms of the crack position (unit:mm)..... | 53 |
| Figure 3-4 Steps of the contour method for residual stress measurement (Paddea, 2015)..... | 54 |
| Figure 3-5 Measured residual stresses in Wall-T110: (a) 2D stress map, and (b) 1D stress distribution along the centre line (average value in the thickness)..... | 56 |

| | |
|--|----|
| Figure 3-6 Measured residual stresses in Wall-Bi120: (a) 2D stress map and (b) 1D stress distribution along the mid-thickness line..... | 57 |
| Figure 3-7 Measured residual stresses in type B specimen: (a) 2D stress map and (b) 1D stress distribution along the mid-thickness line | 57 |
| Figure 3-8 Measured residual stresses in type A specimen: (a) 2D stress map and (b) 1D stress distribution along the mid-thickness line | 58 |
| Figure 3-9 Measured residual stresses in type C specimen: (a) 2D stress map and (b) 1D stress distribution along the mid-thickness line | 58 |
| Figure 3-10 Positions of uncracked ligament in residual stress field of Wall-Bi120 are similar, whereas released stresses in notch zone for type A specimen are higher. | 59 |
| Figure 3-11 Geometry of C(T) specimen (unit: mm)..... | 60 |
| Figure 3-12 Position of C(T) specimens, type AL and PL, in Wall-T145 (C(T) specimen thickness =5 mm) | 61 |
| Figure 3-13 Position of C(T) specimens for fatigue crack growth rate testing, Type A to E, in Wall-Bi120 (C(T) thickness =6 mm) | 62 |
| Figure 3-14 Crack surface of A3 specimen show the smooth surface begin at about $a = 40$ mm, (a) one crack surface with one side face, and (b) two crack surfaces..... | 63 |
| Figure 3-15 Fatigue crack growth rates in WAAM made Ti-6Al-4V, type A..... | 64 |
| Figure 3-16 Fatigue crack growth rates in WAAM made Ti-6Al-4V, type C..... | 64 |
| Figure 3-17 Fatigue crack growth rates in WAAM made Ti-6Al-4V, type B..... | 65 |
| Figure 3-18 Fatigue crack growth rates in WAAM made Ti-6Al-4V, type D | 65 |
| Figure 3-19 Fatigue crack growth rates in WAAM made Ti-6Al-4V, type E..... | 66 |
| Figure 3-20 Fatigue crack growth rates in Ti-6Al-4V of wrought products | 66 |
| Figure 3-21 Fatigue crack growth rates in WAAM made Ti-6Al-4V. Specimens are extracted from Wall-T145. Data are replotted from appendix in Lorant's thesis (2010). (PL: crack propagates parallel to the layers; AL: crack propagates across the layers) | 67 |
| Figure 3-22 Macrograph of the Type A, B and C specimens. | 68 |
| Figure 3-23 Optical micrographs of the WAAM deposited material in Wall-Bi120..... | 69 |
| Figure 3-24 Optical micrographs of crack path when the crack propagates in (a) the substrate of Wall-Bi120 and (b) the WAAM made material | 69 |
| Figure 4-1 Comparison between the experimental results and FE output of the longitudinal residual stress (Liljedahl et al., 2008)..... | 72 |
| Figure 4-2 Procedure of inputting measured residual stress field in Wall-Bi120 sample by using SIGINI..... | 74 |
| Figure 4-3 Comparison of obtained longitudinal residual stresses with experiments..... | 75 |
| Figure 4-4 Geometry change and residual stress redistribution during extracting type B and C specimens (direction 1: longitudinal direction; direction 2: transverse direction; b, c, and d figures share the same spectrum) | 77 |
| Figure 4-5 Finite element mesh for residual stress analysis with mesh size $2\text{ mm} \times 2\text{ mm}$ | 78 |
| Figure 4-6 Mesh convergence study for retained residual stress in C(T) specimen, type C | 78 |
| Figure 4-7 Comparison of longitudinal residual stresses between FEA and the contour measurement, along crack path in Type A specimen..... | 79 |
| Figure 4-8 Comparison of transverse residual stresses between FEA and the contour measurement, along crack path in type B specimen..... | 80 |

| | |
|--|-----|
| Figure 4-9 Comparison of longitudinal residual stresses between FEA and the contour measurement, along crack plane in type C specimen | 80 |
| Figure 4-10 Longitudinal residual stresses along crack path in type A specimen (position used in life prediction)..... | 81 |
| Figure 4-11 Longitudinal residual stresses along crack path in type C specimen (position used in life prediction)..... | 81 |
| Figure 4-12 Positions of uncracked ligament residual stress field of Wall-Bi120 shows that type A specimen is not moment balance. | 82 |
| Figure 4-13 Inputting directly residual stress into C(T) specimen (1: longitudinal; 2: transverse)..... | 83 |
| Figure 4-14 Comparison of retained residual stress by directly building residual stress and building residual stress field in large sample + element removal, type B specimen, transverse residual stress.. | 83 |
| Figure 4-15 Configurations of parts made by WAAM: (a) different height in the wall samples, (b) vertical substrate, (c) crossed walls, (d) curved wall..... | 85 |
| Figure 4-16 Published residual stress profiles for “T” section WAAM made walls, (a) full length of residual stress profile, (b) detailed stress near top of substrate (a&b share the same legend)..... | 86 |
| Figure 4-17 Analytical model for determining the changing of residual stress distribution in both the actual substrate and the virtual substrate due to adding a new layer | 90 |
| Figure 4-18 Analytical model for determining the changing of residual stress distribution due to removing the virtual substrate which represents the effect of clamps | 91 |
| Figure 4-19 Residual stress distribution for “T” section WAAM made wall with 14 mm thick virtual substrate and various WAAM wall heights | 94 |
| Figure 4-20 Residual stress distribution for “T” section WAAM made wall with 33 mm thick virtual substrate and various WAAM wall heights | 95 |
| Figure 4-21 Residual stress distribution for “T” section WAAM part with 83 mm thick virtual substrate and various WAAM wall heights..... | 96 |
| Figure 4-22 Possible three types of residual stress profile in “T” section WAAM made parts | 97 |
| Figure 4-23 Influence of the material yield strength on the residual stress profile (Mercelis et al., 2006)..... | 99 |
| Figure 4-24 Predicted residual stress profile in Wall-T145 | 100 |
| Figure 4-25 Finite element model for residual stress analysis of C(T) specimens in Wall-T145..... | 101 |
| Figure 4-26 Retained residual stresses in C(T) specimens extracted from Wall-T145 (AL and PL) .. | 101 |
| Figure 4-27 Relation of stress component direction and line of measurement points: (a) longitudinal stress normal to the line of measuring points, (b) transverse stress parallel to the line of measuring points, (c) transverse stress normal to the line of measuring points (not practical for contour; not available from published neutron measurement)..... | 102 |
| Figure 5-1 Uniform radial stress to simulate the pin loading in FE model of C(T) specimen | 105 |
| Figure 5-2 Virtual Crack Closure Technique (VCCT) for two-dimensional FE model using eight-noded element (nodal forces and nodal displacements in the x-axis are omitted for clarity)..... | 106 |
| Figure 5-3 Two-dimensional plane stress FE model of C(T) specimen | 108 |
| Figure 5-4 Convergence trend for C(T) specimen (Δa is mesh size around the crack tip)..... | 108 |
| Figure 5-5 Comparison of the crack tip stress intensity factors: FEA vs. closed form solution..... | 109 |
| Figure 5-6 Geometry of the short C(T) specimen (unit: mm) | 110 |
| Figure 5-7 Comparison of stress intensity factors for short C(T) specimen..... | 110 |
| Figure 5-8 Coordinate system for Eq. 5-7. | 111 |

| | |
|--|-----|
| Figure 5-9 Influence of orthotropic Young's modulus in C(T) specimen on the crack tip stress intensity factors..... | 112 |
| Figure 5-10 Influence of bi-material Young's modulus on the crack tip stress intensity factors, for Type A and C specimens, using the microstructure interface. | 114 |
| Figure 5-11 Two-dimensional FE model of C(T) specimen with fine mesh at the crack tip | 115 |
| Figure 5-12 Plastic zone size calculated by elastic-plastic FE analysis, $K = 19.77 \text{ MPa}\sqrt{\text{m}}$ | 116 |
| Figure 5-13 Positions of specimens in Wall-Bi120 and corresponding positions of FE models in residual stress field, type A and C | 119 |
| Figure 5-14 Mode I stress intensity factors due to residual stress in type A and C specimens | 120 |
| Figure 5-15 Two-dimensional FE model of C(T) specimen with seam crack..... | 121 |
| Figure 5-16 Positions of FE models in residual stress field, Type B, D and E specimen | 122 |
| Figure 5-17 Mode I and Mode II stress intensity factors due to residual stress in Type B, D and E specimens | 122 |
| Figure 5-18 Position of FE model in residual stress field, AL specimen | 123 |
| Figure 5-19 Mode I stress intensity factors due to residual stress in AL specimen..... | 123 |
| Figure 5-20 Positions of FE model in residual stress field, type PL specimens..... | 124 |
| Figure 5-21 Mode I and Mode II stress intensity factors due to residual stress in type PL specimens | 124 |
| Figure 6-1 Experimental da/dN vs. ΔK data and AFGROW m for calculating fatigue crack growth rate for various R ratio (some m are omitted for clarity)..... | 129 |
| Figure 6-2 Combined dataset including m and da/dN vs. ΔK for $R = 0.1$ for the substrate and WAAM made Ti-6Al-4V | 130 |
| Figure 6-3 Harter T-method calculation procedure..... | 132 |
| Figure 6-4 Fitted modified Paris equation and experimental da/dN vs. ΔK for $R = 0.1$ for WAAM made Ti-6Al-4V and Ti-6Al-4V of wrought products | 134 |
| Figure 6-5 Positions of the WAAM-substrate interfaces in the C(T) specimens, Type A and C..... | 135 |
| Figure 6-6 Stress intensity factors, $K_{app,max}$ and K_{res} , in the C(T) specimens, Type A and C | 135 |
| Figure 6-7 Effective stress intensity factor ratios for the C(T) specimens, Type A and C | 136 |
| Figure 6-8 Comparison of da/dN vs. a in the Type A specimen, between predictions by the Harter T-method, the modified Paris equation and that ignoring residual stress and three experimental results | 138 |
| Figure 6-9 Comparison of a vs. N curves in the Type A specimen, between predictions by the Harter T-method, the modified Paris equation and that ignoring residual stress and three experimental results | 138 |
| Figure 6-10 Comparison of da/dN vs. a in the Type C specimen, between predictions by the Harter T-method, the modified Paris equation and that ignoring residual stress and three experimental results | 139 |
| Figure 6-11 Comparison of $a-N$ curves in the Type C specimen, between predictions by the Harter T-method, the modified Paris equation and that ignoring residual stress and three experimental results | 139 |
| Figure 6-12 Geometrical interface and microstructure interface in C2 specimen..... | 141 |
| Figure 6-13 Effective stress intensity factor ratios in C(T) specimen, AL type | 142 |
| Figure 6-14 Predicted crack deviation angle for C(T) specimens, type B, D and E | 144 |
| Figure 6-15 Three examples for fatigue crack deviation angles, B1, E1 and D3 specimens. | 144 |

List of tables

| | |
|--|-----|
| Table 2-1 Minimum value of ultimate tensile strength, yield strength and elongation for MA and STA conditions Ti-6-4 plate (AMS 4911J, 2003), in both longitudinal and long transvers orientations; thickness range 4.8–19 mm, room temperature..... | 17 |
| Table 2-2 Measured ultimate tensile strength, yield strength and elongation for MA condition Ti-6-4 at room temperature..... | 19 |
| Table 2-3 Young's modulus and fracture toughness for wrought Ti-6-4 at room temperature | 19 |
| Table 2-4 The minimum value of ultimate tensile strength, yield strength and elongation for AM made Ti-6-4 (ASTM Standard F2924, 2014) (in stress relieved or annealed condition), X, Y, and Z-principal direction, at room temperature..... | 20 |
| Table 2-5 Measured ultimate tensile strength, yield strength and elongation of SLM and EBM made Ti-6-4 at room temperature..... | 21 |
| Table 2-6 Measured fatigue performance of SLM and EBM made Ti-6-4 at room temperature | 22 |
| Table 2-7 Measured fracture toughness of SLM and EBM made Ti-6-4 | 23 |
| Table 2-8 Measured Young's modulus of SLM and EBM made Ti-6-4 at room temperature | 23 |
| Table 2-9 Measured ultimate tensile strength, yield strength and elongation for WAAM and SDM Ti-6-4 at room temperature..... | 25 |
| Table 2-10 Measured fatigue performance of WAAM and SMD made Ti-6-4 at room temperature.... | 26 |
| Table 2-11 Fracture toughness of WAAM Ti-6-4 in as-built condition (Zhang, X. et al., 2017)..... | 26 |
| Table 3-1 Experiments used in this project..... | 49 |
| Table 3-2 Process parameters for fabrication of Wall-Bi120 (Hills, 2014) | 51 |
| Table 3-3 Chemical composition of Ti-6Al-4V wire (wt %) (Martina et al., 2012)..... | 51 |
| Table 3-4 Final geometry of all wall samples..... | 51 |
| Table 3-5 Fatigue crack growth rate testing parameters ($W = 70$ mm, $R = 0.1$ for all) | 62 |
| Table 4-1 Detail for published residual stress profiles | 87 |
| Table 4-2 Published values of the maximum residual stress for butt-welded Ti-6Al-4V | 93 |
| Table 5-1 Measured Young's modulus for WAAM Ti-6-4 (Lorant, 2010 p.79) and values in FE model | 112 |
| Table 5-2 Yield strength in WAAM Ti-6-4 (Lorant, 2010 p.79) and values used in FE (unit: MPa) .. | 115 |

Nomenclature and abbreviations

| | unit | |
|----------------------------|----------------|---|
| ν | - | Poisson's ratio |
| σ_{UTS} | MPa | ultimate tensile strength |
| σ_{YS} | MPa | yield strength |
| σ_L | MPa | Stress in a new layer |
| σ_{RSV} | MPa | Residual stress in virtual substrate |
| θ | ° | Deviation angle of crack |
| a | mm | the distance from center line of applied load to crack tip distance |
| | | crack length |
| a_{i-1} | mm | i th crack length |
| Δa | mm | Increment of crack length |
| da/dN | m/cycle | Fatigue crack growth rate |
| B | mm | Thickness of C(T) specimen |
| C | | Material constant in Paris law |
| d | mm | Neutral axis position |
| E | GPa | Young's modulus |
| E_1, E_2 | GPa | Young's modulus in 1, 2 direction |
| e | % | elongation |
| G | N/m | Strain energy release rate |
| G_{12} | GPa | Shear modulus |
| h_a, h_s, h_{vs} | mm | Height of AM made part, actual substrate, virtual substrate |
| I | m ⁴ | Second axial moment of area |
| K_I, K_{II} | MPa \sqrt{m} | Stress intensity factor in mode I, mode II |
| K_{IC} | MPa \sqrt{m} | Fracture toughness in mode I |
| K_Q | MPa \sqrt{m} | Conditional fracture toughness |
| $K_{app,max}, K_{app,min}$ | MPa \sqrt{m} | Stress intensity factor by maximum, minimum applied load |
| K_{max}, K_{min} | MPa \sqrt{m} | Maximum, minimum Stress intensity factor |
| K_{op} | MPa \sqrt{m} | Stress intensity factor at which the crack re-open |
| ΔK_{eff} | MPa \sqrt{m} | Effective stress intensity factor range |
| ΔK_{app} | MPa \sqrt{m} | Applied stress intensity factor range |
| K_{res} | MPa \sqrt{m} | Stress intensity factor due to residual stress |
| ΔK | MPa \sqrt{m} | Stress intensity factor range |
| L | mm | Length of wall specimen |
| M | N m | Bending moment |
| m | | Material constant in Harter T-method |
| n | | Material constant in Paris law |
| | | Plastic constraint factor |
| N | | Number of cycles |
| ΔN | | Number of cycles over increment of crack length |
| P | kN | Applied load |
| R | | Ratio of applied load |
| R_{eff} | | Ratio of effective stress intensity factor |
| r_p | mm | Crack tip plastic zone size |

| | | |
|------------|----|---|
| U | | $\Delta K_{\text{eff}}/\Delta K$ |
| W | mm | Width of C(T) specimen |
| W_a, W_s | mm | Width of WAAM made part, width of substrate |
| 1D | | One-dimensional |
| 2D | | Two-dimensional |
| AL | | Across the layer |
| AM | | Additive manufacturing |
| CFRP | | Carbon fibre reinforced polymer |
| C(T) | | Compact tension |
| EB | | Electron beam |
| EBM | | Electron beam melting |
| EDM | | Electrical discharge machining |
| FCGR | | Fatigue crack growth rate |
| FE | | Finite element |
| FEM | | Finite element method |
| FSW | | Friction stir welding |
| GTA | | Gas Tungsten Arc |
| HAZ | | Heat affected zone |
| HIP | | Hot isostatic pressing |
| LEFM | | Linear Elastic Fracture Mechanics |
| MA | | Mill annealed |
| M(T) | | Middle tension |
| MTS | | Maximum tangential stress |
| OM | | Optical microscope |
| PL | | Parallel to the layer |
| PWD | | plasma wire deposition |
| RA | | Recrystallization annealed |
| SLS | | Selective laser sintering |
| SLM | | Selective laser melting |
| SDM | | Shaped metal deposition |
| STA | | Solution treated and aged |
| TIG | | Tungsten Inert Gas |
| VCCT | | Virtual Crack Closure Technique |
| VPPA | | Variable Polarity Plasma Arc |
| WAAM | | Wire and arc additive manufacturing |
| WELPC | | Welding Engineering and Laser Processing Centre (in Cranfield University) |

Chapter 1 Introduction

1.1 Why WAAM Ti-6Al-4V?

High strength titanium alloys, especially Ti-6Al-4V, have been used in aircraft primary structures, such as empennage attachment fitting on the Boeing 777 (Boyer, 1992), pylon on the Boeing 787 (Hale, 2006) and the rudder actuator housing on the F-22 (Pike, 2016). Before the carbon fibre reinforced polymer (CFRP) composites were widely used in commercial aircraft, the Boeing 777 airframe had 8.3% titanium alloys by weight (Boyer, 1992). For the new generation commercial aircraft, e.g. the Boeing 787, there are 50% CFRP composites, and titanium alloy has reached 15% by weight (Hale, 2006) for its good compatibility with the CFRP. Aircraft from the Airbus company, A350XWB and A380, consist of 14% and 6% titanium alloys by weight (Zanin, 2012), respectively. The Boeing 787 aircraft designers selected titanium alloy according to the operating environment and loads that a particular component would experience. They considered that “titanium alloy can withstand comparable loads better than aluminium, has minimal fatigue concerns, and is highly resistant to corrosion” (Hale, 2006). It is known that 90% of the titanium alloys used on aero-structures is Ti-6Al-4V (Zanin, 2012).

In the aerospace industry, parts are often machined from forgings. This traditional manufacturing method is often costly in terms of machining operation to make the final geometry and the large waste of materials. The aerospace industry often uses the buy-to-fly ratio to describe such waste. The buy-to-fly ratio is the weight ratio between the raw material used for making a component and the weight of the component itself. In general, the buy-to-fly ratio for aircraft components is 5–20 if using the traditional manufacturing methods; in other words, more than 80% of raw material is scraped off the component (Allen, 2006). As the high prices of both titanium alloys and machining operation for titanium alloys (hard to machine), titanium components become very expensive for the aircraft industry.

One way to overcome such expensive titanium components is using the additive manufacturing (AM) technology. AM process makes a component in an additive approach instead of cutting off materials (subtractive approach). In this way, the buy-to-fly ratio can be

reduced to nearly 1; and hence the cost of component will be reduced. The application of AM to aircraft components has attracted many research attentions. For example, a winner of the Round I of GE's Alternative Manufacturing of Aviation Castings Challenge was Burloak Technologies of Ontario, in Canada, which won a proposal that included design optimization to enable use of the AM to create a component offering 50% of weight and cycle time reduction compared to the baseline production method. Another winner, the buyCastings.com of Miamisburg, in American, combined the AM with other processing techniques to lower the product cycle time and reduce inspection requirements due to improved material qualities. So, both winners considered the AM technology as their innovative manufacturing methods (Anon., 2015).

The term AM includes many different technologies of fabricating a part using a layer by layer strategy (ASTM Standard F2792, 2012). However, not all of them are suitable for the aerospace industry in terms of making large parts. Some of them have been regarded as candidates, e.g. selective laser sintering (SLS), selective laser melting (SLM), electron beam melting (EBM) (Murr et al., 2012) and wire and arc additive manufacturing (WAAM) (Uriondo et al., 2015). Among them, the WAAM process has much higher deposition rate (Martina et al., 2012) and is capable of building large scale parts (>10 kg) (Williams et al., 2016). So, WAAM made titanium parts are the most promising application of AM technology to the aerospace industry. In general, WAAM set-up consists of a combination of arc welding torch and wire feeding unit, which is mounted on either a robot or a computer numerical controlled manipulator, see Fig. 1-1a. A WAAM fabricated part is shown in Fig. 1-1b.

The advantages and benefits of WAAM include:

- WAAM can fabricate parts without using mould, thus saving the cost for moulds and the time for preparing them and leading to shorter lead time and reduced cost.
- The buy-to-fly ratio is significantly reduced. Both the costs for raw material and machining operation can be saved.
- WAAM can produce functionally graded parts (Shen et al., 2016). When WAAM deposits different materials upon one part, each material may be used for its best properties.

- Small production batches are possible, and design changes will cost less.
- Lower level of porosity comparing to the powder based AM products (Wang et al., 2013).

The limitations of WAAM are:

- Current WAAM processes cannot provide a good surface and dimensional precision. They need further machining of the surfaces to obtain these quantities.
- Residual stress exists in parts.

Some materials have been removed from this thesis due to Third Party Copyright. Pages where material has been removed are clearly marked in the electronic version. The unabridged version of the thesis can be viewed at the Lanchester Library, Coventry University.

(a)

(b)

Figure 1-1 Wire and arc additive manufacturing (a) set-up (Martina, 2014 p.28) and (b) WAAM fabricated part (Addison et al., 2015)

Generally, AM process can deposit materials on a substrate. For more economical manufacturing, the substrate can also be used as part of a component. This is called hybrid manufacturing strategy. The study about hybrid manufacturing with the WAAM process has also been studied in Cranfield University (Chen, 2012). A case study of flap track is shown in Fig. 1-2a. Even in some area, real parts have been available. QTD-series insert drills which are made by Mapal, a German-based company, are shown in Fig. 1-2b. The tool shank is machined conventionally and the drill is made by AM.

When using hybrid manufacturing strategy, an interface between AM fabricated alloy and traditional fabricated alloy will inevitably exist. This research is focused on the damage tolerance performance of such inevitable feature, i.e. interface between WAAM fabricated Ti-6Al-4V and wrought Ti-6Al-4V.

Some materials have been removed from this thesis due to Third Party Copyright. Pages where material has been removed are clearly marked in the electronic version. The unabridged version of the thesis can be viewed at the Lanchester Library, Coventry University.

(a) (b)

Figure 1-2 Hybrid manufacturing strategy (a) flap track (Kazanas, 2011) and (b) QTD-series insert drills (Alec, 2015)

1.2 Why damage tolerance?

It is essential for the airworthiness of the civil transport aircraft to fulfil the damage tolerance requirement, which is intended to ensure that if fatigue, corrosion or accidental damage occurs, the remaining structure can withstand reasonable loads without failure until the damage is detected. This means that the damage has to be contained, e.g. grow slowly and remain small enough not to cause a catastrophic accident before the damage could be detected and action could be taken in the routine inspection.

One of important aspects in the damage tolerance analysis is the capability of predicting fatigue crack growth life. When an initial defect exists in a structure, cracks may initiate from it and grow under cyclic loads. If the crack size is longer than a detectable length, then this crack can be detected by non-destructive inspections. If its size is shorter than a so-called “critical crack size”, the structure can still carry working safely even with this crack. Once the crack reaches the critical crack size, the structure may be broken under normal service load. The fatigue crack growth life is defined as the number of cyclic loads when crack grows from detectable length to the critical crack size, see Fig. 1-3. Based on this fatigue crack growth life, an inspection regime can be set up to ensure the detection of damages and prevent the structure from catastrophic fracture (FAA, 1993).

Some materials have been removed from this thesis due to Third Party Copyright. Pages where material has been removed are clearly marked in the electronic version. The unabridged version of the thesis can be viewed at the Lanchester Library, Coventry University.

Figure 1-3 Crack growth history in response to cyclic loads (FAA, 1993)

1.3 Challenges, research questions and approach

Performing damage tolerance analysis for WAAM fabricated parts is very important for application of WAAM technique on aircraft structures. There are some challenges. WAAM made material is different from traditional metal materials in terms of having anisotropic mechanical properties (e.g. Young's modulus, yield strength, fracture toughness and fatigue crack growth rate), inhomogeneous microstructure, as well as containing process induced residual stresses.

According to the Linear Elastic Fracture Mechanics (LEFM), fatigue crack growth rate (FCGR) in materials and part is governed by the crack growth driving force i.e. stress intensity factor, and material resistance to crack growth, that is obtained experimentally and represented by a set of material constants in empirical equations. Crack growth driving force is influenced by residual stress, Young's modulus if the property is anisotropic. Yield strength will affect the effective crack growth driving force due to crack closure effect. On the other hand, material resistance to crack growth is governed by the microstructure characteristics and can be measured by fatigue crack growth experiments. So, these challenges can be separately accounted for when developing predictive tool for fatigue crack growth rates in WAAM fabricated parts. Research approach used in this process is shown in Fig. 1-4.

So, the key research questions of this project are:

- Can fatigue crack growth life be accurately predicted at the WAAM-substrate interface of Ti-6Al-4V parts?

- What is the significance of the residual stress, anisotropic mechanical properties and bi-material microstructure on fatigue life prediction method?

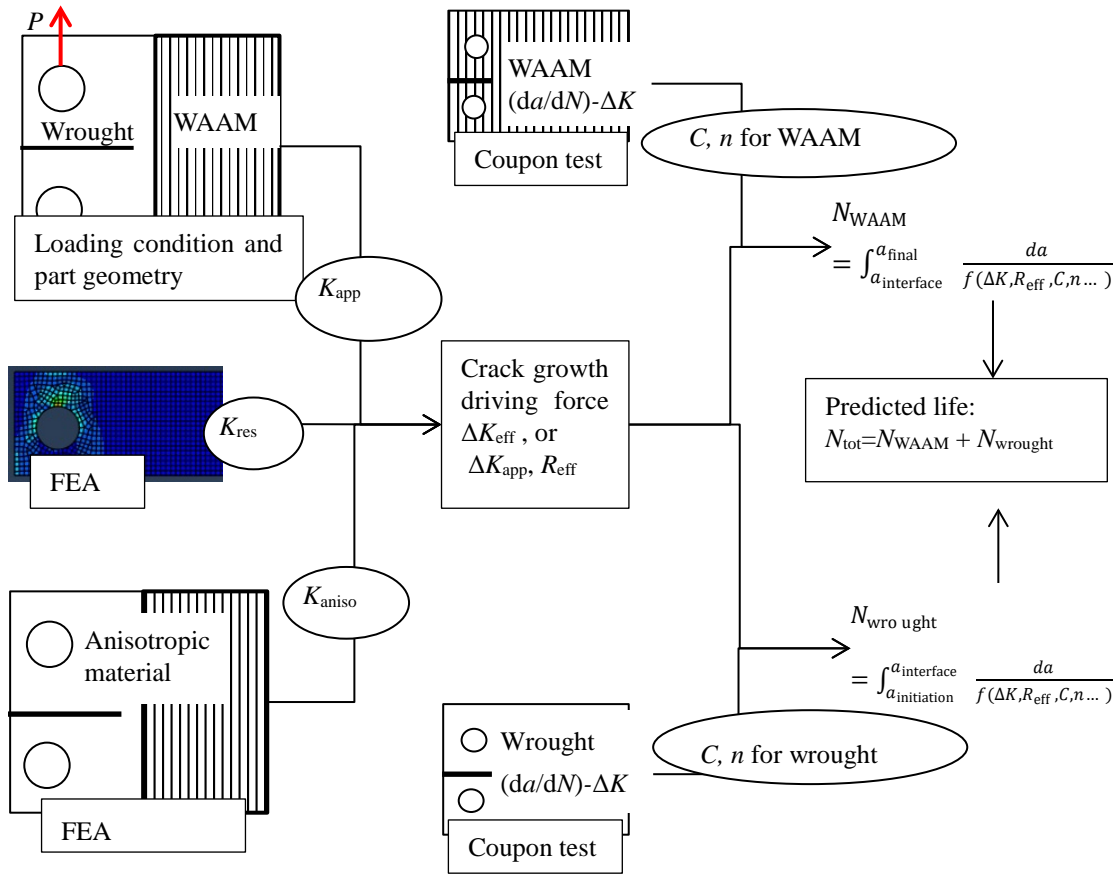


Figure 1-4 Schematic diagram of research approach

1.4 Aim, objectives and scope

This research aims at developing a predictive method for damage tolerance analysis of WAAM made parts, in particular the calculation of fatigue crack growth rate and life, and therefore promoting the application of the WAAM technology to aircraft primary structure as well as guiding the research of WAAM technology in terms of improving the material properties in durability and damage tolerance.

Key Objectives:

- 1) To conduct a complete and comprehensive literature survey on the following topics: a) different AM technologies for making metallic alloys, b) advantages and limitations of each AM process, c) microstructure characteristics of AM built titanium alloys, d) residual stresses arising from the AM process, the magnitude and distribution, and

measurement methods, e) mechanical properties especially the fatigue and damage tolerance properties, i.e. fatigue strength and fatigue crack growth rates, f) fatigue crack growth rate data in Ti-6Al-4V of wrought products and AM made Ti-6Al-4V that account for the microstructure effect and will be used in the fatigue prediction in Objective (7).

- 2) To define a theoretical framework for this project, i.e. theories and methods to be used, in particular, a) the application of finite element method in fracture mechanics, b) empirical method for crack growth rate calculation by incorporating the influences of residual stress and bi-material properties.
- 3) To conduct fatigue crack growth rate measurement for wrought Ti-6Al-4V as a baseline material data to compare with the test results of AM made specimens. The latter is available from collaborators' work.
- 4) To study the influence of anisotropic elastic modulus in WAAM built titanium alloys on the crack tip stress intensity factor calculations.
- 5) To evaluate the magnitude and distribution of residual stress that is retained in the test specimens used in this project. The evaluation is based on test measured residual stresses in a much larger WAAM build sample, from which the test specimens are extracted.
- 6) To determine the crack tip stress intensity factors owing to the applied load and AM process induced residual stresses, using the methods defined in Objective (2).
- 7) To predict the fatigue crack growth rate and life of WAAM made Ti-6Al-4V specimens containing an interface between the wrought and WAAM metals, in two material orientations and three different initial crack positions.
- 8) To analysis the significance of residual stress, anisotropic elastic modulus, and bi-material microstructure on predicting fatigue crack growth rate.

Scope:

Fatigue crack growth behaviour in Ti-6Al-4V alloy made by the WAAM technology is

investigated. It is focused on developing a calculation method for predicting fatigue crack growth rate in AM specimens that contain both process induced residual stress and microstructure changes. The predictive model is demonstrated by predicting fatigue crack growth rate and path in novel AM specimens that contain an interface of two different materials (WAAM made Ti-6Al-4V and Ti-6Al-4V in wrought products; hence bi-material properties in the models), which is a practical design scenario. Calculation of the stress intensity factors has taken account of the aforementioned influential factors. The prediction of fatigue crack growth life is for the constant amplitude load condition and use available generic empirical equations for the crack growth rate. Material mechanical properties, i.e. the elastic modulus, Poisson's ratio, yield strength, and fatigue crack growth rates, are obtained from the literature or collaborators' work.

1.5 Thesis structure

This thesis is organised in three main parts. Part 1 (Chapter 1-3) presents the context, background, state-of-the-art literature survey, and experimental data from related research projects for the PhD research. Part 2 (Chapter 4-6) gives the development of FE models, calculation procedures and results of predicted fatigue crack growth rate and life. Part 3 (Chapter 7) covers key conclusions and recommended future work.

In Part 1, the context, background, research questions and objectives for this PhD are given in Chapter 1. The knowledge used for the research, and the state-of-the-art literature review are given in Chapter 2. Chapter 3 describes the experiments and key results, which were performed by the project collaborators and used in this thesis for validation of the FE models developed in this thesis.

In Part 2, the development of FE models for calculation of stress intensity factors and modelling results are described in Chapter 4 (evaluation of WAAM process induced residual stresses retained in the test specimens) and Chapter 5 (i.e. influence of anisotropic material properties and stress intensity factor due to residual stresses). The prediction of fatigue crack growth life for the bi-material specimens is presented in Chapter 6.

Part 3, Chapter 7 summarises the final conclusions and recommendations for future work.

Chapter 2 Literature Review

This chapter focuses on the detailed literature review on additive manufacturing (AM), various AM processes with particular attention Wire and Arc Additive Manufacturing (WAAM) and the microstructure, mechanical properties (static and fatigue), and fatigue crack growth performance of Ti-6Al-4V produced by AM. The mechanical properties will be compared with Ti-6Al-4V of wrought products and the reason for poor and better performance of WAAM made Ti-6Al-4V will be discussed in detail. In addition, residual stress measurement techniques used in this project will be presented in detail.

2.1 AM processes

AM is a novel near-net-shape fabrication technique to produce solid components. The materials to be deposited are melted by a focused heating source, such as plasma, electron beam or laser and the melted material build a layer. The materials can be of powder or wire. Each layer is a section of a final component. After building all layers, the final three dimensional component is fabricated. AM technologies for metal parts, e.g. wire + arc additive manufacturing (WAAM), electron beam melting (EBM), selective laser sintering (SLS) and selective laser melting (SLM) were reviewed in this section. Attention focused on heating sources, feed metals, temperature and atmosphere of building.

2.1.1 Wire + arc additive manufacturing (WAAM)

WAAM uses an electric arc as heating source to melt the wire material (Martina et al., 2012), as shown in Fig. 2-1. The process is carried out in an inert gas environment to prevent oxidation and contamination. One advantage of WAAM is the lower contamination of wire than powder during feeding process (Mok et al., 2008). Porosity might occur due to the poor quality wire (Wang et al., 2013) and was not observed in work of Wang et al. by preventing contamination. This process has much high deposition rate, 1.8 kg/h (Martina et al., 2012), and is capable of building large scale parts (Williams et al., 2016). The significant heat input leads to high residual stresses in WAAM made parts and several methods have been employed to reduce the influence of residual stress such as symmetrical building, optimising part orientation, and high pressure inter-pass rolling (Martina, 2014). The substrate for WAAM Ti-

6Al-4V is a hot rolled Ti-6Al-4V plate that will be firmly clamped during the deposition process to reduce the deformation due to repeated thermal cycling of the substrate during deposition (Martina et al., 2012).

A similar process is named Shaped Metal Deposition (SMD) in investigation carried out by some researchers (Baufeld and Biest, 2009). SMD uses a tungsten inert gas welding torch as heating source and metal wire is fed during deposition. Similarly, the whole setup was enclosed in an airtight chamber filled with argon.

Some materials have been removed from this thesis due to Third Party Copyright. Pages where material has been removed are clearly marked in the electronic version. The unabridged version of the thesis can be viewed at the Lanchester Library, Coventry University.

Figure 2-1 Schematic of WAAM process equipment (Martina et al., 2012)

2.1.2 Electron beam melting (EBM)

EBM uses a high-energy electron beam to melt the metal powder (Murr et al., 2009), as shown in Fig. 2-2. The metal powder forms a powder bed to feed the material. The process has to be carried out in a vacuum environment. There are two stages in the EBM process. In the first stage, the powder particles are preheated to sinter together. In the second stage, the powder particles are rapidly melted (Facchini et al., 2009). In general, the temperature of powder particles is maintained in a range of 600–700°C. As the powder temperature maintained at high-temperature throughout the process, process induced porosity and residual stresses are lower in EBM made parts.

Some materials have been removed from this thesis due to Third Party Copyright. Pages where material has been removed are clearly marked in the electronic version. The unabridged version of the thesis can be viewed at the Lanchester Library, Coventry University.

Figure 2-2 Schematic of EBM process equipment (Murr et al., 2009) (1) Electron gun assembly; (2) EB focusing lens; (3) EB deflection coils (x-y); (4) powder cassettes; (5) powder (layer) rake; (6) part; (7) build table

2.1.3 Selective laser melting (SLM)

SLM uses a high-energy laser beam to melt the metal powder. The schematic of the process is shown in Fig. 2-3.

Some materials have been removed from this thesis due to Third Party Copyright. Pages where material has been removed are clearly marked in the electronic version. The unabridged version of the thesis can be viewed at the Lanchester Library, Coventry University.

Figure 2-3 Schematic of SLM process equipment (Thijs et al., 2010)

This process is similar to EBM with a difference on the energy source: a laser beam instead of an electron beam. The building process takes place in an inert gas environment (Edwards and Ramulu, 2015) and is maintained at a temperature about 90°C. Like the EBM, the metal powder forms a powder bed. In the SLM, the used metal powder can be recycled (Murr et al., 2012) as the temperature is not as much high as that in the EBM. The thickness of each layer

is around 50 μm . Only 10–20% of the total energy is converted into the laser beam. One of the major concern in SLM is the development of porosity defects that will have adverse effect on the materials performance (Leuders et al., 2013).

2.1.4 Selective laser sintering (SLS)

SLS uses a laser beam to sinter the powder particles. The powder particles are partially melted in the SLS (Vayre et al., 2012). Schematic of the SLS process equipment is shown in Fig. 2-4. Sintering indicates the fusion of powder particles without melting. The thickness of each layer is ranging from 20 μm to 150 μm (Kruth et al., 2005). The SLS process takes place inside an airtight chamber filled with nitrogen gas. The SLS process carries out at a much high temperature which just below the melting point of the powdered metal material.

Some materials have been removed from this thesis due to Third Party Copyright.

Pages where material has been removed are clearly marked in the electronic version. The unabridged version of the thesis can be viewed at the Lanchester Library, Coventry University.

Figure 2-4 Schematic of SLS process equipment (Gibson et al., 2010 p.104)

2.2 Microstructure in Ti-6Al-4V

2.2.1 Wrought products

Ti-6Al-4V contains both α and β phases at room temperature. Heat treatment can influence the microstructure and mechanical properties of Ti-6Al-4V alloy. There are three types of microstructures in titanium alloys of wrought products. The term “wrought” includes forging,

plate, extrusion, sheet and bar. Annealing from the β phase field (β annealed) causes a transformation from β to α phase. The microstructure contains lamellar structure with similar crystal orientation, as shown in Fig. 2-5a. When annealing from the $\alpha + \beta$ phase field combined with hot deformation, microstructure approaching equilibrium equiaxed primary α phase surrounding with retained β phase can be obtained, as shown in Fig. 2-5b. Mill annealing is a such heat treatment which is often given to Ti-6Al-4V of wrought products. Annealing from $\alpha + \beta$ phase (just below β -transus temperature, 980°C) produces a bimodal microstructure, as shown in Fig. 2-5c.

Some materials have been removed from this thesis due to Third Party Copyright. Pages where material has been removed are clearly marked in the electronic version. The unabridged version of the thesis can be viewed at the Lanchester Library, Coventry University.

Figure 2-5 Three types of microstructure in Ti-6Al-4V of wrought products: (a) fully lamellar (Filip et al., 2003), (b) equiaxed (Zhai et al., 2016), (c) bimodal (Boyce and Ritchie, 2001)

Due to the crystallographic texture presents in the α and $\alpha + \beta$ type titanium alloy (Rice et al., 2003 p.5-2), hot-rolled Ti-6Al-4V can develop a texture when a crystallographic direction is closely aligned with the rolling direction. Such texture is well known for promoting anisotropic behaviour with respect to Young's modulus, yield strength, and ultimate tensile strength. Zarkades and Larson (1968) showed that for sheet form Ti-6Al-4V of 1.8 mm thick, the Young's modulus could vary by 30% with direction, as shown in Fig. 2-6a. It is also worth noting that the anisotropy of Young's modulus is greater than for the yield strength and

ultimate tensile strength. Zarkades & Larson (1968) also presented that the yield strength could vary by 17% with direction, and ultimate tensile strength 22%, as shown in Fig. 2-6b&c. However, other Ti-6Al-4V products may not experience hot rolling as much as sheet, so they have not so strong texture and therefore anisotropic mechanical properties.

Some materials have been removed from this thesis due to Third Party Copyright. Pages where material has been removed are clearly marked in the electronic version. The unabridged version of the thesis can be viewed at the Lanchester Library, Coventry University.

Figure 2-6 Anisotropic mechanical properties in Ti-6Al-4V sheet (Zarkades and Larson, 1968):
(a) Young's modulus, (b) yield strength, and (c) ultimate tensile strength.

The source of anisotropic Young's modulus in Ti-6Al-4V of sheet form is texture. As the

directional solidification in AM parts may also result in texture, it is expected that anisotropic Young's modulus exists in AM made Ti-6Al-4V. However, like the texture depends on the thickness of sheet in wrought titanium, the texture in AM made Ti-6Al-4V may also differ between each AM technologies.

2.2.2 WAAM

Ti-6Al-4V parts produced by WAAM experiences complex and repeated thermal heating and cooling cycles during the process. The combined effect of rapid solidification, directional cooling, and phase transformations induced by repeated thermal cycles has an influence on the microstructure of WAAM made Ti-6Al-4V. The macrostructure of the WAAM Ti-6Al-4V contains epitaxially grown large columnar prior- β grains up through the deposited layers, as shown in Fig. 2-7a. The columnar prior- β grains have an average grain width of 1 mm to 2 mm and grow across layers for virtually the entire build height (Wang et al., 2013). Macroscopic bands are also observed in Fig. 2-7a.

In the majority of the WAAM made Ti-6Al-4V, without the top 5 layers or 5 mm, the microstructure is $\alpha + \beta$ lamellar. At the same time, some colonies can be observed. The width of α lamellae depends on the relative position to the macroscopic bands. The microstructure graduated from a finer to a coarser lamellar microstructure, as shown in Fig. 2-7b, and the white bands coincided with the coarsest α lamellae. Between the bands, microstructure is just coarser $\alpha + \beta$ lamellar, as shown in Fig. 2-7c.

The texture in WAAM made Ti-6Al-4V has been reported by Antonysamy (2012 p.185), as shown in Fig. 2-8. A strong $\langle 001 \rangle_{\beta}$ texture could be seen, however, the α phase texture is weak in WAAM. Antonysamy gives the reason that sampling statistic is poor, i.e. the numbers of grains taken for analysis is not enough, as the grains size is very large in the WAAM made Ti-6Al-4V. The texture analysis in both EBM and SLM made Ti-6Al-4V also find the similar result. Formanoir et al. (2016) observed that a strong $\langle 001 \rangle_{\beta}$ texture existed in the building direction of EBM made Ti-6Al-4V, however, the α texture was weaker than the texture of β phase. The reason given by Formanoir et al. is that up to 12 crystallographic α variants could form in each β grain during phase transformation, resulting in a substantial decrease in texture intensity. Simonelli et al. (2014) investigated texture in SLM made Ti-6Al-4V and observed

that α texture is weak. The reason for this given by Simonelli et al. is the multiple variants in columnar β grains.

Some materials have been removed from this thesis due to Third Party Copyright. Pages where material has been removed are clearly marked in the electronic version. The unabridged version of the thesis can be viewed at the Lanchester Library, Coventry University.

Figure 2-7 Microstructure of WAAM made Ti-6Al-4V: (a) macrostructure showing columnar prior- β grains and white bands (Wang et al., 2011), (b) microstructure on white bands, (c) microstructure between the bands (Wang et al., 2013)

Some materials have been removed from this thesis due to Third Party Copyright. Pages where material has been removed are clearly marked in the electronic version. The unabridged version of the thesis can be viewed at the Lanchester Library, Coventry University.

Figure 2-8 Pole figures for WAAM made Ti-6Al-4V: (a) reconstructed β texture and (b) α texture (Antony, 2012 p.185).

By reviewing published microstructure for Ti-6Al-4V of wrought products and WAAM made Ti-6Al-4V, the following findings can be drawn:

- The anisotropic Young's modulus for sheet form Ti-6Al-4V is a result of texture due to hot-rolling.
- The texture is not strong in WAAM, SLM, and EBM made Ti-6Al-4V.
- The microstructure in WAAM made Ti-6Al-4V consists of large columnar prior- β grains with $\alpha + \beta$ lamellar, and some colonies can be observed.

2.3 Mechanical properties of Ti-6Al-4V

2.3.1 In wrought products

Part of mechanical properties at room temperature for Ti-6Al-4V of wrought products can be found in published material specifications, i.e. AMS 4911. The mechanical properties are for mill annealed (MA) or solution treated and aged (STA) heat treatment conditions. So, there are two different heat treatment conditions for Ti-6Al-4V of wrought products and hence different mechanical property requirements for corresponding conditions. Since Ti-6Al-4V plate in MA condition was used in this research as the substrate material in WAAM made samples, the minimum mechanical properties for the MA condition in AMS 4911 are listed in Table 2-1. To understand the effect of heat treatment, mechanical properties for the STA condition are also listed. It can be seen that a difference about 200 MPa exists for the two different heat treatment conditions. Two orientations, longitudinal and long-transverse, have the same minimum values.

Table 2-1 Minimum value of ultimate tensile strength, yield strength and elongation for MA and STA conditions Ti-6-4 plate (AMS 4911J, 2003), in both longitudinal and long transvers orientations; thickness range 4.8–19 mm, room temperature

| Heat treatment | σ_{UTS} (MPa) | σ_{YS} (MPa) | e (%) |
|----------------|-------------------------|------------------------|------------|
| MA | 895 | 825 | 10 |
| STA | 1100 | 1000 | 5 |

Two important aspects are noted:

- 1) these data are the minimum values. The minimum value means that any measured mechanical property must be higher than the minimum value; otherwise the tested

plate is unqualified products. To make a comparison of mechanical property between wrought Ti-6Al-4V and AM made parts, the minimum value should not be used. The reason is that actual mechanical properties for wrought Ti-6Al-4V are also higher than the minimum values. For this reason, measured mechanical properties for wrought Ti-6Al-4V were summarized.

- 2) each of these minimum values is for a specific heat treatment condition. As heat treatment can significantly alter the mechanical properties, about 200 MPa in minimum values requirement, the comparison should be made for the same heat treatment condition. To evaluate the advantage of AM technology, the way of comparing as-built condition AM made Ti-6Al-4V with MA condition wrought Ti-6Al-4V is not correct.

Measured mechanical properties for Ti-6Al-4V in MA condition in open literature are listed in Table 2-2. It is noted that both the ultimate tensile strength and the yield strength measured by Facchini et al. (2009) are lower than the minimum requirements in the aforementioned specifications. As shown later, mechanical properties for both EBM made Ti-6Al-4V and wrought Ti-6Al-4V measured by Facchini et al. are lower. This could mean that the variation in their experiments is large. In contrast to Facchini et al., mechanical properties for both EBM made parts and wrought Ti-6Al-4V measured by Murr et al. (2009) are higher. Therefore, the average of mechanical properties only includes the data from Donachie, Rice et al., and Wang et al. A margin between averaged mechanical properties and the minimum values are also shown in the same table. It can be seen that the actual averaged mechanical properties are higher than the minimum requirements by around 100 MPa in terms of ultimate tensile strength and yield strength. Such margin is very important for requirements to make sure at least 99% of measured data are expected to equal or exceed the required minimum value with a confidence of 95% (Rice et al., 2003 p.9-9).

In addition to the static properties, fatigue and fracture toughness properties have great influence on material performance. In terms of plane strain fracture toughness, K_{IC} , as the thickness of tested plate might not thick enough to obtain a plane strain condition, K_{IC} is often measured from thicker forging and measured data are listed in Table 2-3. Young's modulus for Ti-6Al-4V is also listed in Table 2-3. It is noted that the thickness of forging or plate is not thin enough to produce enough texture and hence could not give rise to significant anisotropic Young's modulus. Therefore, Young's modulus for Ti-6Al-4V of wrought products (sheet excluded) is regarded as isotropic. The high cycle fatigue property for wrought Ti-6Al-4V in Metallic Materials Properties Development and Standardization (MMPDS) handbook (Rice et

al., 2003 p.5-69) are shown in Fig. 2-9. It can be seen that the endurance limit for Ti-6Al-4V of wrought products is about 520 MPa at room temperature.

Table 2-2 Measured ultimate tensile strength, yield strength and elongation for MA condition Ti-6-4 at room temperature

| Products | σ_{UTS} (MPa) | σ_{YS} (MPa) | e (%) | Heat treatment | References |
|----------|-------------------------|------------------------|----------------|-----------------------------|----------------------------|
| Bar | 870 \pm 10 | 790 \pm 20 | 18.1 \pm 0.8 | MA | (Facchini et al., 2009) |
| Forging | 1230 | 1170 | 12 | As-built, (1040°C forging) | (Murr et al., 2009) |
| Forging | 1290 | 1220 | 14 | STA | (Murr et al., 2009) |
| Bar | 945 | 890 | – | MA | (Rice et al., 2003 p.5-67) |
| – | 970 | 900 | 17 | MA | (Donachie, 2000 p.103) |
| – | 1069 | 945 | 10 | MA | (Donachie, 2000 p.24) |
| Bar | 1033 | 950 | 11.7 | MA | (Wang et al., 2013) |
| Average | 1005 | 920 | 14 | MA | – |
| Margin | ~110 | ~100 | ~3 | MA | – |

Table 2-3 Young's modulus and fracture toughness for wrought Ti-6-4 at room temperature

| E^a (GPa) | K_{IC}^b (MPa \sqrt{m}) | Heat treatment |
|----------------|---------------------------------|-------------------|
| 110–117 | 44–66 | MA |

^a Data from (Rice et al., 2003 p.5-53). ^b Data from (Donachie, 2000 p.101).

Some materials have been removed from this thesis due to Third Party Copyright. Pages where material has been removed are clearly marked in the electronic version. The unabridged version of the thesis can be viewed at the Lanchester Library, Coventry University.

Figure 2-9 *S-N* data (test results and best-fit curve) for Ti-6Al-4V of extrusion in MA condition at room temperature, longitudinal direction, unnotched specimens (Rice et al., 2003 p.5-69)

2.3.2 Powder based AM (EBM, SLM)

ASTM F2924 specification gives the minimum value requirements for the mechanical properties of powder bed fusion AM technology, as shown in Table 2-4. Mechanical property requirements for all X, Y, and Z-principal directions equal to the requirements of wrought Ti-6Al-4V in MA condition.

Table 2-4 The minimum value of ultimate tensile strength, yield strength and elongation for AM made Ti-6-4 (ASTM Standard F2924, 2014) (in stress relieved or annealed condition), X, Y, and Z-principal direction, at room temperature

| σ_{UTS} (MPa) | σ_{YS} (MPa) | e (%) | Reduced Area (%) |
|-------------------------|------------------------|------------|---------------------|
| 895 | 825 | 10 | 15 |

The ultimate tensile strength and yield strength of EBM and SLM made Ti-6Al-4V reported in the open literature are listed in Table 2-5. The data were obtained by using machined and polished specimens, and the specimens were directly built rather than being extracted from a much larger part. Hot isostatic pressing (HIP) also was applied to some EBM made specimens.

Murr et al. (2009) concluded that EBM made Ti-6Al-4V part was comparable in strength and elongation to the Ti-6Al-4V of wrought products. Facchini et al. (2009) concluded that EBM made Ti-6Al-4V in as-built condition has higher ultimate tensile strength and the yield strength than wrought Ti-6Al-4V in MA condition. Simonelli et al. and Formanoir et al. did not give conclusions about comparing between AM Ti-6Al-4V and wrought Ti-6Al-4V.

By comparing the average mechanical properties for MA condition with the measured mechanical properties of SLM and EBM made parts, it can be found that EBM or SLM made Ti-6Al-4V in as-built condition have higher yield strength and ultimate tensile strength than that of wrought products in MA condition, but lower than wrought products in STA condition.

As has been noted, mechanical properties measured by Facchini et al. (2009) are always lower in both wrought products and EBM made parts. In contrast to Facchini et al., data measured by Murr et al. (2009) are always higher. The average mechanical properties for STA condition is calculated by adding the minimum value in specification to the margin value, around 100 MPa, which is obtained from MA condition. It seems that the major factor which influences

the mechanical properties of Ti-6Al-4V part is heat treatment condition rather than which processing is used to build Ti-6Al-4V parts.

Table 2-5 Measured ultimate tensile strength, yield strength and elongation of SLM and EBM made Ti-6-4 at room temperature

| Process | σ_{UTS} (MPa) | σ_{YS} (MPa) | e (%) | Heat treatment | References |
|---------|-------------------------|------------------------|----------------|---|--------------------------|
| EBM | 1200 | 1150 | 25 | As-built | (Murr et al., 2009) |
| | 1150 | 1100 | 16 | | |
| EBM | 915 ± 10 | 870 ± 10 | 13.1 ± 0.4 | As-built, 5 specimens | (Facchini et al., 2009) |
| EBM | 870 ± 10 | 795 ± 10 | 13.7 ± 1.0 | HIP, 5 specimens | (Facchini et al., 2009) |
| EBM | 1060 | 997 | 8.8 | As-built, Across layers, 4 specimens | (Formanoir et al., 2016) |
| EBM | 1120 | 1063 | 7.1 | As-built, Along layers, 4 specimens | (Formanoir et al., 2016) |
| SLM | 1143 ± 6 | 978 ± 5 | 11.8 ± 0.5 | As-built, Along layers, 4 specimens | (Simonelli et al., 2014) |
| SLM | 1117 ± 3 | 967 ± 10 | 8.9 ± 0.4 | As-built, Across layers, 4 specimens | (Simonelli et al., 2014) |
| SLM | 1057 ± 8 | 958 ± 6 | 12.4 ± 0.7 | Stress relieved, Along layers, 4 specimens | (Simonelli et al., 2014) |
| SLM | 1052 ± 11 | 937 ± 9 | 9.6 ± 0.9 | Stress relieved, Across layers, 4 specimens | (Simonelli et al., 2014) |
| SLM | 1080 ± 30 | 1008 ± 30 | 1.6 | As-built, Across layers, 5 specimens | (Leuders et al., 2013) |
| average | 1100 | 1001 | 7.7 | As-built | – |

Both SLM (Simonelli et al., 2014) and EBM (Formanoir et al., 2016) made Ti-6Al-4V exhibit a slightly anisotropic mechanical behaviour. Specimens that are loaded across layers have a lower yield strength and ultimate tensile strength than those along layers. Simonelli et al. (2014) explained that interlayer porosity is the source of such anisotropic mechanical properties, as tensile specimens that are loaded across layers have more number of layers.

Fatigue and fracture toughness properties of AM produced Ti-6Al-4V has also been reviewed and are shown in Table 2-6 and Table 2-7.

Table 2-6 Measured fatigue performance of SLM and EBM made Ti-6-4 at room temperature

| Process | Fatigue performance, (Max stress) | Heat treatment, surface condition | References |
|---------|--|---|----------------------------------|
| EBM | 700 MPa, $R = 0.1$, 2×10^6 cycles | HIPed, machined surface | (Greitemeier et al., 2016) |
| EBM | 391 ± 21 MPa, $R = -1$, 2×10^6 cycles | As-built, machined surface | (Facchini et al., 2009) |
| EBM | 441 ± 42 MPa, $R = -1$, 2×10^6 cycles | HIPed, machined surface | (Facchini et al., 2009) |
| SLM | 620 MPa, $R = -1$, 2×10^6 cycles | HIPed, machined surface | (Leuders et al., 2013) |
| SLM | 240 MPa, $R = -0.2$, 0.2×10^6 cycles | As-built, polished surface, along layers | (Edwards and Ramulu, 2014) |
| SLM | 170 MPa, $R = -0.2$, 0.2×10^6 cycles | As-built, polished surface, along layers | (Edwards and Ramulu, 2014) |
| SLM | 100 MPa, $R = -0.2$, 0.2×10^6 cycles | As-built, polished surface, across layers | (Edwards and Ramulu, 2014) |
| SLM | 700 MPa, $R = 0.1$, 2×10^6 cycles | HIPed, machined surface | (Greitemeier et al., 2016) |

Greitemeier et al. (2016) concluded that the high cycle fatigue properties are greatly influenced by the presence of porosity in polished specimens. Leuders et al. (2013) found that the pores within the samples have a significant effect on the fatigue behaviour of SLM Ti-6Al-4V. Edwards and Ramulu (2014) found that the fatigue performance of SLM Ti-6Al-4V were significantly lower than that of wrought products largely due to porosity and residual stresses. All published fatigue properties and conclusions show that the SLM and EBM made Ti-6Al-4V in as-built condition have much lower high cycle fatigue properties than wrought products in MA condition. However, HIP processing can improve the high cycle fatigue properties (Leuders et al., 2013).

Fracture toughness for EBM and SLM Ti-6Al-4V reported in the literature have significant scatter. The fracture toughness of AM Ti-6Al-4V are not always higher than that of wrought products. This might be attributed to porosity, microstructure and residual stresses in AM specimens. Heat treatment and HIP processing might not improve the fracture toughness of

EBM made Ti-6Al-4V due to elevated temperature, 600–700°C, during building. Plane strain fracture toughness for SLM made Ti-6Al-4V is lower than that of wrought products in MA condition.

Table 2-7 Measured fracture toughness of SLM and EBM made Ti-6-4

| Process | Fracture toughness (MPa√m) | Specimen size (mm) | Heat treatment | References |
|---------|-------------------------------|-----------------------|--------------------------------------|----------------------------|
| EBM | 119 (K_Q) | $W = 50, B = 25$ | HIPed | (Greitemeier et al., 2016) |
| EBM | 106.5 (K_Q) | $W = 50, B = 25$ | Annealed | (Greitemeier et al., 2016) |
| EBM | 110 ± 8.9 (K_Q) | $W = 80, B = 40$ | As-built, across layers, 5 specimens | (Edwards et al., 2013) |
| EBM | 102 ± 7.4 (K_Q) | $W = 80, B = 40$ | As-built, across layers, 5 specimens | (Edwards et al., 2013) |
| SLM | 52.4 ± 3.48 (K_{IC}) | $W = 25, B = 12.5$ | As-built, 10 specimens | (Hooreweder et al., 2012) |
| SLM | 15–30 (K_{IC}) | $W = 25, B = 12.5$ | As-built, 6 specimens | (Cain et al., 2015) |

Currently, limited attention is given to Young's modulus of AM made Ti-6Al-4V. Available data of Young's modulus for SLM or EBM are shown in Table 2-8. It can be seen that the Young's modulus for SLM and EBM made Ti-6Al-4V are similar to that of wrought products. Anisotropic Young's modulus is not observed. However, available stress strain curves, in Fig. 2-10, shown that scatter appears for Young's modulus in Vertical-Z specimens, which are loaded across layers. The reason for such scatter might also be the interlayer porosity.

Table 2-8 Measured Young's modulus of SLM and EBM made Ti-6-4 at room temperature

| Process | Young's modulus E (GPa) | orientation | Heat treatment | References |
|---------|------------------------------|---------------|-----------------|--------------------------|
| EBM | 118 ± 5 | – | As-built | (Facchini et al., 2009) |
| SLM | 119 ± 7 | Across layers | As-built | (Simonelli et al., 2014) |
| SLM | 117 ± 6 | Across layers | Stress relieved | (Simonelli et al., 2014) |
| SLM | 115 ± 6 | Along layers | As-built | (Simonelli et al., 2014) |
| SLM | 113 ± 9 | Along layers | Stress relieved | (Simonelli et al., 2014) |

Some materials have been removed from this thesis due to Third Party Copyright. Pages where material has been removed are clearly marked in the electronic version. The unabridged version of the thesis can be viewed at the Lanchester Library, Coventry University.

Figure 2-10 Stress strain curves of the as-built and polished SLM made Ti-6Al-4V (Formanoir et al., 2016) in X-direction (a) and Z-direction (b).

By reviewing published mechanical properties for SLM, EBM and wrought Ti-6Al-4V, the following findings can be drawn:

- Both the EBM and SLM Ti-6Al-4V in as-built condition have higher yield strength and ultimate tensile strength than that of the wrought Ti-6Al-4V in MA condition, but lower than STA condition.
- Both EBM and SLM Ti-6Al-4V exhibit anisotropic mechanical properties. Specimens that are loaded along layers have a higher ultimate tensile strength and yield strength due to less interlayer porosity.
- Both EBM and SLM Ti-6Al-4V in as-built condition have much lower high cycle fatigue properties than wrought products in MA largely due to porosity presence in EBM and SLM made parts.
- EBM Ti-6Al-4V have higher fracture toughness than that of wrought products.
- Young's modulus for both SLM and EBM Ti-6Al-4V are similar to that of wrought products (sheet excluded). Young's modulus are isotropic for them, however, across layers direction have higher scatter than along layers direction.

2.3.3 Wire base AM (WAAM, SMD)

Measured ultimate tensile strength, yield strength and elongation for WAAM and SMD made Ti-6Al-4V in open literature are listed in Table 2-9. It can be seen that the ultimate tensile strength and yield strength for both SMD and WAAM Ti-6Al-4V are slightly lower than that

of wrought products in MA condition. In general, the ultimate tensile strength and yield strength in along layers orientation are higher than that in across layers orientation. On the other hand, the elongation in across layers orientation is higher. The source of anisotropic elongation is prior- β grain boundaries (Wang et al., 2013).

Table 2-9 Measured ultimate tensile strength, yield strength and elongation for WAAM and SDM Ti-6-4 at room temperature

| Process | σ_{UTS} (MPa) | σ_{YS} (MPa) | e (%) | Heat treatment, orientation | References |
|---------|-------------------------|------------------------|----------------|--|------------------------------|
| SMD | 963 ± 25 | 890 ± 30 | 8 ± 2 | As-built, 4 specimens, along layers | (Brandl et al., 2010) |
| SMD | 937 ± 20 | 860 ± 14 | 16.5 ± 2.5 | As-built, 4 specimens, across layers | (Brandl et al., 2010) |
| SMD | 980 ± 10 | 915 ± 15 | 6.5 ± 2.5 | 600 °C /4 h, along layers, 4 specimens | (Brandl et al., 2010) |
| SMD | 975 ± 35 | 890 ± 17 | 12 ± 2.5 | 600 °C /4 h, across layers, 4 specimens | (Brandl et al., 2010) |
| SMD | 960 ± 30 | 898 ± 18 | 13.5 ± 1.5 | 843 °C/2 h, along layers, 4 specimens | (Brandl et al., 2010) |
| SMD | 930 ± 20 | 855 ± 20 | 20.5 ± 2 | 843 °C/2 h, across layers, 4 specimens | (Brandl et al., 2010) |
| SMD | 983 ± 22 | – | – | As-built, along layers, 6 specimens | (Baufeld and Biest, 2009) |
| SMD | 953 ± 14 | – | – | As-built, across layers, 7 specimens | (Baufeld and Biest, 2009) |
| WAAM | 910 | 800 | 13 | As-built, across layers, 12 specimens | (Antonyamy, 2012 p.271) |
| WAAM | 970 | 870 | 6 | As-built, along layers, 6 specimens | (Antonyamy, 2012 p.271) |

Fatigue performance of WAAM and SMD made Ti-6Al-4V in open literature are listed in Table 2-10. Both WAAM (Wang et al., 2013) and SMD (Brandl et al., 2010) Ti-6Al-4V have higher fatigue resistance than that of the wrought products in MA condition. No significant difference between orientations was observed.

Fracture toughness of WAAM Ti-6Al-4V is listed in Table 2-11. This work was performed at Cranfield University, and the author took part in this work. Fracture toughness of WAAM Ti-6Al-4V was comparable with or greater than that of the wrought products (Zhang, X. et al., 2017). In general, the conditional fracture toughness for cracks which propagate across the layers are higher than that along the layers. The reason for this orientation-dependant

difference is banding.

Table 2-10 Measured fatigue performance of WAAM and SMD made Ti-6-4 at room temperature

| Process | Fatigue performance, (Max stress) | Heat treatment, surface condition | References |
|---------|---|--|-----------------------|
| WAAM | >600 MPa, $R = 0.1$, 10×10^6 cycles | As-built, surface roughness 0.4 μm | (Wang et al., 2013) |
| SMD | >770 MPa, $R = 0.1$, 10×10^6 cycles | As-built, 17 specimens; 843 °C/2 h, 17 specimens, polished surface | (Brandl et al., 2010) |

Table 2-11 Fracture toughness of WAAM Ti-6-4 in as-built condition (Zhang, X. et al., 2017).

| Plane strain fracture toughness K_{IC} (MPa $\sqrt{\text{m}}$) | Conditional fracture toughness K_Q (MPa $\sqrt{\text{m}}$) | Specimen size (mm) | Crack orientation | Used wire |
|---|---|-----------------------|-------------------|-----------|
| 73.2 | – | $W = 70, B = 18.5$ | Across layers | Grade 5 |
| – | 70.9 | $W = 70, B = 18.5$ | Along layers | Grade 5 |
| – | 82.1 | $W = 70, B = 19.1$ | Across layers | Grade 5 |
| – | 74.3 | $W = 70, B = 19.2$ | Along layers | Grade 5 |
| – | 96.2 | $W = 70, B = 18.0$ | Across layers | Grade 23 |
| – | 95.1 | $W = 70, B = 18.0$ | Along layers | Grade 23 |

Young's modulus for WAAM Ti-6Al-4V are 117 GPa and 136 GPa for specimens that across the layers, 124 GPa and 123 GPa for along the layers (Lorant, 2010 p.79). It can be seen that WAAM Ti-6Al-4V has higher Young's modulus than wrought products. Again, high scatter appears for specimens that are across the layers.

By reviewing published mechanical properties for SLM, EBM, WAAM and SMD made Ti-6Al-4V, the following findings can be drawn:

- Both SMD and WAAM Ti-6Al-4V in as-built condition have lower ultimate tensile strength and yield strength than that of wrought products in MA condition.
- A slightly anisotropic mechanical behaviour exists in WAAM and SMD made parts. Specimens that are loaded along layers have a higher ultimate tensile strength and yield strength. For both WAAM and SMD Ti-6Al-4V, the elongation in across layers orientation is higher.
- Both WAAM and SMD Ti-6Al-4V have higher fatigue resistance than that of wrought

products in MA condition.

- Both WAAM and SMD Ti-6Al-4V in as-built condition have comparable or greater fracture toughness than that of wrought products in MA condition. SLM Ti-6Al-4V has lower fracture toughness.
- For WAAM made Ti-6Al-4V, cracks that are across the layers have higher fracture toughness than that along the layers.
- WAAM Ti-6Al-4V has slightly higher Young's modulus than wrought products. At the same time, specimens that are loaded across layers have higher scatter in Young's modulus.

2.4 Residual stress measurement techniques

Residual stress measurement techniques can be divided into destructive and non-destructive methods (Withers et al., 2008). In practice, residual stress cannot be measured directly; instead the stress must be inferred from a measure of the elastic strain, displacement or secondary quantity, such as the speed of sound, magnetic signature, hardness, and fatigue crack growth rate (Bao and Zhang, 2010) that can be related to the stress.

2.4.1 Non-destructive techniques

Two mostly used non-destructive techniques are neutron diffraction and X-ray diffraction, which usually measure the elastic strain of specific atomic lattice planes. Both neutron and X-ray diffraction provides the elastic lattice strains at a particular location through *Bragg's Law* by measuring the change of the strained lattice spacing with respect to a stress-free reference lattice spacing (Withers and Bhadeshia, 2001). As neutron diffraction can provide a large penetration, > 20 mm of steel, it is well established for the study of residual stress deep inside components (Ganguly et al., 2006). Unless applied in combination with destructive layer removal, conventional X-ray diffraction is limited to a depth of a few microns from the surface of components (Withers et al., 2008).

To obtain reliable residual stress measurement, it is usually necessary to have an accurate measure of d_0 , the stress-free spacing, for both neutron diffraction and X-ray diffraction (Withers and Bhadeshia, 2001).

Although neutron diffraction provides three components of residual stress, the profile of residual stress can only be obtained by measuring points at least along a line (for thin component) that is perpendicular to the desired stress component. As only one line is measured in most published experiments on AM made parts, the residual stress profile can only be built for one stress component. For the neutron diffraction method, as the profile of residual stress is a combination of many data points, it is sometimes not self-balanced.

2.4.2 Destructive techniques

The destructive techniques infer the residual stress from the displacement or elastic strain incurred by completely or partially relieving the residual stress by removing material or introducing crack or slot (Withers et al., 2008). The destructive techniques include layer removal method (Kandil et al., 2001), slitting method (Cheng and Finnie, 2007), incremental hole drilling (Sicot et al., 2003) and contour method (Prime, 2001).

Layer Removal:

Layer removal technique relates the change of curvature or strain to the residual stresses. It is applicable only to samples with simple geometries such as plates. This technique provides only one-dimensional macrostress profile. When layers are removed from one side of the specimen containing residual stresses, the remaining stresses become unbalance and the specimen will bend. The strain at the opposite side or curvature of the specimen depends on the average of original residual stress present in the layer that has been removed and on the elastic properties of the remainder of the specimen. By carrying out a series of strain measurements after successive layer removals one-dimensional profile of macrostress in the original plate can then be deduced (Kandil et al., 2001).

The layer removal technique has been used successfully for coatings. An assumption that residual stresses to be measured vary only in the direction normal to the layers is made (Cheng and Finnie, 2007 p.5). This means that the measured residual stress by removing one layer is an average of stresses over the whole layer. Like neutron and X-ray diffraction techniques, the profile of residual stress obtained by the layer removal might be not self-balanced.

Slitting Method:

Slitting method involves cutting a small slot to release the residual stress in the slot while the strain at the opposite side is monitored. By steadily increasing the depth of the slot, the profile of residual stress normal to the plane of slot can be obtained (Cheng and Finnie, 2007, p. 6)

The slitting method is much faster to carry out than the layer removal method. It is worth noting that the similar assumption in the layer removal method is made. This means that the measured residual stress for one increment of slot is an average of stresses through the thickness. Again, the profile of residual stress obtained by the slitting method might be not self-balanced.

Incremental Hole-Drilling:

The incremental hole-drilling involves drilling a small hole around which the strain is measured. The introduction of the hole relaxes the residual stresses at that location and causes the local strains on the surface around the hole to change correspondingly. When incrementally deepening the hole, the variation of residual stress with depth can be deduced (Sicot et al., 2003).

It is often referred to as a 'semi-destructive' technique, since the small hole will not significantly influence the structural integrity of the part. However, it is difficult to obtain reliable measurements much beyond a depth equal to the diameter. In most cases, the drilled hole is blind with a depth which is about its diameter (Sicot et al. 2004). This method provides the two in-plane components of the stress tensor. The incremental hole-drilling provides residual stresses for a small volume like the neutron and X-ray diffraction rather than the layer removal and the slitting methods.

Contour Method:

The contour method involves making a cut to separate a part and measuring the contour of new surface in order to determine the displacements caused by releasing of the residual stresses. By applying the opposite of the measured displacements to the surface as a displacement boundary condition in a finite element model, the original residual stresses normal to the plane of the cut can be deduced (Prime, 2001).

The contour method provides two dimensional residual stress map. Although one components of stress tensor are provided, these are enough to build profile of residual stress. Furthermore, the residual stress profile measured by the contour method is self-balanced. Unlike the layer removal method, the obtained residual stresses are original stresses at the plane of cut rather than an average of stresses along the component of stress tensor.

2.5 Fatigue crack growth rates of Ti-6Al-4V

2.5.1 Fatigue crack growth rates in wrought products

2.5.1.1 Effects of microstructure

Up to now, there is no reliable quantitative relationship between fatigue crack growth rate (FCGR) and microstructure in Ti-6Al-4V alloy. Available qualitative relationship which describes effects of microstructure on FCGR is summarized.

Three different types of microstructures have been found in annealed Ti-6Al-4V alloy: fully lamellar (also called basket weaves), bimodal (also called duplex), and equiaxed (also called globular), see Fig. 2-5. Amongst these three, the equiaxed microstructure, (commonly present in wrought products), yields the highest crack growth rates (Donachie 2000 p. 105). The fully lamellar microstructure, which is often observed in AM parts, can achieve the lowest FCGR. In fully lamellar microstructure, the prior- β grain size the $\alpha + \beta$ lamellar colony size and the thickness of α lamellae are important parameters affecting the FCGR. FCGR increases with decreasing α lamellae size and colony size (Shademan et al., 2004). Colony refers to parallel platelets belonging to the same variant of the Burgers relationship. A schematic definition of lamellar parameters is shown in Fig. 2-11.

Some materials have been removed from this thesis due to Third Party Copyright. Pages where material has been removed are clearly marked in the electronic version. The unabridged version of the thesis can be viewed at the Lanchester Library, Coventry University.

Figure 2-11 Schematic parameters of lamellar microstructure: D : prior- β grain size, d : colony size of the $\alpha + \beta$ lamellar, t : thickness of α lamellae (Sieniawski et al., 2013)

Previously mentioned three types of microstructure are obtained in annealing processes which have a low cooling rate. However, air cooling, which is an intermediate cooling rate, may occur during depositing material in an AM process, and then can give fine acicular (also called needlelike) α phase. If the cooling rate increases further, the martensitic phase α' can be obtained (Hooreweder et al., 2012). These two types of microstructure can also be obtained in conventional Ti-6Al-4V alloy of wrought products. However, research on FCGR for these microstructures in conventional Ti-6Al-4V of wrought products has not been found.

Another important parameter affecting FCGR is the α phase along the prior- β grain boundary which weakens the grain boundary and promotes crack initiation and propagation and therefore leads to premature failure. In conventional wrought Ti-6Al-4V, the grain boundary α phase is broken by hot working, forging, to avoid premature failure (Donachie, 2000 p.100). As will be shown later in Section 3.6 or Fig. 6-8, FCGR increased due to crack propagation along the prior- β grain boundary in A3 specimen which is WAAM made Ti-6Al-4V.

2.5.1.2 Effects of stress ratio

The effect of stress ratio R on FCGR has been researched quantitatively. One important feature of R ratio effect is dependence on microstructure. This means that effects of stress ratio R vary with microstructure. FCGR for α - β forging (which may have bimodal microstructure, forging temperature between pure α and pure β phase), and MA condition are compared in Fig. 2-12. These FCGR data are taken from material database for Harter T-method in AFGROW. It can be seen that, at a given ΔK the effect of stress ratio R is greater for bimodal microstructure than equiaxed microstructure (a factor of 2.5 and 4 can be found in equiaxed and bimodal microstructure when compared at $R = 0.1$ and 0.5). The above mentioned factor is determined by $(da/dN)_{R1}/(da/dN)_{R2}$.

Although the effect of R is investigated quantitatively, the variation in microstructure with respect to various manufacturing conditions can have significant effect on FCGR. Therefore, in order to simplify the comparison, FCGR data for similar microstructure, i.e. equiaxed microstructure (wrought Ti-6Al-4V in MA condition) is compared and presented below.

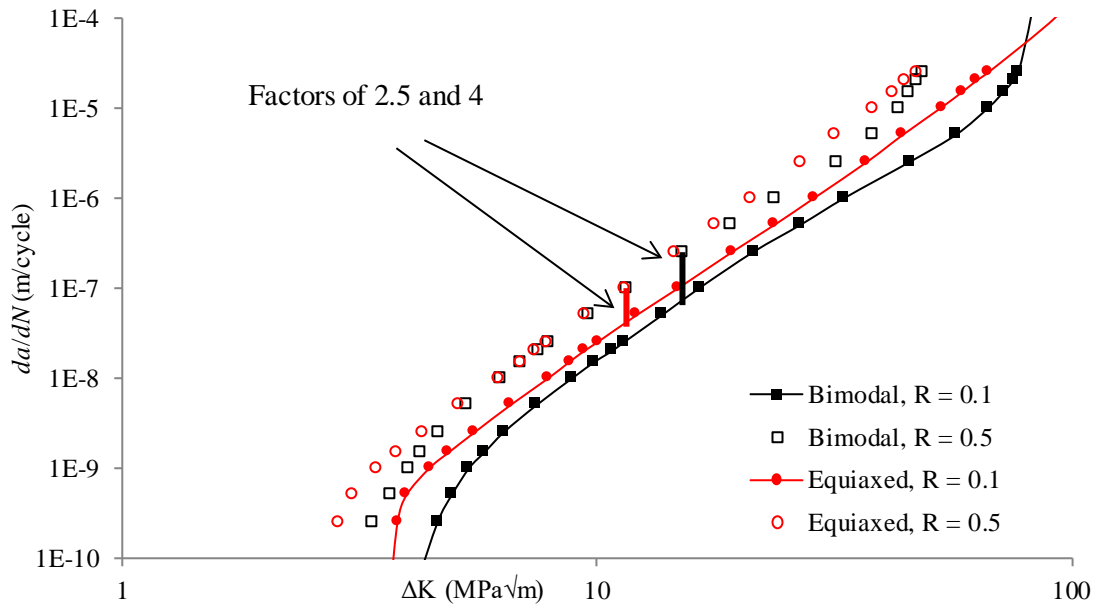


Figure 2-12 Effect of stress ratio R on FCGR for wrought Ti-6Al-4V, comparison between bimodal and equiaxed microstructures. Re-plotted from AFGROW

When R changed from 0.1 to 0.5, the FCGR of equiaxed Ti-6Al-4V alloy can be increased by a factor of 2 to 10, if all data were considered together. FCGR data conducted by Feddersen and Hyler (1971), Shih and Wei (1973), and Harrington (n.d.) are shown in Fig. 2-13a, Fig. 2-13b, and Fig. 2-14, respectively. These data are compared together, see Fig. 2-15. It can be seen that, when R ratio is changed from 0.1 to about 0.5 and range of stress intensity factor, ΔK , is between 20 to 40 MPa \sqrt{m} , FCGR can be increased by a factor of 2 to 3. The FCGR data conducted by Dubey et al. (1997) and Shademan et al. (2004) are presented in Fig. 2-16 and Fig. 2-17, respectively. Those data are also compared together, see Fig. 2-18. It can be seen that, when R ratio changed from about 0.1 to 0.5 and ΔK is under 20 MPa \sqrt{m} , FCGR can be increased by a factor of around 10.

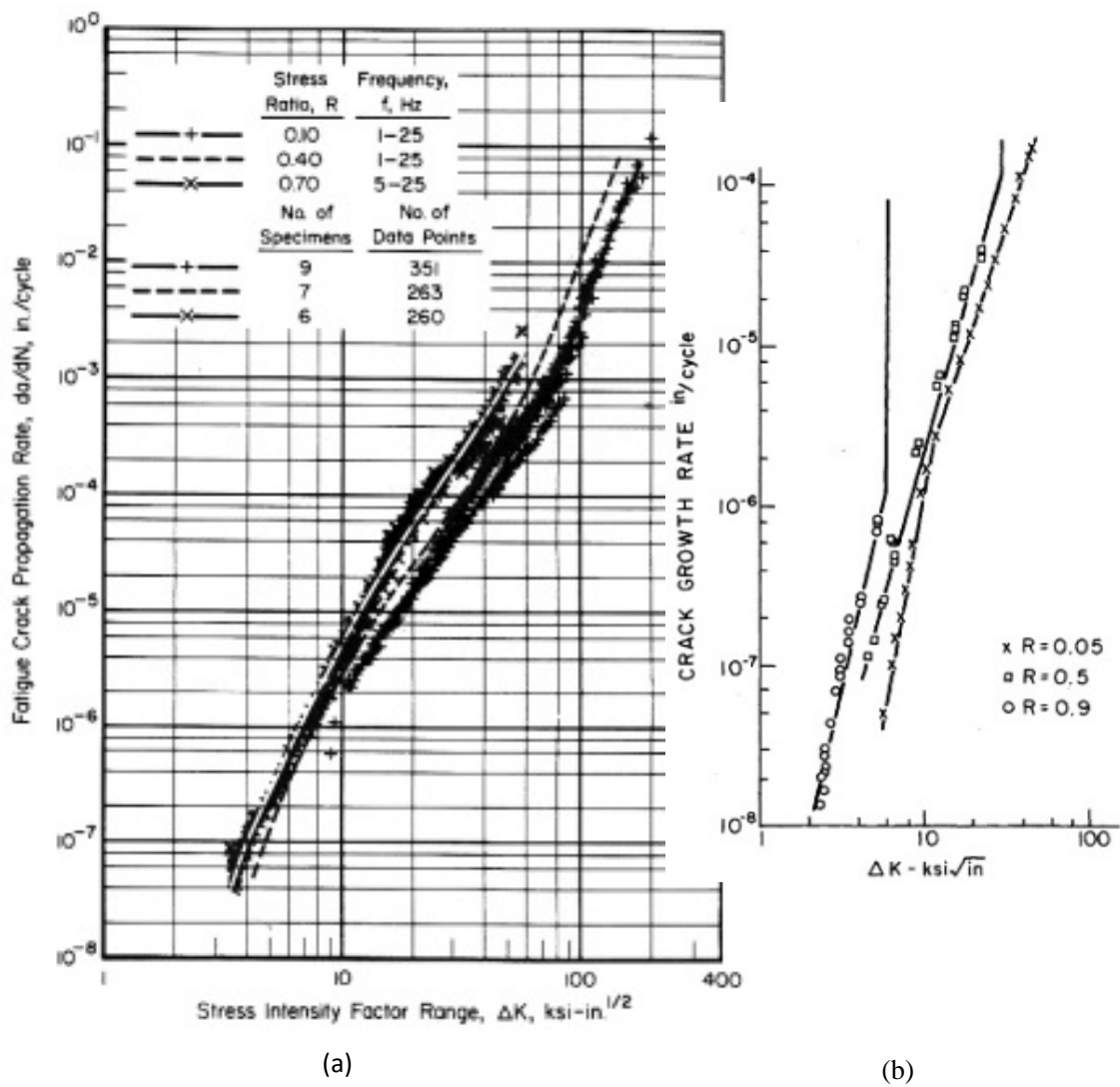


Figure 2-13 Fatigue crack growth rates for Ti-6Al-4V of wrought products in mill annealed condition, a) by Feddersen & Hyler (1971), b) by Shih & Wei (1973)

Some materials have been removed from this thesis due to Third Party Copyright. Pages where material has been removed are clearly marked in the electronic version. The unabridged version of the thesis can be viewed at the Lanchester Library, Coventry University.

Figure 2-14 Fatigue crack growth rates for Ti-6Al-4V of wrought products in mill annealed condition (Harrington, n. d.)

Some materials have been removed from this thesis due to Third Party Copyright. Pages where material has been removed are clearly marked in the electronic version. The unabridged version of the thesis can be viewed at the Lanchester Library, Coventry University.

Figure 2-15 Fatigue crack growth rates data for Ti-6Al-4V of wrought products in mill annealed condition showing R ratio effect. ΔK is between 20 to 40 MPa $\sqrt{\text{m}}$. Data are re-plotted from Feddersen & Hyler (1971), Shih & Wei (1973), and Harrington (n. d.).

Some materials have been removed from this thesis due to Third Party Copyright. Pages where material has been removed are clearly marked in the electronic version. The unabridged version of the thesis can be viewed at the Lanchester Library, Coventry University.

Figure 2-16 Fatigue crack growth rates for Ti-6Al-4V of wrought products in mill annealed condition by Dubey et al. (1997)

Some materials have been removed from this thesis due to Third Party Copyright. Pages where material has been removed are clearly marked in the electronic version. The unabridged version of the thesis can be viewed at the Lanchester Library, Coventry University.

Figure 2-17 Fatigue crack growth rates for Ti-6Al-4V of wrought products in mill annealed condition by Shademan et al. (2004), the microstructure D is mill annealed condition, (a) $R = 0.1$, (b) $R = 0.25$, (c) $R = 0.5$ and (d) $R = 0.8$.

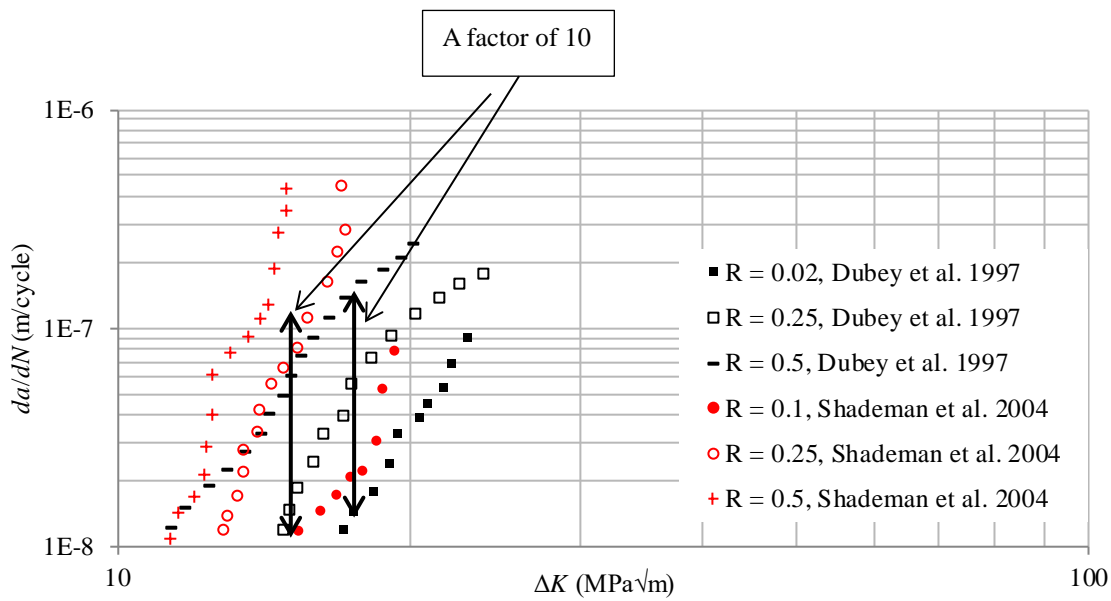


Figure 2-18 Fatigue crack growth rates data for Ti-6Al-4V of wrought products in mill annealed condition showing the R ratio effect. ΔK is under $30 MPa\sqrt{m}$. Data are re-plotted from Dubey et al. (1997) and Shademan et al. (2004).

2.5.1.3 Magnitude of variability

The variability of FCGR in neighbouring specimens at a given ΔK can cover a factor of 2 (Clark and Hudak, 1975). In their study, all specimens were extracted from a single steel plate, and thus the source of variability can only arise from experimental measurement. So, it is expected that FCGR tests conducted for Ti-6Al-4V also might give rise to variability with a factor of 2. The definition of this factor here is $(da/dN)_{\max}/(da/dN)_{\min}$ at a given ΔK for a given R ratio.

For FCGR data of wrought Ti-6Al-4V in MA condition, the variability of FCGR can cover a factor of 10 (Donachie, 2000 p.109). One extreme case is shown in Fig. 2-19. These data were for 6 heats of Ti-6Al-4V plate in MA condition. Heat is a term to state that materials are from the same furnace at the one operation. The uncertainties of parameters in microstructure, texture, and data measurement exist together. In Fig. 2-19, the maximum variability of FCGR covers a factor of 10.

Some materials have been removed from this thesis due to Third Party Copyright. Pages where material has been removed are clearly marked in the electronic version. The unabridged version of the thesis can be viewed at the Lanchester Library, Coventry University.

Figure 2-19 Fatigue crack growth rates data for mill annealed Ti-6Al-4V of wrought products showing variability (Donachie, 2000 p.109). Data are for 6 heats of plate.

Many researchers have published FCGR data for Ti-6Al-4V, and the data for MA condition at about $R = 0.1$ were summarized, see Fig. 2-20. It can be seen that, there is a noticeable variation in the tests results performed across various laboratories. The variation is ranging from a factor of 2 to 10.

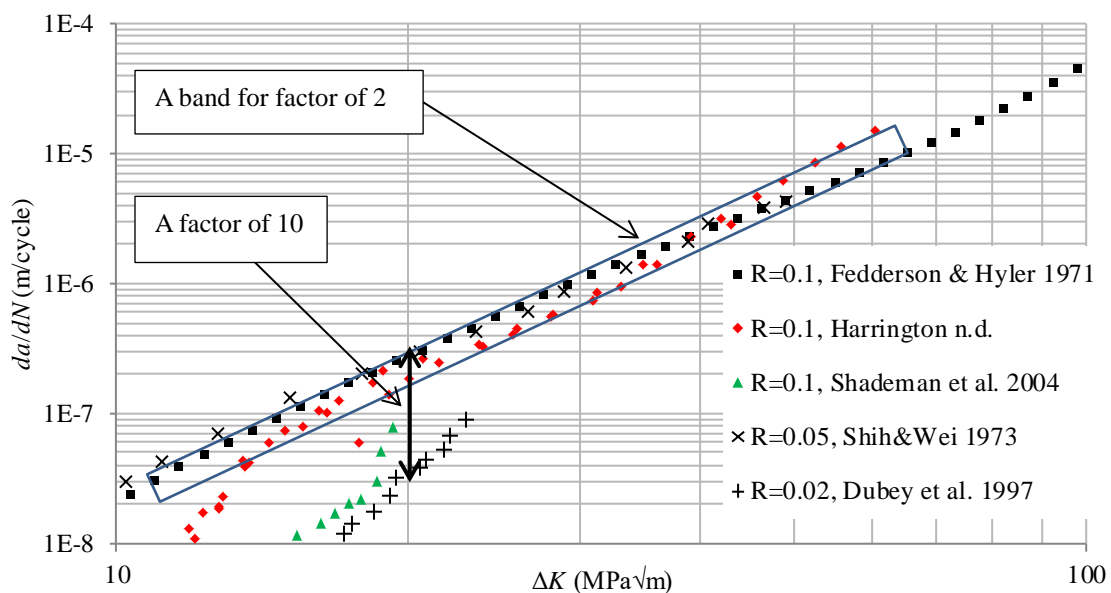


Figure 2-20 Fatigue crack growth rates data for mill annealed Ti-6Al-4V of wrought products showing variability. Data are re-plotted from Feddersen & Hyler (1971), Harrington (n. d.), Shademan et al. (2004), Shih & Wei (1973), and Dubey et al. (1997).

By reviewing fatigue crack growth rates in wrought products, the following findings can be drawn:

- The equiaxed microstructure yields the highest growth rates. The fully lamellar microstructure can achieve the lowest growth rates.
- The grain boundary α phase might increase the fatigue crack growth rates.
- The effect of R can cover a factor of 2 to 3 for equiaxed microstructure when R changed from 0.1 to about 0.5 and ΔK is between 20 to 40 MPa $\sqrt{\text{m}}$; whereas for ΔK under 20 MPa $\sqrt{\text{m}}$, the factor is 10.
- The variability of fatigue crack growth rate can cover a factor of 2 to 10.

2.5.2 FCGR in AM

There are two ways to estimate the FCGR in AM built part: one is by microstructure, the other is by experimental tests. The microstructure method cannot provide values of FCGR and only give a guide for FCGR. The experimental measurement method for AM part is more complicated than measuring the wrought Ti-6Al-4V due to three reasons: residual stress, heat treatment, and microstructure. These three factors introduce large variability in FCGR. Although material orientation, which means that crack is across layers or along layers, may have influence on FCGR, material orientation is easy to describe and its influence can be understood by using FCGR with different material orientations. However, experimental measurement of residual stress is not as easy as determining crack orientation. In the open literature, it is observed not all the FCGR data is published along with the residual stress measurements. Furthermore, the effect of residual stress on FCGR depends on the applied loads and specimen geometry. Secondly, heat treatment can relieve the residual stress, however, the magnitude of stress relief depend on the temperature and time during heat treatment. As different researchers may use different heat treatment parameters, comparison of FCGR for heat treated condition may appear large variability. Heat treatment also changes the microstructure of AM fabricated part and therefore leads to change of FCGR. Finally, there will be significant variation in the microstructure of parts produced with various AM process. This will further influence the FCGR. These three reasons make experimental FCGR

data difficult for comparison.

To get a clear comparison of FCGR in AM made Ti-6Al-4V, the published FCGR are divided into three groups: as-built without residual stress, as-built with residual stress, and heat treated, i.e. residual stress relieved and microstructure changed. It is worth noting that some researchers published data without considering or mentioning the effect of residual stress. However, their data are still compared as without or with residual stress.

2.5.2.1 Selective Laser Melting (SLM)

The microstructure of as-built SLM Ti-6Al-4V in two published research (Hooreweder et al., 2012; Cain et al., 2015) are both fine acicular martensitic phase α' with columnar prior- β grain. The width of columnar grain is about 150 μm . The microstructure of heat treated SLM is either acicular α with columnar prior- β grain after being heated to 650°C for 4 hours, or lamellar microstructure after being heated to 890°C for 2 hours (Cain et al., 2015). It can be seen that all of these microstructures should have lower FCGR than wrought Ti6Al-4V in MA condition.

The FCGR data by Hooreweder, et al. are shown in Fig. 2-21, and by Cain, et al. Fig. 2-22. When comparing FCGR data from experimental tests, this data can be divided into three groups. For the as-built without residual stress group, the FCGR is lower than that of MA condition which has equiaxed microstructure, as shown in Fig. 2-23. The reason for without residual stress is that the planes of specimen are parallel to the layers during depositing, although residual stress was not mentioned in these published works.

Hooreweder et al. (2012) concluded that FCGR properties did not significantly differ between the SLM Ti-6Al-4V and wrought Ti-6Al-4V in MA condition. However, their reference data for wrought Ti-6Al-4V was measured by themselves, which has lower FCGR. When comparing with the same reference data which was measured by Fedderson & Hyler (1971), the SLM specimen has lower FCGR than that of wrought Ti6Al-4V in MA condition.

The FCGR data for as-built with residual stress group are compared in Fig. 2-24. It can be seen that residual stress makes the FCGR higher by a factor of 5 at their loading condition.

The FCGR data for heat treated specimens are compared in Fig. 2-25. It can be seen that

FCGRs do not significantly differ between heat treated SLM Ti-6Al-4V and wrought Ti-6Al-4V in MA condition. This is due to reduction in residual stresses, and improved microstructure after heat treatment. The total effect of heat treatment makes its FCGR between the as-built with residual stress and as-built without residual stress. The influence of material orientation is not observed when comparing among -XY, -XZ, and -ZX orientations.

Cain et al. (2015) also concluded that FCGR properties did not significantly differ between SLM Ti6Al-4V and wrought Ti6Al-4V in MA condition. However, 2/3 of their FCGR data were for heat treated specimen, so their conclusion refers to the stress relieved condition. On the other hand, although their discussion covered residual stress aspect, the estimation of residual stress effect is only qualitative. They concluded that FCGR relationship between build directions may be due to residual stress.

By comparing published FCGR for SLM Ti-6Al-4V, the following findings can be drawn:

- In as-built condition, SLM Ti-6Al-4V has lower FCGR than wrought Ti-6Al-4V in MA condition. The effect of residual stress can cover a factor of 5.
- After heat treatment FCGR in SLM Ti-6Al-4V is similar to the wrought Ti-6Al-4V in MA condition.
- FCGR property is much less influenced by specimen orientation relative to build direction, i.e. crack orientation.

Some materials have been removed from this thesis due to Third Party Copyright. Pages where material has been removed are clearly marked in the electronic version. The unabridged version of the thesis can be viewed at the Lanchester Library, Coventry University.

Figure 2-21 Fatigue crack growth rates for SLM made Ti-6Al-4V tested at $R = 0.1$ by Hooreweder et al. (2012)

Some materials have been removed from this thesis due to Third Party Copyright. Pages where material has been removed are clearly marked in the electronic version. The unabridged version of the thesis can be viewed at the Lanchester Library, Coventry University.

Figure 2-22 Fatigue crack growth rates for SLM Ti-6Al-4V tested at $R = 0.1$ by Cain et al. (2015) (a) the XY specimen orientation, (b) the XZ specimen orientation, (c) the XZ specimen orientation, (d) the AB condition, (e) the SR condition and (f) the HT condition. (AB: as-built, SR: stress relief treatment, HT: heat treatment)

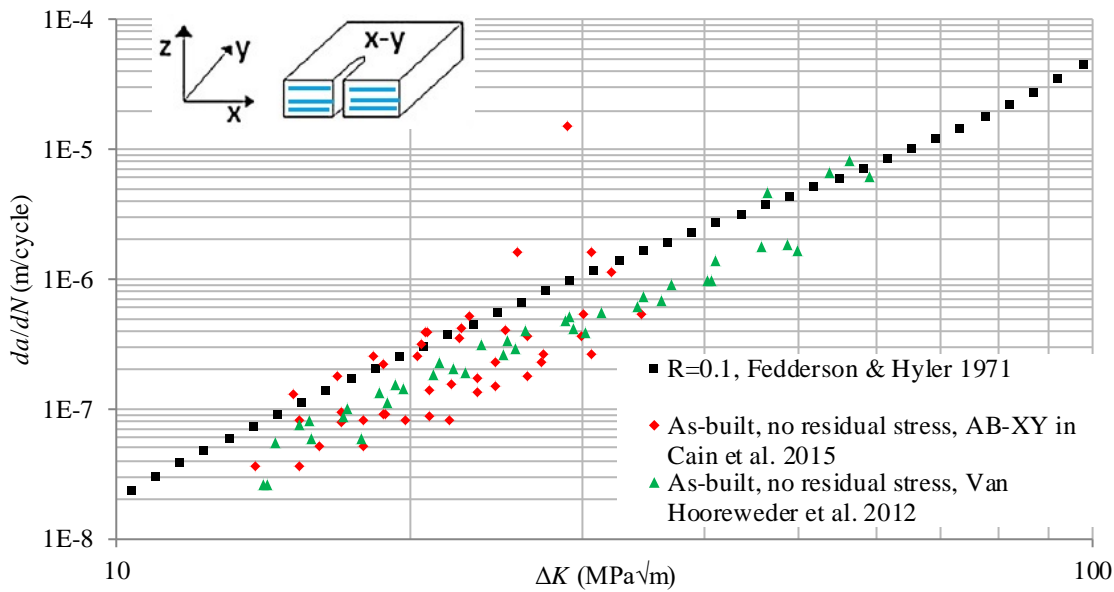


Figure 2-23 Comparison of fatigue crack growth rates data for SLM Ti-6Al-4V tested at $R = 0.1$ in as-built condition. As planes of specimen are parallel to the layers during depositing, this can be regarded as no residual stress. Fedderson & Hyler 1971 is wrought Ti-6Al-4V data. Data are re-plotted from Fedderson & Hyler (1971), Cain et al. (2015) and Van Hooreweder et al. (2012).

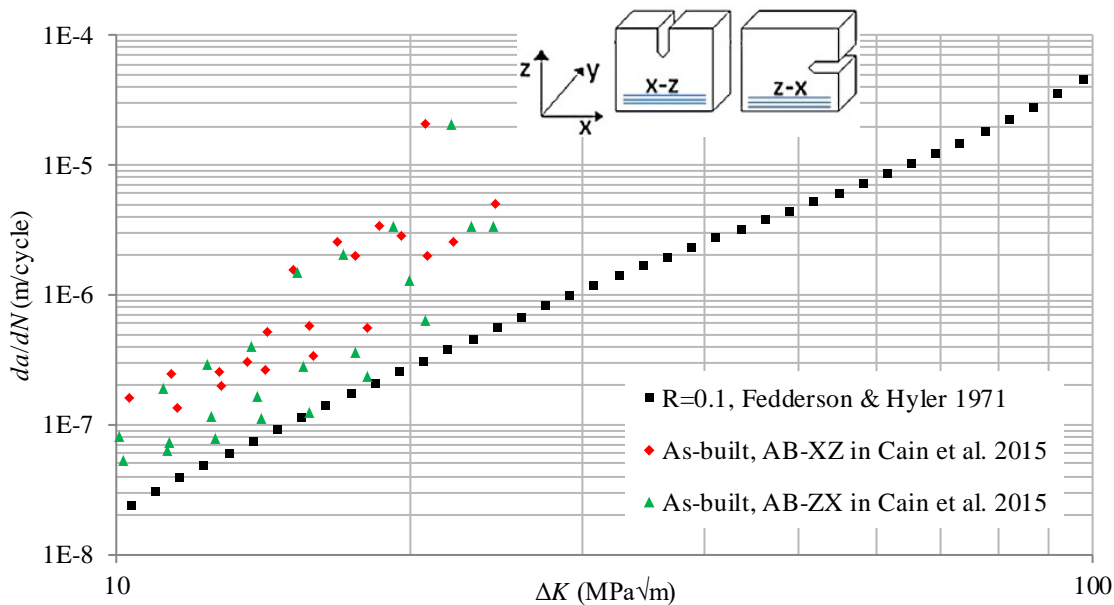


Figure 2-24 Comparison of fatigue crack growth rates data for SLM made Ti-6Al-4V tested at $R = 0.1$ in as-built condition. Residual stress measurement was not conducted. Fedderson & Hyler 1971 is wrought Ti-6Al-4V data. Data are re-plotted from Fedderson & Hyler (1971), and Cain et al. (2015).

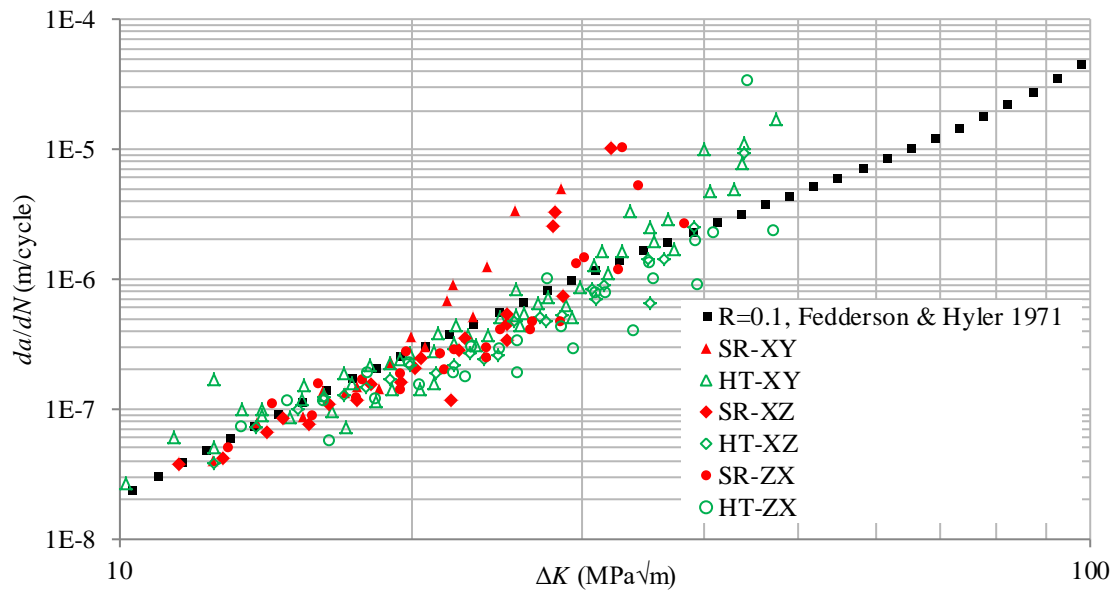


Figure 2-25 Comparison of fatigue crack growth rates data for SLM Ti-6Al-4V tested at $R = 0.1$ in heat treated, SR: 650°C for 4 hours, and HT: 890°C for 2 hours. Feddersen & Hyler 1971 is wrought products data. Data are re-plotted from Feddersen & Hyler (1971), and Cain et al. (2015).

2.5.2.2 Electron Beam Melting (EBM)

The microstructure of EBM made Ti-6Al-4V depends on processing parameters. For example, when a layer thickness is $\sim 700 \mu\text{m}$ (Edwards et al., 2013), the microstructure is lamellar with coarse α platelets, and some α colonies could be observed, as shown in Fig. 2-26 a. When a layer thickness is $\sim 100 \mu\text{m}$ (Murr et al., 2009; Facchini et al. 2009), the microstructure is still lamellar, however, the acicular α platelets oriented in various directions and no colony exists, as shown Fig. 2-26b and c. For work of Greitemeier et al. (2016), no detailed information about manufacturing was reported, and the microstructure is a coarser lamellar. For work of Zhai et al. (2016), layer thickness is not reported, and fine lamellar microstructure is observed.

Columnar prior- β grains are elongated along the build direction and continuously passed across multiple layers. The size of columnar prior- β grains are not mentioned in the work of Murr et al., Edwards et al., Zhai et al., and Greitemeier et al., while the size of columnar prior- β grain is $50 \mu\text{m}$ in the work of Facchini et al. It can be seen that the microstructure of EBM made Ti-6Al-4V has not obvious α colony, so its FCGR should be slightly lower than that in wrought Ti-6Al-4V in MA condition.

As EBM processes were typically carried out at elevated temperature of 600–700°C, and therefore lower temperature gradient introduced less as-built residual stress. On the surface of 0–30 μm , residual stresses may be tensile or compressive with a magnitude ranging from 70 MPa to –140 MPa, while in the subsurface of 30–254 μm , residual stresses is always tensile with a magnitude less than 35 MPa (Edwards et al., 2013). Residual stresses in the center of EBM made sample did not measured, however, it was assumed that residual stress have a negligible effect in the work of Edwards et al.

Some materials have been removed from this thesis due to Third Party Copyright. Pages where material has been removed are clearly marked in the electronic version. The unabridged version of the thesis can be viewed at the Lanchester Library, Coventry University.

Figure 2-26 Microstructure of EBM Ti-6Al-4V. (a) layer thickness was $\sim 700 \mu\text{m}$ (Edwards et al., 2013), (b) layer thickness was $\sim 100 \mu\text{m}$ (Murr et al., 2009), (c) layer thickness was $\sim 100 \mu\text{m}$ (Facchini et al., 2009).

FCGR data from experimental tests by Edwards et al. are shown in Fig. 2-27, by Greitemeier et al. Fig. 2-28a, and by Zhai et al. Fig. 2-28b, respectively. Edwards et al. (2013) gave a conclusion that FCGR of EBM made Ti-6Al-4V were comparable to the wrought Ti-6Al-4V. Other researchers did not give conclusions about overall FCGR of EBM Ti-6Al-4V, and their focuses were fatigue crack growth threshold of EBM Ti-6Al-4V.

As residual stress is much less in EBM Ti-6Al-4V, all FCGR data are compared together without dividing into groups, as shown in Fig. 2-29. It can be seen that all FCGR data are similar. However, HIPed EBM Ti-6Al-4V has slightly lower FCGR data.

Some materials have been removed from this thesis due to Third Party Copyright. Pages where material has been removed are clearly marked in the electronic version. The unabridged version of the thesis can be viewed at the Lanchester Library, Coventry University.

Figure 2-27 Fatigue crack growth rates for EBM Ti-6Al-4V tested at $R = 0.1$ by Edwards et al. (2013).

Some materials have been removed from this thesis due to Third Party Copyright. Pages where material has been removed are clearly marked in the electronic version. The unabridged version of the thesis can be viewed at the Lanchester Library, Coventry University.

Figure 2-28 Fatigue crack growth rates for EBM made Ti-6Al-4V tested at $R = 0.1$ by (a) Greitemeier et al. (2016) and (b) Zhai et al. (2016). (AF: as-fabricated, HT: heat treated, 950°C for 1 hour plus 500–600°C for 3–8 hours, HIP: hot isostatic pressing, at 920°C and 1000 bar for 2 hours, annealed: 710°C for 2 hours).

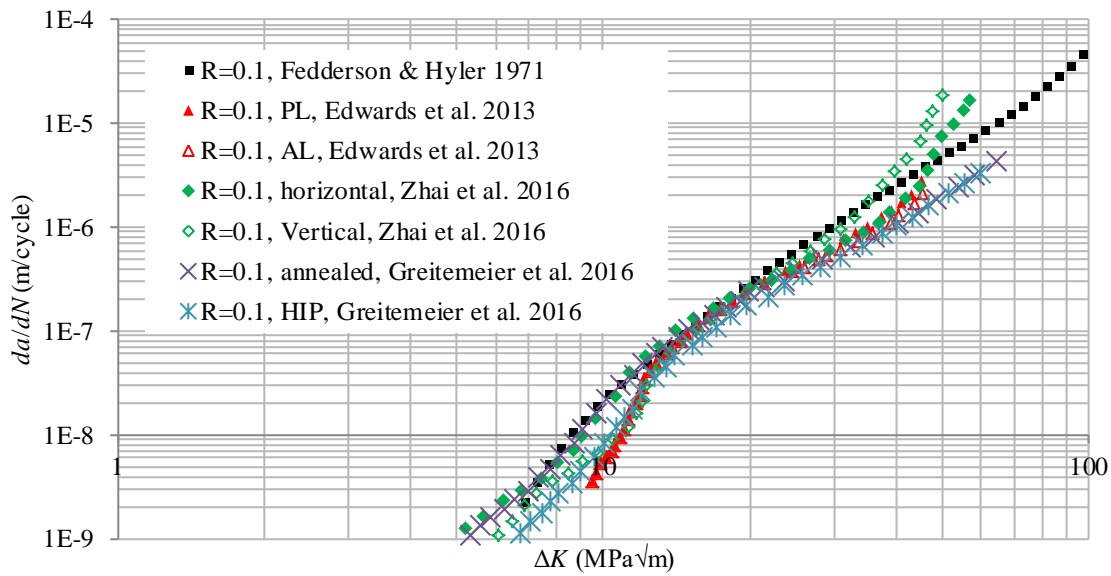


Figure 2-29 Comparison of fatigue crack growth rates data for EBM Ti-6Al-4V tested at $R = 0.1$ in heated treated and as-built. Fedderson & Hyler 1971 is wrought Ti-6Al-4V data. Data are re-plotted from Fedderson & Hyler (1971), Edwards et al. (2013), Greitemeier et al. (2016), and Zhai et al. (2016).

By comparing published FCGR for EBM made Ti-6Al-4V, the following findings can be drawn:

- In as-built condition, EBM Ti-6Al-4V has similar FCGR property to wrought Ti-6Al-4V in MA condition.
- Heat treatment has much less influence on FCGR of EBM made Ti-6Al-4V.
- Hot isostatic pressing has slightly improvement on FCGR of EBM Ti-6Al-4V.
- For EBM made Ti-6Al-4V, FCGR property is much less influenced by specimen orientation relative to build direction, i.e. crack orientation.

2.6 Summary of literature survey

The microstructure in wrought Ti-6Al-4V depends on its heat treatment condition. The microstructure can be fully lamellar, bimodal or equiaxed $\alpha + \beta$ phase. The source of anisotropic mechanical properties in Ti-6Al-4V of sheet form is texture. The equiaxed microstructure yields the highest FCGR. The fully lamellar microstructure can achieve the lowest FCGR. The effect of R can cover a factor of 2 to 3 for equiaxed microstructure when R changed from 0.1 to about 0.5 and ΔK is between 20 to 40 MPa√m.

The microstructure in WAAM Ti-6Al-4V consists of large columnar prior- β grains with $\alpha + \beta$ lamellar, and some colonies can be observed. The texture in WAAM, SLM and EBM Ti-6Al-4V is not strong.

Young's modulus for both SLM and EBM Ti-6Al-4V are similar to that of wrought products (sheet excluded). However, WAAM Ti-6Al-4V has slightly higher Young's modulus than wrought products. In SLM, EBM and WAAM Ti-6Al-4V, specimens that are loaded across layers have higher scatter than along layers direction.

Both SMD and WAAM Ti-6Al-4V in as-built condition have lower ultimate tensile strength and yield strength than that of wrought products in MA condition. Both EBM and SLM Ti-6Al-4V have higher ultimate tensile strength and yield strength than wrought products in MA condition, but lower than STA condition.

A slightly anisotropic mechanical behaviour exists in EBM, SLM, WAAM and SMD made parts. Specimens that are loaded along layers have a higher ultimate tensile strength and yield strength. For both WAAM and SMD Ti-6Al-4V, the elongation in across layers orientation is higher.

Both EBM and SLM Ti-6Al-4V in as-built condition have much lower high cycle fatigue properties than wrought products in MA condition. However, both WAAM and SMD Ti-6Al-4V have higher fatigue resistance than that of wrought products in MA condition.

EBM, WAAM and SMD Ti-6Al-4V in as-built condition have comparable or greater fracture toughness than that of wrought products in MA condition. SLM Ti-6Al-4V has lower fracture toughness. For WAAM made Ti-6Al-4V, cracks that are across the layers have higher fracture toughness than that along the layers.

In as-built condition, EBM Ti-6Al-4V has similar FCGR property to the wrought Ti-6Al-4V in MA condition. Whereas SLM Ti-6Al-4V has lower FCGR if residual stress has no contribution. Residual stress in SLM Ti-6Al-4V may make measured FCGR data higher by a factor of 5.

Heat treatment has much less influence on FCGR of EBM Ti-6Al-4V. Hot isostatic pressing has slightly improvement on FCGR of EBM Ti-6Al-4V. However, heat treatment has

influence on SLM Ti-6Al-4V. Total effect of heat treatment makes FCGR in SLM Ti-6Al-4V similar to the wrought Ti-6Al-4V in MA condition.

For both SLM and EBM Ti-6Al-4V, FCGR property is much less influenced by specimen orientation relative to build direction, i.e. crack orientation.

Self-balanced residual stress profile can only be provided by the contour method. Unless stresses at each point are measured accurately, the profiles provided by other reviewed techniques are might not self-balanced.

The neutron diffraction, X-ray diffraction, incremental hole-drilling and contour methods provide the stresses in a particular small volume, whereas the layer removal method provides the averaged stress along the width and length of a layer, the slitting method provides the averaged stress through the thickness of a part.

Although three or two components of residual stress can be obtained by neutron and X-ray diffraction, the residual stress profile for only one component can be built due to self-balance requirement.

Chapter 3 Experiments Used in This Project

3.1 Introduction

Fatigue crack growth rate (FCGR) experiments on Ti-6Al-4V of wrought products were conducted by the author of this thesis and other experimental works reviewed in this Chapter were carried out by collaborators at Cranfield University (crack growth tests) or The Open University (residual stress measurement). The experimental tests used in this project and corresponding conductors are listed in Table 3-1.

Table 3-1 Experiments used in this project

| Sample geometry (number of specimen) | Experiment type | Heating source | Conductor and References |
|---|---|-------------------------------|--|
| C(T) (4) cut from Wrought products (1) | FCGR | — | Author of this thesis |
| C(T) (4) cut from Wall-T145 (1) | FCGR | Tungsten Inert Gas Welding | Lorant (2010) |
| C(T) (15) cut from Wall-Bi120 (3) | FCGR | Plasma | Hills (2014) |
| Wall-Bi120 (1) | Contour measurement of residual stress | | Paddea (Zhang, J. et al., 2016a) |
| C(T) (3) cut from Wall-Bi120 (1) | Contour measurement of residual stress | | Paddea (Zhang, J. et al., 2016b), (Paddea, 2015) |
| Wall-T110 (1) | Contour measurement of residual stress | | Paddea (Paddea, 2015) |

Note: — C(T): compact tension geometry; Wall-Bi120: WAAM-substrate wall of 120 mm height; Wall-T110: WAAM wall of 110 mm height build on a flat substrate of wrought Ti-6Al-4V.

All experiments that are used to obtain FCGR data and residual stress profiles are described in this chapter. The parameters of WAAM process for producing the samples are also described.

3.2 The WAAM process

All samples were made by the WAAM technology using Ti-6Al-4V wires. Sample with T-shaped cross section of 145 mm build height (denoted by Wall-T145) was manufactured by Tungsten Inert Gas (TIG) welding (Lorant, 2010), by the Welding Engineering and Laser Processing Centre (WELPC) at Cranfield University. The power source used an alternative

current at a high frequency, which was developed by the VBC group, a British company. The heat input parameter was the same as the WAAM process using plasma torch.

Bi-material samples of 120 mm total height (denoted by Wall-Bi120) and WAAM alone sample with T-shaped cross section of 110 mm build height (denoted by Wall-T110) were made using an in-house developed system, plasma wire deposition (PWD), also by the WELPC at Cranfield University (Hills, 2014). This system melts Ti-6Al-4V wire by a plasma torch and deposits the molten metal to a substrate or previously deposited layers. When the plasma torch moves along a designed path, the deposited molten material forms a thin layer of sliced cross-section. After completing one layer, the sample is allowed to cool down to below 100 °C (Martina et al., 2012) before a new layer is built upon it. This process is repeated layer by layer until the complete sample is built.

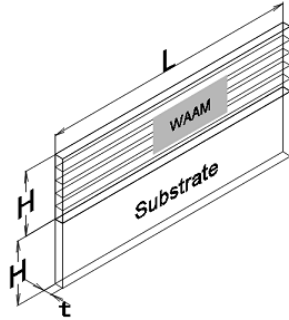
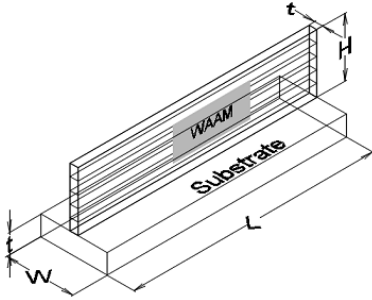
The in-house PWD system (Martina et al., 2012) mainly consists of a plasma torch, a power source, a trailing shield, pure shield argon gas supply system and an airtight tent. The plasma torch and the substrate of sample are housed in an airtight tent containing argon as the shielding gas. The Liburdi Engineering PW-400C plasma torch is used for PWD system. The trailing shield is 100 mm long. The power source is Liburdi Pulseweld LP 4000-VC.

3.3 Samples made by WAAM

All WAAM made samples were built on their own substrates. Each substrate is a Ti-6Al-4V plate and the heat treatment condition of the plate is mill annealed (MA). For samples with T-shaped cross section, i.e. wall built on a flat substrate: Wall-T145 and Wall-T110, the substrates were firmly clamped by jigs. For Wall-Bi120, the substrate was vertical and loosely clamped. The process parameters for Wall-Bi120 are shown in Table 3-2, which are reported in Hills' thesis (2014). The process parameters for Wall-T110 are similar to that of Wall-Bi120. For Wall-T145, the torch traveling speed is 3.5 mm/s, the layer height is 1 mm, and the Ti-6Al-4V wire diameter is 1.2 mm (Lorant, 2010). The chemical composition of Ti-6Al-4V wire is shown in Table 3-3, which are reported in (Martina et al., 2012). The final geometry of the samples is listed in Table 3-4. All samples are in the as-built condition, i.e. without post-process treatment.

Table 3-2 Process parameters for fabrication of Wall-Bi120 (Hills, 2014)
 Some materials have been removed from this thesis due to Third Party Copyright. Pages where material has been removed are clearly marked in the electronic version. The unabridged version of the thesis can be viewed at the Lanchester Library, Coventry University.

Table 3-4 Final geometry of all wall samples

| Sample label | Geometry $L \times H \times t$ (mm) | Configuration |
|--------------|--|--|
| Wall-Bi120 | WAAM: $445 \times 60 \times 8$ Substrate: $445 \times 60 \times 8$ |  |
| Wall-T110 | WAAM: $500 \times 110 \times 6$ Substrate: $500 \times 60 \times 7$ ($L \times W \times t$) |  |
| Wall-T145 | WAMM: $835 \times 145 \times 6$ Substrate: $835 \times 60 \times 7$ ($L \times W \times t$) | |

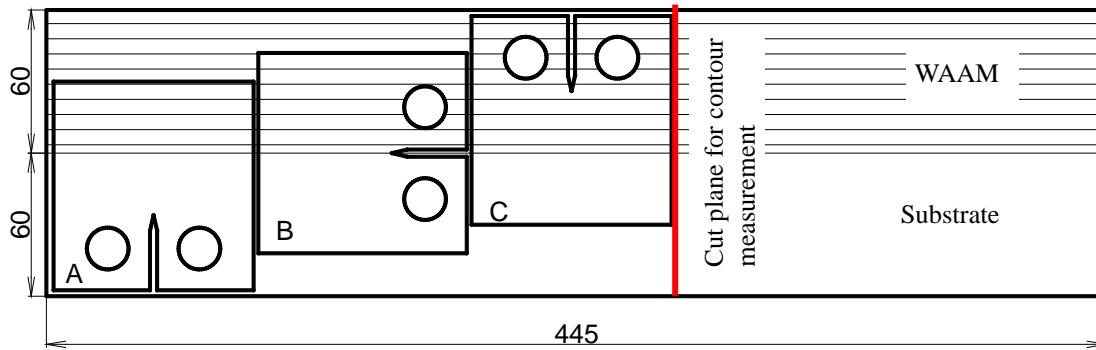
A total of six walls were made ($4 \times$ Wall-Bi120, $1 \times$ Wall-T110, and $1 \times$ Wall-T145). One Wall-Bi120 was used for residual stress measurement in both the wall itself and C(T) specimens that were extracted from the wall. Other three Wall-Bi120 samples were used to

produce multiple C(T) specimens for FCGR tests. Wall-T110 was used for residual stress measurement and Wall-T145 was used for extracting C(T) specimens to measure the FCGR in WAAM alone material.

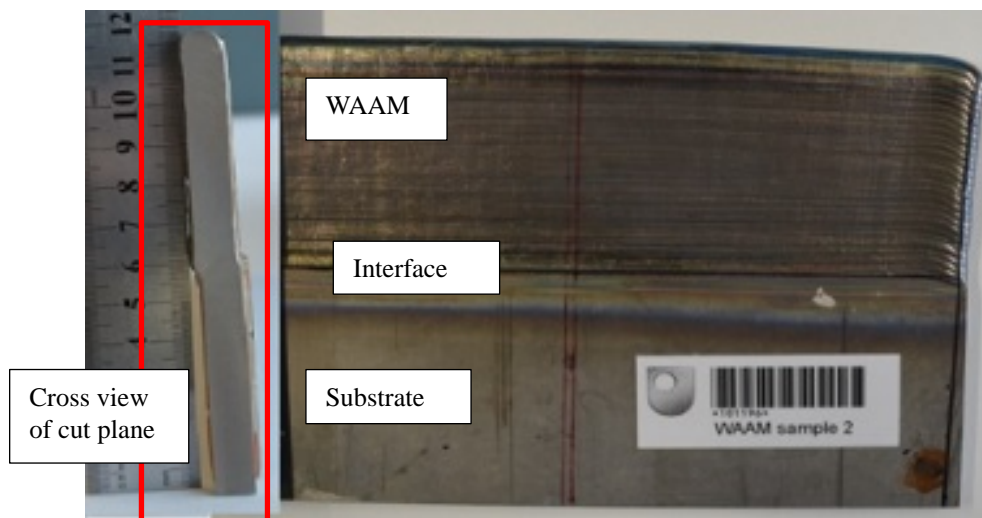
3.4 Residual stress measurements

3.4.1 Approach

Residual stresses in Wall-T110, Wall-Bi120, and three C(T) specimens (Type A, B and C) were measured by the contour method at The Open University. Diagrams showing the locations of cut planes for contour measurement are given in Fig. 3-1 for Wall-Bi120, Fig. 3-2 for Wall-T110 and Fig. 3-3 for C(T) specimens.



(a)



(b)

Figure 3-1 Cut planes in Wall-Bi120 for contour measurement, (a) schematic cut plane (unit: mm); (b) photos of Wall-Bi120 and cross section view of cut plane

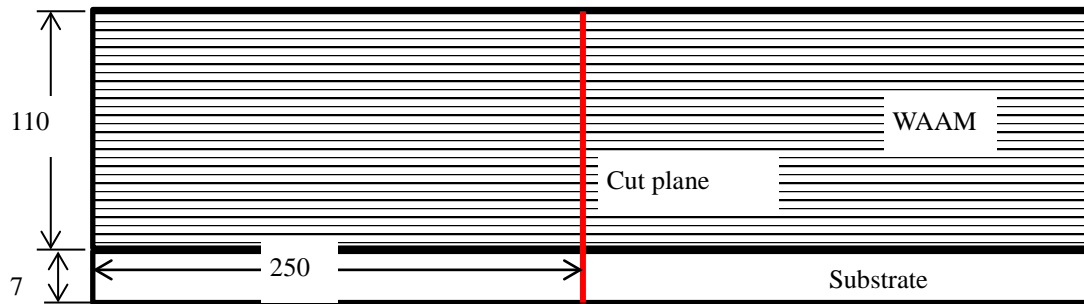


Figure 3-2 Cut plane in Wall-T110 for contour measurement (unit: mm)

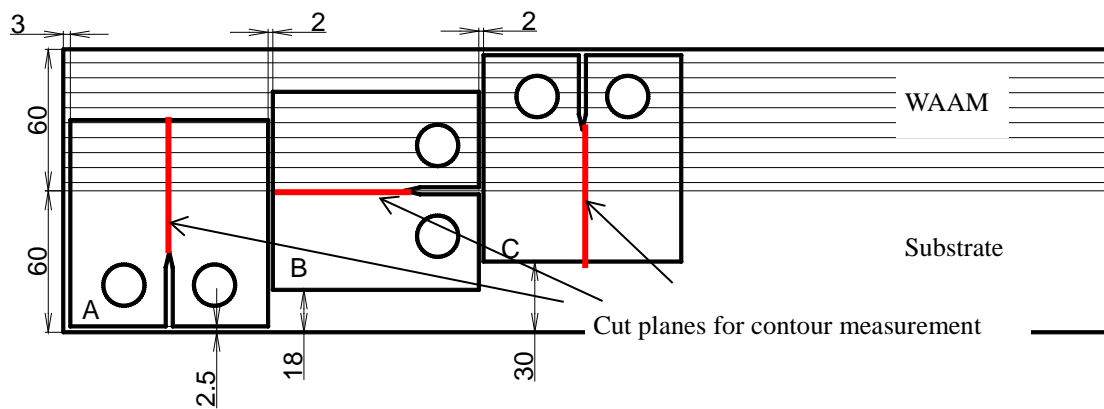


Figure 3-3 Position of C(T) specimens in Wall-Bi120 and cut planes in C(T) specimens for contour measurement, Type A, B and C specimens in terms of the crack position (unit:mm)

The contour method involves following steps (Zhang, J. et al., 2016a):

- Making a cut in the sample, at the plane normal to the component of stress tensor which is to be measured.
- Measuring the displacement profile of the cut surfaces.
- Data analysis to smooth the displacement data.
- Analyzing displacement data by finite element (FE) method to obtain stress map.

Such contour method steps are schematically shown in Fig. 3-4.

An Agie Charmilles wire electrical discharge machining (EDM) machine (FI-440CS) with a 150 μm diameter brass wire was employed to make the cut in samples. The EDM machine was worked in the “finishing” or “skim” mode to minimise symmetric artefacts. Sacrificial layers were bonded to the outer surfaces of the samples in the vicinity of the cut plane to mitigate wire entry and exit cutting artefacts. The samples were clamped to a fixture to avoid any free movement during the cutting operation. Prior to cutting, the samples and clamping

fixtures were left to reach thermal equilibrium conditions within the EDM deionised water tank.

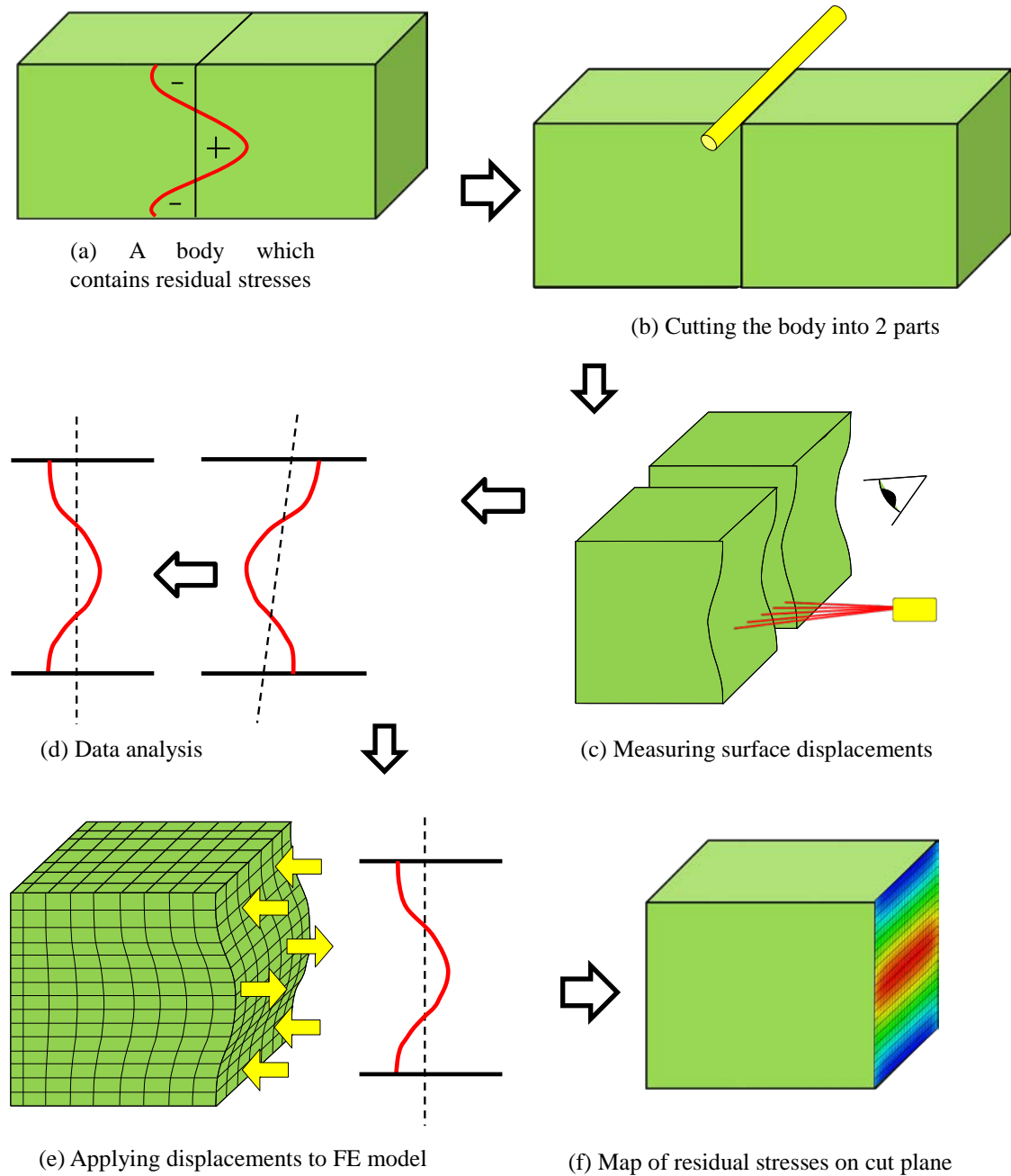


Figure 3-4 Steps of the contour method for residual stress measurement (Paddea, 2015)

Following wire EDM cutting, the sectioned samples were cleaned, dried and left in a temperature controlled laboratory to reach thermal equilibrium before starting displacement profile measurements. The displacement profile of the opposing cut surfaces were measured using a Zeiss Eclipse co-ordinate measuring machine (CMM), fitted with a Micro-Epsilon

laser probe and a 4 mm diameter ruby-tipped Renishaw PH10M touch trigger probe. The resolution of the Micro-Epsilon laser triangulation displacement sensor is $0.15\text{ }\mu\text{m}$ at the maximum sampling rate. The measurement point spacing adopted was on a 0.1 mm grid. Furthermore, the outlines of the cut part were measured with the touch probe to define the geometry of the cutting surfaces for the data processing step.

After measuring the displacement profile, the measured data from two cut faces were aligned and averaged, see Fig. 3-4d. Then the displacements were applied to the cut plane in an FE model and the resultant stress component normal to the cut plane was calculated and named as measured residual stresses, see Fig. 3-4e&f. FE models based on the measured outlines of the cut part were built using the ABAQUS code. Linear hexahedral elements with reduced integration (C3D8R) were used to mesh the models. The FE models were assumed to have homogeneous isotropic elastic properties with a room temperature Young's modulus of 113.8 GPa and Poisson's ratio of 0.342.

3.4.2 Results

3.4.2.1 Wall-T110

The measured two-dimensional (2D) longitudinal residual stress map and one-dimensional (1D) stress distribution along the center line in Wall-T110 sample are shown in Fig. 3-5.

The maximum tensile residual stresses are observed near the interface between the WAAM deposited part and the substrate. The maximum value of the stress is around 700 MPa, which is slightly under the yield strength of Ti-6Al-4V. In the first few deposited layers the effect of WAAM process is very similar to welding a plate; therefore such tensile residual stress with a magnitude about yield strength is as expected. Furthermore, the distribution of residual stress in the heat affected zone of the substrate is similar to that in a welded plate.

Balancing compressive residual stress is observed in the top half of the wall (Wall-T110). The profile of compressive residual stress is rather smooth, despite a sudden drop at the top layer (height 110 mm). Such drop happened near the edge of the cut plane and its reason needs further investigation.

The high compressive residual stresses at the base of the sample are observed. These compressive stresses and the tensile stress in the WAAM made part form a self-balanced force system.

Some fluctuations are observed in the lower half of WAAM part. These fluctuations do not match the expected profile of residual stress and its reason needs further investigation.

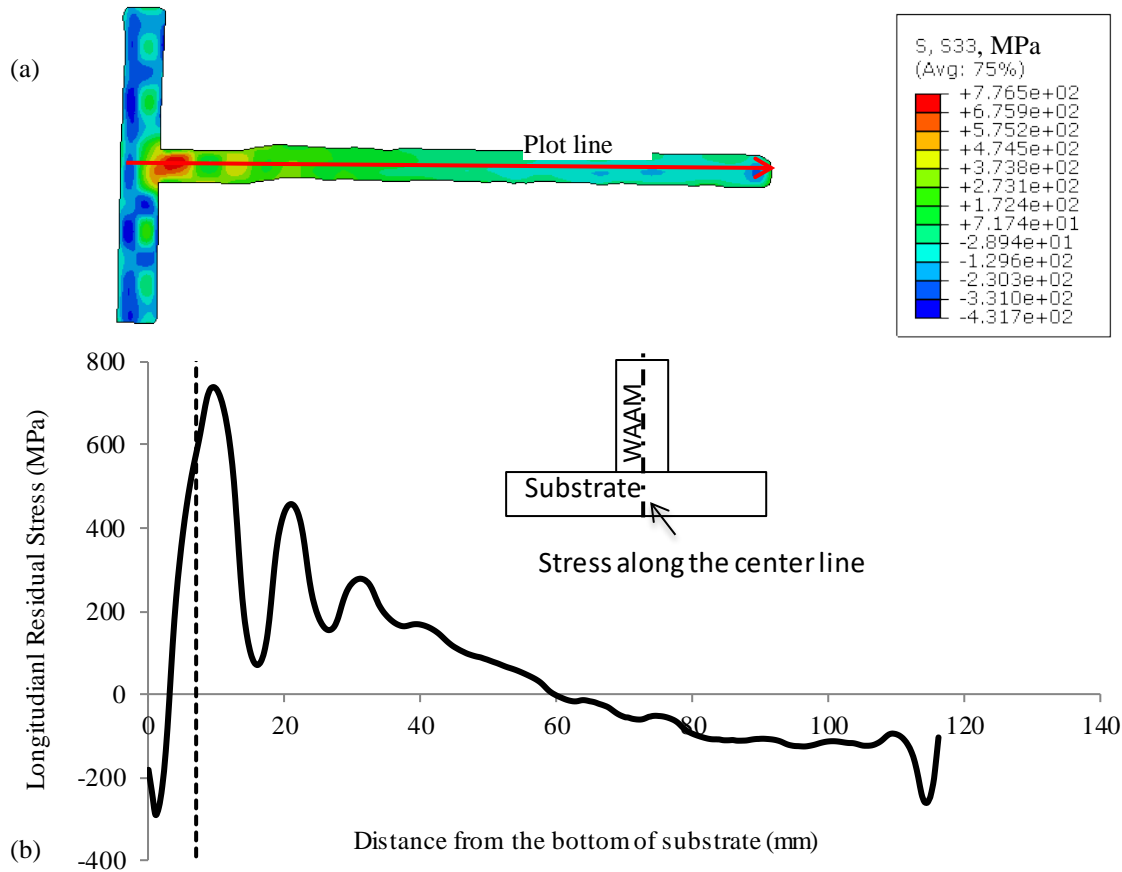


Figure 3-5 Measured residual stresses in Wall-T110: (a) 2D stress map, and (b) 1D stress distribution along the centre line (average value in the thickness)

3.4.2.2 Wall-Bi120

The measured 2D longitudinal residual stress map and 1D stress distribution along the mid-thickness line in the WAAM-substrate bi-material wall (Wall-Bi120) are shown in Fig. 3-6.

An inclined line segment of profile is observed in the substrate. This is a result of bending in the wall. The inclined line changed at a position which is near the interface between the WAAM Ti-6Al-4V and substrate. The reason is the residual stress become rise in the heat affect zone.

The tensile residual stress is observed near the top of Wall-Bi120. This means that the bending curve in Wall-Bi120 is lower than that in Wall-T110. Again, the profile of residual stress is rather smooth in upper half of Wall-Bi120.

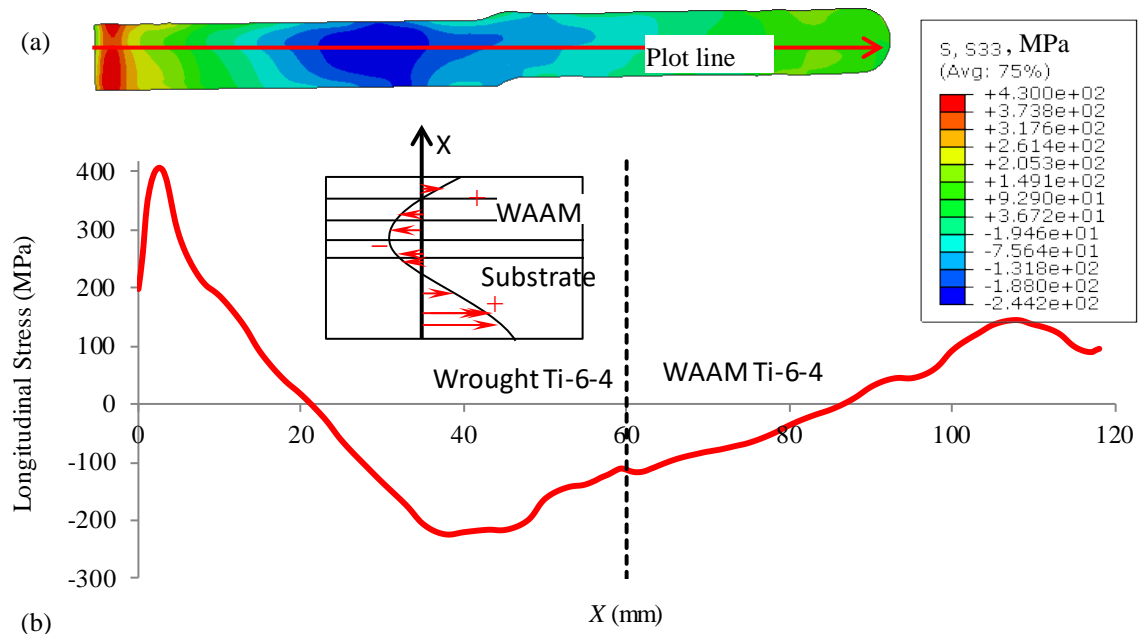


Figure 3-6 Measured residual stresses in Wall-Bi120: (a) 2D stress map and (b) 1D stress distribution along the mid-thickness line

3.4.2.3 C(T) specimens

The measured 2D longitudinal residual stress map and 1D stress distribution along the mid-thickness line of C(T) specimens are shown in Fig. 3-7, Fig. 3-8 and Fig. 3-9 for Type B, A and C, respectively.

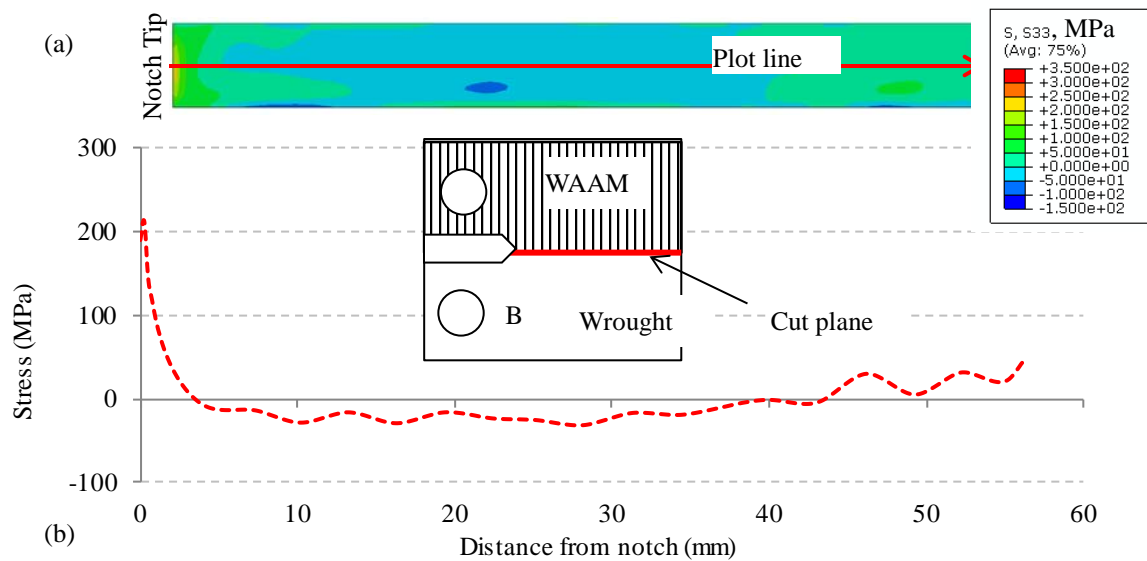


Figure 3-7 Measured residual stresses in type B specimen: (a) 2D stress map and (b) 1D stress distribution along the mid-thickness line

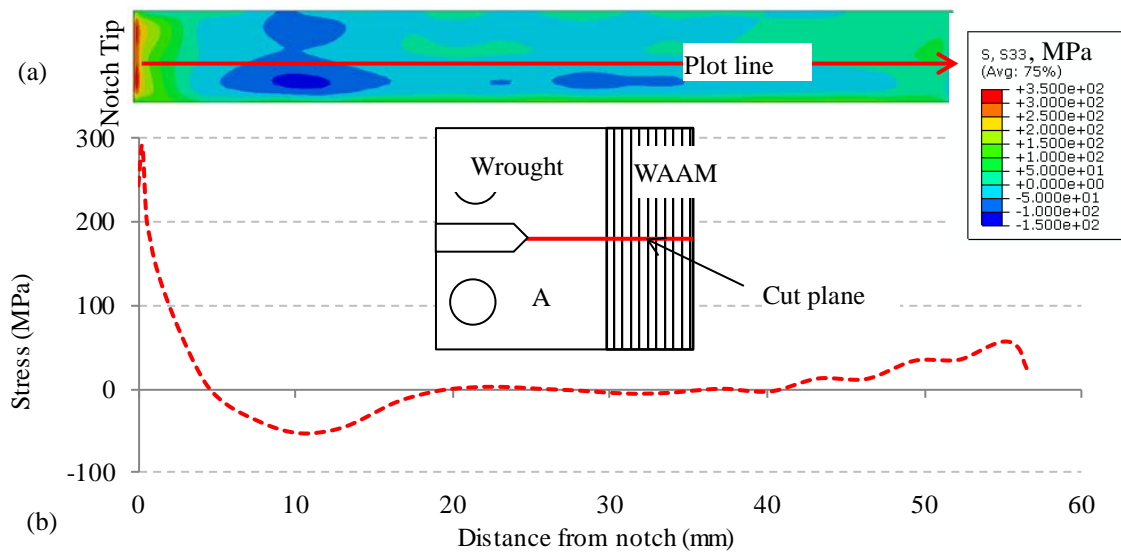


Figure 3-8 Measured residual stresses in type A specimen: (a) 2D stress map and (b) 1D stress distribution along the mid-thickness line

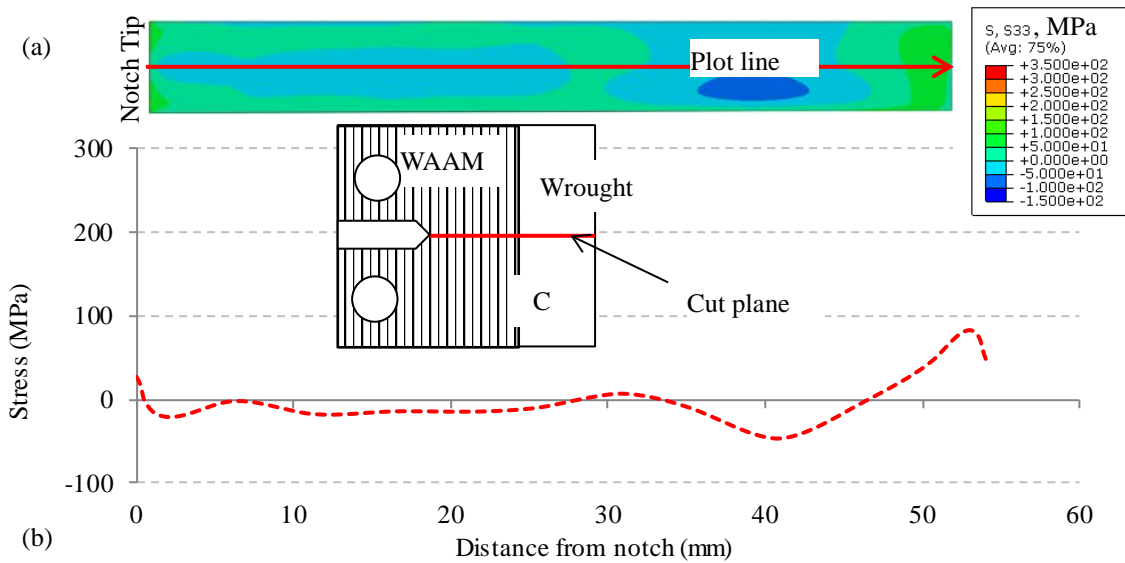


Figure 3-9 Measured residual stresses in type C specimen: (a) 2D stress map and (b) 1D stress distribution along the mid-thickness line

It is worth noting that residual stress profile in three C(T) specimens is different from that in the wall sample. The difference is that the stresses near the notch are increased by the influence of the notch root, i.e. stress concentration appears near the notch. Furthermore, the residual stress in the notch zone influences the magnitude of such increasing. In fact, the position of uncracked ligament in residual stress profile for the Type A and C specimens only have a difference about 4 mm. However, the stresses near the notch in type A are much higher

than that in Type C. The reason is that the released residual stresses in notch zone for type A specimen are larger than that in type C, as shown in Fig. 3-10.

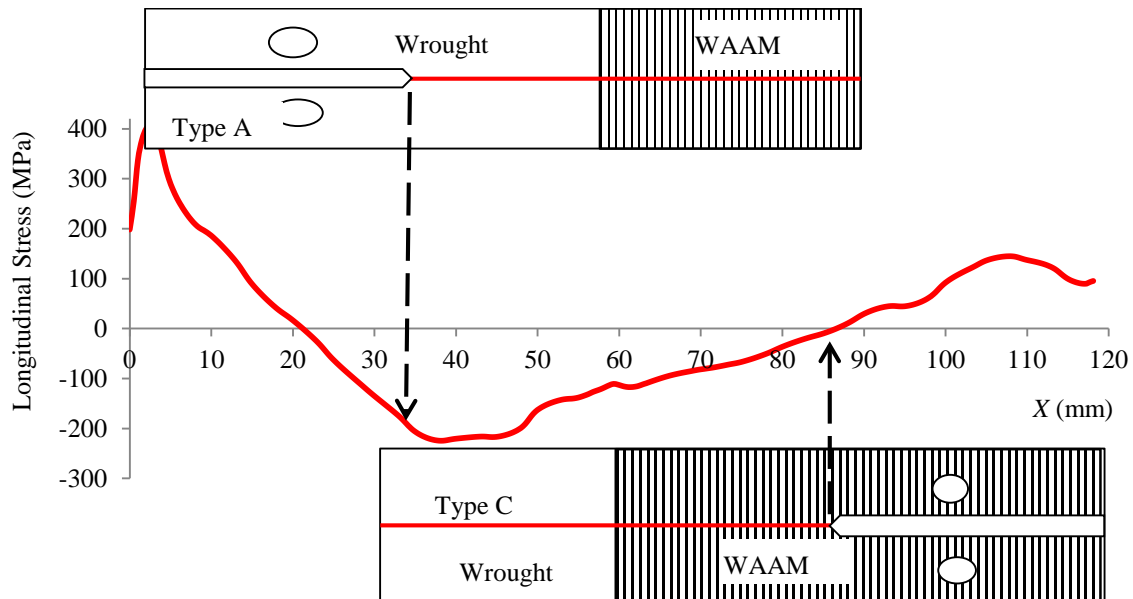


Figure 3-10 Positions of uncracked ligament in residual stress field of Wall-Bi120 are similar, whereas released stresses in notch zone for type A specimen are higher.

As the position of residual stress profile for the Type A and C specimens are similar, two similar drops in stress are observed in their profiles. For Type A specimen, the drop is at 10 mm from notch root, and for Type C it is 40 mm.

For the type B specimen, transverse residual stress is presented as it is perpendicular the crack path and contribute to the crack growth driving force. Although the transverse residual stress is not expected (i.e. very low value in the wall), this residual stress component still appears in the C(T) specimen due to redistribution of the longitudinal residual stress in the wall. The distribution of the transverse residual stress due to longitudinal residual stress is a profile with tensile stresses at both ends. Again, residual stress in the notch root zone has increased owing to stress concentration effect.

3.5 C(T) specimens for FCGR tests

Standard compact tension specimens, C(T), according to ASTM-E647-11, were extracted from the wall samples. All C(T) specimens have a width of 70 mm and detail dimensions are shown in Fig. 3-11. However, the thickness of specimens from Wall-Bi120, Wall-T145 and

wrought samples are 6 mm, 5 mm, and 7.1 mm, respectively.

All C(T) specimens were machined in Cranfield University's engineering workshop. For WAAM made samples, the surface roughness of both sides were skimmed off and then holes and other edges were machined. The notches were made by electrical discharge machining (EDM). Scribe lines were marked by the Vernier gauge along the potential crack growth path to aid in fatigue crack length measurement.

3.5.1 Wrought products (L-T, T-L)

For C(T) specimens of Ti-6Al-4V for wrought products, the L-T orientation (loading in the longitudinal direction and crack growth in the long transverse direction) and T-L orientation (loading in the transverse direction and crack growth in the longitudinal direction) were machined. A total of four specimens were machined, and each orientation had two specimens.

However, one L-T specimen from wrought sample has a little different dimension. The length of 87.5 mm is actually 84.5 mm, and other dimensions were machined as requirements. The stress intensity factors in this specimen were calculated by FE method.

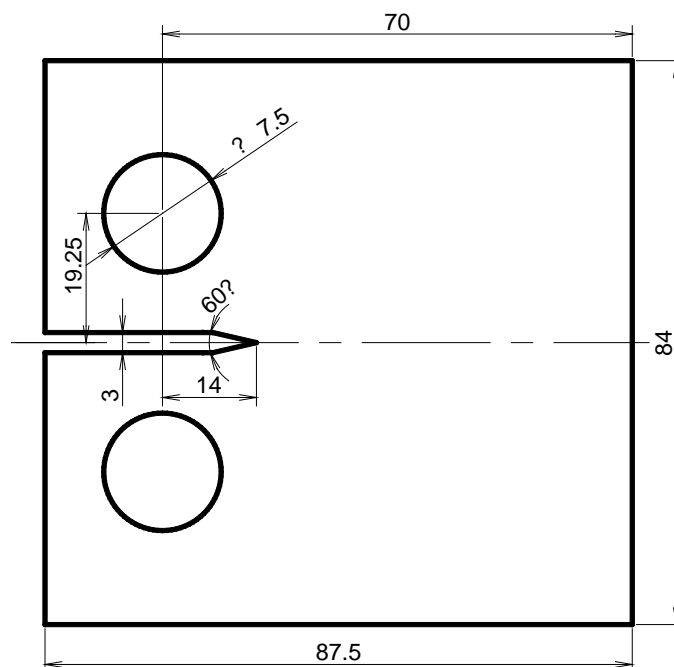


Figure 3-11 Geometry of C(T) specimen (unit: mm)

3.5.2 Pure WAAM specimens cut from Wall-T145 (AL, PL)

For pure WAAM made C(T) specimens (cut from the T-walls without substrate plate), both AL orientation (crack propagates in the direction across the layers) and PL orientation (crack propagates in the direction parallel to the layers, or along the layers) specimens were machined off from the wall. A total of eight C(T) specimens were extracted from Wall-T145 and four of them were used for FCGR tests. The position and definition of AL and PL type C(T) specimens in Wall-T145 are shown in Fig. 3-12. The other four were used for fracture toughness tests in (Lorant, 2010), which is not relevant to this Thesis; hence not mentioned in this chapter.

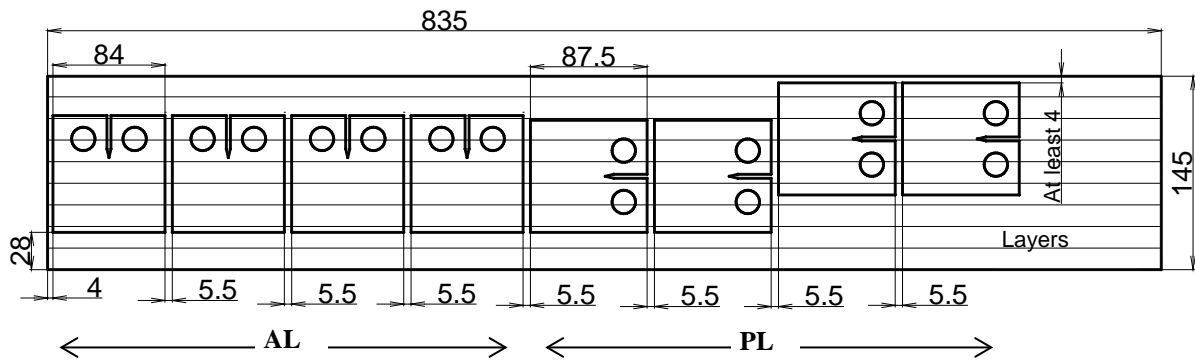


Figure 3-12 Position of C(T) specimens, type AL and PL, in Wall-T145 (C(T) specimen thickness = 5 mm)

3.5.3 WAAM-substrate interface specimens cut from Wall-Bi120 (A, B, C, D, E)

For C(T) specimens which include WAAM-substrate interface, five configurations were tested. These C(T) specimens were denoted by letters from A to E, see Fig. 3-13. The Type A configuration was machined such that the crack perpendicular to the interface and initiate in the substrate and then propagate into the WAAM made material. In the Type C configuration, the crack was also perpendicular to the interface, but initiate in the WAAM made material and then propagate into the substrate. The Type B, D and E configurations were designed such that the crack is parallel to the interface. In the Type B configuration, the crack was initiated just at the interface. The Type D and E configurations have the initial crack either 3 mm above or below the interface, respectively. As three Wall-Bi120 samples were machined, each configuration had three specimens and a total of 15 specimens were used for FCGR tests.

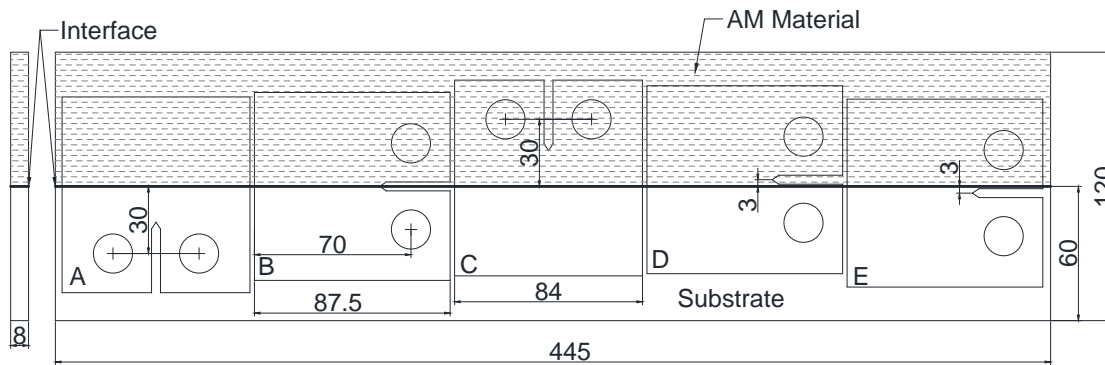


Figure 3-13 Position of C(T) specimens for fatigue crack growth rate testing, Type A to E, in Wall-Bi120 (C(T) thickness = 6 mm)

3.6 Fatigue crack growth rate tests

Fatigue crack growth rate tests were conducted according to ASTM E647-11. Fatigue pre-cracking was conducted first, until a fatigue crack of 3 mm length was initiated at the notch root. Then, constant amplitude cyclic loads were applied until the displacements of loading holes were so large that cyclic loads cannot be applied. Parameters for these tests are summarized in Table 3-5.

Table 3-5 Fatigue crack growth rate testing parameters ($W = 70$ mm, $R = 0.1$ for all)

| Specimens | Test Machine | Fatigue precracking | Constant amplitude loads | Crack size measurement |
|---|--|--|--|--------------------------------------|
| L-T and T-L $B=7.1$ mm Extracted from plate in MA condition | Instron 8031, load capacity 50 kN | $P_{\max} = 8$ kN for 2.5 mm $P_{\max} = 7$ kN for further 0.5 mm | $P_{\max} = 6$ kN $f=10$ Hz | travelling microscope ($\times 7$) |
| Type A-E $B=6$ mm Extracted from Wall-Bi120 | Instron 8031, load capacity 50 kN | $P_{\max} = 6$ kN for 2.5 mm $P_{\max} = 5$ kN for further 0.5 mm | $P_{\max} = 5$ kN $f=10$ Hz | travelling microscope ($\times 7$) |
| AL and PL $B=5$ mm Extracted from Wall-T145 | DMG servo-hydraulic, load capacity 20 kN | — | $P_{\max} = 2.4$ kN $P_{\max} = 2.1$ kN $f=8$ Hz | Direct Current Potential Drop |

Recorded output was the crack length vs. load cycles. The incremental polynomial method as recommended by ASTM E647 test standard was used to obtain the relationship of fatigue

crack growth rate (da/dN) vs. applied stress intensity factor range (ΔK) from the original test output data. The number of points that used to fit the crack length, a , in incremental polynomial method was seven.

For the bi-material specimens (WAAM-substrate), following observations are made. Photos of crack surface of the A3 specimen are shown in Fig. 3-14 and FCGR da/dN vs. ΔK plots for all three Type A specimens are shown in Fig. 3-15. Comparing to the wrought specimens, higher FCGR in Type A specimens for ΔK from 15 to 20 $\text{MPa}\sqrt{\text{m}}$ was observed. It is also seen that FCGR for the A3 specimen are much higher than that for A1 and A2 specimens from about $\Delta K = 40 \text{ MPa}\sqrt{\text{m}}$, which corresponds to a crack length of about 40 mm. Smooth fracture surfaces can be observed at about 40 mm crack length. The smooth surfaces are just like a surface of prior- β grains in WAAM made Ti-6Al-4V. The possible reason is that the FCGR become faster when crack propagates along the boundary of prior- β grains. However, no further investigation was performed to find the grain boundary α phase.

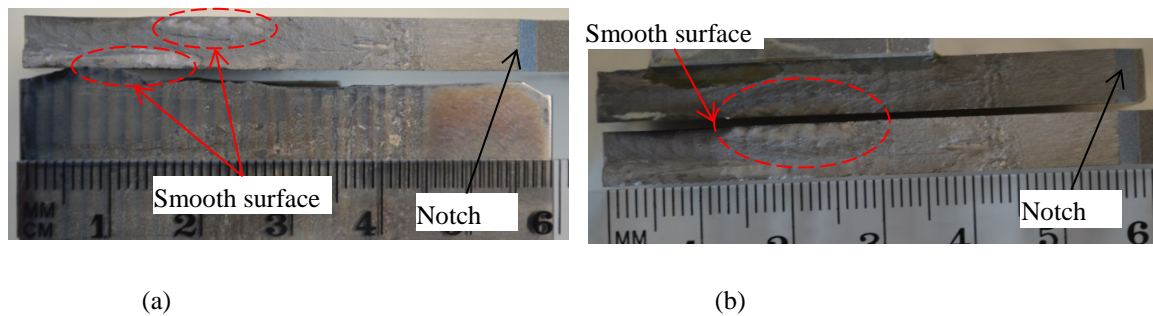


Figure 3-14 Crack surface of A3 specimen show the smooth surface begin at about $a = 40 \text{ mm}$, (a) one crack surface with one side face, and (b) two crack surfaces

The da/dN vs. ΔK plots for type C, B, D and E specimens are shown in Fig. 3-16, Fig. 3-17, Fig. 3-18 and Fig. 3-19, respectively. FCGR data for Ti-6Al-4V of wrought products are shown in Fig. 3-20. FCGR for pure WAAM specimens are shown in Fig. 3-21.

The da/dN vs. ΔK plots for specimens from both Wall-Bi120 and wrought Ti-6Al-4V show overall good agreement among each configuration. The variability of da/dN for them is less than 2, whereas a slightly bigger variability is shown for specimens from Wall-T145.

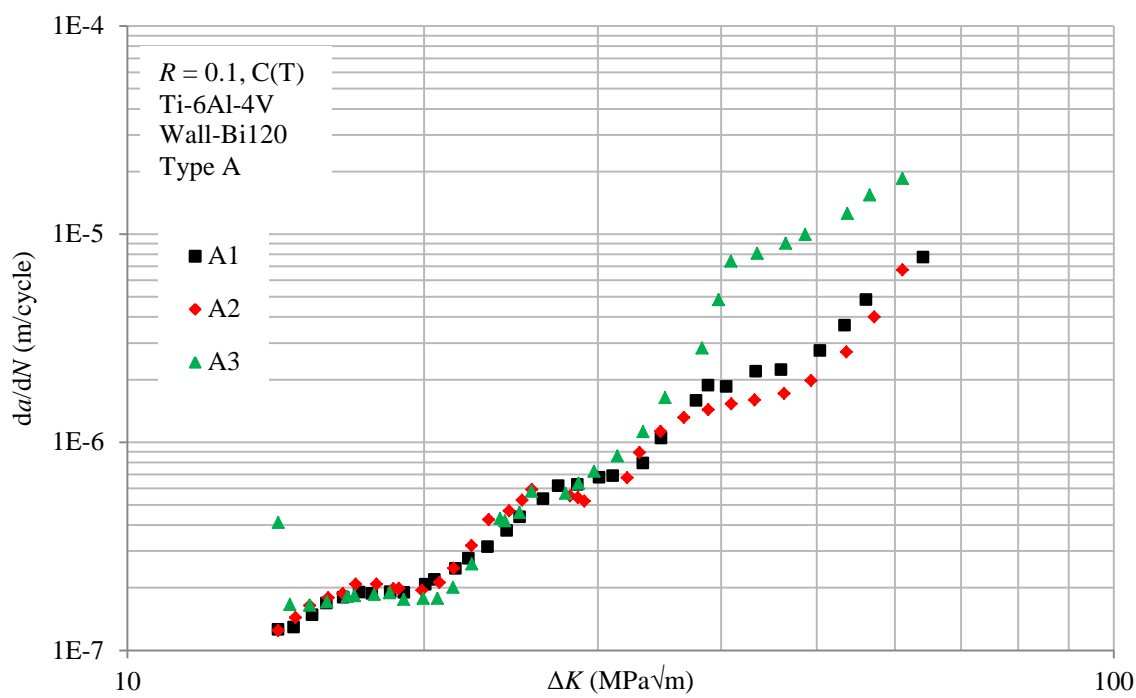


Figure 3-15 Fatigue crack growth rates in WAAM made Ti-6Al-4V, type A

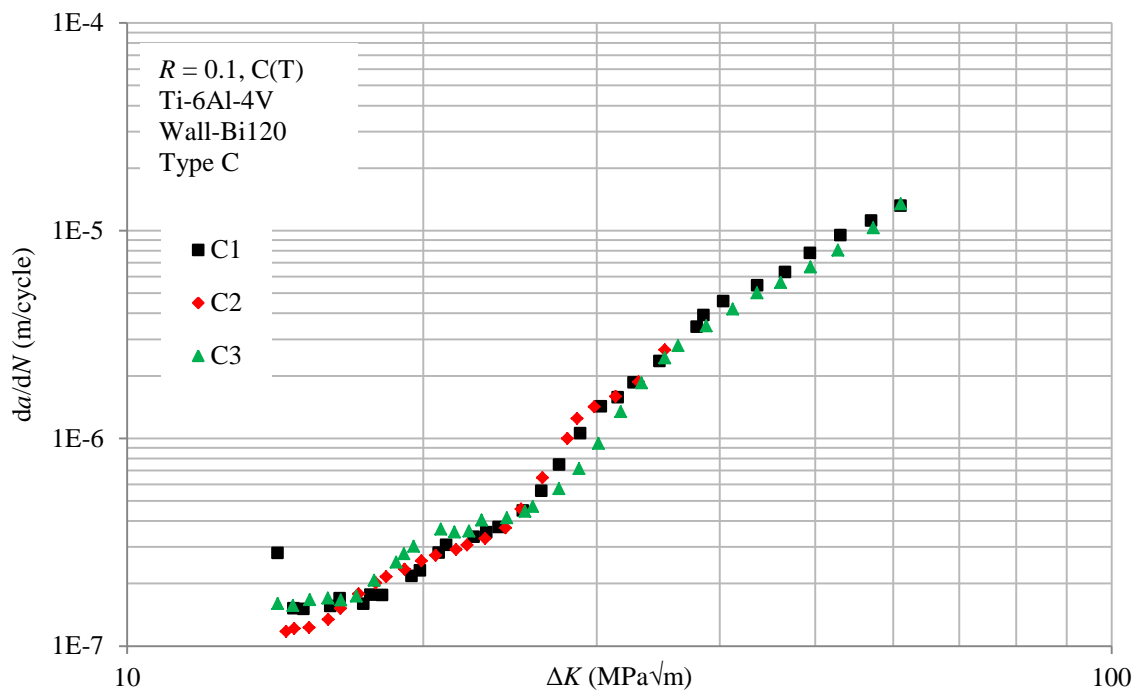


Figure 3-16 Fatigue crack growth rates in WAAM made Ti-6Al-4V, type C

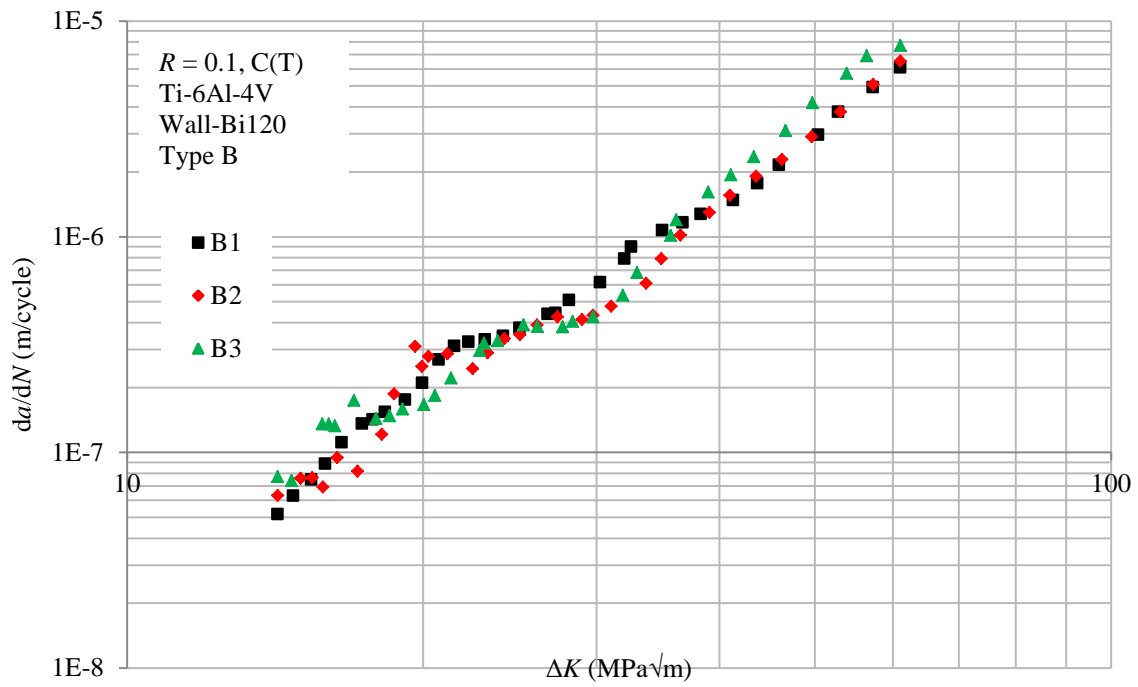


Figure 3-17 Fatigue crack growth rates in WAAM made Ti-6Al-4V, type B

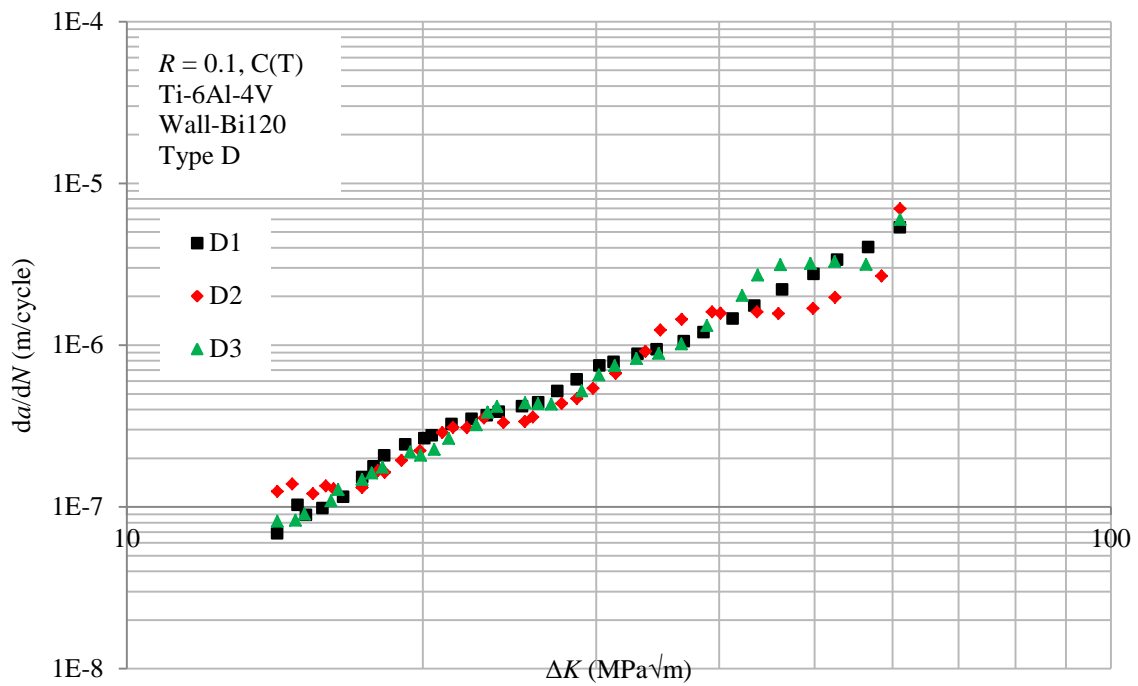


Figure 3-18 Fatigue crack growth rates in WAAM made Ti-6Al-4V, type D

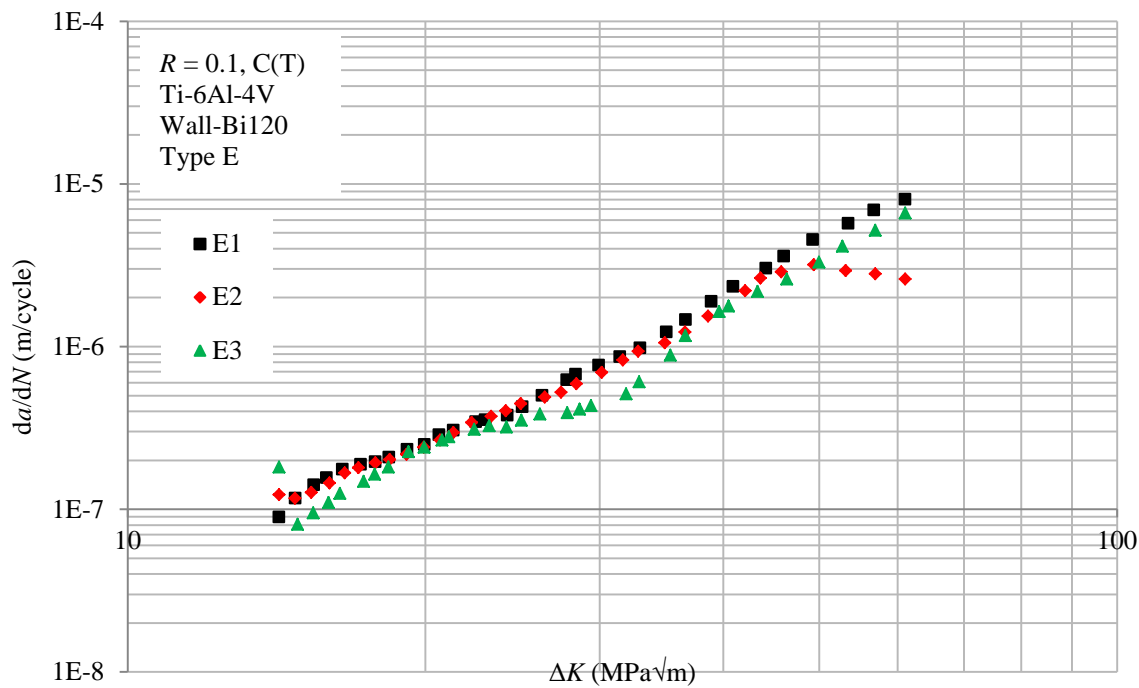


Figure 3-19 Fatigue crack growth rates in WAAM made Ti-6Al-4V, type E

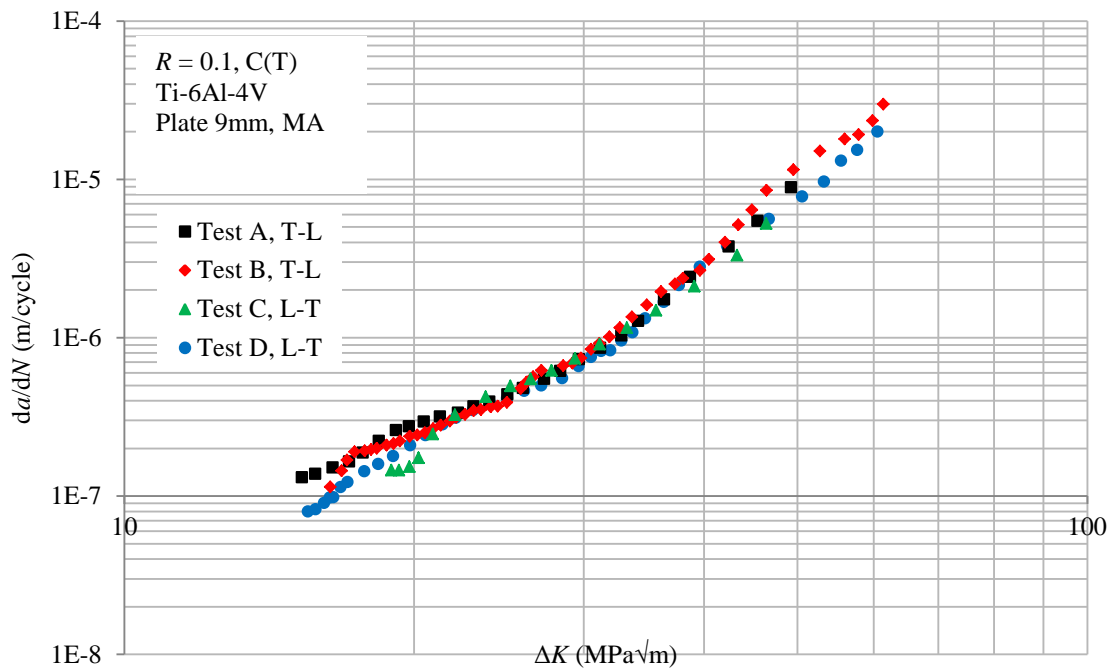


Figure 3-20 Fatigue crack growth rates in Ti-6Al-4V of wrought products

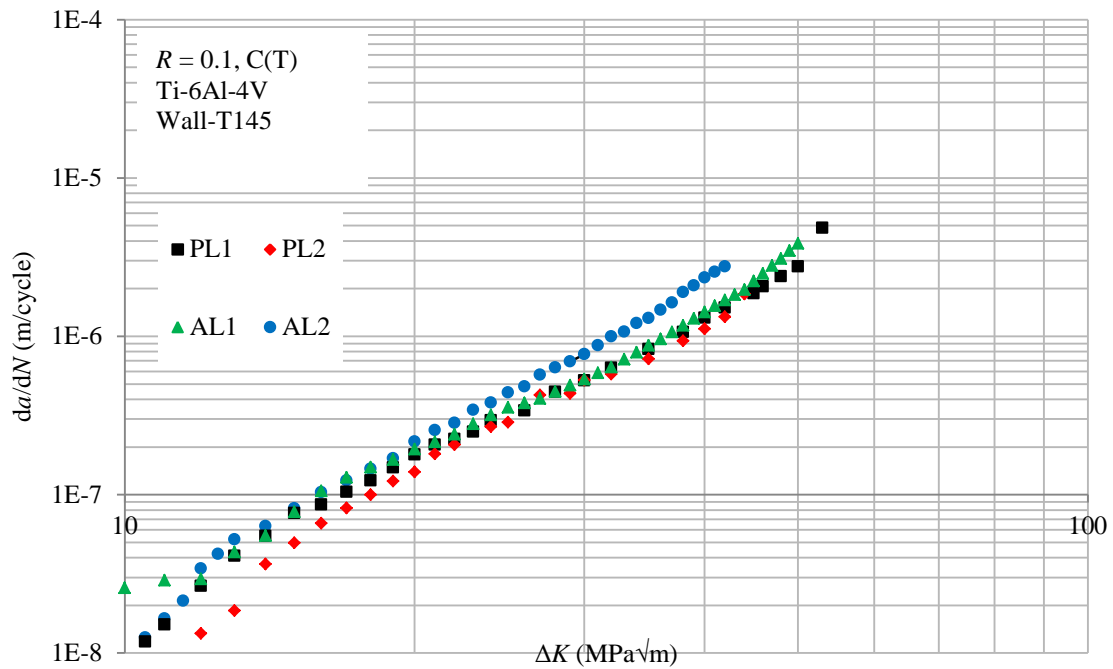


Figure 3-21 Fatigue crack growth rates in WAAM made Ti-6Al-4V. Specimens are extracted from Wall-T145. Data are replotted from appendix in Lorient's thesis (2010). (PL: crack propagates parallel to the layers; AL: crack propagates across the layers)

3.7 Optical microscope (OM) observation

The aim of OM observation is to verify the microstructure in the Wall-Bi120. Furthermore, OM photos are better for demonstrating the crack path deviation in C(T) specimens.

After the FCGR tests, the C(T) specimens which were extracted from Wall-Bi120, were cut into a smaller size in order to prepare for the OM observation. First, the OM samples were mechanically ground using silicon carbide (SiC) paper starting with 120 grit and progressing through 240, 1200, and 2400 grit papers. The final polishing was performed on a polishing cloth with colloidal silica suspension. This step was followed by chemical etching with Kroll's reagent (2% HF, 4% HNO₃) for 25 seconds.

Macrostructure of type A, B, and C specimens are shown in Fig. 3-22. It can be seen that, in the Type A configuration, the crack is perpendicular to the interface and initiates in the substrate and then propagates into the WAAM made material. Whereas the crack initiates in the WAAM made material and then propagates into the substrate in the Type C configuration. It is worth note that the crack do not initiate at the interface as expected in the Type B

configuration. The crack propagates towards the substrate in the Type B configuration.

The optical microstructure of WAAM deposited Ti-6Al-4V is shown in Fig. 3-23. It can be seen that microstructure in WAAM made material is $\alpha + \beta$ lamellar and no colony is observed.

The crack paths in both WAAM made Ti-6Al-4V and the substrate are shown in Fig. 3-24. It can be seen that the crack path in the substrate is rather smooth, whereas a rather tortuous path is observed in the WAAM made material.

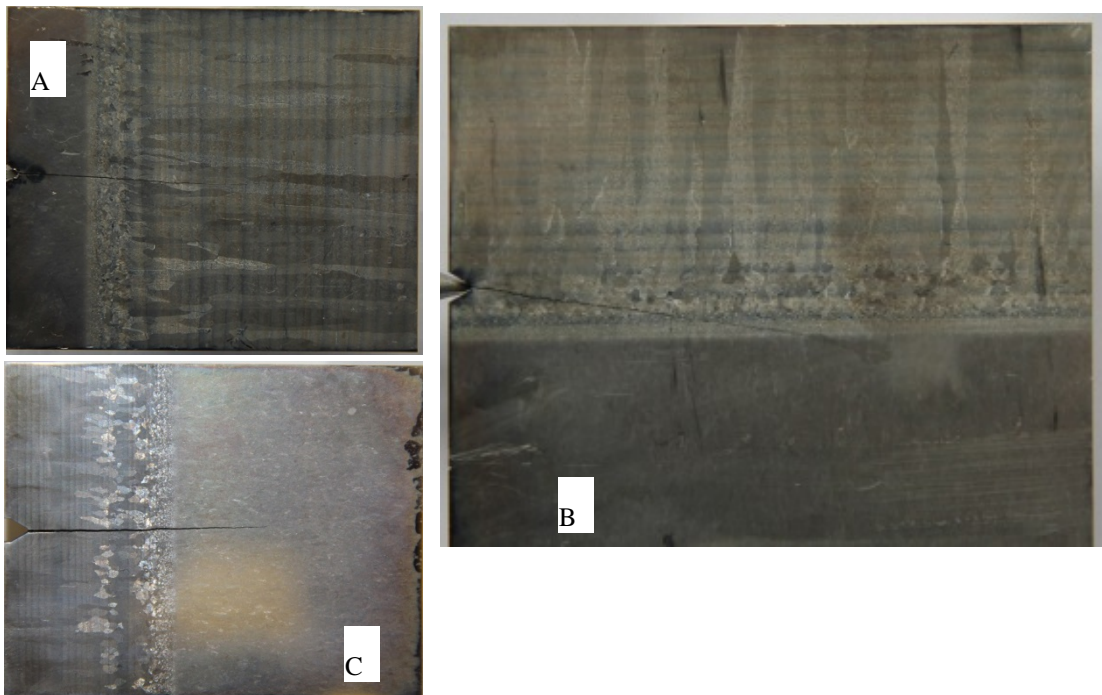


Figure 3-22 Macrograph of the Type A, B and C specimens.

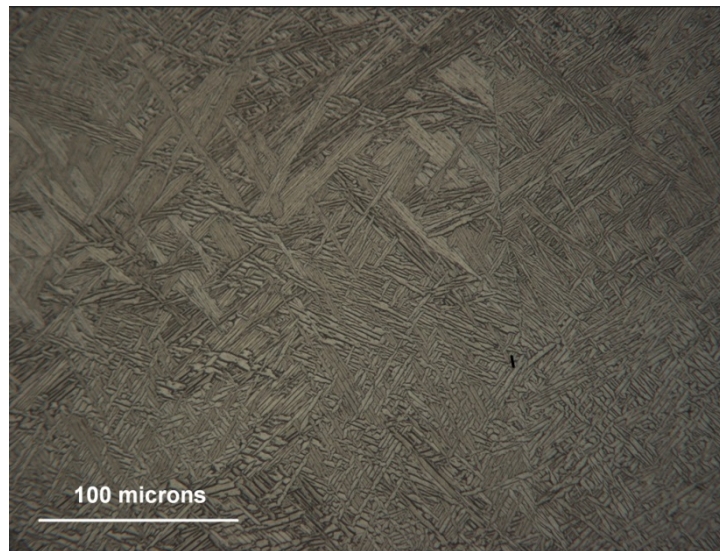


Figure 3-23 Optical micrographs of the WAAM deposited material in Wall-Bi120

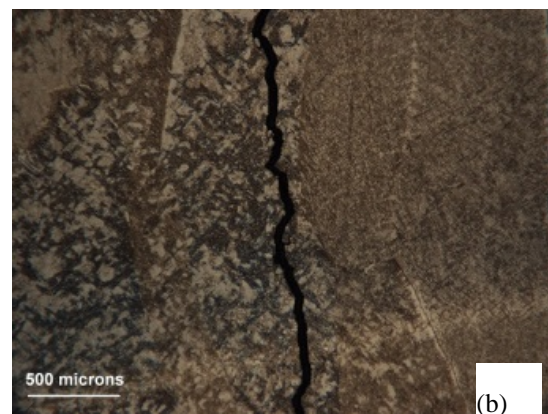


Figure 3-24 Optical micrographs of crack path when the crack propagates in (a) the substrate of Wall-Bi120 and (b) the WAAM made material

Chapter 4 Residual Stress Analysis

4.1 Introduction

When considering the influence of residual stress in a WAAM made part, one difficulty is to obtain the residual stress profile. Ways to obtain residual stress profile in additive manufactured parts include analytical method, thermal-mechanical FE analysis, and experimental measurement including neutron and X-ray diffraction methods (non-destructive evaluation) and contour methods (destructive method). In this PhD project, residual stress profiles in WAAM walls were obtained by the contour method. To obtain residual stress distribution in C(T) specimens, FE method was employed to model the process of residual stress redistribution during extracting the C(T) specimens from a wall. First, the residual stress distribution in a large wall was modelled by inputting residual stresses obtained from experimental measurement. Second, the process of extracting C(T) specimens was modelled by using the element removal method. These two steps can provide the residual stress distribution in the C(T) specimens. However, it was found that directly inputting the measured initial stress values in the wall into the final C(T) geometry can also provide the same residual stress distribution. In Section 4.4, the two methods of directly inputting initial stresses and inputting initial stresses into wall followed by the element removal were compared. In Section 4.5, three types of residual stress profiles were evaluated by the author of this Thesis through an analytical model. Residual stresses in Wall-T145 were subsequently estimated by extending measured residual stress profile in Wall-T110, and then the residual stress retained in the C(T) specimens were evaluated. Measured da/dN vs. ΔK data for pure WAAM Ti-6Al-4V was obtained from Wall-T145, under the assumption that residual stress in the small C(T) is very low so that the FCGR data was obtained from a residual stress-free condition. Therefore, it is necessary to support this assumption by obtaining residual stress profile in Wall-T145. In Section 4.6, the reason for not using the transverse residual stress component is discussed.

4.2 Modelling residual stress in Wall-Bi120

4.2.1 SIGINI

A method of modelling residual stresses in a structure by FEM is to input the measured residual stress values by an ABAQUS subroutine called SIGINI. This method has been widely used by many modellers (Bao et al., 2010; Lei et al., 2000; Liljedahl et al., 2008). Analysis process in the SIGINI routine includes three steps. First, the residual stresses values were written into an FE subroutine, SIGINI. Subsequently, the residual stresses were input into elements in the FE model by the SIGINI. In this thesis, the same residual stress distribution was inputted by using the SIGINI subroutine to every material plane that is parallel to the cutting plane throughout the whole wall. Finally, the obtained residual stresses were checked by comparing stresses values in FE model to experimental values after achieving a self-equilibrium state.

The obtained full residual stress fields have been partially verified. Residual stresses along the potential crack path were measured by the neutron diffraction. A reasonable agreement was obtained between experimental results and FE output (Liljedahl et al., 2008). Furthermore, when crack grew under fatigue loading, the agreements were still reasonable, as shown in Fig. 4-1.

Some materials have been removed from this thesis due to Third Party Copyright. Pages where material has been removed are clearly marked in the electronic version. The unabridged version of the thesis can be viewed at the Lanchester Library, Coventry University.

Figure 4-1 Comparison between the experimental results and FE output of the longitudinal residual stress (Liljedahl et al., 2008)

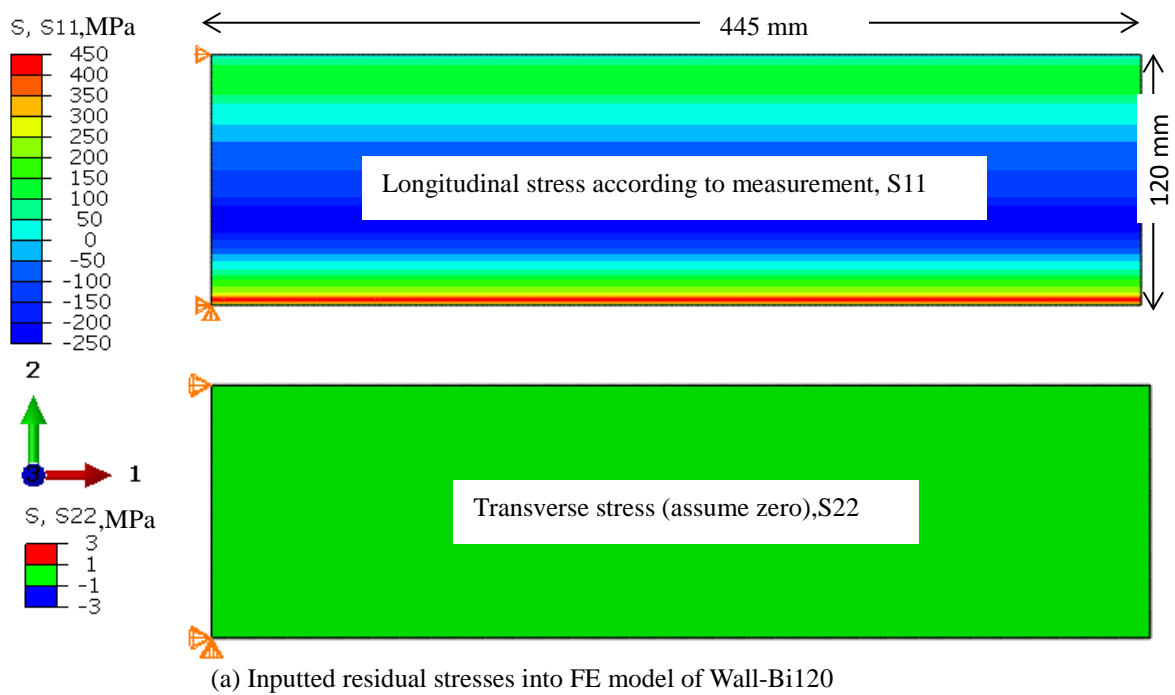
4.2.2 Wall-Bi120

The first thing of analysing residual stress is to obtain the required residual stress distribution in the wall. A 2D FE model of Wall-Bi120 was constructed to obtain this required residual stress distribution. The geometry of FE model is just the geometry of Wall-Bi120 prior to cutting step during the contour method residual stress measurement, which has been shown in previous section, see Fig. 3-1. Plane stress elements (second order element designated as CPS8 in ABAQUS) were used to mesh the model. The size of element is $0.5 \text{ mm} \times 0.5 \text{ mm}$. This size is based on a mesh convergence study to obtain residual stress distribution in C(T) specimens. Isotropic material properties, i.e. Young's modulus of 113.8 GPa and Poisson's ratio of 0.342 were used since the difference between the wrought substrate and WAAM Ti-6AL-4V in the two major material directions is within 15%. In terms of the boundary

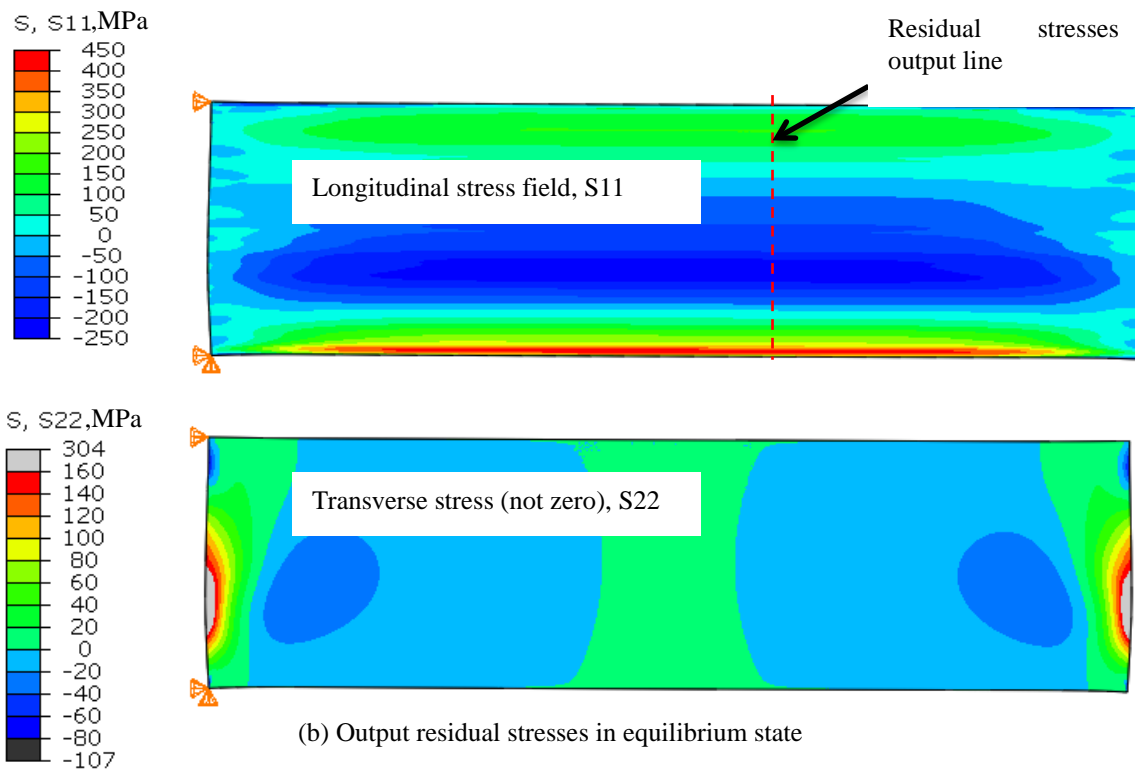
conditions only the rigid body displacements were constrained and allow deformation in all other directions. Residual stresses were applied to whole area of FE mesh by using the SIGINI and the input data into SIGINI were the measured 1D residual stress distribution without any scale on magnitude, see Fig. 4-2a. Linear elastic analysis procedure without external load is performed to achieve the equilibrium state, see Fig. 4-2b. The obtained longitudinal residual stresses are compared to the experimental measured residual stresses, as shown in Fig. 4-3. As residual stresses vary spatially, the output stress line in FE model must be corresponding to the cutting plane in the contour measurement.

As demonstrated, the amplitude of measured residual stress distribution is inputted into FE model that can produce required longitudinal residual stress distribution, so the measured values need not to be scaled. The reason for this is that the cut plane is far away from the free edges in the 2D FE model, which represent two ends in the wall. If the cutting plane is not far away from the two edges, or the sample prior to cutting is not long enough, measured residual stress distribution need to be scaled up in order to build the required residual stresses.

Another important thing is that transverse residual stress appeared near the left and right edges in FE model. The reason for this is the deformation near the two free edges, which is caused by the longitudinal residual stress and Poisson's contraction that result in transverse residual stress.



(a) Inputted residual stresses into FE model of Wall-Bi120



(b) Output residual stresses in equilibrium state

Figure 4-2 Procedure of inputting measured residual stress field in Wall-Bi120 sample by using SIGINI

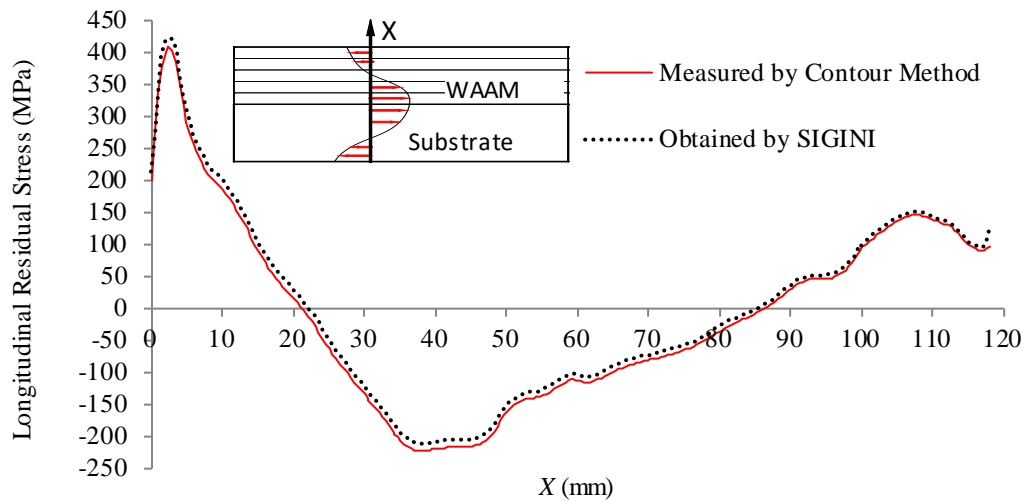


Figure 4-3 Comparison of obtained longitudinal residual stresses with experiments

When measuring residual stresses by the contour method, the displacement profile is measured first, and then residual stresses are obtained from such displacements by an FE analysis. This FE analysis step needs the Young's modulus. So, the Young's modulus has an influence on the magnitude of measured residual stress field. When considering the bi-material sample of two different Young's modulus, the error in measured residual stress field was nearly inevitable if bi-material properties are not considered. In this research work, the measured residual stress field did not come from FE model of two different Young's modulus. So, the measured residual stress field is expected to have some errors. However, the difference between Young's modulus for WAAM made material and the substrate is within 15%. The Young's modulus for Ti-6Al-4V of wrought products has a range from 110 to 117 GPa and the longitudinal Young's modulus for WAAM made Ti-6Al-4V has a value of 124 GPa.

4.3 Evaluation of retained residual stress in C(T) specimens

As is known, both extracting a specimen and growth of a crack may change the retained residual stress distribution in specimen. Both of these scenarios can be predicted by FEM (Law et al., 2010; Liljedahl et al., 2008). In this section, the retained residual stress distribution in specimen was predicted by using the SIGINI subroutine and the element removal method.

Following the inputting of residual stress in previous Wall-Bi120 FE model, the elements that represent the cut off material were removed from the FE model. Then, the FE model achieved

a new equilibrium state based on the retained FE mesh and new residual stress distribution appeared. The geometry of C(T) specimens is shown in previous section, see Fig 3-11, and the positions of specimens are shown in Fig. 3-3 and Fig. 3-13. It is noted that the position of Type A and C specimens in two figures are different. The reason of using position in Fig. 3-3 is to compare with experimental measurement and the aim of using positions in Fig. 3-13 is to calculate the stress intensity factors due to residual stress for further analysis.

As the element removal procedure was following the building of residual stress procedure, which is shown in previous section, the elements type, element size and the elastic material property were the same as previous description. The procedure of extracting C(T) specimen was cutting a block of C(T) size, creating the holes and then cutting the notch. During such extracting procedure, geometry change and residual stress redistribution of two examples, type B and C specimens in Fig. 3-3, are shown in Fig. 4-4. New boundary conditions were applied to each specimen to constrain the rigid body movement but allow deformation in any direction. Again, linear elastic analysis procedure without external load was performed to achieve new equilibrium state in the C(T).

Mesh convergence study was conducted on element sizes of 0.5×0.5 , 1×1 , 2×2 and 4×4 (unit: mm \times mm). The mesh size of 2×2 is shown in Fig. 4-5. The longitudinal residual stress in type C specimens are compared among different element sizes, as shown in Fig. 4-6. It can be seen that residual stress distributions are very similar, indicating that acceptable results can be obtained even with the coarse mesh discretization. As the mesh convergence aimed to demonstrate overall retained residual stress field in the C(T) specimen, the stress values at the crack tip were omitted. A stress singularity existed at the crack tip. Theoretically the stress is infinite at the crack tip, and therefore increasing the mesh density will not yield a converged stress value at the crack tip. This crack tip stress normally has a negligible effect on the overall retained stresses, so it was omitted in comparison. The computing times for all sizes were less than 5 minutes. The mesh size of 0.5×0.5 was used for all later residual stress analysis.

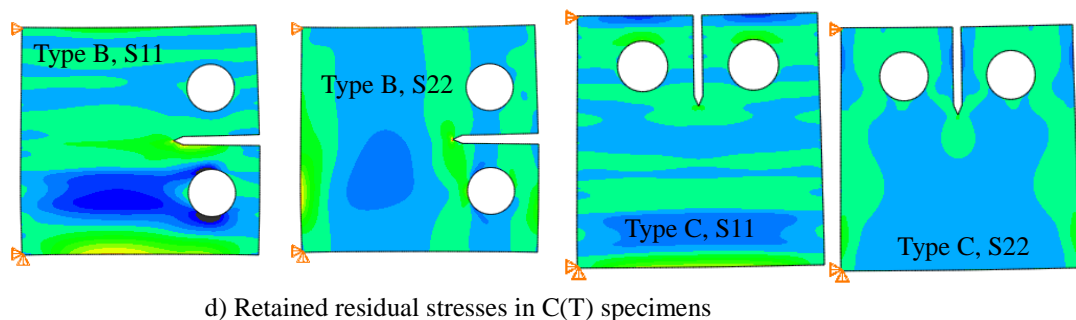
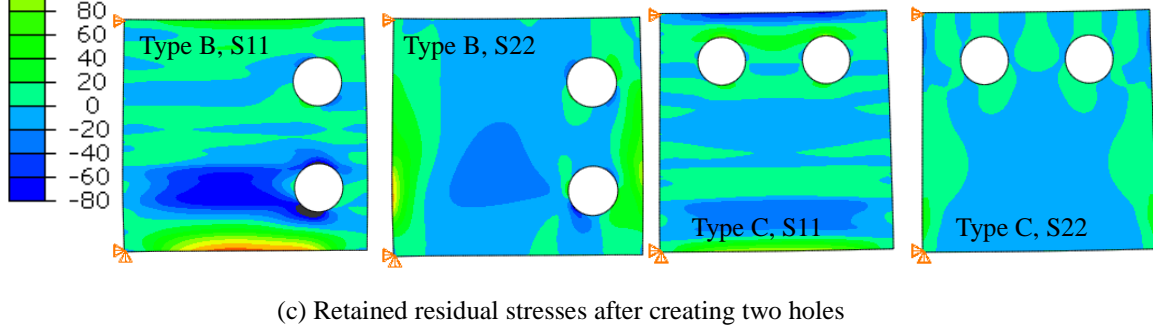
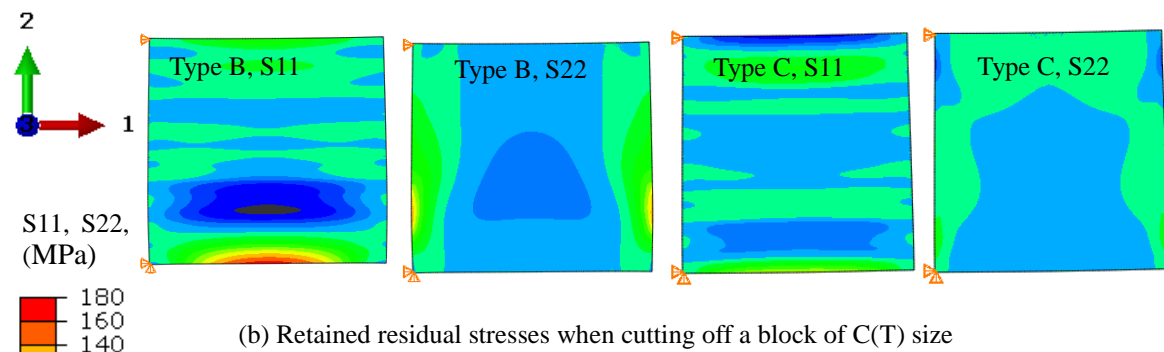
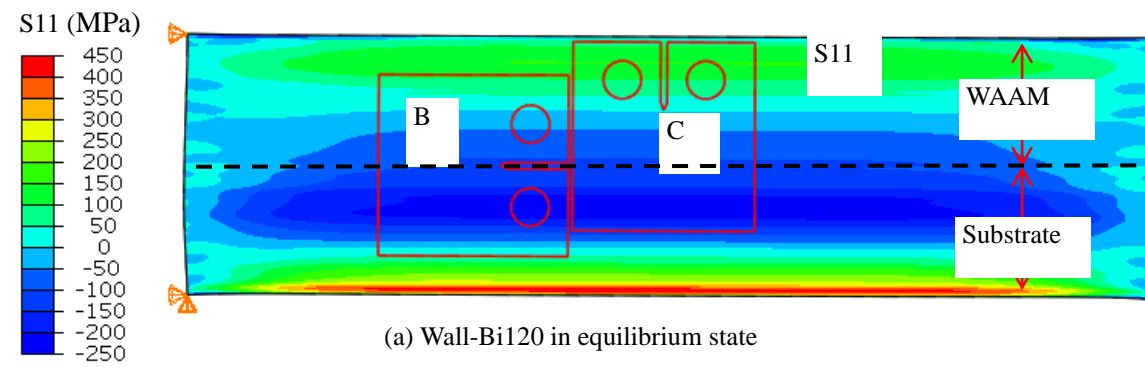


Figure 4-4 Geometry change and residual stress redistribution during extracting type B and C specimens (direction 1: longitudinal direction; direction 2: transverse direction; b, c, and d figures share the same spectrum)

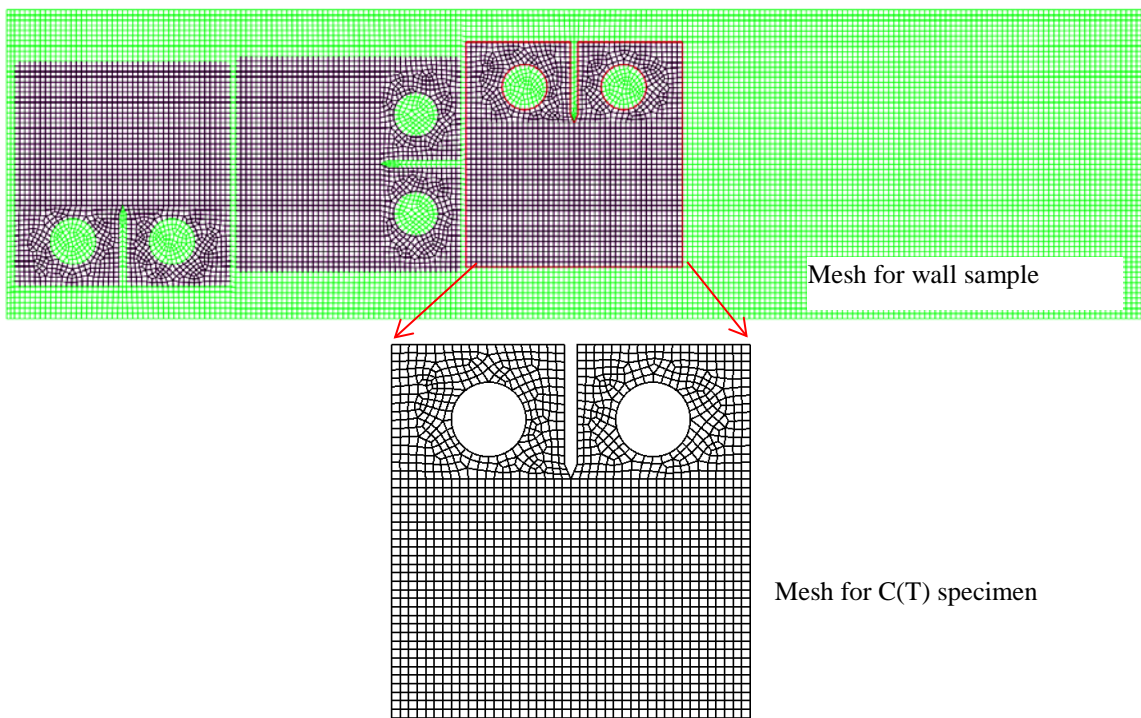


Figure 4-5 Finite element mesh for residual stress analysis with mesh size $2\text{ mm} \times 2\text{ mm}$

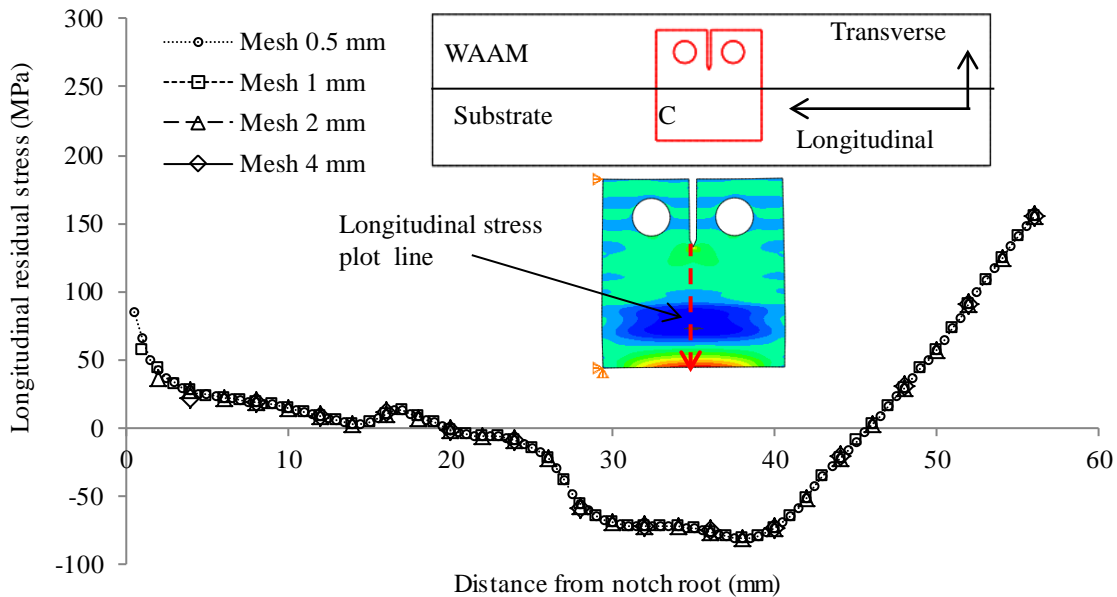


Figure 4-6 Mesh convergence study for retained residual stress in C(T) specimen, type C

Retained residual stress in C(T) specimens according to Fig. 3-3 by FE analysis are compared with experimental measured residual stress data, as shown in figures 4-7, 4-8 and 4-9. A good agreement has been obtained for type B and C specimen. However, for type A specimen, the contour method provides a higher residual stress in the range from 0 to 5 mm distance from

the notch root. At the same time, the residual stress in the range from 40 to 56 mm distance from the notch root shows the same trend. The reason for this is that the type A specimen is very near to the end of Wall-Bi120. The ends of Wall-Bi120 are the position for starting or stopping each layer. It is well known that the residual stress near the starting and stopping of a weld is higher than that in other position. So, it is expected that the residual stress near the ends of Wall-Bi120 is higher. And hence, the FE analysis underestimates the residual stress in type A specimen.

It is noted that both longitudinal and transverse residual stress appeared in all specimens. The output residual stress component was transverse direction in the Type B specimen, as transverse direction is normal to the crack path.

The retained residual stress in C(T) specimens according to Fig. 3-13 by FE analysis are shown in figures 4-10 and 4-11. These residual stress distributions will be used for calculating stress intensity factor in next chapter.

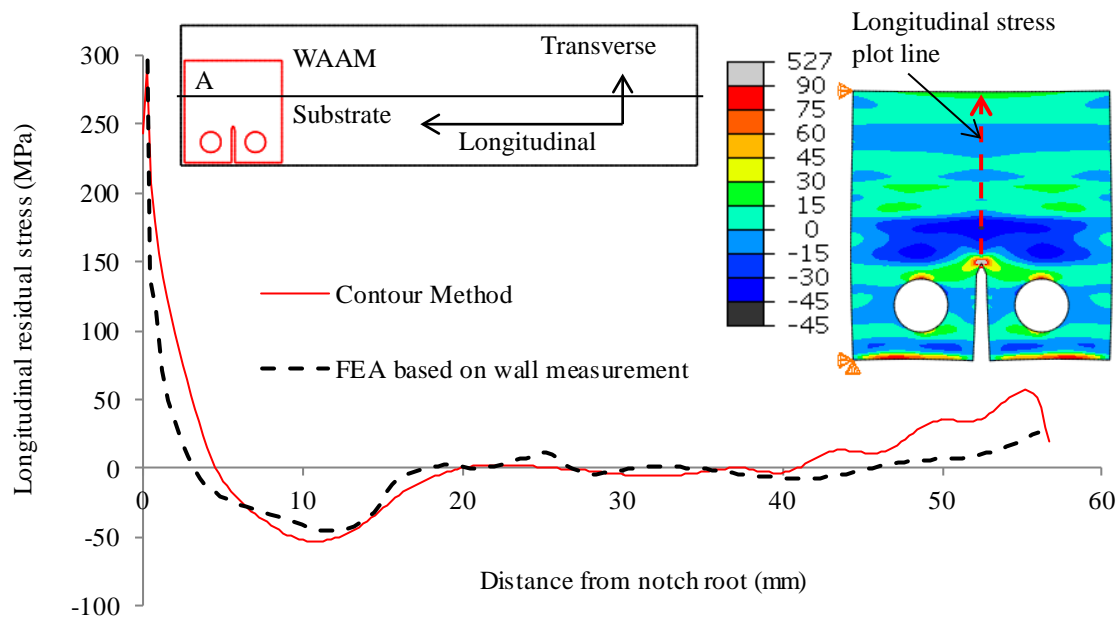


Figure 4-7 Comparison of longitudinal residual stresses between FEA and the contour measurement, along crack path in Type A specimen

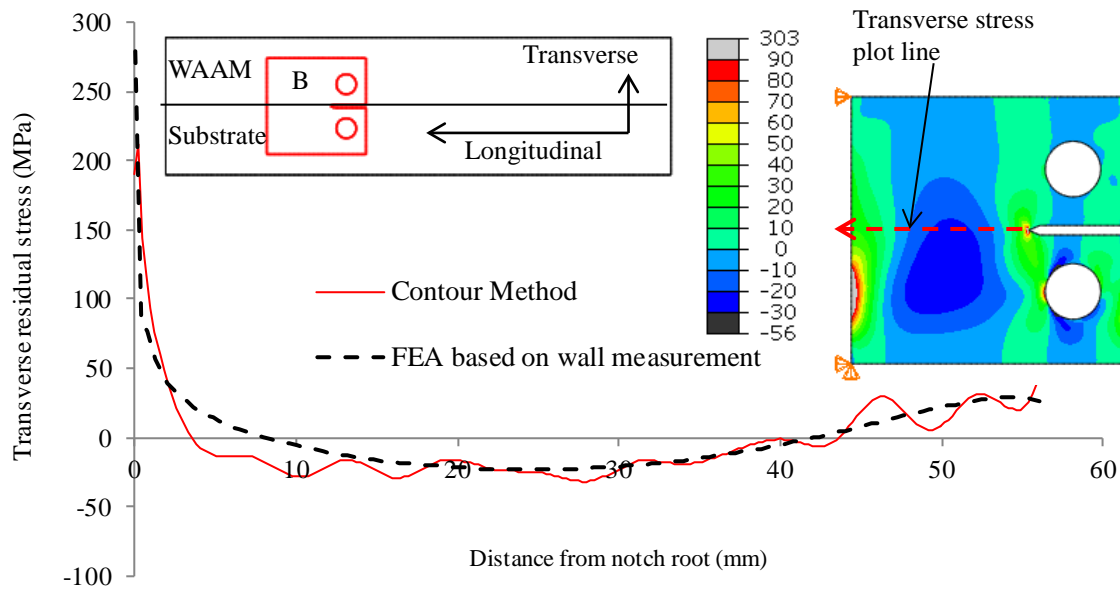


Figure 4-8 Comparison of transverse residual stresses between FEA and the contour measurement, along crack path in type B specimen

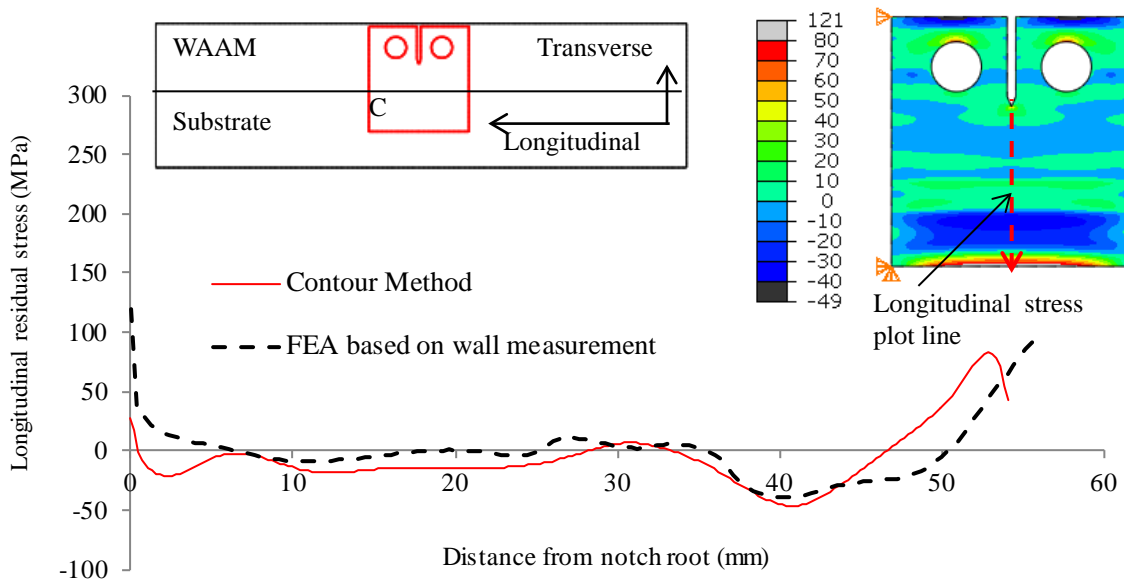


Figure 4-9 Comparison of longitudinal residual stresses between FEA and the contour measurement, along crack plane in type C specimen

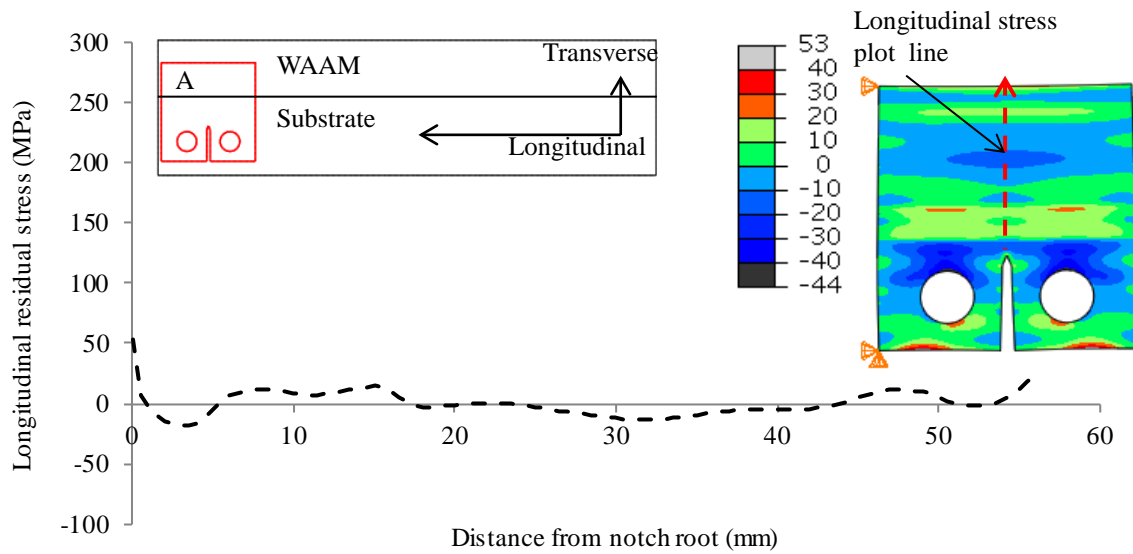


Figure 4-10 Longitudinal residual stresses along crack path in type A specimen (position used in life prediction)

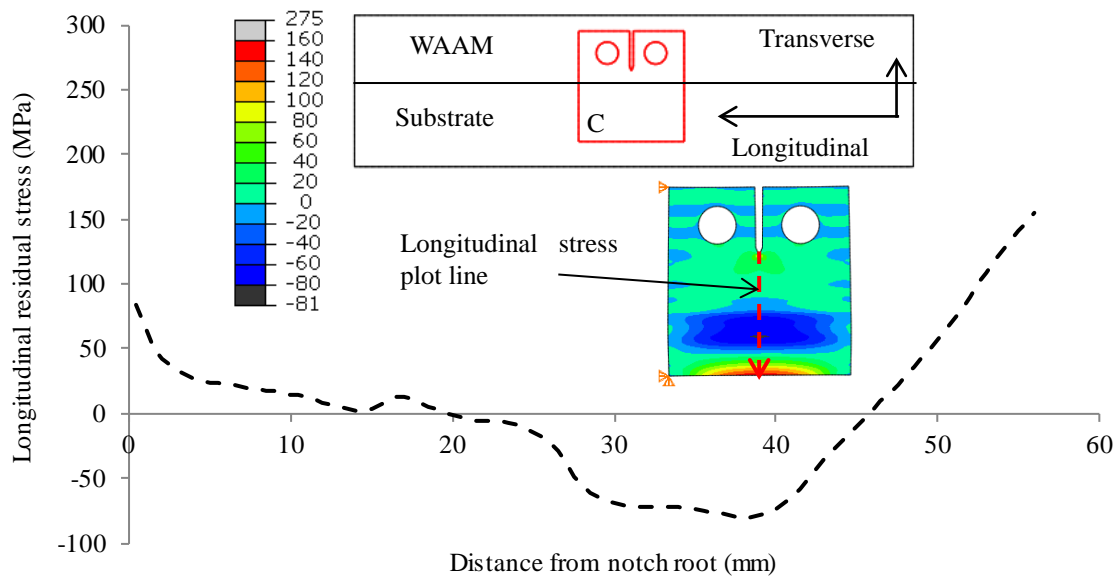


Figure 4-11 Longitudinal residual stresses along crack path in type C specimen (position used in life prediction)

It is noted that the retained residual stress in the Type A specimen is much less than that in the Type C specimen. Unlike the reason mentioned in Section 3.4.2.3, the source for the less stress in the Type A specimen is that the residual stresses profile in uncracked ligament is not moment balance, as shown in Fig. 4-12. After self-moment-balancing, the retained residual stress becomes much less.

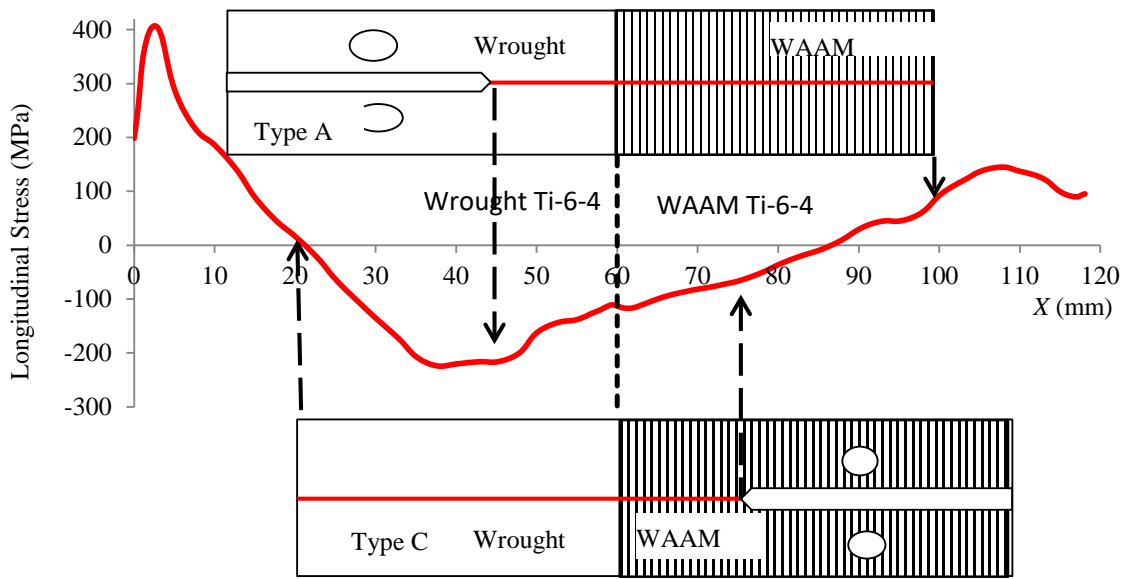


Figure 4-12 Positions of uncracked ligament residual stress field of Wall-Bi120 shows that type A specimen is not moment balance.

4.4 Inputting directly residual stress into C(T) specimen

Another method of obtaining retained residual stress in a specimen is inputting directly residual stress into FE model with the geometry of C(T) specimen. This method has also been used by Law et al. (2010), and is tested herein by comparing residual stress obtained by the two methods. Like modelling residual stress in a wall sample, the measured residual stresses distribution in wall sample were written into the SIGINI subroutine. Then, the same residual stress distribution was applied to every parallel plane throughout the whole C(T) specimen. It is noted that the position of C(T) specimen in residual stress field must be corresponding to its position in the wall sample. For example, the residual stress field has the same width of wall sample, and the correct position of the type C specimen is 20 mm from the bottom of residual stress field, as shown in Fig. 4-13. After a linear elastic analysis step, the FE model of specimen achieved equilibrium state and residual stress in C(T) specimen redistributed.

Directly obtained residual stress distribution was compared with that by method of inputting residual stress in large wall sample and then cutting to small C(T) specimen. Both methods always give exactly the same residual stress values at every point on the plot line, if the same mesh is used in C(T) specimen. One example of comparison, type B specimen cutting

according to Fig. 3-3, is shown in Fig. 4-14.

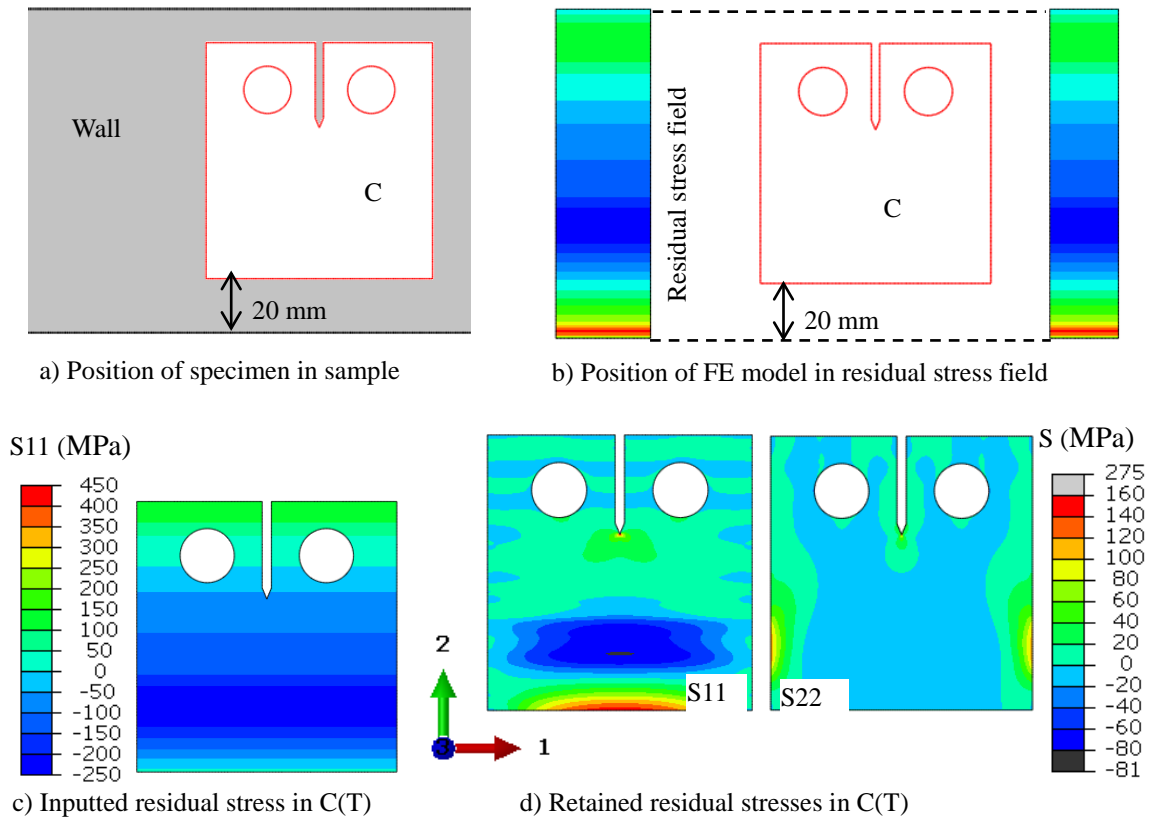


Figure 4-13 Inputting directly residual stress into C(T) specimen (1: longitudinal; 2: transverse)

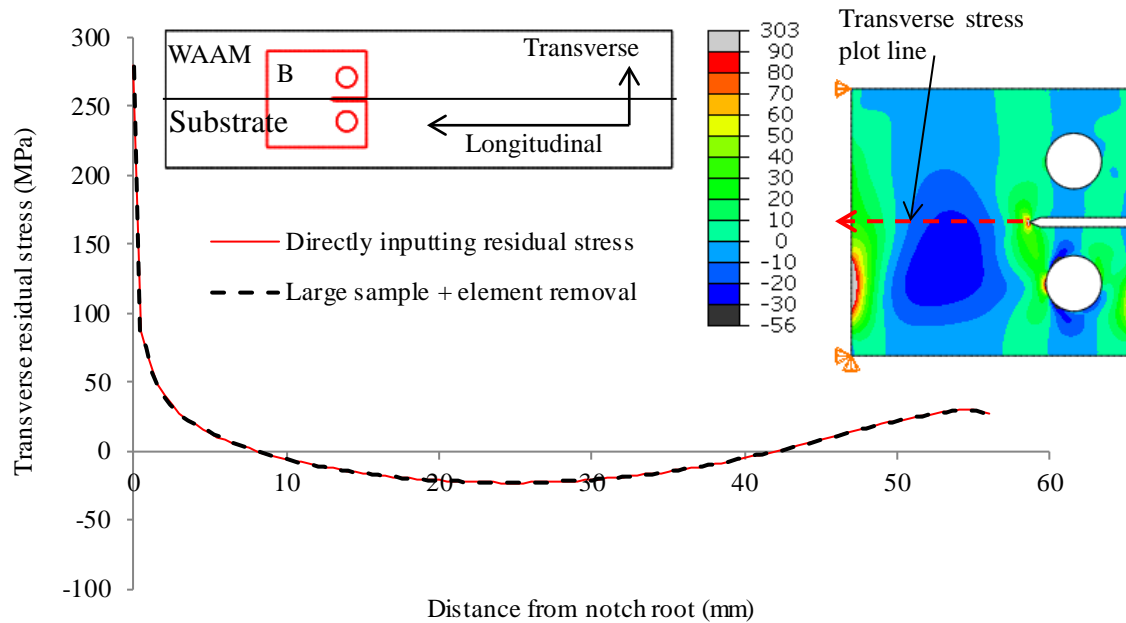


Figure 4-14 Comparison of retained residual stress by directly building residual stress and building residual stress field in large sample + element removal, type B specimen, transverse residual stress.

Such comparisons have been conducted for other residual stress distributions and specimen geometry. The aim of conducting such study is to eliminate the influence of residual stress distribution and specimen geometry on the direct input method. A Variable-Polarity Plasma-Arc (VPPA) weld residual stress distribution (Kartal et al., 2008) with a M(T) specimen geometry, and an AM wall residual stress distribution (Hoye et al., 2014) with a C(T) specimen geometry have been used to make comparison. Both of them gave the same conclusion: both methods provide exactly the same residual stress distribution. An intuitive explanation of this conclusion is that both FE models, directly inputting residual stress vs. cutting off specimen from large sample, have the same modelling information and should have same output information under linear elastic analysis procedure. In this research, both models have the same final geometry, same boundary conditions, same residual stress distribution by the SIGINI, same mesh and hence the same retained residual stresses.

In further analysis of stress intensity factors, the method for modelling residual stress is directly inputting residual stress. But the retained residual stress distributions have been compared between two methods to make sure the same residual stress distribution is obtained.

4.5 Evaluation of Residual Stress by Analytical Approach

4.5.1 Introduction

There is a generic residual stress profile for welds, but not for AM made parts. In welded joints, the generic residual stress profile has a generic shape, i.e. “bell” shape (residual stress in welded butt joint has a tensile residual stress zone with a width related to the heat affected zone (HAZ), and compressive residual stress zone with a balancing value in all rest of the part). However, in WAAM parts, a generic residual stress profile has not been established. The reason for this problem is that WAAM parts experience heat cycles in all deposited layers, and this deposited part has variable height. Furthermore, the configuration of substrate is also variable, as shown in Fig. 4-15. All these geometries and sizes mean that there is no generic residual stress profile in WAAM parts.

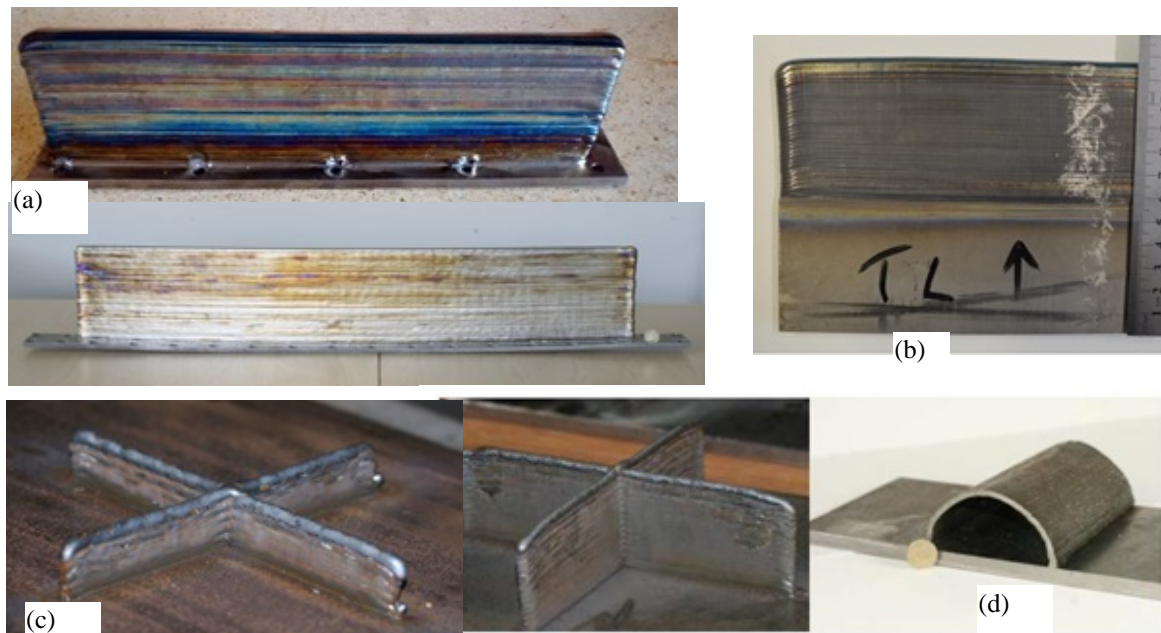


Figure 4-15 Configurations of parts made by WAAM: (a) different height in the wall samples, (b) vertical substrate, (c) crossed walls, (d) curved wall

In this section, available FE and experimental measured residual stress profiles are summarized first, and then an analytical model will be established. Residual stress profile in a “T” section WAAM part with the height of 145 mm, called Wall-T145, will be estimated based on a combination of the analytical model and measured residual stress profile in Wall-T110. After that, the retained residual stress in C(T) specimens from Wall-T145 are evaluated.

4.5.2 Published residual stress profiles

For the configuration that a WAAM made wall stands on a horizontal substrate, “T” section, published residual stress profiles are summarized in Fig. 4-16. Details about the manufacturing methods and residual stress measurement are summarised in Table 4-1.

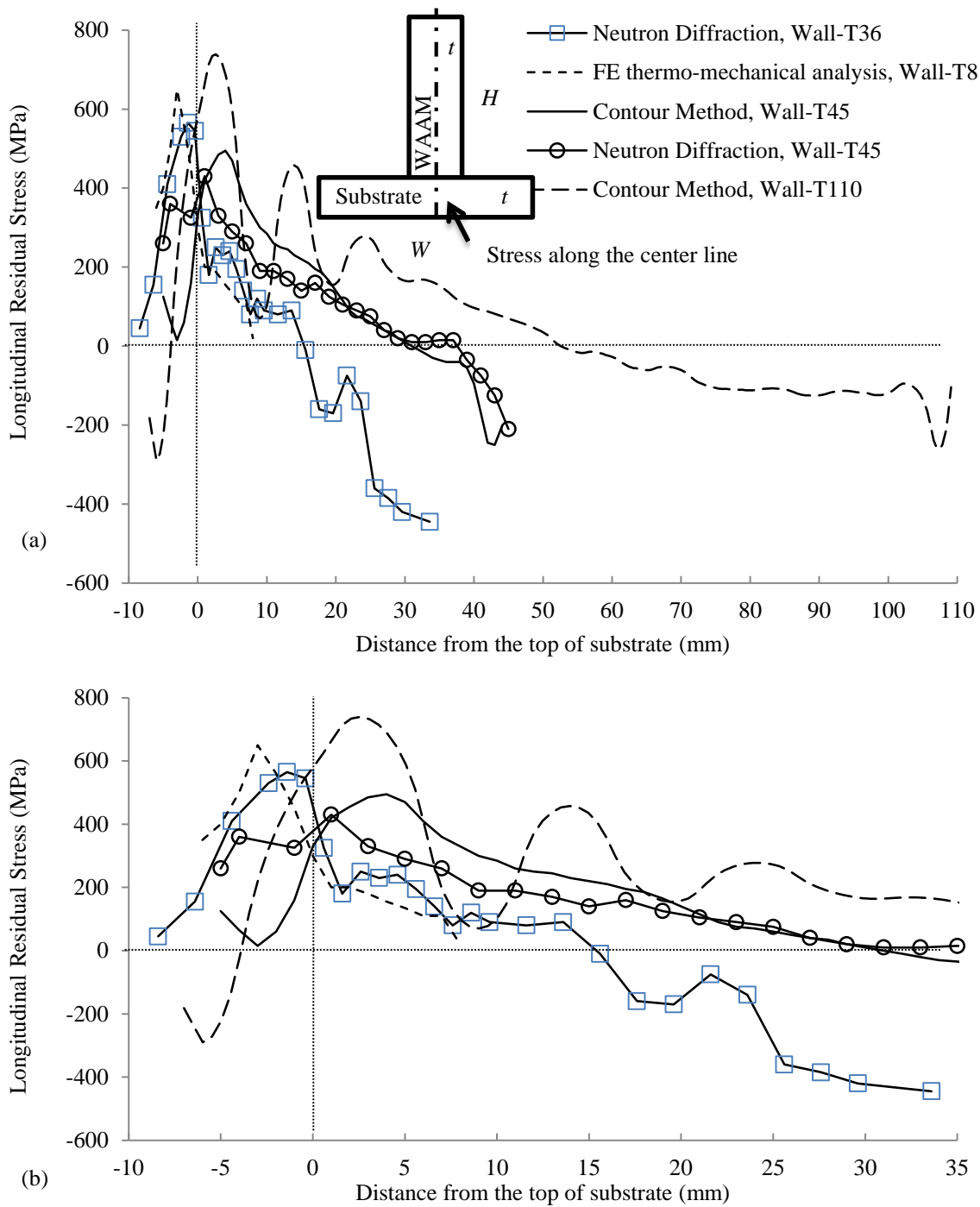


Figure 4-16 Published residual stress profiles for "T" section WAAM made walls, (a) full length of residual stress profile, (b) detailed stress near top of substrate (a&b share the same legend)

Table 4-1 Detail for published residual stress profiles

| Sample label | Wall $H \times t$ (mm) ^a | Substrate $W \times t$ (mm) ^a | Residual stress method | Heating source | Clamps | Reference |
|--------------|---------------------------------------|--|-------------------------------|----------------|------------------------------|--------------------------|
| Wall-T8 | 8 × 6.4 | 60 × 6 | FEA | TIG | – | (Ding, 2012, p.115) |
| Wall-T36 | 36×5 (measure) 40×8 (as-deposited) | 100 × 12 | Neutron diffraction | GTA | With bolt holes on substrate | (Hoye et al., 2014) |
| Wall-T45 | No mention (40 layers) | 60 × 6 | Neutron diffraction & Contour | TIG | No mention | (Colegrove et al., 2014) |
| Wall-T110 | 110 × 6 | 60 × 7 | Contour | Plasma | loosely | (Paddea, 2015) |

^a H : height; W : width; t : thickness

Ding (2012) analysed the residual stress in a “T” section WAAM made sample by FE thermo-mechanical analysis. The height of wall sample is 8 mm in her study. Hoye et al. (2014) measured the residual stress in Wall-T36 by the neutron diffraction method. The Wall-T36 was built with height of 40 mm and thickness of 8 mm, and the substrate was clamped by bolts. Then, the wall was machined to a size of 36 mm high and 5 mm thick to measure the residual stress. Paddea (2015) measured residual stress by the contour method in Wall-T110, which is the sample used in this thesis. Colegrove et al. (2014) measured the residual stress in Wall-T45 by both neutron diffraction and contour method. The height of WAAM made was obtained by the coordinates of residual stress profile. A rather good agreement has been seen between neutron diffraction and contour method measure residual stress profile.

For the “T” section WAAM made walls, the following observations can be drawn from the available residual stress profiles:

- Maximum tensile residual stress locates near the interface between the WAAM made part and the substrate, and the values are from 400 MPa to 700 MPa.
- Minimum residual stress locates at the top of the wall or becomes negative to balance the tensile stress.
- The 1D averaged residual stress profiles do not appear to be self-balanced, see Fig. 4-16. As the residual stress profiles are measured along the center line, the

measurements represent averaged stresses in WAAM made material, whereas in the substrate, the measurements represent local stresses.

- The overall residual stress field should be self-balanced if 2D stress map is available and also consider the stress in the substrate.

4.5.3 Analytical model

This analytical model is based on three concepts: layer-by-layer accumulating, layer residual stress, and virtual substrate. The overall residual stress profile is evaluated from a knowledge of specimen dimensions, layer residual stress value and clamping condition.

The layer-by-layer accumulating concept has been successfully used for predicting residual stress in coating production (Tsui et al., 1997) and has been applied to predicting residual stress in SLM made part (Shiomi et al., 2004; Mercelis et al., 2006). When the AM component is formed layer-by-layer, the residual stress is changed after each layer addition. Although the residual stress for each successive incremental layer is the same, each of these layers deposits on a “substrate” of changing height. Therefore, a succession of force and moment balances determines the changing of residual stress distribution in the “substrate”. The final residual stress distribution will differ significantly from that which deposits the whole AM part in a single operation.

However, an assumption was made during their calculation (Shiomi et al., 2004): the width of substrate and that of SLM made part were the same. This assumption has slight influence on their experiments: the width of substrate is 9 mm and SLM made part 5 mm. But this assumption is not suitable for “T” section WAAM part: the width of substrate is 60 mm and WAAM made part 6 mm. The same assumption was also made during work of Mercelis et al. (2006). In this thesis, beam theory will be used to eliminate this assumption.

Another assumption in analytical models by Shiomi et al. and Mercelis et al. were that the tensile stress in new layer was equal to the material's yield strength. This assumption will be replaced by layer residual stress concept, which is the residual stress in a layer at the time when it is not affected by the heating of the proceeding deposited layers. When only 1 layer is

deposited, the value of this layer residual stress should be very close to the value of residual stress in weld joint. This concept provides a way to estimate the layer residual stress through experimental measured residual stresses in weld joint.

The virtual substrate assumption in this analytical model is to overcome the clamping during WAAM processing. By the observation of author, many WAAM samples made at Cranfield University were clamped. Furthermore, the residual stress changed significantly when the clamps were removed during FE simulation (Ding, 2012). Although the aim of clamping is to resist the movement of the substrate during processing, its the actual effect have to include the resistance of bending, shrinkage, and expansion of the substrate. Such effect is taken into account by using a virtual substrate, as the virtual substrate can also resists bending, shrinkage and expansion of the actual substrate. Furthermore, the virtual substrate can be removed like removing clamps.

The analytical model is a “T” section beam, as shown in Fig. 4-17. It is assumed that the width of virtual substrate is equal to that of the actual substrate, however this is not necessary. The width of virtual substrate can be different from that of the actual substrate, if detail information about clamping condition is available.

By addition of the i^{th} new layer, the changing of residual stress distribution in both the actual and virtual substrate can be obtained by the beam theory:

$$\Delta\sigma_i(z) = -\frac{M}{I}(z-d) - \frac{\Delta h W_a \sigma_L}{h_a W_a + (h_s + h_{vs}) W_s} \quad 4-1$$

where $\Delta\sigma_i(z)$ is the change of residual stress distribution from $z = 0$ to $z = h_a + h_s + h_{vs}$, caused by the addition of the i^{th} new layer. Here M is the bending moment caused by σ_L , I is second axial moment of area and d is the neutral axis position. σ_L is layer residual stress and be estimated through residual stresses in weld joint. It can be seen that both the force and moment balances have been satisfied. When using the dimensions in the model, M , I and d are:

$$M = \Delta h W_a \sigma_L (h_a + h_s + h_{vs} - d) \quad 4-2$$

$$I = \frac{h_a^3 W_a}{12} + h_a W_a \left(\frac{h_a}{2} + h_s + h_{vs} - d \right)^2 \quad 4-3$$

$$+ \frac{(h_s + h_{vs})^3 W_s}{12} + (h_s + h_{vs}) W_s (h_s + h_{vs} - d)^2$$

$$d = \frac{h_a W_a \left(\frac{h_a}{2} + h_s + h_{vs} \right) + \frac{(h_s + h_{vs})^2}{2} W_s}{h_a W_a + (h_s + h_{vs}) W_s} \quad 4-4$$

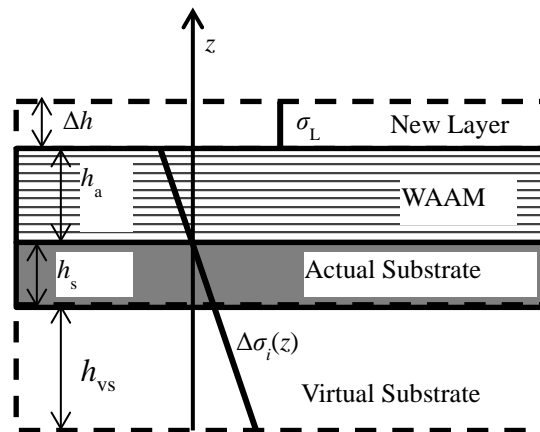
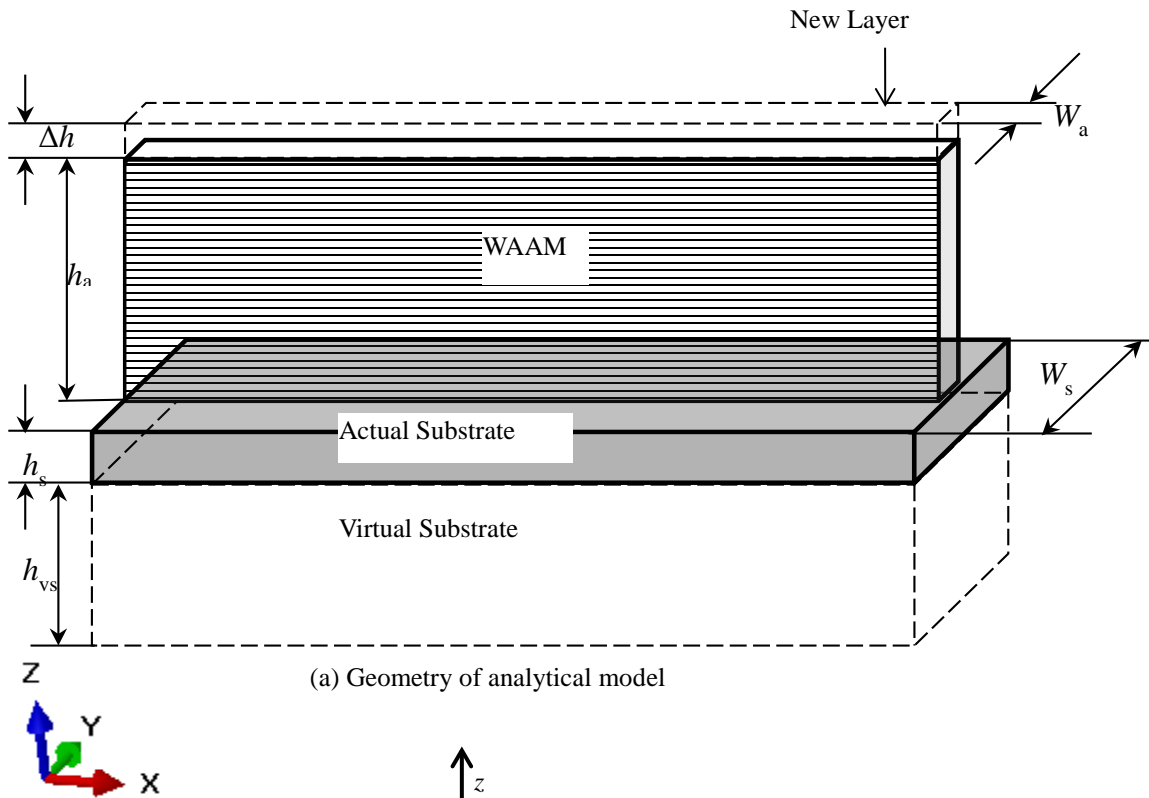


Figure 4-17 Analytical model for determining the changing of residual stress distribution in both the actual substrate and the virtual substrate due to adding a new layer

In the building process, the residual stress distribution in the wall, the actual substrate, and virtual substrate is obtained by adding incremental layer residual stress of each new layer:

$$\sigma(z) = \sum_{i=1}^n \Delta\sigma_i(z) + \sum_{i=1}^n \sigma_L(z) \quad 4-5$$

After obtaining the residual stress distribution through layer-by-layer accumulating, the final residual stress distribution which is influence by removing the clamps will be modelled by removing the virtual substrate. This change of residual stress distribution can be modelled as shown in Fig. 4-18.

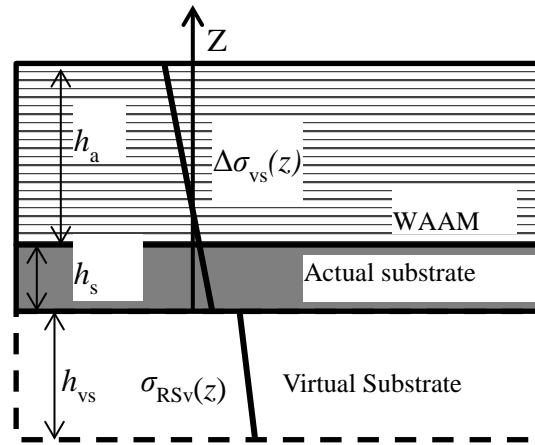


Figure 4-18 Analytical model for determining the changing of residual stress distribution due to removing the virtual substrate which represents the effect of clamps

Using the beam theory again, the changing of residual stress distribution due to removing virtual substrate can be obtained:

$$\Delta\sigma_{vs}(z) = \frac{M}{I} (z - d) + \frac{\int_{-h_{vs}}^0 W_s \sigma_{RSv}(z) dz}{h_a W_a + h_s W_s} \quad 4-6$$

where $\Delta\sigma_{vs}(z)$ is the changing of residual stress distribution from $z = 0$ to $z = h_a + h_s$, caused by the removing of the virtual substrate, $\sigma_{RSv}(z)$ is the residual stress in the virtual substrate prior to removing, M is bending moment caused by $\sigma_{RSv}(z)$, I is second axial moment of area, d is the neutral axis position of final geometry without the virtual substrate. It can be seen that both the force and moment balances have been satisfied. When using the dimensions in the

model, M , I and d are:

$$M = \int_{-h_{vs}}^0 W_s \sigma_{RSv}(z)(z - d)dz \quad 4-7$$

$$I = \frac{h_a^3 W_a}{12} + h_a W_a \left(\frac{h_a}{2} + h_s - d \right)^2 \quad 4-8$$

$$+ \frac{h_s^3 W_s}{12} + h_s W_s (h_s - d)^2$$

$$d = \frac{h_a W_a \left(\frac{h_a}{2} + h_s \right) + \frac{h_s^2}{2} W_s}{h_a W_a + h_s W_s} \quad 4-9$$

After removing the virtual substrate, the final residual stress distribution in the wall and the substrate is obtained.

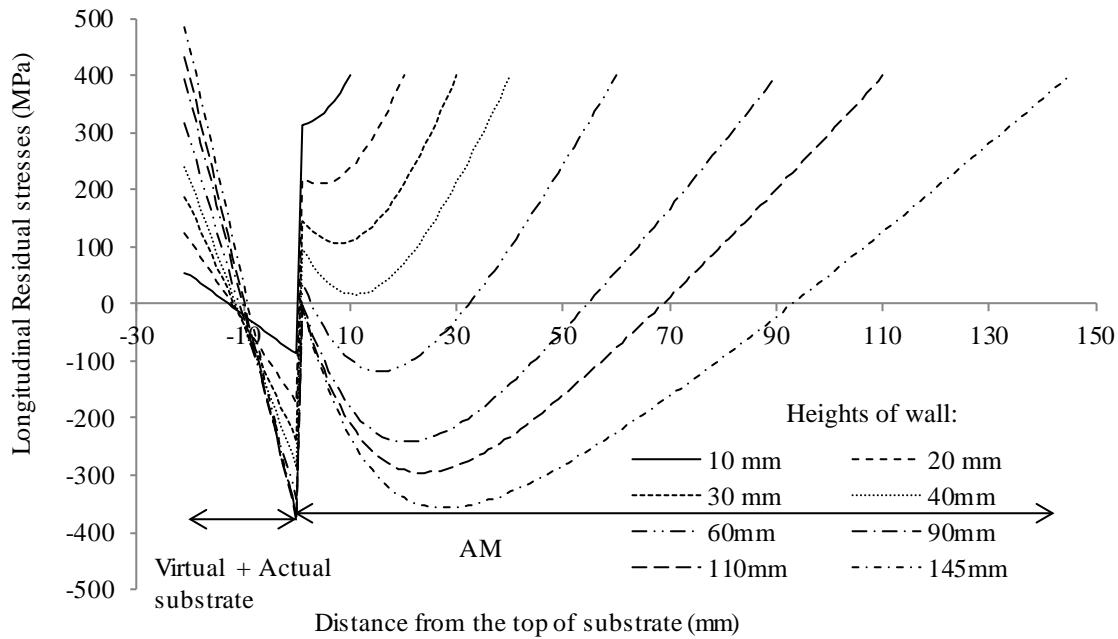
4.5.4 Layer residual stress and three types of residual stress profiles

A simple assumption is often made that the tensile residual stress is a result of contraction of metal when cooling down from liquid to room temperature, and the magnitude of tensile residual stress in a new layer is equal to the yield strength of material. Indeed, it is true, but only for the last layer. The reason for this is not the topic of this thesis, and Leggatt (2008) has given some explanation. Published values of the maximum residual stress for Ti-6Al-4V welds are summarised, as shown in Table 4-2. It can be seen that the maximum tensile residual stress value has a magnitude from 300 MPa to 700 MPa rather than the yield strength of Ti-6Al-4V. In reviewed three welding methods, the TIG welding has the same heating source to that for Wall-T145. However, both Wall-T145 and Wall-T110 were firmly clamped by jigs during deposition (Section 3.3), and therefore more stiff clamping condition may give rise to higher residual stress (Leggatt, 2008). So, a higher value than 300 MPa should be used as layer residual stress for the analytical model in this study. The value of 400 MPa was used on the first attempt.

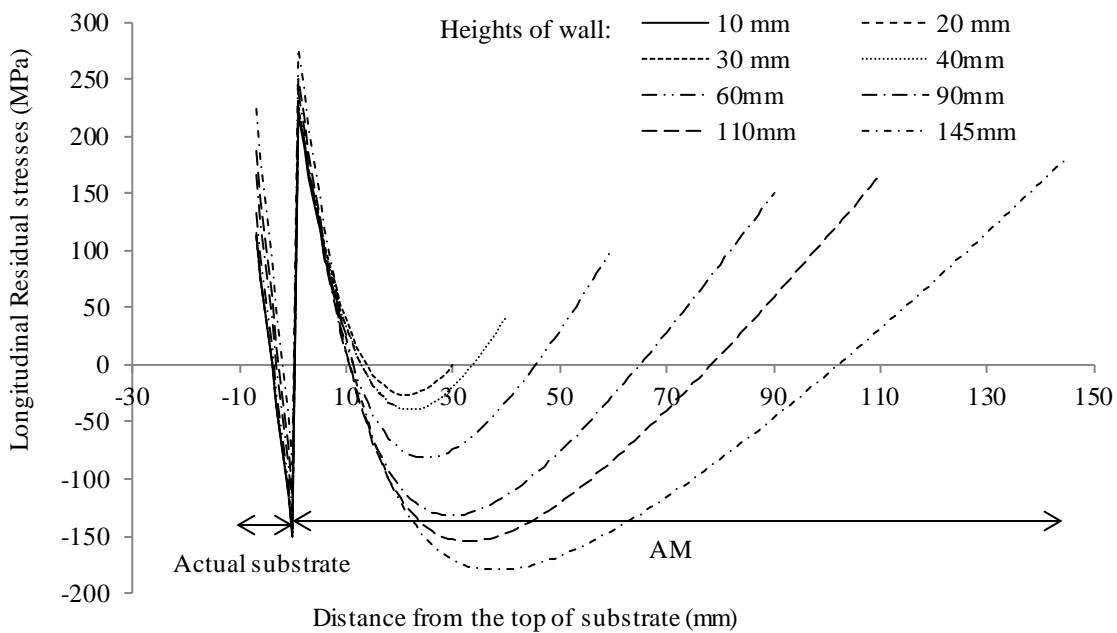
Table 4-2 Published values of the maximum residual stress for butt-welded Ti-6Al-4V

| Heating source | Max residual stress (MPa) | Width of tensile residual stress zone (mm) | Experimental method | Size of weld L×W×t (mm) | Reference |
|----------------|---------------------------|--|--|-------------------------|-----------------------|
| FSW | 300 | 14 | Adjusted compliance ratio method, On-line Crack-compliance | 510×300×2 | (Pasta, et al., 2008) |
| TIG | 300 | 30 | Neutron diffraction | 250×250×2 | (Bruno, et al., 2004) |
| Laser beam | 500-700 | 10-14 | Hole drilling | 200×100×4 | (Liu, et al., 2009) |

Using the analytical model, three thickness of virtual substrate with various height of WAAM made part have been performed to predict the residual stress profile. All of these cases have the same actual substrate of 60 mm wide and 7 mm thick, and the WAAM made part has a thickness of 6 mm. The thickness of incremental layer is 1 mm. Calculated residual stress distributions for 14 mm, 33 mm and 83 mm thick virtual substrate with and without clamps are shown in figures 4-19, 4-20 and 4-21, respectively.

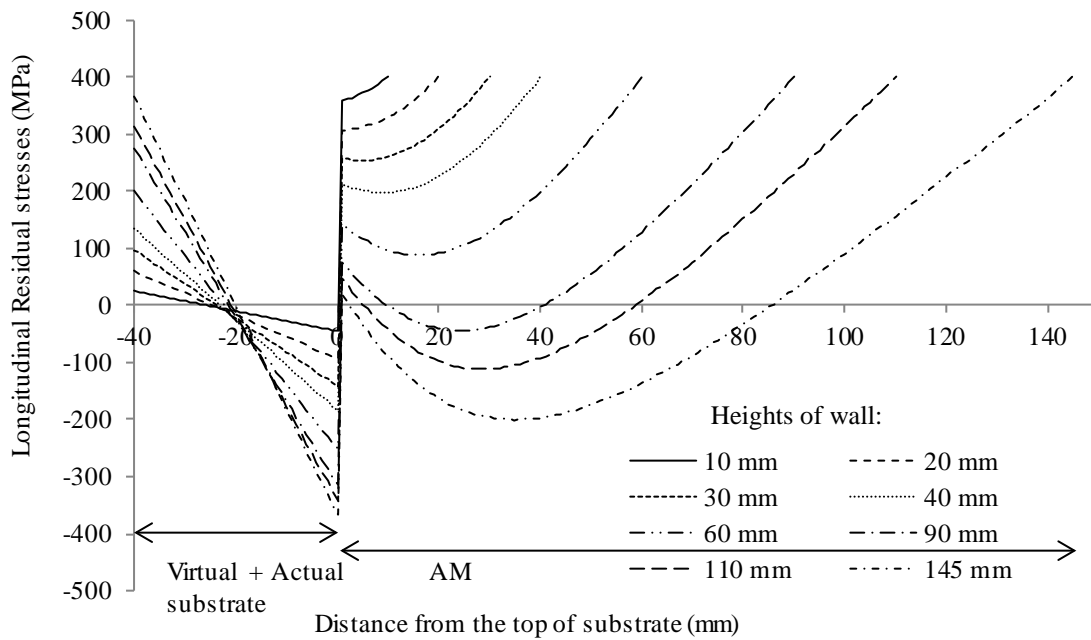


(a) Clamping simulated by virtual substrate of 14 mm thickness

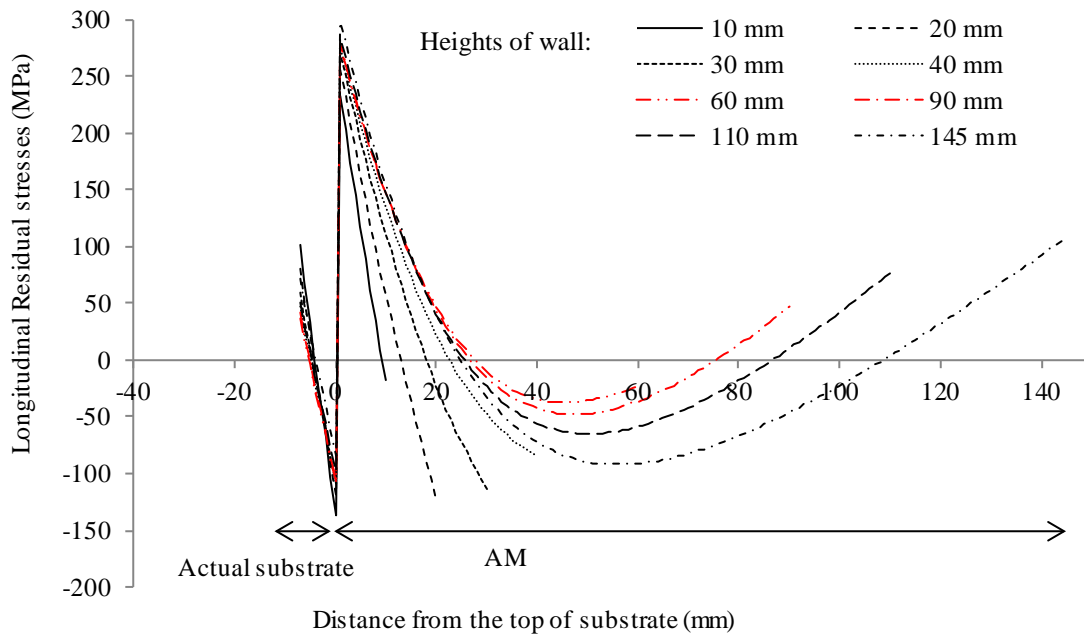


(b) Final residual stress distribution without virtual substrate

Figure 4-19 Residual stress distribution for “T” section WAAM made wall with 14 mm thick virtual substrate and various WAAM wall heights

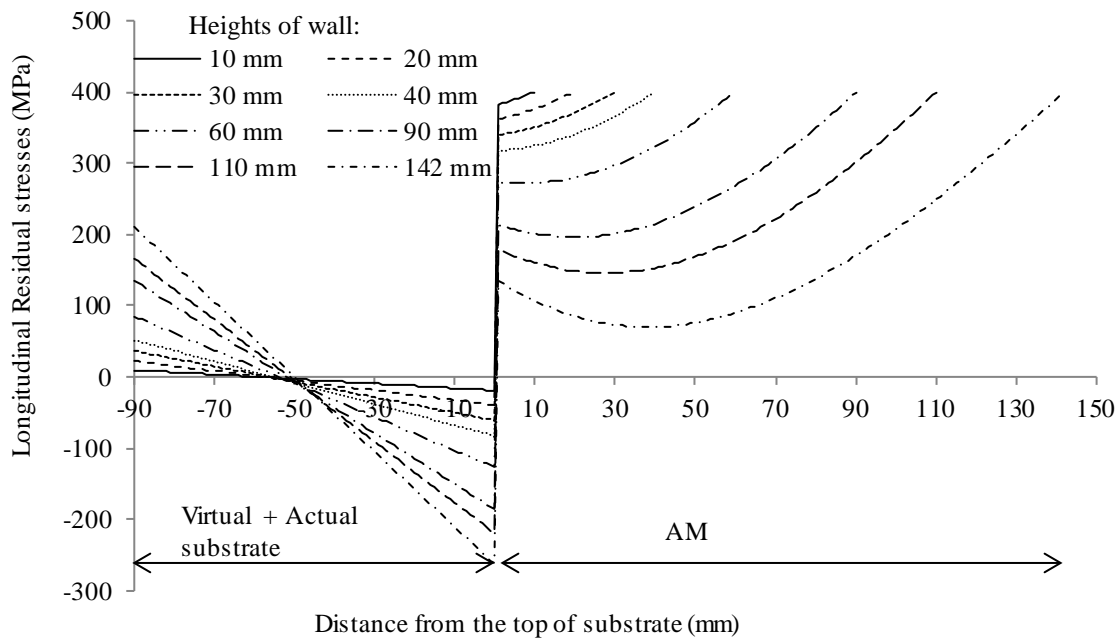


(a) Clamping simulated by virtual substrate of 33 mm thickness

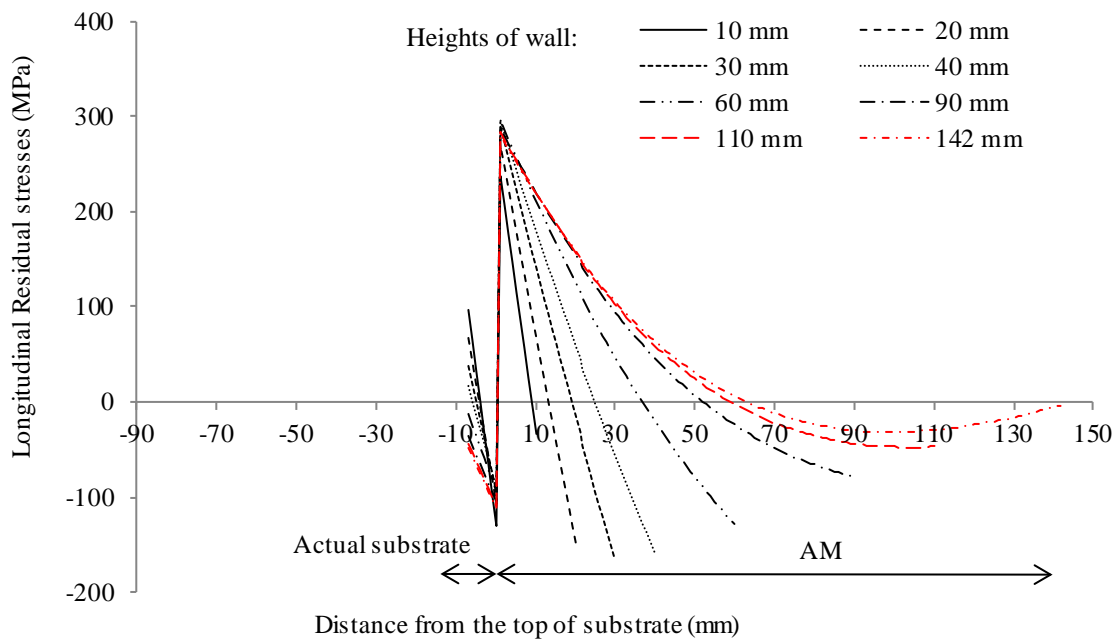


(b) Final residual stress distribution without virtual substrate

Figure 4-20 Residual stress distribution for “T” section WAAM made wall with 33 mm thick virtual substrate and various WAAM wall heights



(a) Clamping simulated by virtual substrate of 83 mm thickness



b) Final residual stress distribution virtual substrate

Figure 4-21 Residual stress distribution for "T" section WAAM part with 83 mm thick virtual substrate and various WAAM wall heights

From the above residual stress evaluations (Fig. 4-19 – 4-21), three conclusions can be drawn

for residual stress profile in WAAM made part, i.e. the residual stress in the substrate is not included:

- No generic residual stress profile appears in WAAM made part. The reasonable trend of residual stress profile is to extend residual stress profile of a lower wall to a higher wall.
- The maximum tensile residual stress locates at the WAAM-substrate interface.
- Residual stress locating near the top of the WAAM made part is changed with the height of WAAM made part. It might be the minimum tensile stress if the height of wall is small, be compression if the height of wall is large, and be tensile stress with compressive residual stress in the middle zone of the WAAM made part if the height of wall is much large.

From the above residual stress distributions, the types of residual stress profiles fall into three groups, as shown in Fig. 4-22. It is noted that in the substrate, the predicted residual stress distributions significantly differ from the measured residual stress distributions. The reason for this is that the predicted residual stress is averaged over entire width of substrate while the experimental measured residual stress is in the heat affected zone, as shown in Fig. 4-22.

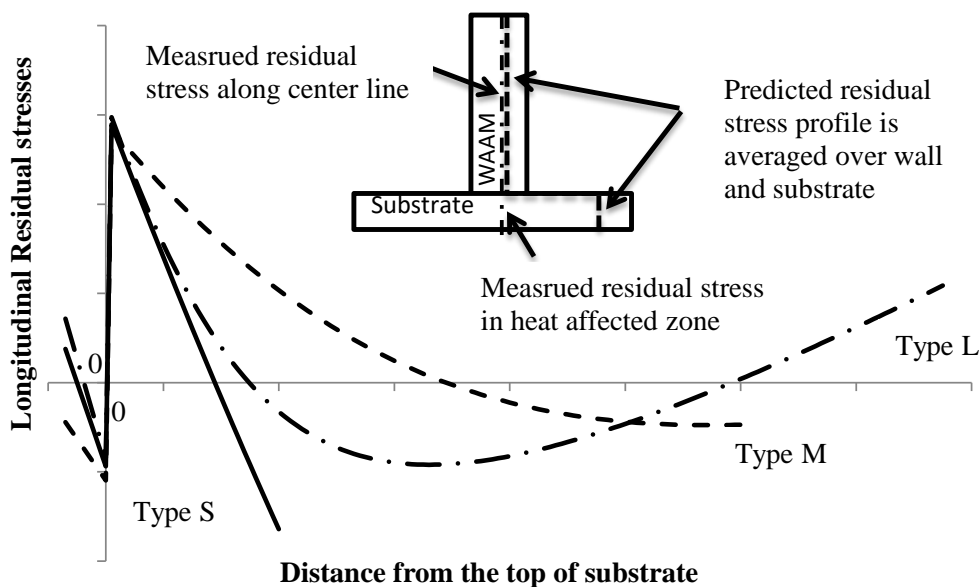


Figure 4-22 Possible three types of residual stress profile in “T” section WAAM made parts

The type S residual stress profile has the compressive residual stress near the top of the

WAAM made wall and the height of the wall is often small. The Wall-T8 and Wall-T 36 have residual stress profiles of the type S, see Fig. 4-16. The type M residual stress profile also has the compressive residual stress near the top of the wall, however the magnitude of compression is smaller and the height of wall is larger. The Wall-T45 and Wall-T110 have residual stress profile of the type M, see Fig. 4-16. The type L residual stress profile has the tensile residual stress near the top of the wall with compressive residual stress in the middle zone of the WAAM made part, and the height of wall is much large. The type L residual stress profile has not been found in any open literature.

To obtain accurate residual stress distribution in wall samples, two main processing parameters are essential: (1) virtual substrate geometry, which is influenced by clamping condition, (2) layer residual stress, which is influenced by the heat input, material properties and other building parameters. At this stage, such two parameters are not available. So, analytical model can only provide generic trend of residual stress profile.

Three types of residual stress profiles have been obtained by analytical model and two of three types have been observed in published work. The type L residual stress profile has not been found in the open literature. However, it is expected that when higher wall sample is made, this type of residual stress profile should be observed.

It is worth noting that the assumption of the value for layer residual stress has no influence on the profile. As such prediction only used the trend of residual stress distribution between various heights, such trend of residual stress distribution will not be changed by the value of layer residual stress. The same conclusion had already been mentioned in work of Mercelis et al. (2006). They plotted the residual stress profiles for different material yield strength and the shapes of those profiles were the same, as shown in Fig. 4-23.

Some materials have been removed from this thesis due to Third Party Copyright. Pages where material has been removed are clearly marked in the electronic version. The unabridged version of the thesis can be viewed at the Lanchester Library, Coventry University.

Figure 4-23 Influence of the material yield strength on the residual stress profile (Mercelis et al., 2006).

4.5.5 Residual stress distribution in Wall-T145

The residual stress distribution in the Wall-T145 will be predicted with the help of measured residual stress distribution in the Wall-T110. First, it is assumed that both the Wall-T145 and the Wall-T110 have the same processing parameters, mainly the same clamping condition, so that both residual stress distributions belong to one of the same virtual substrate in above three figures (4-19 – 4-21). Second, one of residual stress distribution which is similar to that of the Wall-T110, will be extended by a ratio of heights, 145/110.

In both Fig. 4-20 and Fig. 4-21, this kind of extension can be found. In the Fig. 4-20, in which the thickness of virtual substrate is 33 mm, the height of 60 mm has the similar residual stress profile to that of the Wall-T110, therefore, residual stress distribution for 90 mm might be the residual stress profile of the Wall-T145, since $145/110 \approx 90/60$. In Fig. 4-21, in which the thickness of virtual substrate is 83 mm, the height of 110 mm has the similar residual stress profile to that of the Wall-T110, therefore, residual stress distribution of 142 mm might be the residual stress profile of the Wall-T145, since $145/110 \approx 142/110$. It must be admitted that such prediction is not very objective. The predicted residual stress profile for Wall-T145 is shown in Fig. 4-24.

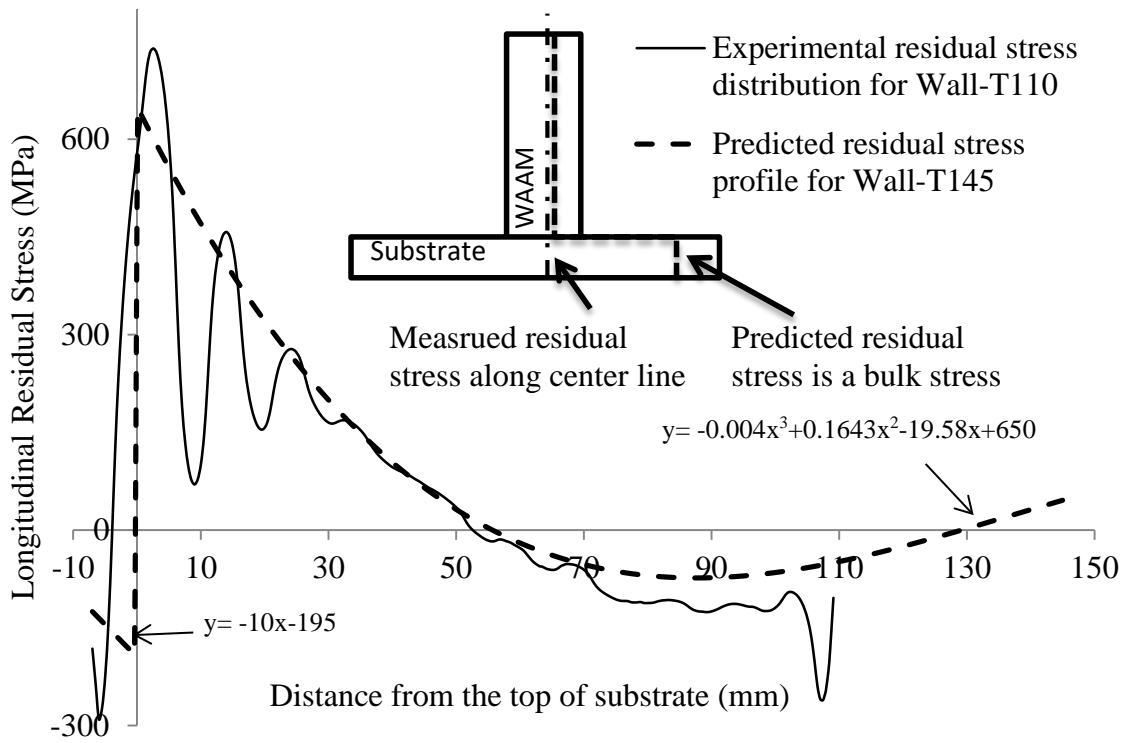


Figure 4-24 Predicted residual stress profile in Wall-T145

4.5.6 Retained residual stress in C(T) specimens(AL, PL)

Following the prediction of residual stress profile in Wall-T145, retained residual stress in C(T) specimens extracted from the Wall-T145 was calculated by FEM. The geometry of C(T) specimens has been shown in previous chapter, Fig. 3-11 and the positions of AL and PL specimens has been shown in Fig. 3-12.

Solid elements (second order element designated as C3D20 in ABAQUS) were used to mesh the model, as shown in Fig. 4-25. The reason for using solid elements is that the Wall-T145 is a three dimensional part. The size of element is $3 \times 3 \times 3 \text{ mm}^3$. Isotropic Young's modulus of 113.8 GPa and Poisson's ratio of 0.342 are used for the material properties. Boundary conditions just constrain the rigid body movement but allow deformation in any direction. The longitudinal residual stress, which is shown in Fig. 4-24, was applied to whole area of FE mesh by using the SIGINI. After removing the elements which surround the C(T) specimens, residual stress along the crack path from the notch root were plotted, as shown in Fig. 4-26.

In this thesis, an assumption was made that the FCGR data for pure WAAM made Ti-6Al-4V

was obtained from a residual stress-free condition. The FCGR data were measured from C(T) specimens extracted from the Wall-T145. However, the study in this section shows that such assumption is not valid.

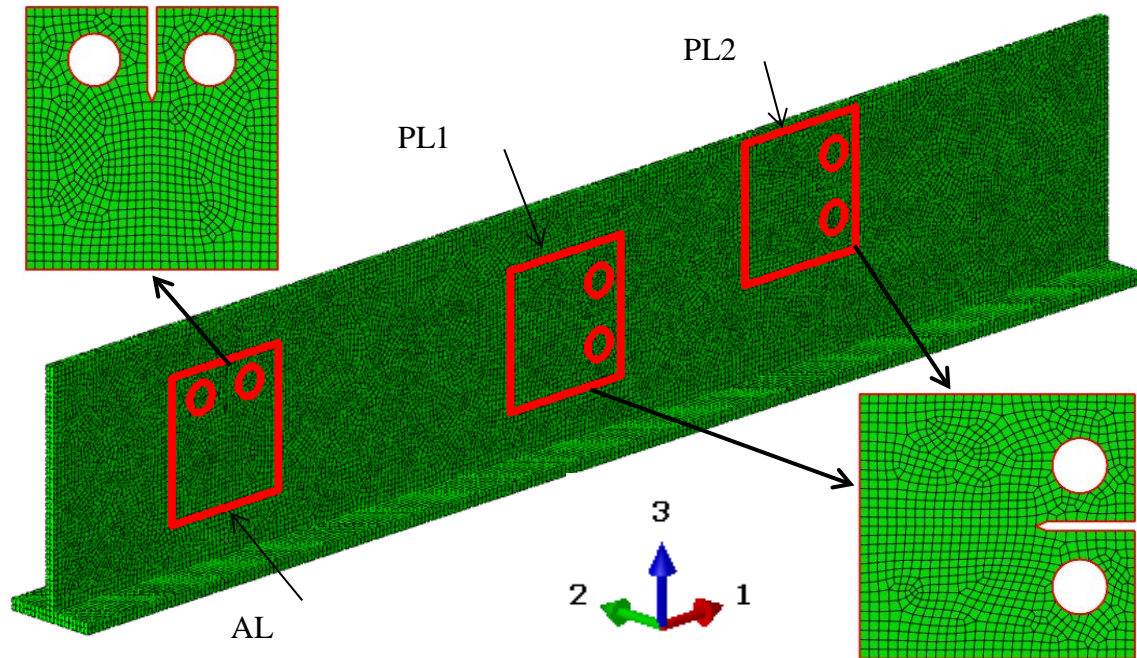


Figure 4-25 Finite element model for residual stress analysis of C(T) specimens in Wall-T145

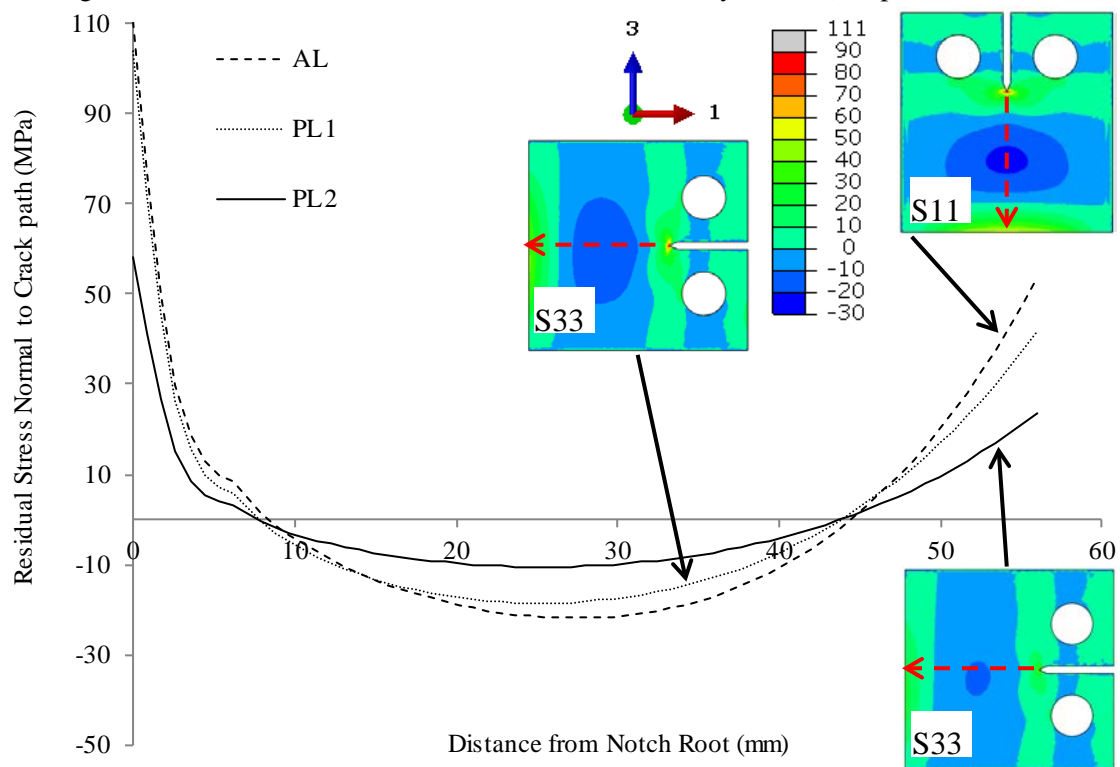


Figure 4-26 Retained residual stresses in C(T) specimens extracted from Wall-T145 (AL and PL)

4.6 Measured transverse residual stress

Residual stress component in the transverse direction to the welding torch movement direction was not taken into account in the residual stress analysis. The reason for ignoring the transverse residual stress is that the measured component is along its own direction, i.e. stress component parallel to the line of measurement points, as shown in Fig. 4-27b.

As is known, residual stresses are self-equilibrating, so that both the resultant force and moment balance must be satisfied. When calculating the force balance in the transverse direction, these transverse forces need corresponding normal area to multiply with transverse stresses. But now, each transverse component locates at different points, therefore all these normal area are not in the same plane. The equation for force balance which includes all measured transverse component cannot be built. When calculating moment balance in transverse direction, these transverse forces go through the same point and all items in equation become zero.

It is possible to introduce transverse residual stress into FE model. However, after an equilibrium step, transverse residual stresses become nearly zero. The reason for becoming zero is that there is no opposite stress to build a self-balanced condition for a plane that is normal to transverse residual stress.

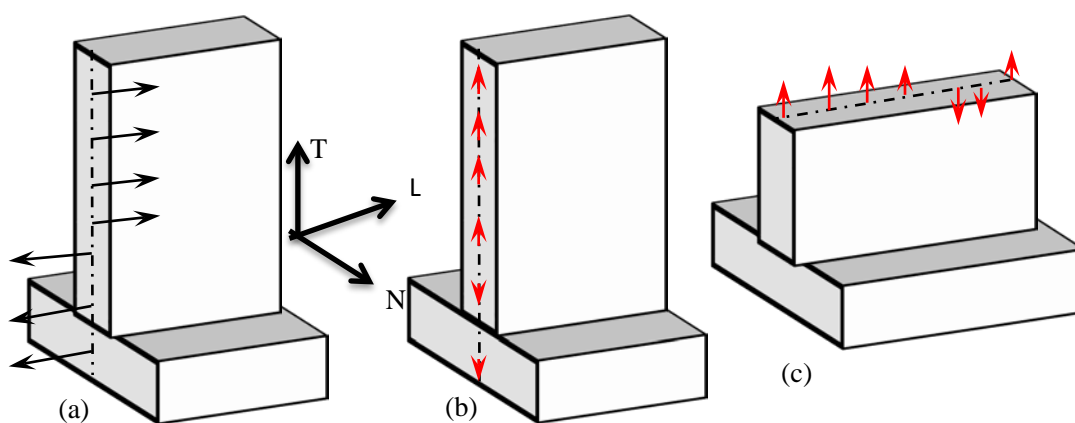


Figure 4-27 Relation of stress component direction and line of measurement points: (a) longitudinal stress normal to the line of measuring points, (b) transverse stress parallel to the line of measuring points, (c) transverse stress normal to the line of measuring points (not practical for contour; not available from published neutron measurement)

Although transverse residual stresses with a magnitude about half of longitudinal residual stress are often reported by many researchers when carrying out neutron diffraction experiments, transverse stress profile is not the purpose of their experiments. After obtaining the longitudinal stress profile, transverse stresses can be obtained at the same time and at the same point, as they have to measure the strains in all three directions to calculate the longitudinal stresses. So, transverse stresses along a line that is parallel to the stress component direction often appear in articles. However, this does not mean that these transverse residual stresses can be used for residual stress analysis, as self-balanced condition cannot be obtained.

The way to provide useful transverse residual stresses is to measure stress component along a path normal to its direction. As longitudinal residual stresses are measured along a transverse line, as shown in Fig. 4-27a, transverse residual stresses should be measured along a longitudinal line, as shown in Fig. 4-27c.

Chapter 5 Calculation of Stress Intensity Factors

5.1 Introduction

All fatigue experiments were performed using the C(T) geometry, therefore only C(T) specimens were modelled to calculate the crack tip stress intensity factors. All FE models in this chapter are two-dimensional. First, some common aspects for FE model of C(T) specimen are described, i.e. load application, mesh convergence test. At the same time, the crack tip stress intensity factors for a smaller C(T) specimen are calculated, in order to obtain stress intensity factors in this specimen. Second, the influence of anisotropic material properties on stress intensity factor is simulated. Third, the small scale yielding requirement in the LEFM is checked. Finally, residual stresses are applied and the stress intensity factors due to residual stress are calculated. Work described in Section 5.5.1 was developed in collaboration with Dr. J. Zhang of Beihang University during his visit to Cranfield University in 2014-2015.

5.2 Isotropic material under applied load

5.2.1 Pin loading

C(T) specimen is loaded by pins, and the pin loading is modelled as a uniform radial stress applied to the edge of pin holes over an angle of 20° , as shown in Fig. 5-1a. In the actual specimen, the bearing stresses caused by the pin loading are concentrated over a small arc on the edge of the holes due to the undersized pin diameter (ASTM Standard E647, 2011), as shown in Fig. 5-1b. The research work conducted by Newman (1974) has suggested this arc should be less than 45° . Thus, the angle of 20° is used in this project.

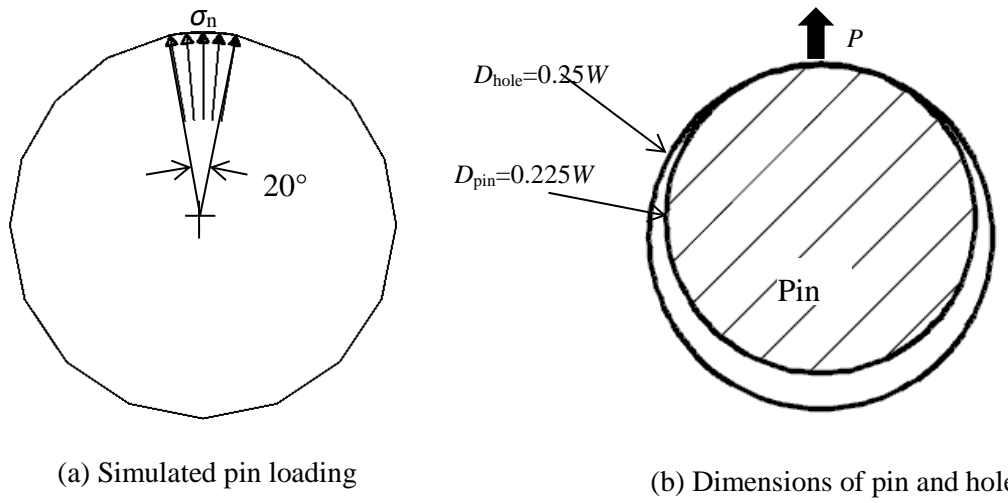


Figure 5-1 Uniform radial stress to simulate the pin loading in FE model of C(T) specimen

5.2.2 Crack tip stress intensity factor

To calculate the stress intensity factor, stresses in front of the crack tip or displacements behind the crack tip can be used (Anderson, 2012 p.558). However, these two methods have many post process steps for each crack length. It is easier to first compute the strain energy release rate, G , and then obtain K from G . In this thesis, the Virtual Crack Closure Technique (VCCT) is used for computing the strain energy release rate based on the displacements and forces around the crack tip obtained from the FE analysis. VCCT was originally proposed by Rybicki & Kanninen (1977). This technique has been widely used by scientists and engineering researchers.

After an analysis in two-dimensional FE model, nodal forces and nodal displacements can be obtained. Then, the nodal forces and nodal displacements around the crack tip, as shown in Fig. 5-2, are used to calculate the G value.

The strain energy release rate for Mode I and Mode II, G_I and G_{II} , are given by

$$G_I = \frac{-1}{2\Delta a} [Y_i(v_l - v_{l*}) + Y_j(v_m - v_{m*})] \quad 5-1$$

$$G_{II} = \frac{-1}{2\Delta a} [X_i(u_l - u_{l*}) + X_j(u_m - u_{m*})] \quad 5-2$$

where Δa is the length of elements around the crack tip, and Y_i , Y_j , X_i , X_j are the nodal force

components in the y - and x -axis at the nodes i and j , respectively, and $v_l, v_{l^*}, v_m, v_{m^*}, u_l, u_{l^*}, u_m, u_{m^*}$ are the nodal displacement components in the y - and x -axis at the nodes l, l^*, m, m^* , respectively (Krueger, 2004). With plane stress or plane strain assumption, nodal force component and nodal displacement component normal to the plane are missing. It can be seen that the strain energy release rate, G , is calculated by the energy released over crack surface created when the crack is extended by an element length.

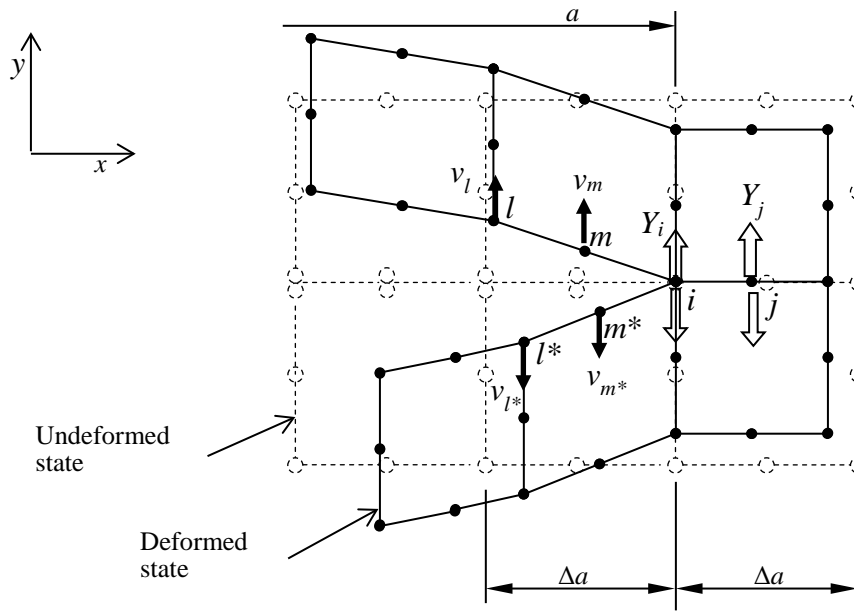


Figure 5-2 Virtual Crack Closure Technique (VCCT) for two-dimensional FE model using eight-noded element (nodal forces and nodal displacements in the x -axis are omitted for clarity)

For linear elastic materials, the crack tip stress intensity factor, K , and the strain energy release rate, G , are uniquely related (Anderson, 2012 p.59). The K_I and K_{II} are given by

$$K_I = \sqrt{\frac{E G_I}{1 - (\alpha_k \nu)^2}} \quad 5-3$$

$$K_{II} = \sqrt{\frac{E G_{II}}{1 - (\alpha_k \nu)^2}} \quad 5-4$$

where $\alpha_k = 0$ for the plane stress and 1 for the plane strain condition, E is the Young's modulus and ν is the Poisson's ratio.

5.2.3 FE model of C(T) specimen

In fact, an analytical solution of stress intensity factor for C(T) geometry exists. The reason to go through this FE analysis is to verify the FE model for anisotropic material and residual stress later. A two-dimensional plane stress FE model of C(T) specimen was constructed to obtain the crack tip stress intensity factors by the pin loading. The geometry of C(T) specimen is the same as already shown in Fig. 3-11. Only the top half of the specimen needed to be modelled as a consequence of symmetry in both geometry and pin loading. The geometry of the FE model and symmetry boundary conditions are shown in Fig. 5-3. In the FE model, symmetry boundary conditions were employed by constraining the displacement normal to the symmetry line. The nodes that represent the crack were not constrained, as shown in Fig. 5-3. At the end of the symmetry line, the x displacement was constrained to prevent rigid body movement of the FE model. Different crack lengths were obtained by releasing the displacement constraints along the crack path. The pin loading were modelled as a uniform radial stress applied to the edge of holes over an angle of 20° . As the length and width of C(T) specimens are at least 10 times higher than the thickness and the applied load is parallel to plane of specimens, plane stress situation can be used for analysis. Two-dimensional plane stress elements (second order element designated as CPS8 in ABAQUS) were used to mesh the specimen. The element size was $0.25 \text{ mm} \times 0.25 \text{ mm}$ along the crack path, as shown in Fig. 5-3. Homogeneous and isotropic Young's modulus of 113.8 GPa and Poisson's ratio of 0.342 were used for the material properties. Although higher Young's modulus of 124 GPa was measured in WAAM Ti-6Al-4V, the crack tip stress intensity factor for isotropic material does not depend on the Young's modulus. As can be seen from a closed form solution, Eq. 5-5, the Young's modulus term is not required. Linear elastic static load analysis procedure was performed and the stress intensity factors were obtained by the VCCT.

A mesh sensitivity study was conducted for the crack tip stress intensity factors with $a = 17 \text{ mm}$ and $a = 56 \text{ mm}$ under several values of $1/\Delta a$ (Δa is mesh size around the crack tip). Calculated stress intensity factors are compared in Fig. 5-4.

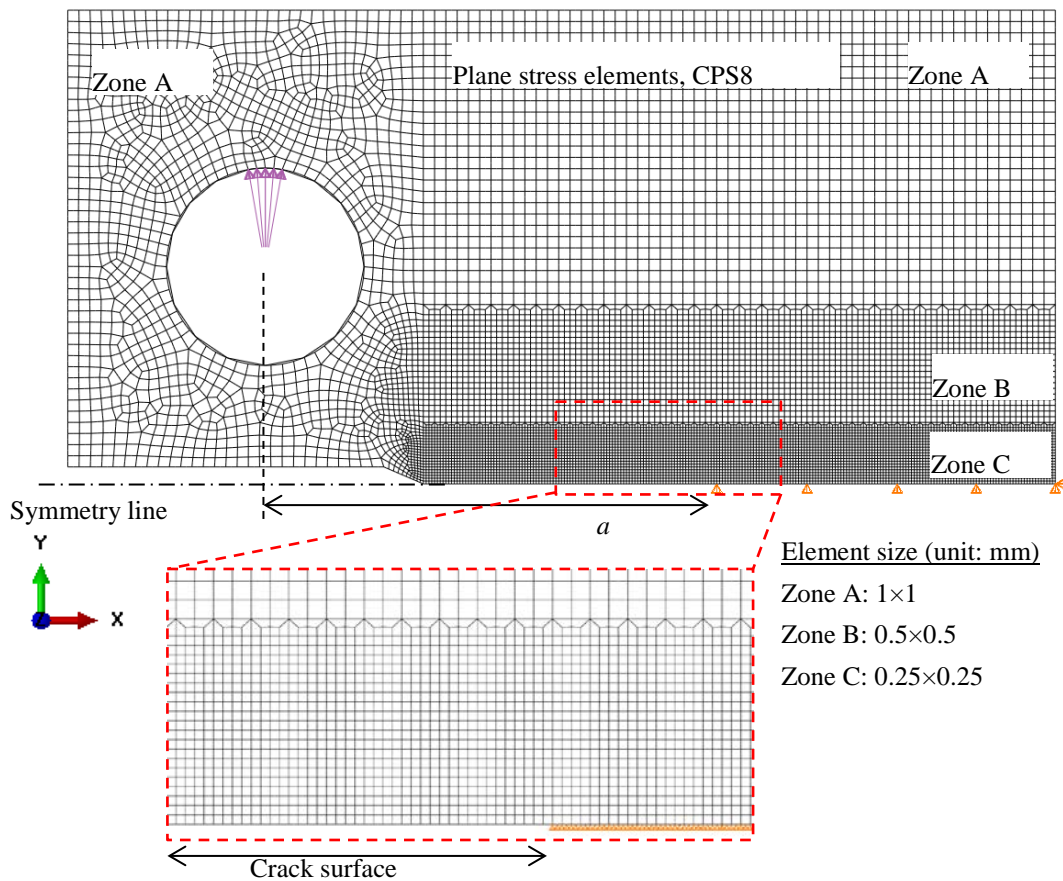
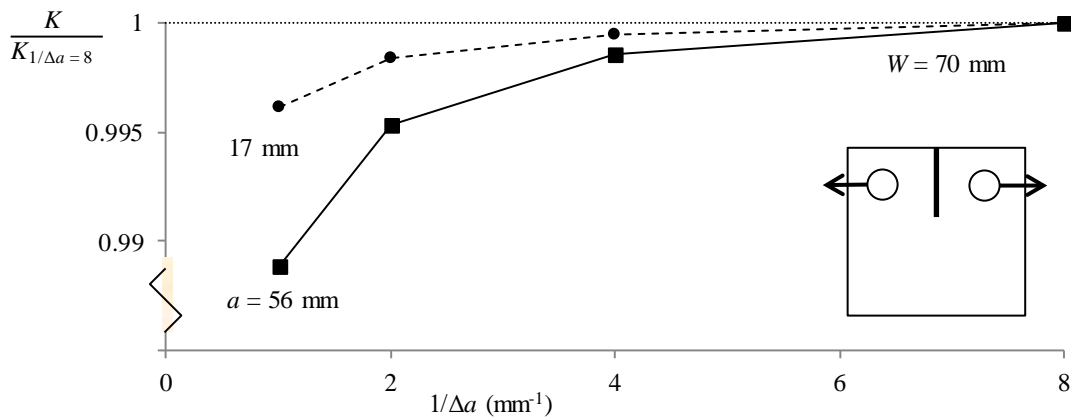


Figure 5-3 Two-dimensional plane stress FE model of C(T) specimen

Figure 5-4 Convergence trend for C(T) specimen (Δa is mesh size around the crack tip)

For ease of comparison, the stress intensity factors were normalized with respect to their values for $1/\Delta a = 8$. The convergence is quite sufficient at $1/\Delta a = 4$ for $a = 17$ mm and 56 mm, which are the shortest and the longest crack lengths in the testing range. Thus, $1/\Delta a = 4$, which is mesh size of 0.25×0.25 mm², is sufficiently small for all other crack lengths.

5.2.4 Numerical results

The FE model has been run for several crack lengths and the numerical results are compared with the solution by the closed form expression in (ASTM Standard E647, 2011), as shown in Fig. 5-5. For ease of comparison, the stress intensity factors were normalized with respect to their values by the closed form solution. The difference between FE outputs and the closed form solution are less than 0.5%. The closed form solution is presented here for ease of check:

$$K = \frac{P}{B\sqrt{W}} \frac{(2 + \alpha)}{(1 - \alpha)^{\frac{3}{2}}} (0.886 + 4.64\alpha - 13.32\alpha^2 + 14.72\alpha^3 - 5.6\alpha^4) \quad 5-5$$

where $\alpha = a/W$, P is the pin load, B the specimen thickness, and W the specimen width measured from the pin holes centre line.

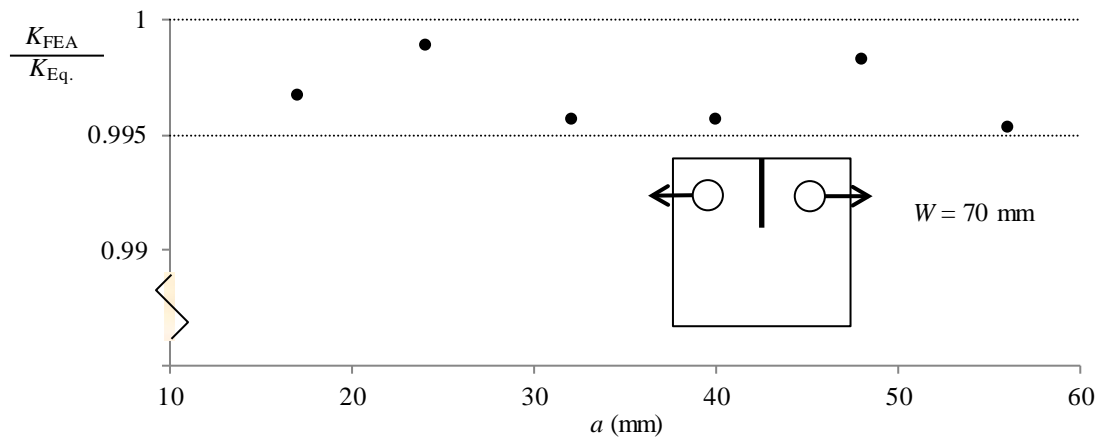


Figure 5-5 Comparison of the crack tip stress intensity factors: FEA vs. closed form solution

5.2.5 FE model of short C(T) specimen

During the machining of C(T) specimens, one specimen had different dimension. The actually length of 84.5 mm should be 87.5 mm, as shown in Fig. 5-6. The stress intensity factors in this short specimen were calculated by FE method. In the FE model for short C(T) specimen, all aspects were the same as the previous two-dimensional FE model for standard sized C(T) specimen, except the dimension. The FE model for short C(T) was run for several crack lengths and the outputs were fitted to Eq. 5-6:

$$K = \frac{P}{B\sqrt{W}} \frac{(2 + \alpha)}{(1 - \alpha)^{\frac{3}{2}}} (0.886 + 4.64\alpha - 13.32\alpha^2 + 14.72\alpha^3 - 5.6\alpha^4) \quad 5-6$$

where $\alpha = (70/66.5)a/W$, P is the pin load, B the specimen thickness, and W the width for standard sized specimen. In this case, the pin load was $P = 5.4$ kN over a thickness of 7.1 mm, and the standard width was $W = 70$ mm. At the same time, the output are compared with the solution for standard sized C(T) specimen, Eq.5-5, as shown in Fig. 5-7. The maximum difference, $(K_{\text{short,FEA}} - K_{\text{standard,Eq}})/K_{\text{standard,Eq}}$, is 14% at $a = 42.6$ mm.

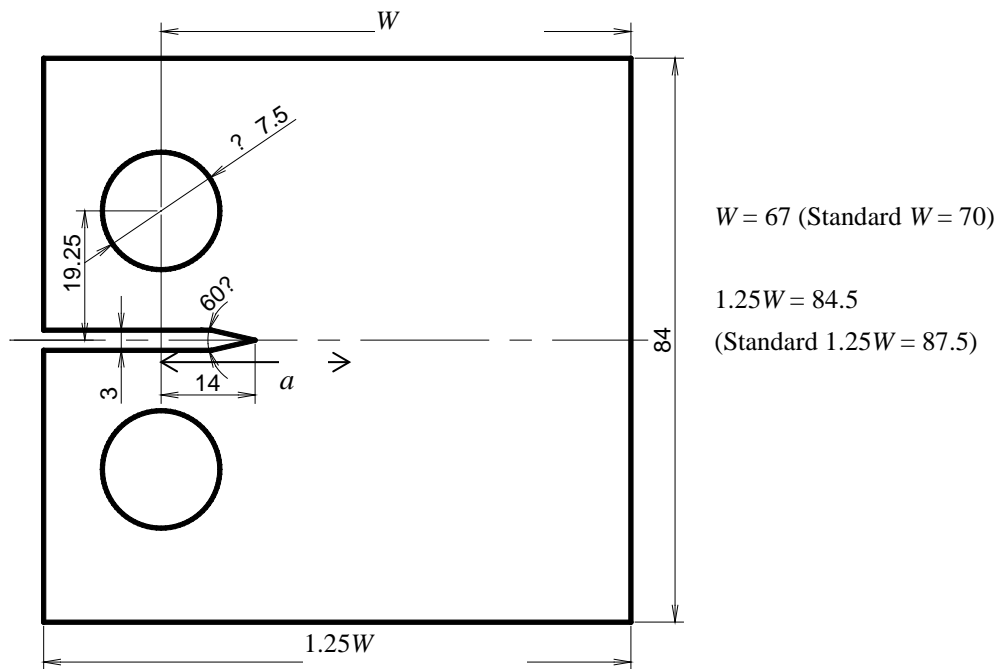


Figure 5-6 Geometry of the short C(T) specimen (unit: mm)

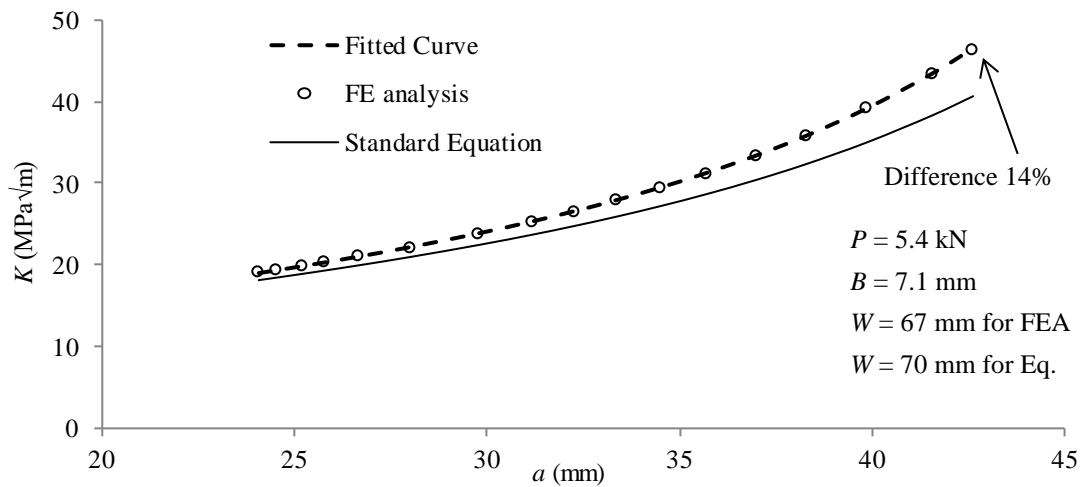


Figure 5-7 Comparison of stress intensity factors for short C(T) specimen

5.3 Influence of anisotropic Young's modulus

The anisotropic Young's modulus in WAAM made Ti-6Al-4V was assumed as an orthotropic problem in this project, i.e. torch movement direction is I -axis and transvers direction is 2-axis. Tada et al. (2000 p. 514) investigated the stresses at the crack tip in orthotropic material, and gave equation below for the effective Young's modulus:

$$E_{\text{eff}} = \frac{\sqrt{2E_1E_2}}{\sqrt{(E_1/E_2)^{1/2} + E_1/(2G_{12}) - \nu_{12}}} \quad 5-7$$

where E_{eff} is effective Young's modulus for orthotropic materials, E_1 and E_2 are the Young's modulus in I - and 2-axis, G_{12} is the shear modulus, and ν_{12} is the Poisson's ratio. The coordinate system for Eq. 5-7 is shown in Fig. 5-8.

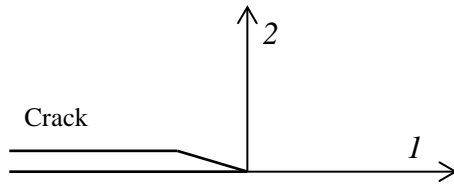


Figure 5-8 Coordinate system for Eq. 5-7.

The crack tip stress intensity factor in orthotropic material is related to G as:

$$K = \left[\frac{E_{\text{eff}}G}{1 - (\alpha_k \nu)^2} \right]^{1/2} \quad 5-8$$

where $\alpha_k = 0$ for plane stress and 1 for plane strain, G is the strain energy release rate, ν is the Poisson's ratio.

5.3.1 FE model of C(T) specimen with orthotropic Young's modulus

In the FE model, the orthotropic Young's modulus was inputted by using the “lamina” material type in ABAQUS. The geometry, boundary conditions, pin loading, elements type and mesh size were the same as two-dimensional FE model of C(T) specimen in Fig. 5-3.

5.3.2 Numerical results for two cases of orthotropic Young's modulus

The measured Young's modulus are summarized in Table 5-1 and the Young's modulus used in FE analysis are also shown in the same table. The specimens for measuring Young's modulus

were extracted from Wall-T145 sample (Lorant, 2010 p. 79). As the heat input parameters for Wall-T145 was the same as that for Wall-Bi120 (Section 3.2) from which the C(T) specimens were extracted, these values can represent Young's modulus in WAAM made Ti-6Al-4V which was used in this research. When using the measured Young's modulus, two extreme conditions, $E_{22}/E_{11} = 1.10$ and 0.94 , were obtained for AL type C(T) specimen. The numerical results of the crack tip stress intensity factors are shown in Fig. 5-9. For ease of comparison, the stress intensity factors are normalized with respect to their values by closed form solution for isotropic material, Eq. 5-5. In these two extreme conditions, the difference in crack tip stress intensity factors is about $\pm 1\%$ over a range from $a = 17$ mm to 56 mm. It can be seen that anisotropic Young's modulus has much less influence on stress intensity factors of pure WAAM made Ti-6Al-4V C(T) specimen.

Table 5-1 Measured Young's modulus for WAAM Ti-6-4 (Lorant, 2010 p.79) and values in FE model

| | Measured | Used in FE model | |
|---|----------|----------------------|----------------------|
| | | $E_{22}/E_{11}=0.94$ | $E_{22}/E_{11}=1.10$ |
| E_{11} , troch movement direction (GPa) | 123, 124 | 124 | 124 |
| E_{22} , transverse direction (GPa) | 117, 136 | 117 | 136 |
| ν | — | 0.342 | 0.342 |
| G (GPa) | — | 42.7 | 42.7 |

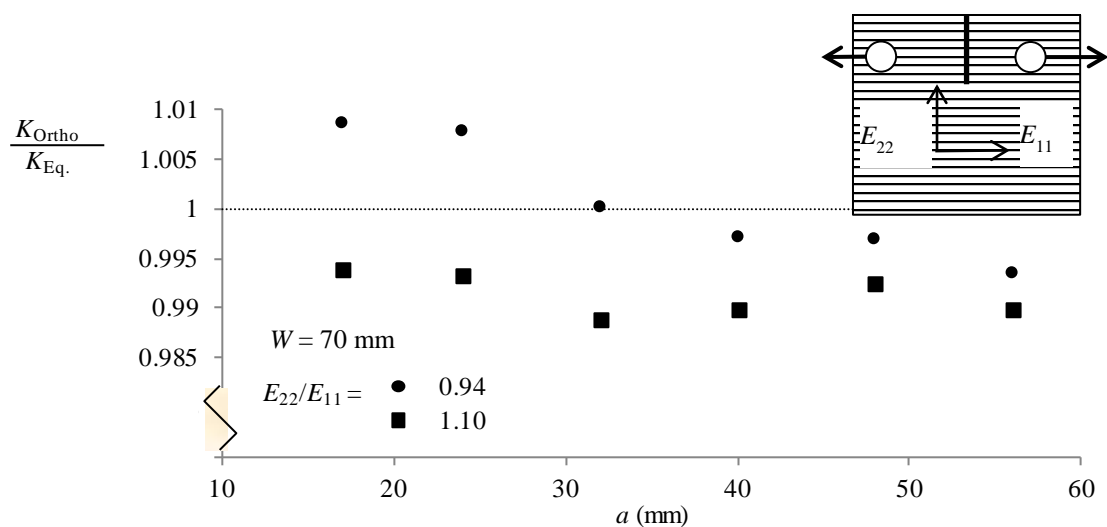


Figure 5-9 Influence of orthotropic Young's modulus in C(T) specimen on the crack tip stress intensity factors

5.4 Influence of bi-material Young's modulus

It is worth note that Young's modulus in WAAM Ti-6Al-4V is higher than that in Ti-6Al-4V of wrought products. In this section the high orthotropic Young's modulus in WAAM Ti-6Al-4V and normal isotropic Young's modulus in wrought Ti-6Al-4V were applied to the same FE model.

5.4.1 FE model of C(T) specimen with bi-material Young's modulus

Like the previous FE model, the orthotropic Young's modulus was inputted by using the “lamina” material type in ABAQUS. The geometry, boundary conditions, pin loading, elements type and mesh size were the same as two-dimensional FE model of C(T) specimen in Fig. 5-3. The interface between the two different Young's moduli is the interface of two different microstructure, which locates at $a = 26$ mm for the type A specimen and $a = 34$ mm for type C specimen.

5.4.2 Numerical results for two cases of crack growth directions

The used orthotropic Young's moduli in FE model have been summarized in Table 5-1. The used isotropic Young's modulus is 113.8 GPa and Poisson's ratio is 0.342. The numerical results of the crack tip stress intensity factors for one extreme condition, $E_{22}/E_{11} = 0.94$, are shown in Fig. 5-10. For ease of comparison, the stress intensity factors are normalized with respect to their values by closed form solution for isotropic material, Eq. 5-5.

It can be seen that an increase of crack tip stress intensity factors exists for the type C specimen when crack tip approaches the interface, whereas a decrease exists for the type A. The maximum increase is less than 5% and the maximum decrease is also less than 5%. At the same time, such influence becomes weaker when the crack tip is 5 mm far away from the interface. Once the crack tips have gone through the interface, there is no influence.

The reason for this is that the higher Young's modulus part bears more loads than the lower Young's modulus part in a bi-material uncracked ligament. For the type C specimen, the crack initiates from the WAAM Ti-6Al-4V with higher Young's modulus. When crack tip approaching the bi-material interface, the higher Young's modulus WAAM Ti-6Al-4V bears

more loads and hence shows an increase in the crack tip stress intensity factor.

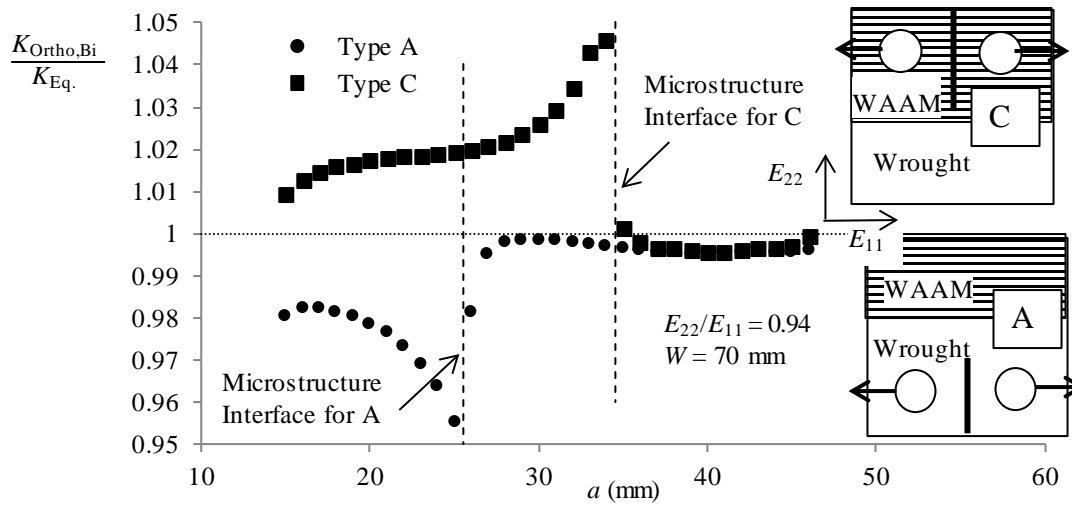


Figure 5-10 Influence of bi-material Young's modulus on the crack tip stress intensity factors, for Type A and C specimens, using the microstructure interface.

5.5 Influence of yield strength on LEFM applicability

The purpose of this work was to check the requirement of small scale yielding in LEFM. The WAAM made Ti-6Al-4V not only has anisotropic Young's modulus but also different yield strength from its wrought substrate. The change of yield strength results in different size of the plastic zone at the crack tip. In this section, the size of plastic zone was calculated by FE analysis and analytical approach. It is found that the plastic zone is small and the specimens are of sufficient planar size to remain predominantly elastic condition during testing.

5.5.1 FE Model of C(T) specimen with fine mesh at crack tip

A two-dimensional plane strain FE model of C(T) specimen was constructed to simulate the size of plastic zone at the crack tip. The geometry of C(T) specimen is the same as that in Fig. 3-11. Like previous two-dimensional FE model of C(T) specimen in Section 5.2.3, half of the specimen was constructed, boundary conditions was applied to represent both the crack and the symmetry line, and pin load was applied as uniform radial stress. But, two-dimensional plane strain elements (second order element designated as CPE8 in ABAQUS) were used to mesh the structure. Although the overall stresses in C(T) specimen is the plane stress situation, the stress status in the crack tip plastic zone is different. The stresses near the crack tip are higher than the surrounding material and the material near the crack tip tries to

contract. But the surrounding material prevent it from doing so. Such constraint causes a triaxial state of stress near the crack tip. The plane strain status is better for describing this triaxial state of stress than the plane stress assumption. The element size was $1.25 \mu\text{m} \times 1.25 \mu\text{m}$ at crack tip, as shown in Fig. 5-11. Isotropic Young's modulus of 113.8 GPa and Poisson's ratio of 0.342 were used for material properties, as anisotropic Young's modulus does not make significant difference (Section 5.3). Perfect plasticity was used for modelling the plastic behaviour. Two extreme values of yield strength were used in FE model as summarized in Table 5-2. Nonlinear static load analysis procedure was performed.

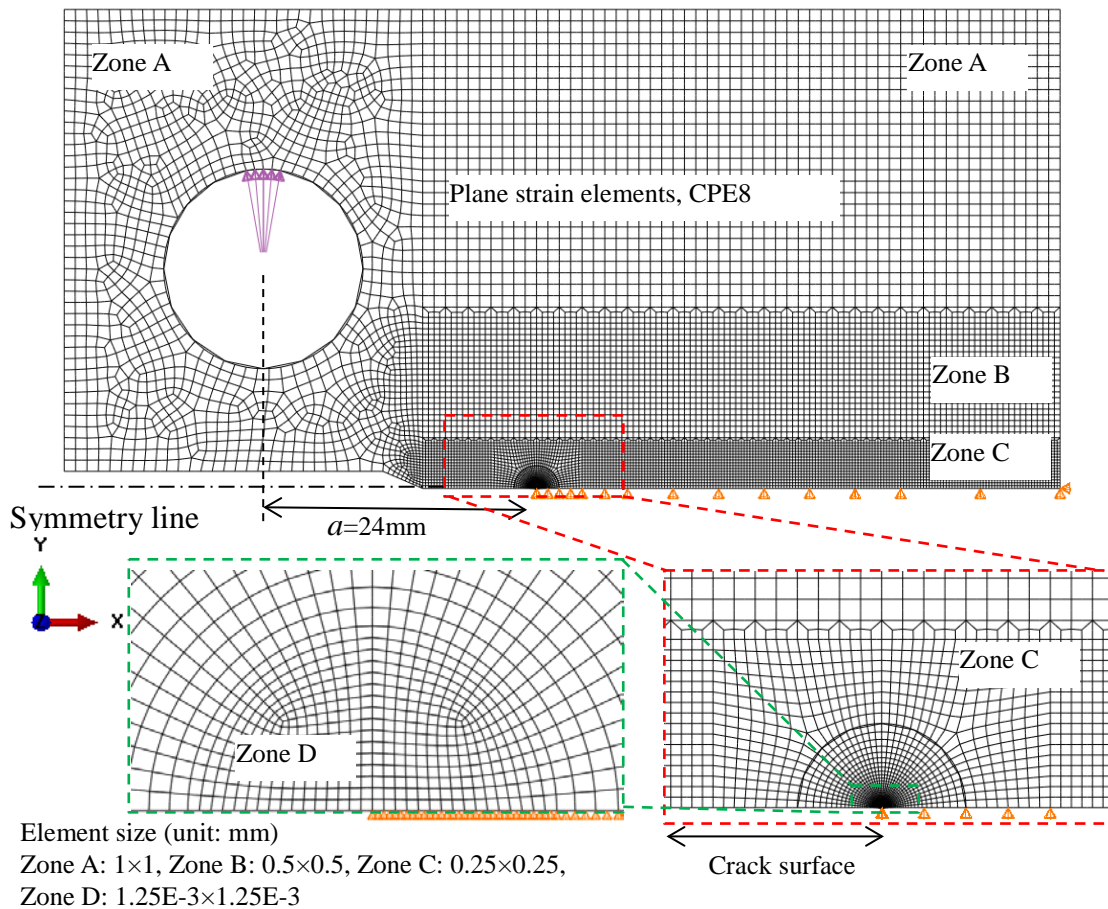


Figure 5-11 Two-dimensional FE model of C(T) specimen with fine mesh at the crack tip

Table 5-2 Yield strength in WAAM Ti-6-4 (Lorant, 2010 p.79) and values used in FE (unit: MPa)

| Ti-6Al-4V, σ_{ys} | Measured | In FE model |
|--------------------------|----------|---------------|
| WAAM, across layer | 800, 820 | Isotropic 800 |
| WAAM, parallel layer | 835, 845 | |
| Wrought | - | 860 |

5.5.2 Plastic zone size at the crack tip

Given $P = 5$ kN, $B = 6$ mm, and $a = 24$ mm, the stress intensity factor at the crack tip is $K = 19.77 \text{ MPa}\sqrt{\text{m}}$. The load, 5 kN, is the maximum fatigue load in the FCGR tests for C(T) specimens extracted from Wall-Bi120. When yield strength of $\sigma_{YS} = 800$ MPa and 860 MPa were used, the size of plastic zone at the crack tip by elastic-plastic FE analysis were 0.016 mm and 0.014 mm, respectively, as shown in Fig. 5-12. To give a good illustration, the contour maps of half FE model are displayed in mirror style.

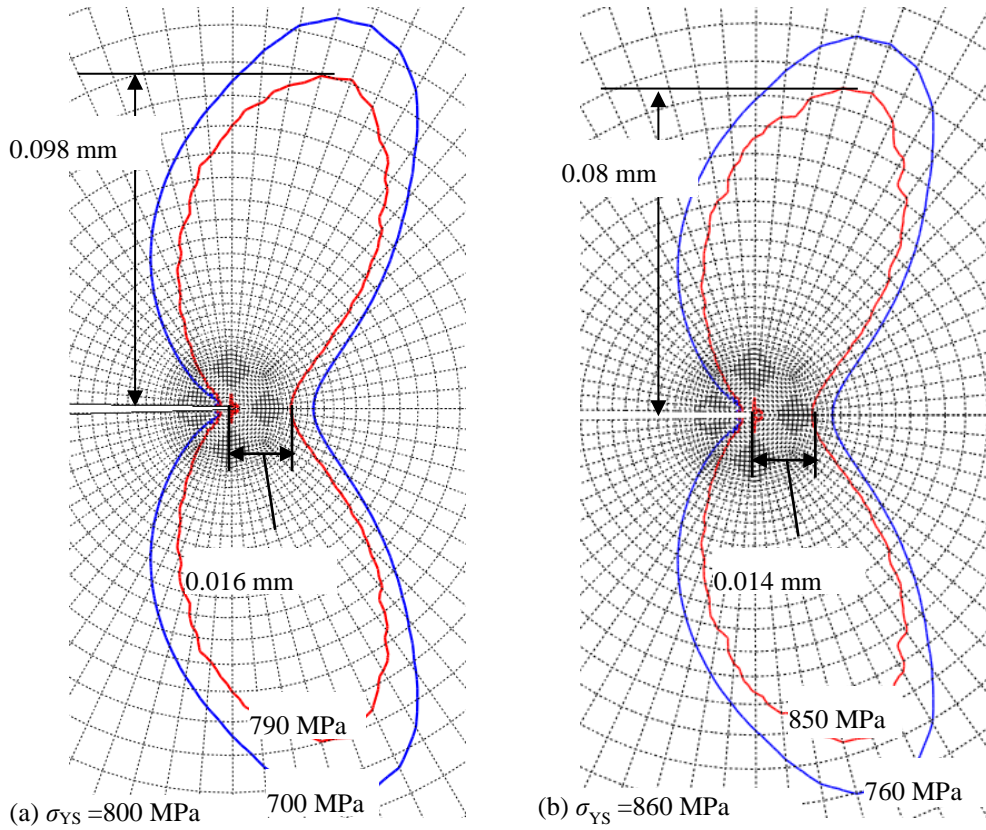


Figure 5-12 Plastic zone size calculated by elastic-plastic FE analysis, $K = 19.77 \text{ MPa}\sqrt{\text{m}}$

The analytical approach for the size of plastic zone is related (Anderson, 2012 p.62):

$$r_p = \frac{1}{n\pi} \left(\frac{K_I}{\sigma_{YS}} \right)^2 \quad 5-9$$

where r_p is the distance from the crack tip to the plastic zone boundary along crack plane, n is plastic constraint factor, σ_{YS} is the yield strength and K_I is Mode I stress intensity factor. In

reality, $n = 2.3-5$, to account for the finite thickness effect between the plane stress and plane strain conditions.

Given $K_I = 19.77 \text{ MPa}\sqrt{\text{m}}$, $n = 5$, $\sigma_{YS} = 800 \text{ MPa}$ and 860 MPa , it yields:

$$r_p = \frac{1}{5\pi} \left(\frac{K_I}{\sigma_{YS}} \right)^2 = \frac{1}{5\pi} \left(\frac{19.77}{800} \right)^2 = 0.039 \text{ mm}$$

$$\text{and, } r_p = \frac{1}{5\pi} \left(\frac{K_I}{\sigma_{YS}} \right)^2 = \frac{1}{5\pi} \left(\frac{19.77}{860} \right)^2 = 0.034 \text{ mm}$$

Comparing the plastic zone size from FE analysis, the difference is $(0.016 - 0.014)/0.014 = 14\%$. Comparing the plastic zone size from analytical approach, the difference is $(0.039 - 0.034)/0.034 = 15\%$. By two methods, the difference of yield strength has no much influence on the plastic zone size.

When comparing the results from FE analysis and analytical approach, it is noted that the difference between two methods is significant: $(0.039 - 0.016)/0.016 = 140\%$. The reason for this is that the plastic constraint factor n is determined from an empirical rule, so the used analytical equation is actually an empirical equation. However, in the FE analysis employing the plane strain elements implies a very large thickness of specimen hence underestimates the plastic zone size in front of the crack tip.

The requirement of predominantly elastic condition in FCGR test standard (ASTM Standard E647, 2011) is:

$$(W - a) \geq \frac{4}{\pi} \left(\frac{K_{\max}}{\sigma_{YS}} \right)^2 \quad 5-10$$

where a is the distance from center line of applied load to crack tip, $W-a$ is the uncracked ligament. In extreme case, where $a = 50 \text{ mm}$ and $K_{\max} = 73.4 \text{ MPa}\sqrt{\text{m}}$, under $P_{\max} = 5 \text{ kN}$, we find:

$$\frac{4}{\pi} \left(\frac{K_{\max}}{\sigma_{YS}} \right)^2 = \frac{4}{\pi} \left(\frac{73.4}{800} \right)^2 = 10.7 \text{ mm}$$

It is less than $W-a$ (20 mm). So, the specimens are of sufficient planar size to remain predominantly elastic condition during testing.

It is noted that Eq. 5-10 is a requirement of predominantly elastic condition rather than an estimation of plastic zone size. The plastic zone size by both FE analysis and Eq. 5-9 is sufficiently small that the plastic zone is embedded within an elastic singularity zone. So, the crack-tip stress conditions can still be characterized by the stress intensity factors, K_{\min} and K_{\max} . In this experimental condition, plastic zone size is sufficiently small and its influence has been included in the K_{\min} and K_{\max} (Anderson, 2012 p.452). However, larger plastic zone will give rise to more plasticity induced crack closure, and the crack growth rate will be reduced.

5.6 Stress intensity factors due to residual stress

The crack tip stress intensity factor due to residual stress, K_{res} , was evaluated based on the superposition principle proposed by Parker (1982):

$$K_{\text{res}} = K_{\text{tot}} - K_{\text{app}} \quad 5-11$$

where K_{res} is the stress intensity factor due to residual stress, K_{tot} is the total value of stress intensity factor by applied load and residual stress, and K_{app} is the stress intensity factor by applied load. The superposition principle states that the crack tip stress intensity factor due to two or more loads acting together is equal to the sum of the stress intensity factors due to each load acting separately.

5.6.1 FE model of Type A and C specimen and numerical results

Two-dimensional plane stress FE model of C(T) specimen was used to simulate the stress intensity factors in the type A and C specimens, since both specimen geometry and residual stress fields are symmetrical in these two types. The geometry of FE model, element type, CPS8, and element size were the same as FE model of C(T) specimen in Fig. 5-3. The pin loading and the material properties were also the same as the FE model in Section 5.2.3. Residual stress field was applied to the FE model by inputting directly the residual stress field, as shown in Fig. 5-13. This method has been tested and described in Section 4.4.

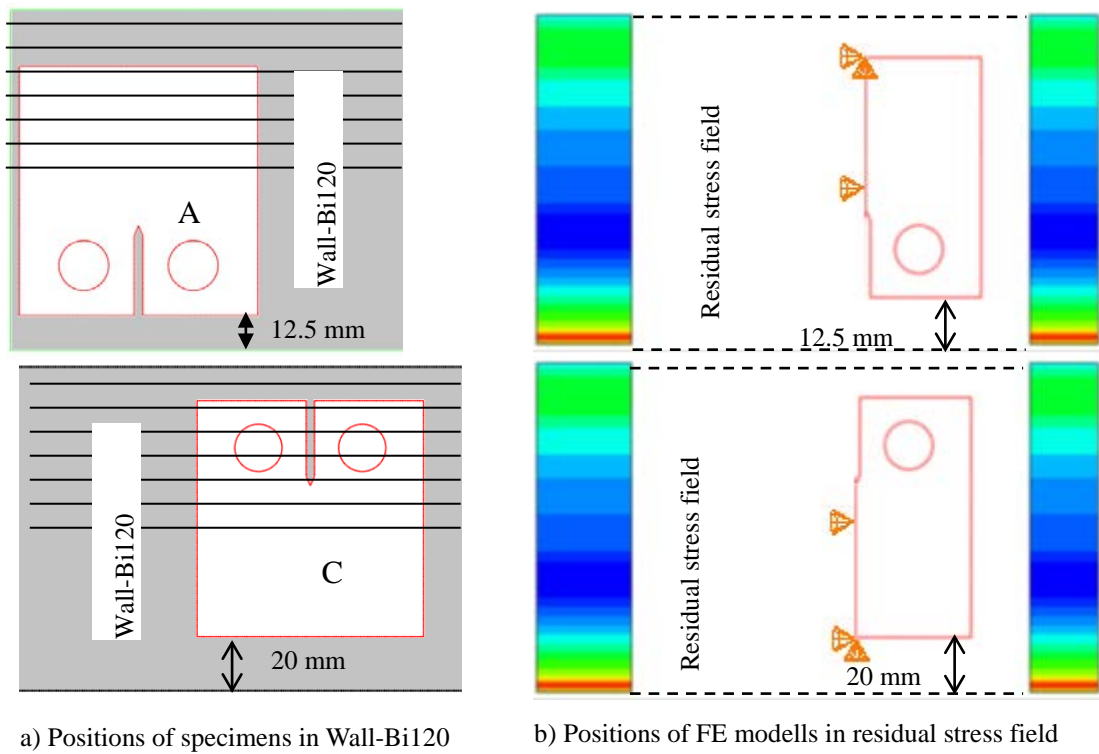


Figure 5-13 Positions of specimens in Wall-Bi120 and corresponding positions of FE models in residual stress field, type A and C

The crack tip stress intensity factors due to residual stress for type A and C are shown in Fig. 5-14. It is noted that K_{res} in the type C specimen is much higher than that in the type A specimen. The maximum value of K_{res} in the type C is higher than the maximum K_{res} in the type A by $10 \text{ MPa}\sqrt{\text{m}}$. In the type A specimen, even negative K_{res} appears at the beginning of the crack growth. The reason for this is that retained residual stresses in the type A specimen, see Fig. 4-10 are lower than that in the type C, see Fig. 4-11. The reason for the difference between retained residual stresses has been explained in Section 4.3.

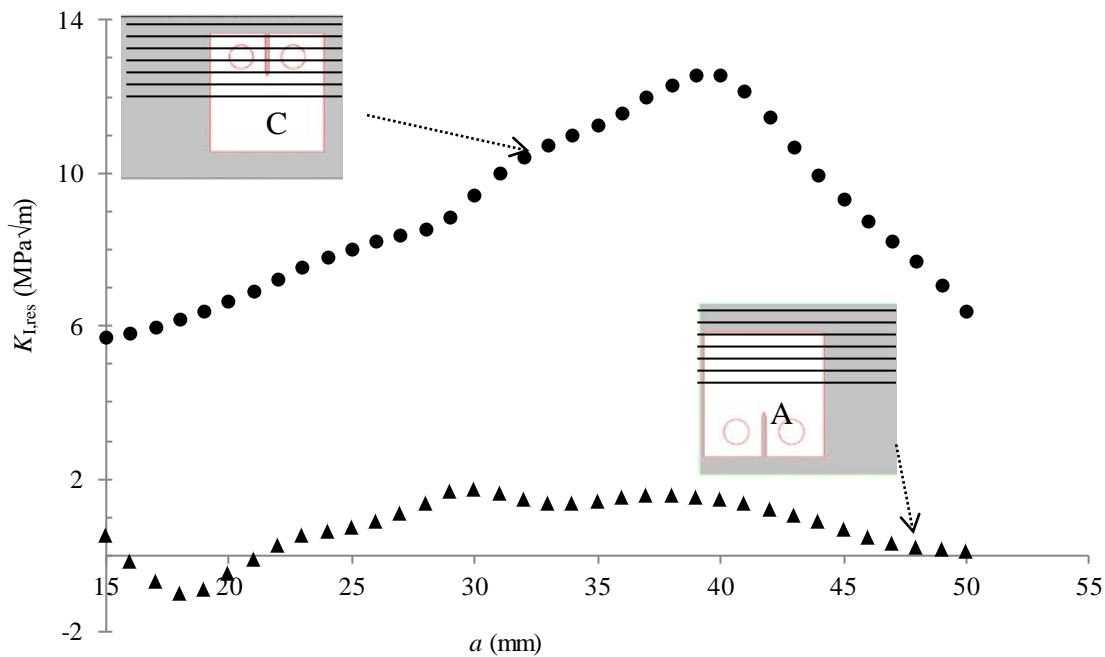


Figure 5-14 Mode I stress intensity factors due to residual stress in type A and C specimens

5.6.2 FE model of type B, D and E specimens and numerical results

Two-dimensional plane stress FE model of C(T) specimen was constructed to simulate the stress intensity factors in the type B, D and E specimens. Although the specimen geometry is symmetrical, the residual stress field is not symmetrical in these specimens. Therefore, the FE model cannot use symmetrical lines, and the cracks cannot be modelled as free boundary condition. In this FE model, the crack was created by using “seam” on which ABAQUS software put duplicate nodes. Then, those duplicate nodes were bonded together by applying surface-to-surface “contact” interactions. The contact interaction property in normal behaviour was “hard contact” with “no separation”, which meant neither penetration nor separation were allowed. In tangential behaviour, the contact interaction property was “rough”, which meant no relative sliding motion between two contacting surfaces was allowed. Such contact interactions were applied twice, i.e. in the first contact interaction, one crack surface was defined as “master” surface and the opposite crack surface was defined as “slave” surface, and then, in the second contact interaction, the previous “master” surface was defined as “slave” surface and the previous “slave” surface was defined as “master” surface. Different crack lengths were obtained by releasing the contact interactions segment by

segment along the crack paths. The boundary condition just prevented rigid body movement of the FE model, see Fig. 5-15.

The other aspects of this FE model were the same as the two-dimensional FE model of C(T) specimen described in Section 5.2.3, i.e. the geometry of FE model, element type, element size, pin loading, material properties and analysis procedure. The FE model is shown in Fig. 5-15.

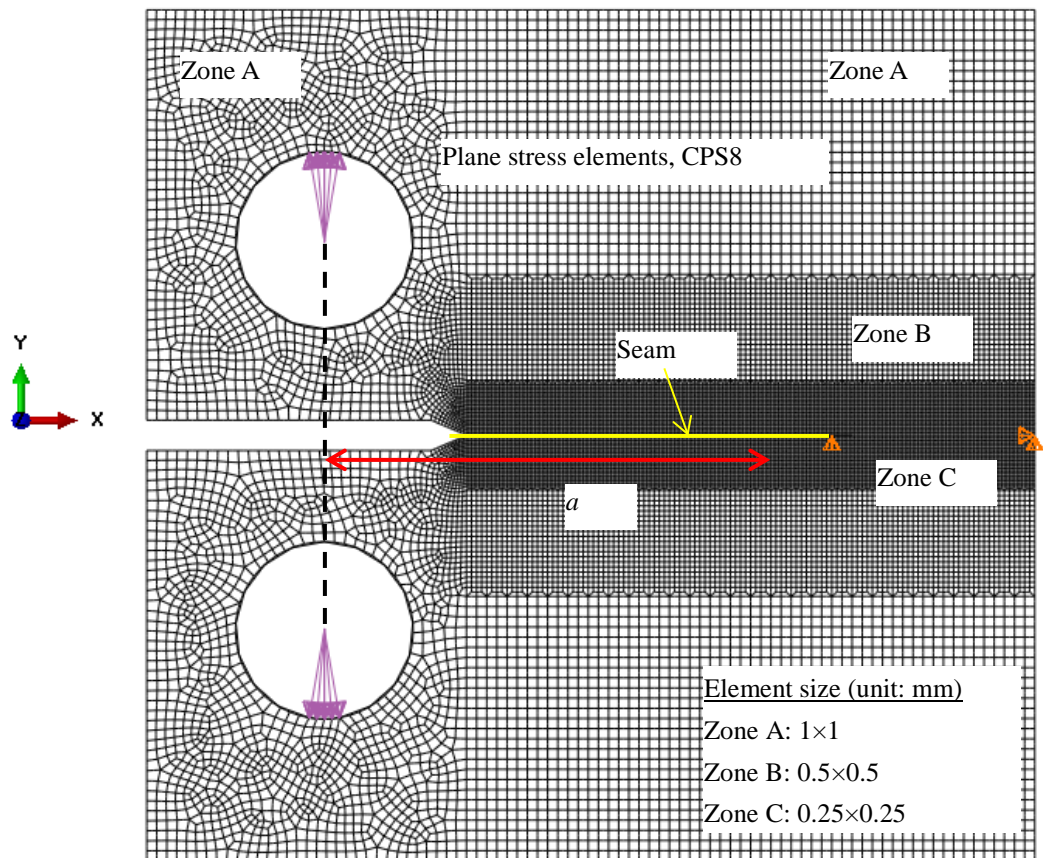


Figure 5-15 Two-dimensional FE model of C(T) specimen with seam crack

Residual stress field was applied to the FE model by directly inputting the corresponding residual stress value, as shown in Fig. 5-16.

The crack tip stress intensity factors due to residual stress for Type B, D and E are shown in Fig. 5-17. There are both Mode I and Mode II stress intensity factors specimens. All K_{res} were obtained by subtracting K_{app} from K_{tot} .

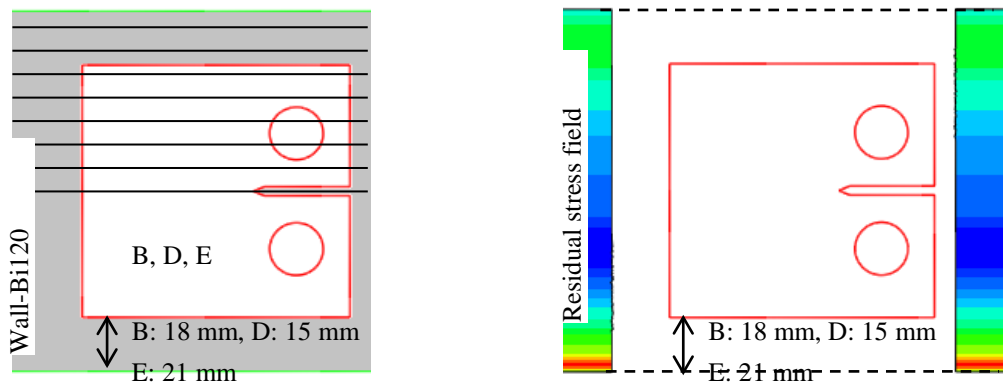


Figure 5-16 Positions of FE models in residual stress field, Type B, D and E specimen

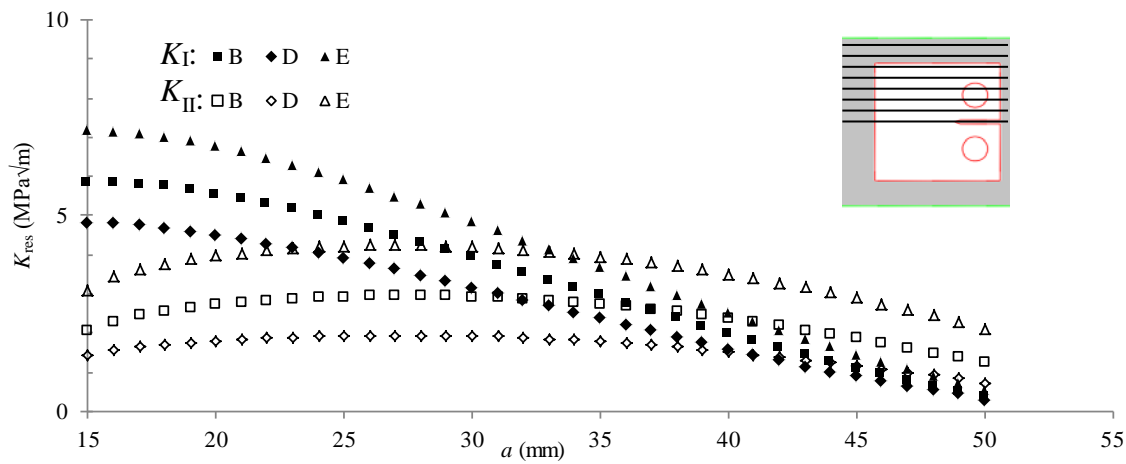


Figure 5-17 Mode I and Mode II stress intensity factors due to residual stress in Type B, D and E specimens

5.6.3 Numerical results for pure WAAM specimen (AL)

Two-dimensional plane stress FE model of C(T) specimen described in Section 5.6.2 was used to calculate the stress intensity factors in pure WAAM specimen. For crack across layers type, AL, residual stress field was applied to the FE model by directly inputting the residual stress field, as shown in Fig. 5-18. The crack tip stress intensity factors due to residual stress for AL specimen are shown in Fig. 6-16. The stress intensity factors, K_{res} , were obtained by subtracting K_{app} from K_{tot} .

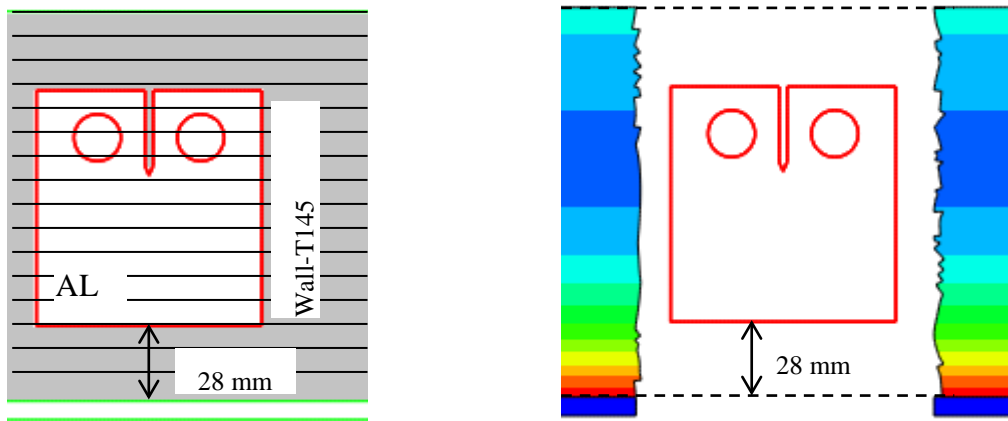


Figure 5-18 Position of FE model in residual stress field, AL specimen

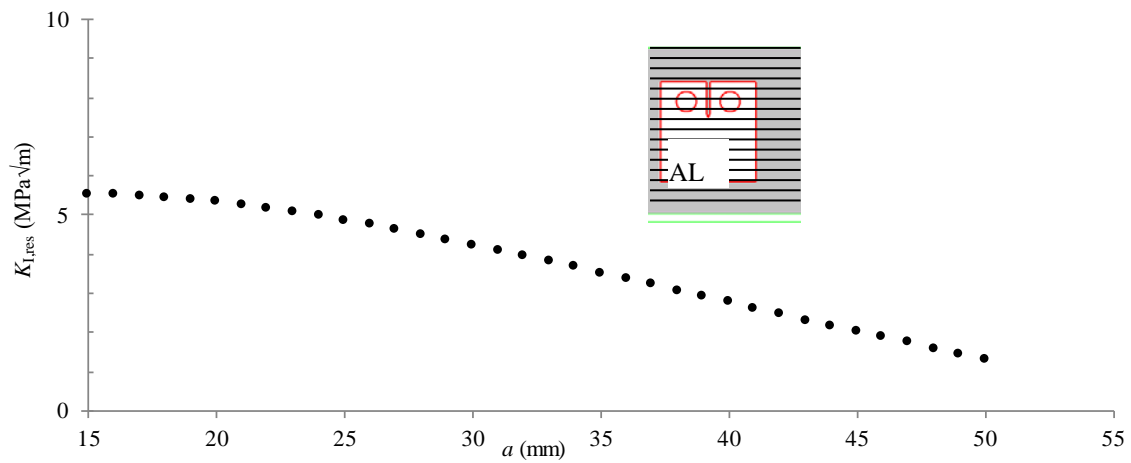


Figure 5-19 Mode I stress intensity factors due to residual stress in AL specimen

5.6.4 Numerical results for PL specimen

Two-dimensional plane stress FE model of C(T) specimen described in Section 5.6.2 was used to simulate the stress intensity factors in the type PL specimens. Residual stress field was applied to the FE model by directly inputting the corresponding residual stress value, as shown in Fig. 5-20. The crack tip stress intensity factors due to residual stress for type PL specimens are shown in Fig. 5-21. There are both Mode I and Mode II stress intensity factors in the type PL specimens. The stress intensity factors, K_{res} , were obtained by subtracting K_{app} from K_{tot} .

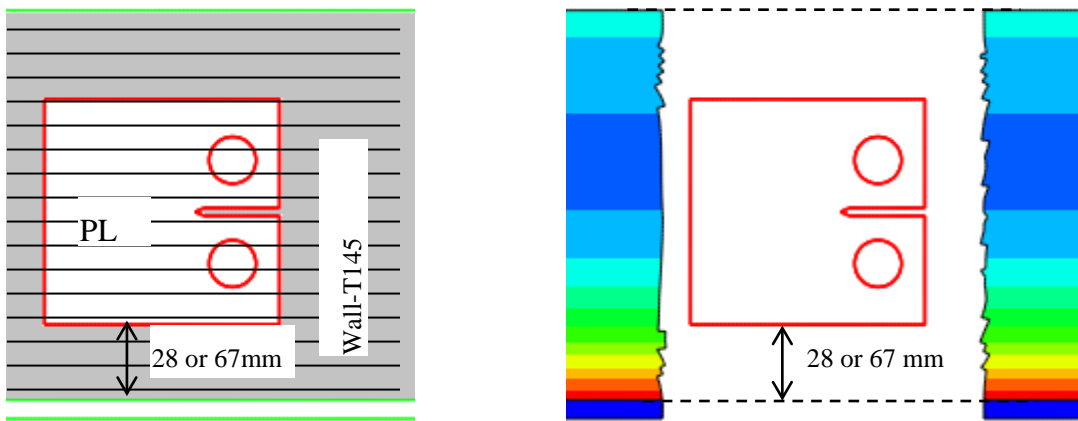


Figure 5-20 Positions of FE model in residual stress field, type PL specimens

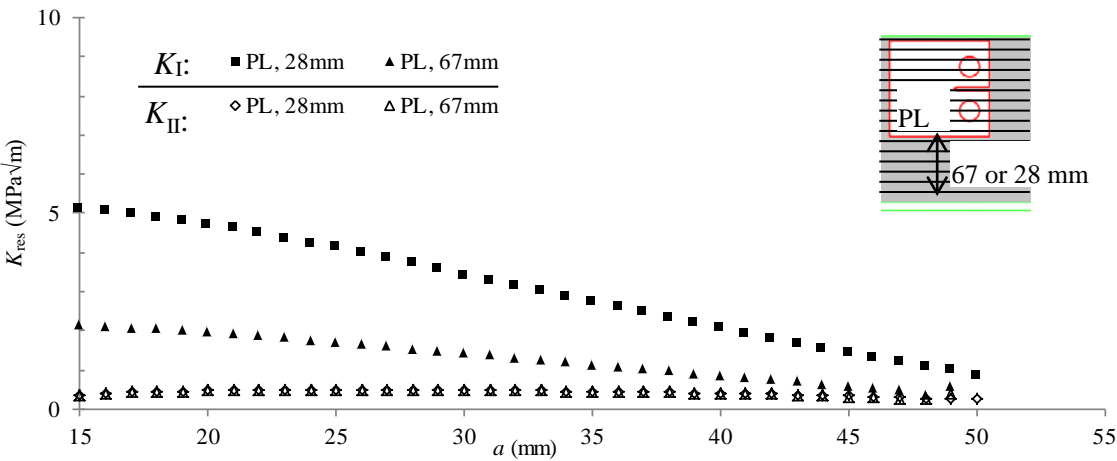


Figure 5-21 Mode I and Mode II stress intensity factors due to residual stress in type PL specimens

Chapter 6 Prediction of Fatigue Crack Growth Life

6.1 Introduction

Fatigue crack growth life was predicted based on the theory of the Linear Elastic Fracture Mechanics (LEFM). After obtaining the stress intensity factors owing to the applied load and residual stresses (Chapter 5), two empirical laws were employed to calculate the fatigue crack growth rate (FCGR); they are the Harter T-method and the modified Paris equation. Residual stress has been recognized as a more influential factor than microstructure on FCGR in welded aluminium joints (Bussu and Irving, 2003). For Ti-6Al-4V, when the effect of residual stress was included, predicted FCGR was in reasonably good agreement with experimental results for friction stir weld (Pasta et al., 2006). Previous analysis in Chapter 5 has shown that anisotropic Young's modulus has negligible influence on the stress intensity factors. Difference in Young's modulus only has an influence of less than 5% on FCGR near the interface. However, the WAAM Ti-6Al-4V has significant different FCGR from that in wrought Ti-6Al-4V. Thus, the strategy of predicting fatigue crack growth life in WAAM-substrate specimen is to include the influence of residual stress on stress intensity factors, but neglects the influence of anisotropic Young's modulus (in WAAM material) and bi-material Young's modulus (between WAAM and wrought material). The effect of microstructure on FCGR in wrought Ti-6Al-4V and WAAM Ti-6Al-4V was taken into account by using the corresponding FCGR in specific material. The strategy of such prediction is shown in Fig. 1-4. Fatigue crack growth life has been predicted for the Type A and C specimens, and compared with experimental test results of C(T) specimens. Prediction of fatigue crack trajectory in the B, D, E specimens has also been attempted, but the agreement with test measurement was very poor. Reasons for this are explained.

6.2 Fatigue crack growth rate model

Typically, FCGR data can be described as a functional relationship in the following form:

$$\frac{da}{dN} = f(\Delta K, R, C, n) \quad 6-1$$

where da/dN is crack growth per cycle, ΔK is $K_{\max} - K_{\min}$, R is K_{\min}/K_{\max} , C and n are material constants that are determined experimentally. The influence of the plastic zone and plastic wake on FCGR is implicit in Eq. 6-1, since the size of the plastic zone depends only on K_{\min} and K_{\max} (Anderson, 2012 p.452).

To calculate the influence of residual stress on FCGR, the superposition method proposed by Parker (1982) is adopted, which is based on the LEFM principle. The key equations are:

$$\Delta K_{\text{eff}} = (K_{\text{app,max}} + K_{\text{res}}) - (K_{\text{app,min}} + K_{\text{res}}) = \Delta K_{\text{app}} \quad 6-2$$

$$R_{\text{eff}} = \frac{K_{\text{app,min}} + K_{\text{res}}}{K_{\text{app,max}} + K_{\text{res}}} \quad 6-3$$

where ΔK_{eff} is the “effective” stress intensity factor range considering both the applied load and residual stress field, K_{res} is the stress intensity factor due to residual stress, $K_{\text{app,max}}$, $K_{\text{app,min}}$ and ΔK_{app} are the maximum, minimum and range of stress intensity factor by applied load, R_{eff} is effective stress intensity factor ratio.

Based on this superposition method, residual stress effect is accounted for by the term called the “effective stress intensity factor ratio”, R_{eff} , which replaces the R ratio known as the stress ratio or load ratio in the classical da/dN vs. ΔK functional relationship. To accomplish the calculation of FCGR at various R_{eff} , two methods can be used: the interpolation method and empirical models. Interpolation method needs a collection of FCGR curves in a range of various R ratios covering the range of various R_{eff} . FCGR at any R_{eff} ratio can then be calculated by interpolating the FCGR values between two adjacent R ratios. The empirical model method, uses material constants to account for the R ratio effect. By using material constants from similar titanium alloy, the empirical model for WAAM made Ti-6Al-4V can be constructed.

6.2.1 Selection of FCGR model

Many descriptions for the f have been proposed. Most of the descriptions were either based on physical models of the crack growth process or on equations that describe the trends in the data.

The Paris law is the most successful and popular model for describing FCGR in the central region for specific values of stress ratio (Anderson, 2012 p.453). The Paris law is given by the general form:

$$\frac{da}{dN} = C \Delta K^n \quad 6-4$$

where da/dN is crack growth rate, ΔK is $K_{\max} - K_{\min}$, C and n are material constants that are determined experimentally.

To use the Paris law to accurately model the material fatigue crack growth behaviour, several R values (positive and negative, are required to cover the entire range of R values in the analysis) for da/dN vs. ΔK plots must be available. However, only one R ratio ($R = 0.1$) for da/dN vs. ΔK plot of WAAM Ti-6Al-4V was available in this PhD work, so, the Paris law cannot be used.

The Walker equation provided the first simple equations that accounted for the stress ratio shift (Anderson, 2012 p.486). The Walker equation is given by the general form:

$$\frac{da}{dN} = C \left(\frac{\Delta K}{(1-R)^n} \right)^m \quad 6-5$$

where da/dN is crack growth per cycle, ΔK is $K_{\max} - K_{\min}$, R is K_{\min}/K_{\max} , C , m and n are material constants that are determined experimentally. It is noted the numerical values of C and n are different from the values in Paris law. The Harter T-method is an adaptation of the Walker equation taken on a point-by-point basis. In this PhD work, the Harter T-method will be used.

The “crack closure” phenomenon is now recognized as one of the most influential mechanisms during fatigue crack growth. It has become the default interpretation of stress ratio effects and has been used on many fatigue life prediction models (Anderson, 2012 p.458).

When considering the “crack closure” phenomenon, K_{op} , the stress intensity factor at which the crack re-opens, can be used to account for the R ratio effect. A number of investigators have attempted to correlate K_{op} to R ratio, but with limited success (Anderson, 2012 p.463).

No crack closure was observed for stress ratio R greater than 0.3 in Ti-6Al-4V (Shih and Wei, 1973). However, when R ratio is greater than 0.3, crack growth rate still be influenced by R ratio. Shih and Wei suggested that crack closure cannot fully account for the effect of R ratio on crack growth. Katcher and Kaplan (1974) studied FCGR under $R = 0.08, 0.30, 0.50, 0.7, 0.8$ and noticed that the FCGR increased 2–3 times as the R ratio from 0.08 to 0.30, and again increased 1.5–2 times as R ratio from 0.30 to 0.50. When R ratio increased from 0.7 to 0.8, no further increase in FCGR was noted. In this PhD work, descriptions based on “crack closure” physical model for Ti-6Al-4V in recrystallization annealed (RA) condition by Katcher and Kaplan (1974) will be used.

6.2.2 Harter T-method

The AFGROW software provides the material constants of Harter T-method for Ti-6Al-4V plate in MA condition. This material is the same as the substrate material used in this thesis with respect to the alloy designation, product form and heat treatment condition.

6.2.2.1 Material Constants

The Harter T-method has two sets of material constants: one set includes da/dN vs. ΔK relationship for $R = 0$, another set includes corresponding m which are material constants that control the influence of the R ratio, as shown in Fig. 6-1.

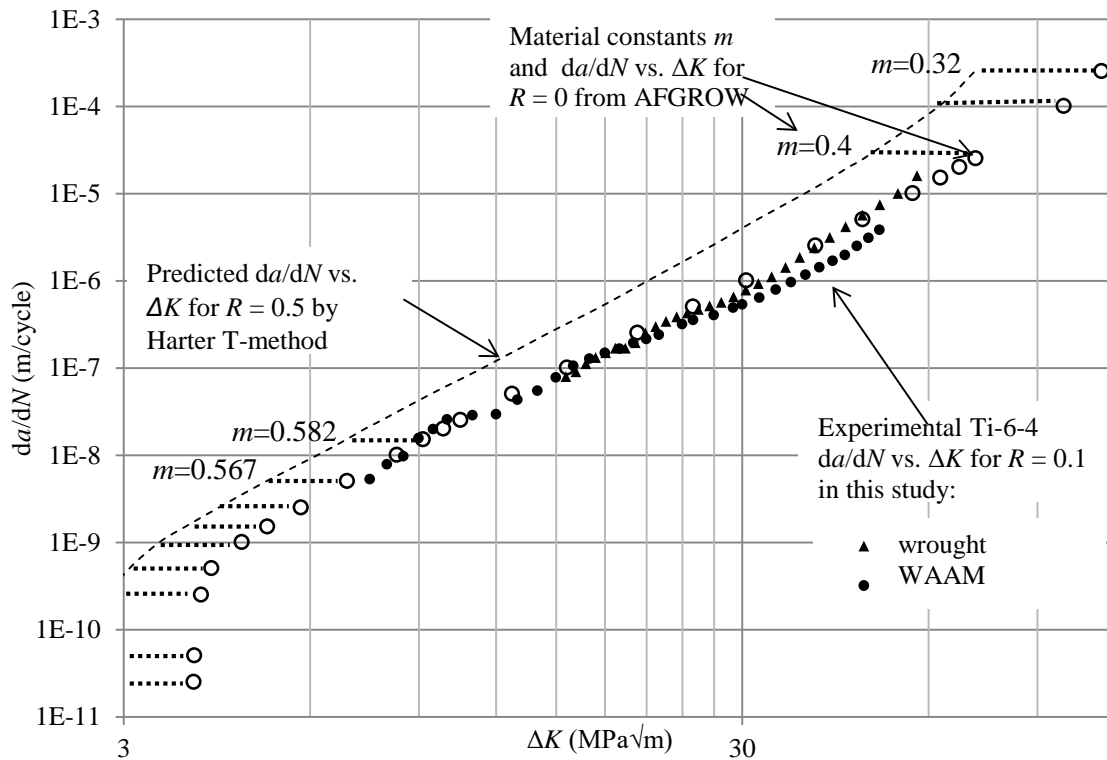


Figure 6-1 Experimental da/dN vs. ΔK data and AFGROW m for calculating fatigue crack growth rate for various R ratio (some m are omitted for clarity)

In Fig. 6-1, the material constants of the Harter T-method are described by using plots da/dN vs. ΔK on double logarithmic scale graph. The material constant, m , is noted beside each da/dN vs. ΔK point. Some m are omitted for clarity. The experimental FCGR data are also described and they are a logarithmic average from several specimens. At the same time, a prediction of da/dN vs. ΔK for $R = 0.5$ by the Harter T-method is shown.

In this study, only material constants of m in AFGROW were adopted to account for the influence of “effective stress intensity factor ratio”, R_{eff} . These m values were combined with da/dN vs. ΔK relationship for $R = 0.1$, which was from experimental tests conducted using WAAM Ti-6Al-4V and the same Ti-6Al-4V plate of the substrate. The reason for doing this is to try as much as possible to make sure data are from the same materials as Wall-Bi120.

6.2.2.2 Combining m values with experimental FCGR Dataset

The m parameters in the Harter T-method FCGR dataset are point to point, and any points for different R ratio share the same m parameter if these points have the same da/dN value. As the points in experimental FCGR dataset are not identical to the points in AFGROW’s FCGR

dataset, the experimental FCGR dataset must be interpolated to obtain the points that have the same da/dN values as the FCGR points provided by AFGROW. Such interpolation is done by using logarithmic interpolation. At the end of each FCGR curve, logarithmic extrapolation is used. The experimental FCGR dataset and the logarithmic interpolated and extrapolated FCGR dataset are shown in Figure 6-2.

The logarithmic interpolation can be expressed as:

$$(\lg \Delta K)_{\text{int}} = \frac{(\lg \Delta K)_1 - (\lg \Delta K)_2}{(\lg \frac{da}{dN})_1 - (\lg \frac{da}{dN})_2} \left(\lg \left(\frac{da}{dN} \right)_{\text{int}} - \lg \left(\frac{da}{dN} \right)_2 \right) + (\lg \frac{da}{dN})_2 \quad 6-6$$

where int represents da/dN vs. ΔK point by interpolation, 1 and 2 represent the neighbouring da/dN vs. ΔK points.

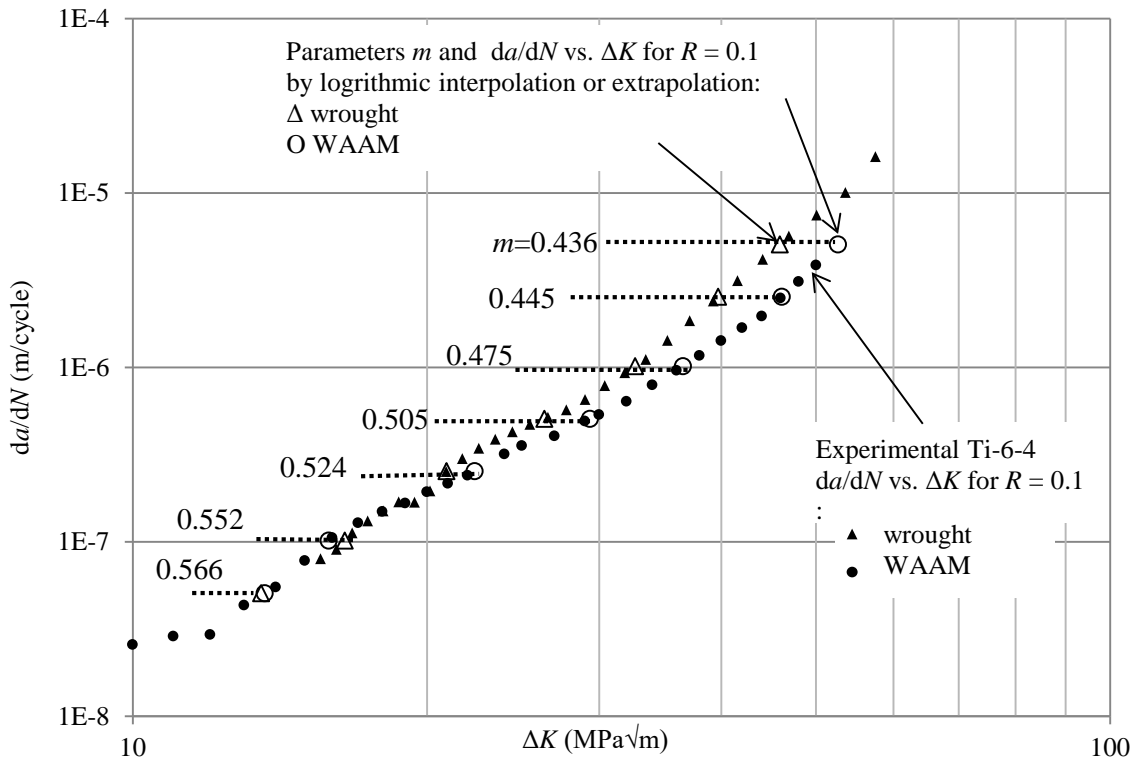


Figure 6-2 Combined dataset including m and da/dN vs. ΔK for $R = 0.1$ for the substrate and WAAM made Ti-6Al-4V

The assumption made is that the difference in the R ratio shift (not FCGR) between WAAM Ti-6Al-4V and wrought Ti-6Al-4V in MA condition, which is a part of the influence of microstructure on FCGR, can be ignored. As Ti-6Al-4V substrate and WAAM Ti-6Al-4V

have the same alloy designation, it is reasonable that such assumption will not have significant error. Therefore, the parameters of wrought Ti-6Al-4V are used in this study to calculate the FCGR for both the substrate and WAAM Ti-6Al-4V.

6.2.2.3 Calculation procedure

The standard calculating procedure has been described in AFGROW technical manual (Harter, 2008) which obtain da/dN for any desired R value from da/dN vs. ΔK data for $R = 0$ value. However, the data in standard procedure for calculating are starting from $R = 0$ instead of 0.1 value. So, it is necessary to describe calculation procedure used in this thesis.

The calculation procedure has three steps, as shown in Fig. 6-3.

Step 1: A given ΔK value has two nearest ΔK_1 values in the interpolated experimental FCGR dataset, i.e. $\Delta K_{1,Low}$ and $\Delta K_{1,High}$. The ΔK_1 is da/dN vs. ΔK dataset for R_1 , and ΔK_2 for R_2 . The corresponding da/dN_{Low} and da/dN_{High} can be searched for in the interpolated experimental FCGR dataset, and then m_{Low} , m_{High} can be searched for according to da/dN values.

Step 2: At each point, ΔK_2 is given by the following relationship (Harter, 2008)

$$\Delta K_2(1-R_2)^{m-1} = \Delta K_1(1-R_1)^{m-1} \quad 6-7$$

where R value for the known experimental FCGR dataset ($R_1 = 0.1$ for experiments in this PhD work) is noted as R_1 , and the desired R value is noted as R_2 .

By calculating the two ΔK_2 values, which are $\Delta K_{2,Low}$ and $\Delta K_{2,High}$, the relationship of da/dN vs. ΔK for the desired R_2 between $\Delta K_{2,Low}$ and $\Delta K_{2,High}$ has been built.

Step 3: Check if the given ΔK value is between $\Delta K_{2,Low}$ and $\Delta K_{2,High}$: if so, just do a logarithmic interpolation in the established da/dN vs. ΔK curve and obtain corresponding da/dN for R_2 . If not, just select the next nearest point to repeat the calculation procedure. The reason for this is to keep the given ΔK value is between $\Delta K_{2,Low}$ and $\Delta K_{2,High}$.

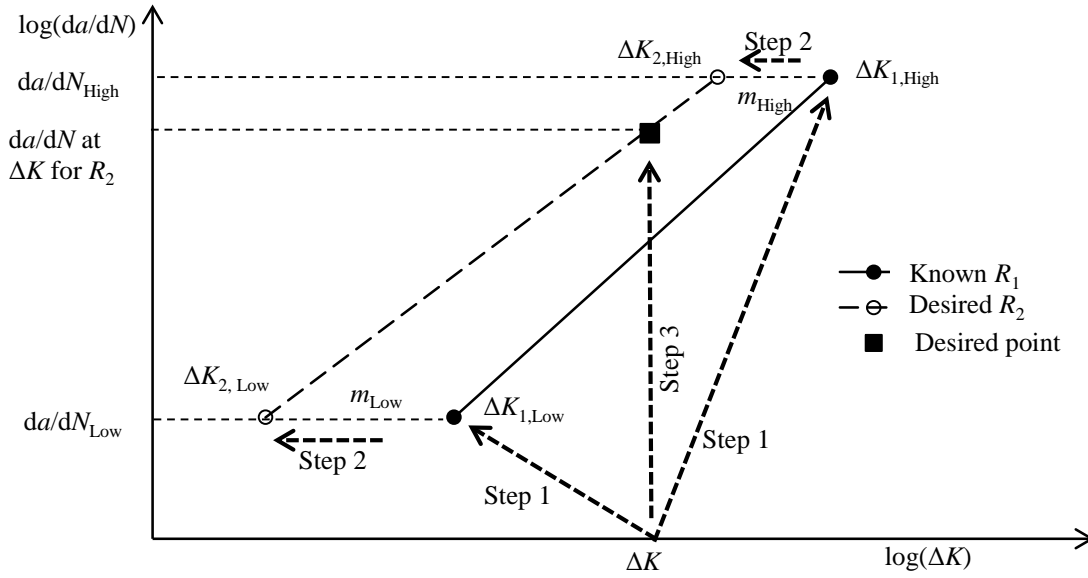


Figure 6-3 Harter T-method calculation procedure

6.2.3 Modified Paris equation

When considering the “crack closure” phenomenon, the driving parameter for crack growth is the “effective crack tip stress intensity factor range” ΔK_{eff} (Elber, 1970). It is a function of K_{op} , the stress intensity factor at which the crack re-opens. The ΔK_{eff} is defined as

$$\Delta K_{eff} = K_{max} - K_{op} \quad 6-8$$

The physical meaning of this equation is that the portion of the cycle that is below K_{op} does not contribute to fatigue crack growth.

An effective stress intensity factor range ratio is also defined as

$$U = \frac{\Delta K_{eff}}{\Delta K} \quad 6-9$$

Modified Paris equation for FCGR proposed by Elber (1970) has a form

$$\frac{da}{dN} = C(\Delta K_{eff})^n \quad 6-10$$

where C and n are material constants. The numerical values of C and n are different from the values in Paris law. If the C and n in the Paris law were obtained from a no-crack-closure condition, the numerical values in the modified Paris equation and the Paris law can be the

same. These C and n can be obtained from experiments with any R ratio.

In this thesis, empirical modified Paris equation for recrystallization annealed (RA) Ti-6Al-4V by Katcher and Kaplan (1974) is used

$$\frac{da}{dN} = C(U\Delta K_{app})^n \quad 6-11$$

where C and n are material constants that are determined experimentally, and for the range of $0.08 < R < 0.35$, the U is $0.73 + 0.82R$ (Katcher and Kaplan, 1974). It can be seen later, the maximum R_{eff} is 0.35 and the minimum R_{eff} is 0.04 for Type A and C. However, the overall range of R_{eff} are within the limits.

For measured da/dN vs. ΔK dataset in this PhD project, applied load ratio is 0.1, and parameters C and n were obtained by curve fitting. Fit the experimental $\lg(da/dN)$ vs. $\lg(\Delta K)$ dataset to a straight line

$$\lg\left(\frac{da}{dN}\right) = A + B\lg(\Delta K) \quad 6-12$$

where A and B are curve fitting coefficients.

Then rewrite Eq. 6-11

$$\lg\left(\frac{da}{dN}\right) = \lg C + n\lg U + n\lg \Delta K \quad 6-13$$

Combining Eq. 6-12 and 6-13, parameters C and n are given by

$$n = B \quad 6-14$$

$$C = 10^{(A - n\lg U)} \quad 6-15$$

$$U = 0.73 + 0.82R = 0.73 + 0.82 \times 0.1 = 0.812 \quad 6-16$$

After having C and n , the fitted modified Paris equation for WAAM made Ti-6Al-4V and Ti-6Al-4V in wrought products are

$$\frac{da}{dN} = 4.345 \times 10^{-11} [(0.73 + 0.82R)\Delta K]^{2.998} \text{ for WAAM made Ti-6Al-4V} \quad 6-17$$

$$\frac{da}{dN} = 4.682 \times 10^{-12} [(0.73 + 0.82R)\Delta K]^{3.819} \text{ for wrought products} \quad 6-18$$

The fitted modified Paris equations are compared with experimental data in Fig. 6-4. When calculating the FCGR with the influence of residual stress, applied load ratio, R , should be replaced by R_{eff} .

The assumption made is that the difference in the R ratio shift, which is a part of the influence of microstructure on FCGR, among Ti-6Al-4V in RA and MA condition as well as in WAAM made Ti-6Al-4V can be ignored. As all materials have the same alloy designation, it is reasonable that such assumption will not have significant error.

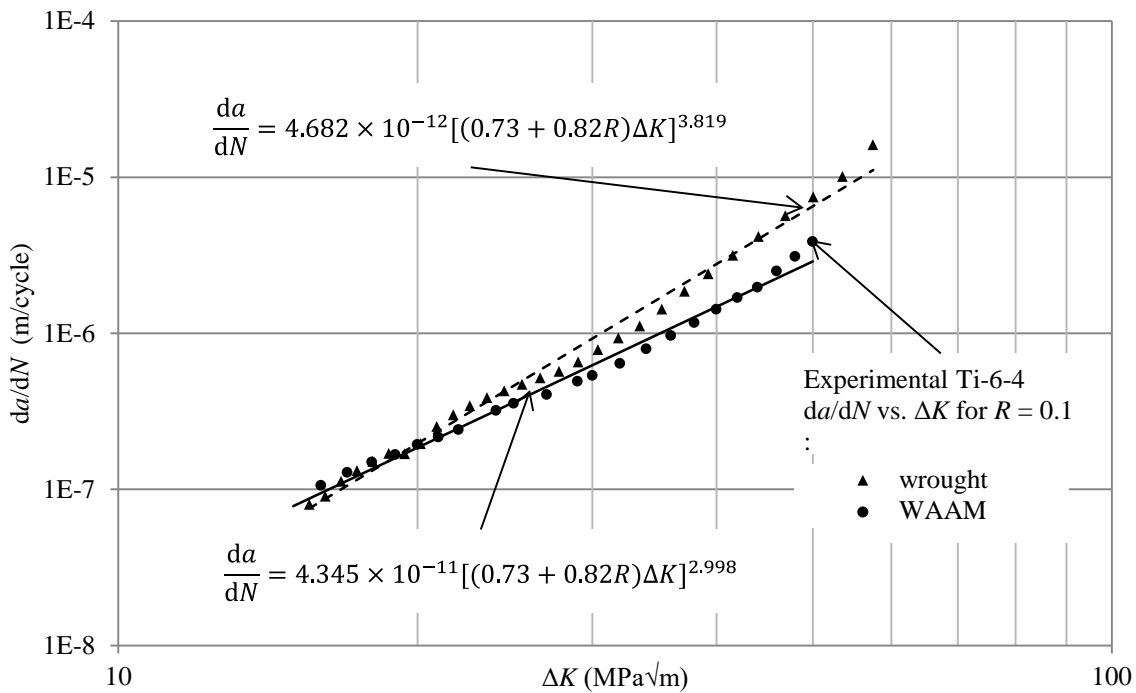


Figure 6-4 Fitted modified Paris equation and experimental da/dN vs. ΔK for $R = 0.1$ for WAAM made Ti-6Al-4V and Ti-6Al-4V of wrought products

6.3 Fatigue crack growth life in the Type A and C specimens

6.3.1 Fatigue crack growth rates and predicted life

Positions of C(T) specimens in Wall-Bi120 sample have been shown in Fig. 3-13. The

geometrical WAAM-substrate interface positions of the Type A and C specimens are shown in Fig. 6-5. From the loading and geometry parameters, as shown in Table 3-5, the maximum applied stress intensity factors, $K_{app,max}$ were calculated by using Eq. 5-5, and are plotted as a function of crack length, a , which is defined as the distance from center line of loading holes to the crack tip, as shown in Fig. 6-6. This definition is in accordance with the ASTM standard E647. The stress intensity factors due to residual stress are also plotted in Fig. 6-6, which are the numerical results presented in Fig. 5-14.

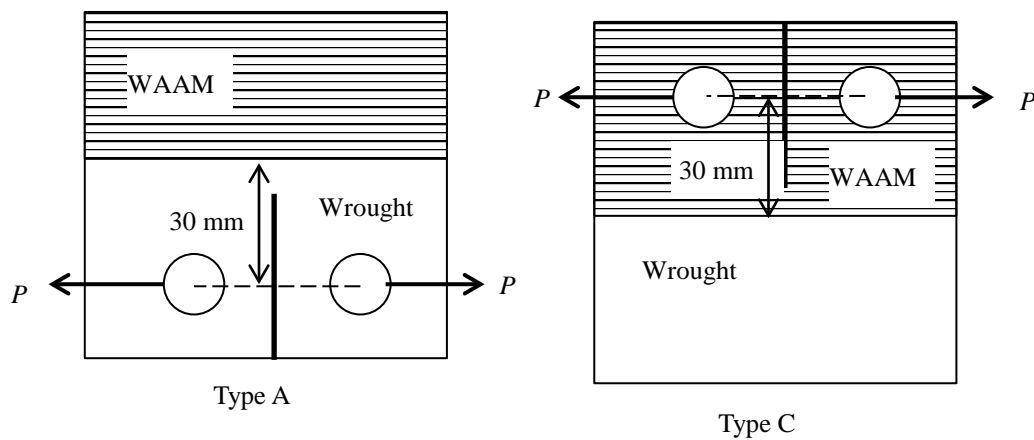


Figure 6-5 Positions of the WAAM-substrate interfaces in the C(T) specimens, Type A and C

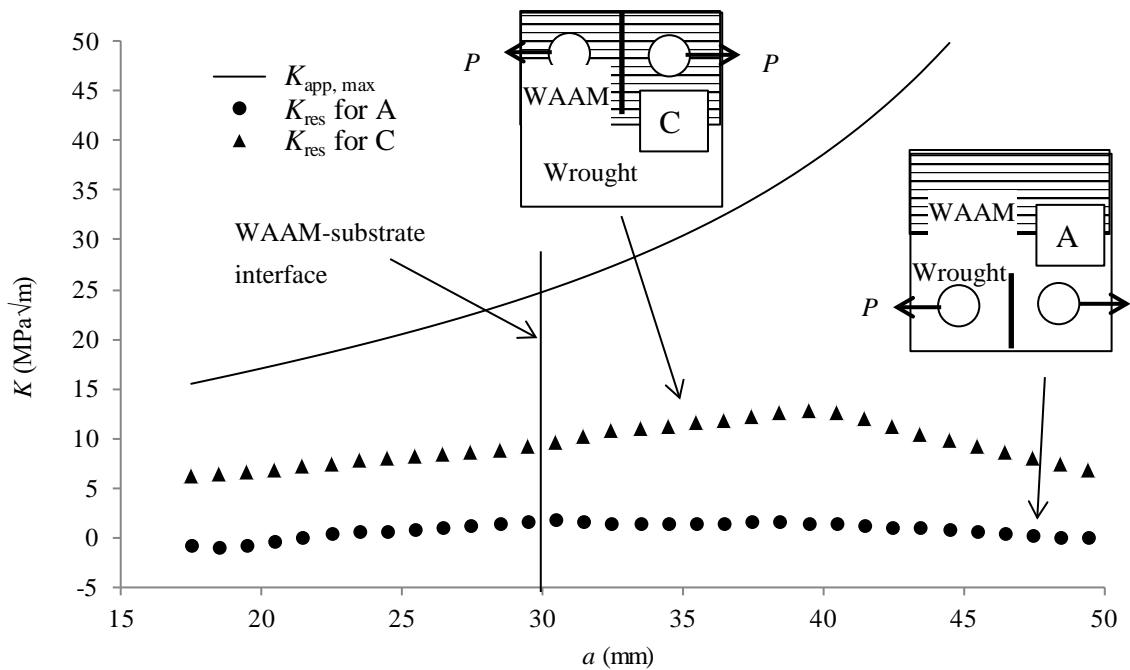


Figure 6-6 Stress intensity factors, $K_{app,max}$ and K_{res} , in the C(T) specimens, Type A and C

The minimum applied stress intensity factors were calculated from the maximum value and R ratio of 0.1, $K_{app,min} = 0.1 \times K_{app,max}$. Using the superposition method, Eq. 6-3, the “effective stress intensity factor ratio”, R_{eff} , were calculated and are plotted as a function of a , as shown in Fig. 6-7.

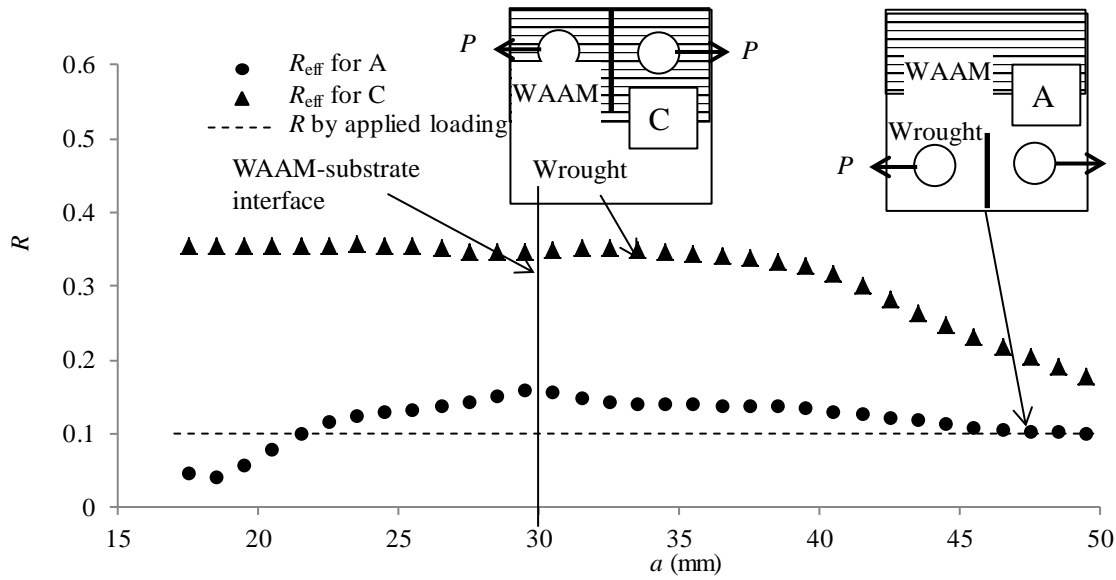


Figure 6-7 Effective stress intensity factor ratios for the C(T) specimens, Type A and C

It is noted that the maximum value of R_{eff} in the Type C specimen is about 0.35, and Type A is less than 0.15. Furthermore, R_{eff} are in the range $0.04 < R_{eff} < 0.35$, which is nearly the range for the modified Paris equation, $0.08 < R < 0.35$. However, the range $0.04 < R_{eff} < 0.08$ is located before $a = 20$ mm. By starting the crack tip at 20 mm, the range of R_{eff} can be strictly kept in $0.08 < R_{eff} < 0.35$. The Harter T-method is not influenced by this R_{eff} range.

The relationship of da/dN vs. a was calculated by both the Harter T-method and the modified Paris equation, and are compared with experiments results, see Fig. 6-8 for the Type A and Fig. 6-10 for type C. The calculation methods of da/dN for various R_{eff} have been described in Section 6.2.2 and 6.2.3. The calculations were performed by Excel software.

Fatigue crack growth life is described as the number of cycles required to propagate a crack from an initial length a_0 to i th length a_i . The number of cycles at a_i is given by

$$N_i = N_{i-1} + \Delta N_i \quad 6-19$$

where $\Delta N_i = \frac{\Delta a_i}{(\frac{da}{dN})_i}$

$$\Delta a_i = a_i - a_{i-1}$$

where N_{i-1} is the number of cycles at a_{i-1} , ΔN_i the number cycles from a_{i-1} to a_i , and $(da/dN)_i$ is the average FCGR between a_i and a_{i-1} . In these calculations, all Δa were selected 1 mm. The initial length of a_0 was 20 mm for the Type A specimen and 18 mm for the Type C. The reason for starting the crack tip at 20 mm for the Type A specimen is to keep the range of R_{eff} can be strictly limited within $0.08 < R_{\text{eff}} < 0.35$. The calculations were performed by Excel software. The relationships of a - N are compared in Fig. 6-9 for the Type A and Fig. 6-11 for the type C.

To clearly show the influence of residual stress on FCGR, one calculation that just consider the bi-material FCGR but ignore the residual stress were performed and the predicted FCGRs and fatigue crack growth life are shown in figures 6-8 to 6-11. It can be seen that ignoring the residual stress will result in overestimated fatigue crack growth life. At the same time, the Harter T-method provides better predictions than others.

An abnormal thing is that experimental results for A3 specimen are much larger after $a = 40$ mm, as shown in Fig. 6-8. The reason for this is that the crack propagated along the prior- β grain boundary. The photos for crack surface of the A3 specimens have been shown in Fig. 3-14 to provide an evidence of the prior- β grain boundary. It has been mentioned in Section 2.5.1.1 that gain boundary α phase can provide weak source for crack initiation and propagation (Donachie, 2000 p.100). Although further microstructure investigation was not done to find the gain boundary α phase, the photos for crack surface show that a part of crack face is along the prior- β grain boundary. When part of crack face propagated along the prior- β grain boundary, the FCGR increased significantly.

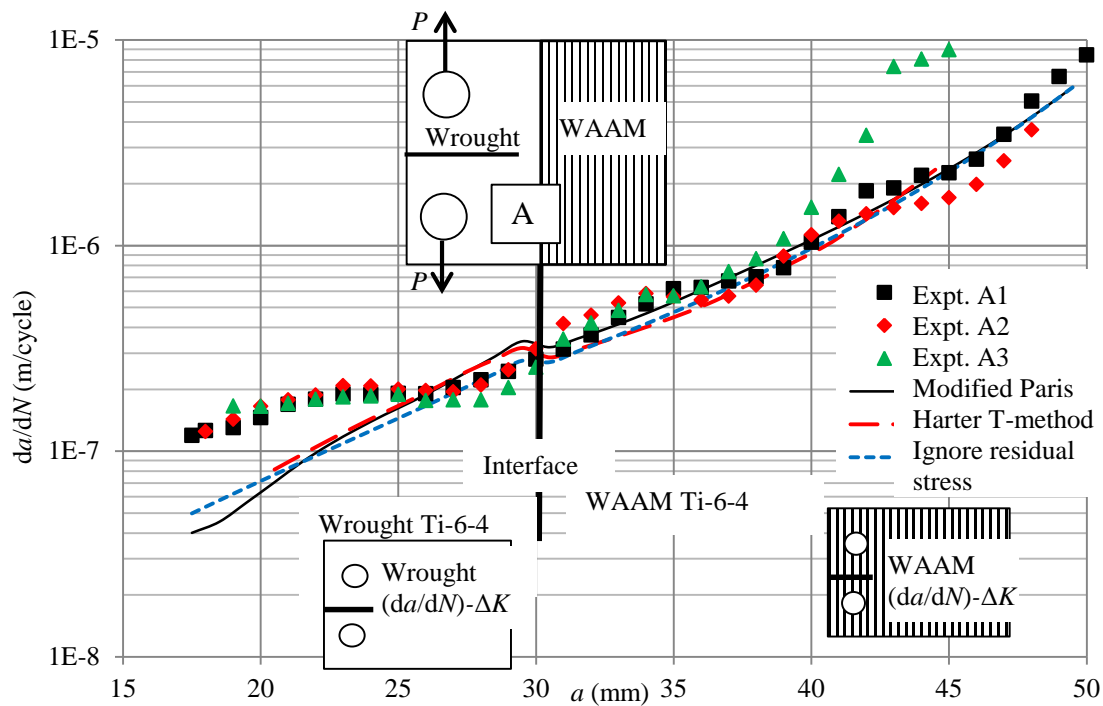


Figure 6-8 Comparison of da/dN vs. a in the Type A specimen, between predictions by the Harter T-method, the modified Paris equation and that ignoring residual stress and three experimental results

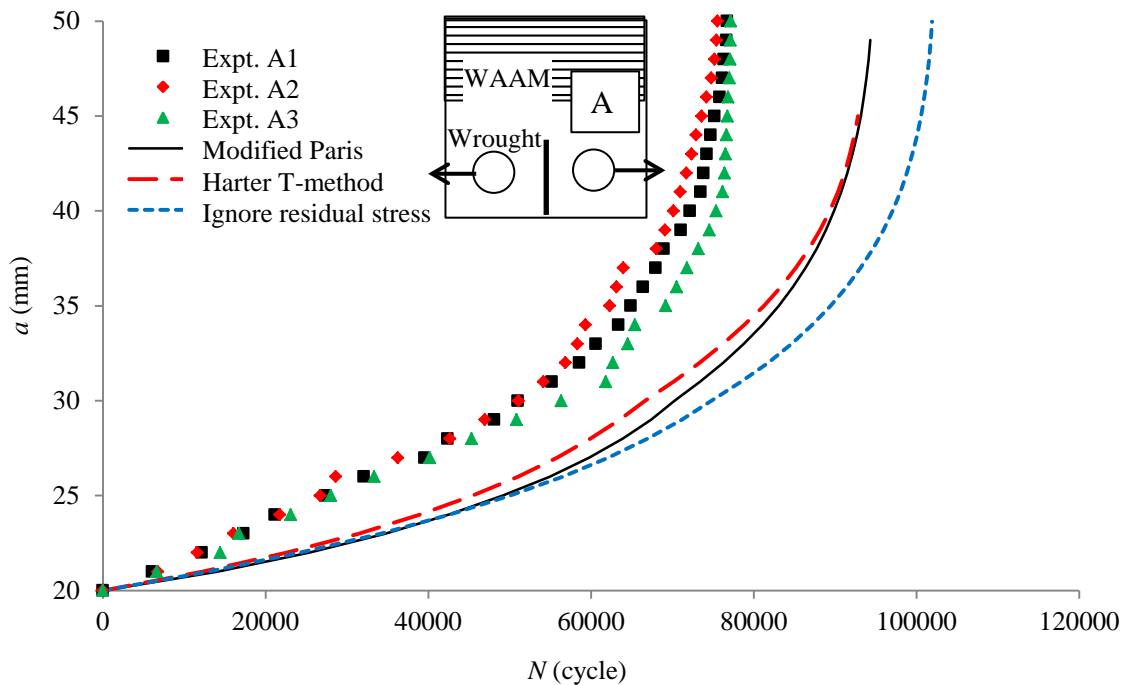


Figure 6-9 Comparison of a vs. N curves in the Type A specimen, between predictions by the Harter T-method, the modified Paris equation and that ignoring residual stress and three experimental results

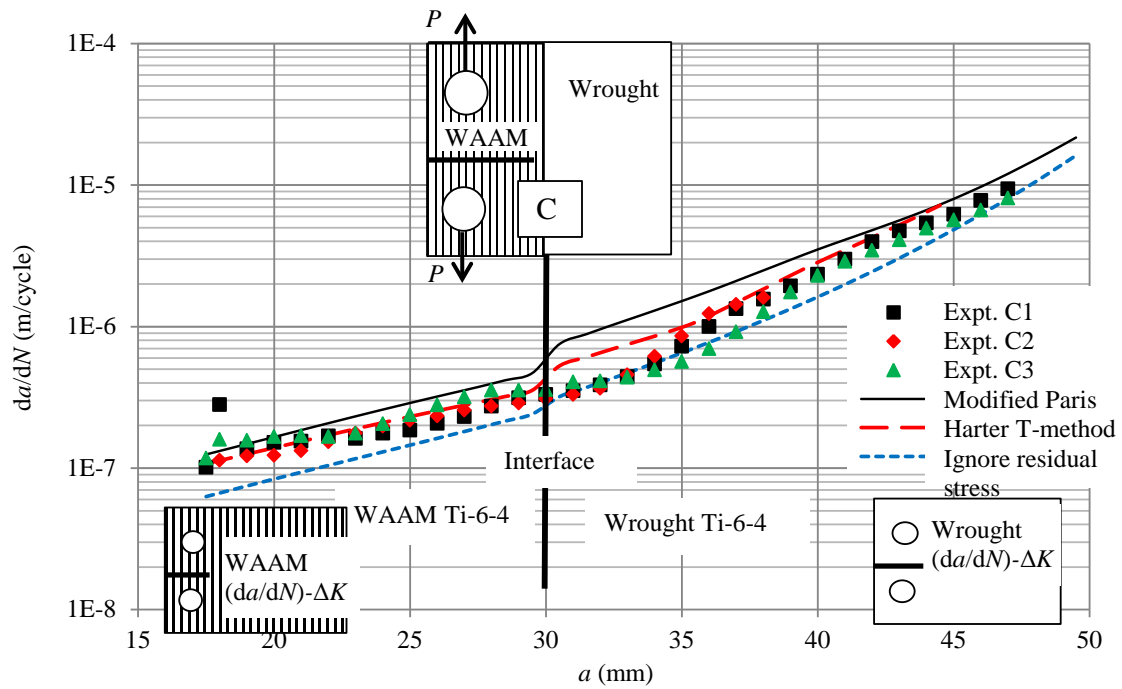


Figure 6-10 Comparison of da/dN vs. a in the Type C specimen, between predictions by the Harter T-method, the modified Paris equation and that ignoring residual stress and three experimental results

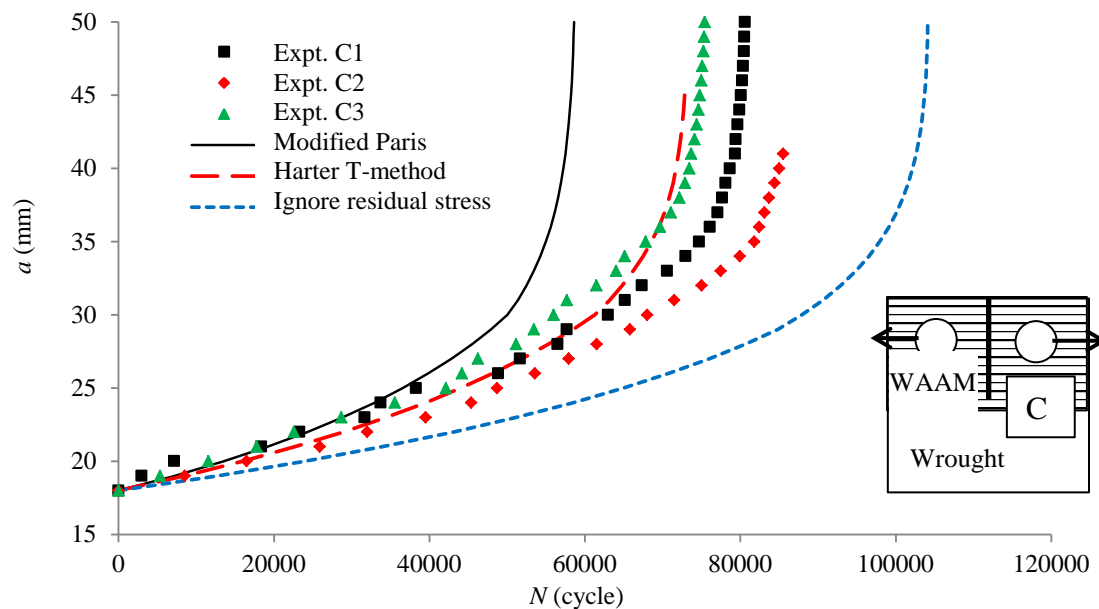


Figure 6-11 Comparison of a - N curves in the Type C specimen, between predictions by the Harter T-method, the modified Paris equation and that ignoring residual stress and three experimental results

For the FCGRs over the distance from 18 mm to 25 mm in the Type A specimen, see Fig. 6-8,

there is considerable discrepancy between the predicted FCGRs and the experimental results. The reason for this is that the actual retained residual stress in the Type A specimen is larger than that expected by FE analysis. In section 4.3, the higher retained residual stresses have been noticed and explained by the distance to the end of the Wall-Bi120, as shown in Fig. 4-7. Now, the same reason can be used to explain higher actual FCGRs in the Type A specimens. The ends of Wall-Bi120 are the positions for starting or stopping each layer and have higher residual stress. As the position for the Type A specimen is close to the end of Wall-Bi120, higher retained residual stress is expected. Therefore, higher FCGRs appeared in the Type A specimens.

One clear thing in Fig. 6-8 is that the higher predicted da/dN are observed over a distance from 26 mm to 30 mm. On the other hand, in Fig. 6-10 which is for Type C, the predicted data are also higher than the experimental results over a distance from 30 mm to 34 mm. The reason for this is the discrepancy between the geometrical interface position and microstructure interface position.

According to the geometrical position for Wall-Bi120, which is plotted in Fig. 3-13, the geometrical interface position for the Type A and Type C specimens are 30 mm far from the line of loading centres, see Fig. 6-5. Therefore, during predicting fatigue crack growth life, this geometrical interface was adopted as microstructure interface, which means that one side of the geometrical interface is WAAM made Ti-6Al-4V and another side is Ti-6Al-4V of wrought products. However, Fig. 6-12 which is macrostructure photo of C2 specimen shows there is a distance of 4 mm between the geometrical interface and the microstructure interface. Such distance give rise to use fatigue crack growth rates data for wrought products to predict actual WAAM made Ti-6Al-4V over 4 mm long distance in both the Type A and C specimens. So, the predicted FCGRs are higher than the experimental results over this 4 mm distance. Furthermore, inaccurate interface position will reduce the predicted fatigue crack growth life in both Type A and C specimens.

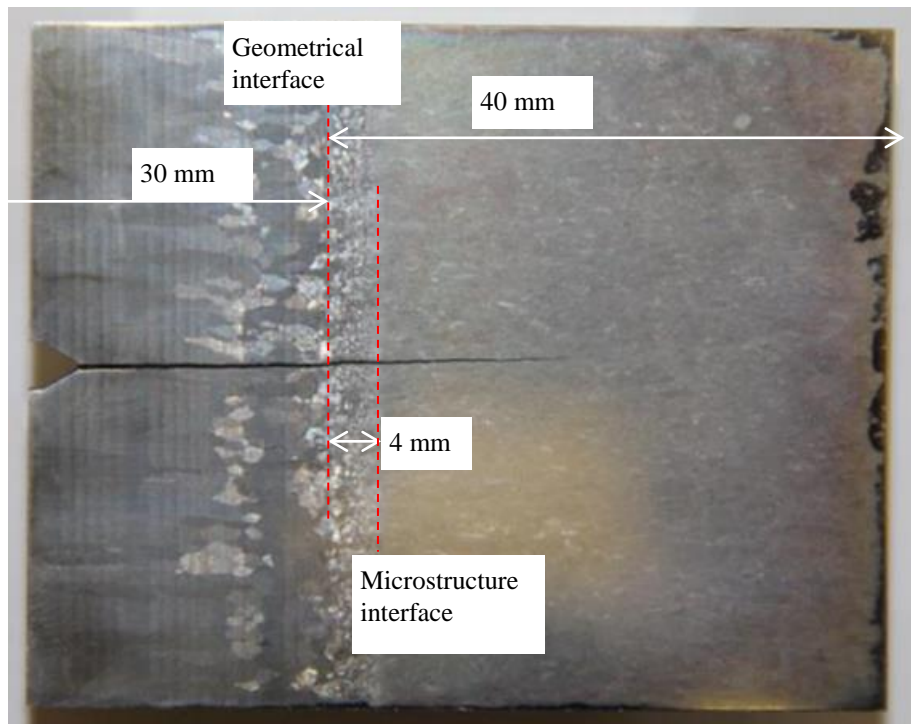


Figure 6-12 Geometrical interface and microstructure interface in C2 specimen

When comparing the accuracy of predicted FCGRs in WAAM Ti-6Al-4V, it is noted that the accuracy of the Type A is better than that of the Type C. For the Type A, the predicted FCGRs are a little lower or higher than the experiments over the distance from 34 mm to 50 mm. For the Type C, the predicted FCGRs are always a little higher than the experiments over the distance from 18 mm to 34 mm. The reason is due to one assumption that the da/dN vs. ΔK data for pure WAAM made Ti-6Al-4V were from specimen without residual stress. As the influence of residual stress depends on the applied loads, the da/dN vs. ΔK data were not equally affected by the residual stress in pure WAAM specimen, and hence resulted in that the prediction of one sample is more accurate than another.

Using residual stress profile developed in Section 4.5.5, the R_{eff} can be obtained for AL specimen, see Fig. 6-13. The calculation procedure used the experimental load, $P_{\text{max}} = 2.4$ kN, and geometry parameters which has been shown in Table 3-5. The “effective stress intensity factor ratio”, R_{eff} , for AL specimen are plotted as a function of ΔK , as shown in Fig. 6-13.

As the applied stress intensity factors range at $a = 30$ mm for the Type A and C specimens is $\Delta K = 22.7$ MPa $\sqrt{\text{m}}$, the FCGR data range from 14 MPa $\sqrt{\text{m}}$ to 22.7 MPa $\sqrt{\text{m}}$ were used for

prediction in the Type C specimen and the FCGR data range from 22.7 MPa√m to 40 MPa√m for the Type A. In this way, the data range used for the Type C has higher R_{eff} than that for the Type A, and gives rise to less accuracy.

This assumption also gave rise to double accounting for the effect of residual stress. The increase of da/dN by the residual stress had been accounted for in the measured da/dN vs. ΔK data for WAAM made Ti-6Al-4V and then the effect of residual stress was accounted for again during prediction by considering R shift effect. This will reduce the predicted fatigue crack growth life in both Type A and C specimens.

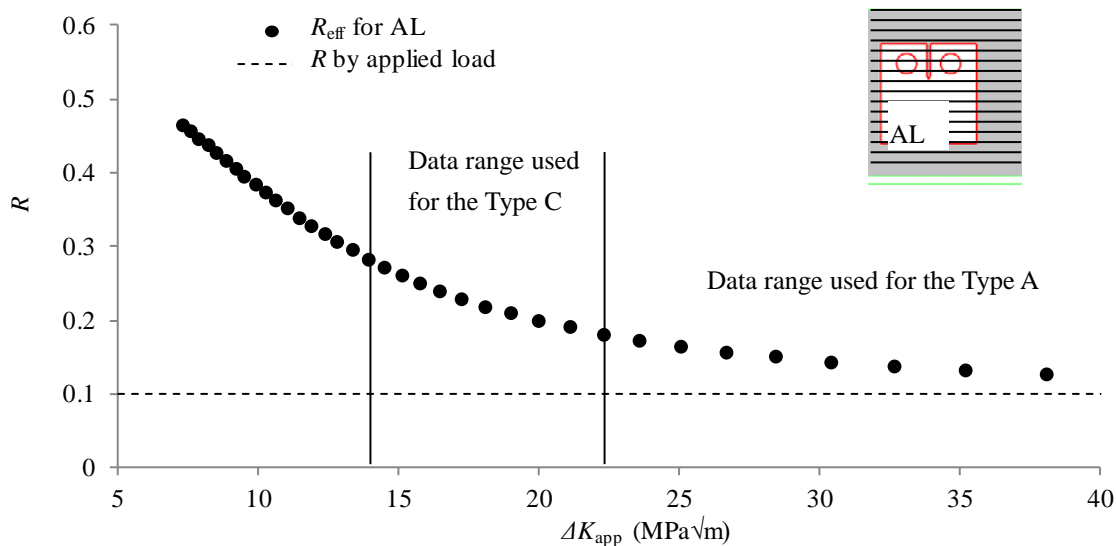


Figure 6-13 Effective stress intensity factor ratios in C(T) specimen, AL type

6.4 Crack trajectory in Type B, D and E

Although the Type B, D and E specimens were uniaxial loaded, the crack tips were in a biaxial loaded state. The reason for this is that the potential fatigue crack paths were parallel with the WAAM-substrate interface, and hence longitudinal residual stress resulted in transverse stress, which was perpendicular to the potential crack path. In this way, the stress condition in the Type B, D and E specimens is a mixed mode loading condition.

For fatigue crack growth life prediction the fatigue crack growth direction is of importance to estimate the FCGRs. Several criteria have been proposed regarding the crack growth

deviation angle under mixed mode loading condition.

One of the most used criteria is the maximum tangential stress (MTS) criterion proposed by Erdogan and Sih (1963). This criterion states that crack propagates along the radial direction on which the tangential stress becomes maximum. Comparison of this criterion with experimental results shows that the MTS criterion predicts the angle of crack growth well for Aluminium alloys (Plank and Kuhn, 1999).

Dahlin and Olsson (2002) considered the effect of plasticity on the fatigue crack path direction and proposed the MTS_p (subscript p for elastic-plastic) criterion. The criterion states that the fatigue crack will grow in the direction perpendicular to the maximum tangential stress on a radius, well inside the cyclic plastic zone. However, the calculation of this criterion is rather complex.

To predict the deviation angle, the MTS criterion were used:

$$\theta_{MTS} = \cos^{-1} \left(\frac{3K_{II}^2 + \sqrt{K_I^4 + 8K_I^2 K_{II}^2}}{K_I^2 + 9K_{II}^2} \right) \quad 6-20$$

where K_I , K_{II} , are the maximum stress intensity factors for Mode I and Mode II during cyclic loading, respectively.

When considering the effect of residual stress, K_I and K_{II} were replaced by

$$K_I = K_{I,app,max} + K_{I,res} \quad 6-21$$

$$K_{II} = K_{II,res} \quad 6-22$$

where $K_{I,app,max}$ is the maximum stress intensity factor for Mode I by the applied force, $K_{I,res}$ and $K_{II,res}$ are the stress intensity factors due to residual stress, for Mode I and Mode II, respectively.

The process of calculating the crack trajectories should be by repeated calculating the deviation angle of crack at each crack tip, and then extending the crack over an increment. As no good agreement has been obtained in this step, no further calculation about fatigue crack growth lives was performed.

Again, the maximum applied stress intensity factors, $K_{app,max}$ were calculated by using Eq. 5-5, the stress intensity factors due to residual stress have also been presented in Fig. 5-17. It is important to note that these calculations were based on straight crack path rather than predicted curve of crack trajectory.

The predicted deviation angle for Type B, D and E is shown in Fig. 6-14. Three examples of measured deviation angles are shown in Fig. 6-15. For B1 specimen the deviation angle is about 4° , and E1 and D3 are about 2° .

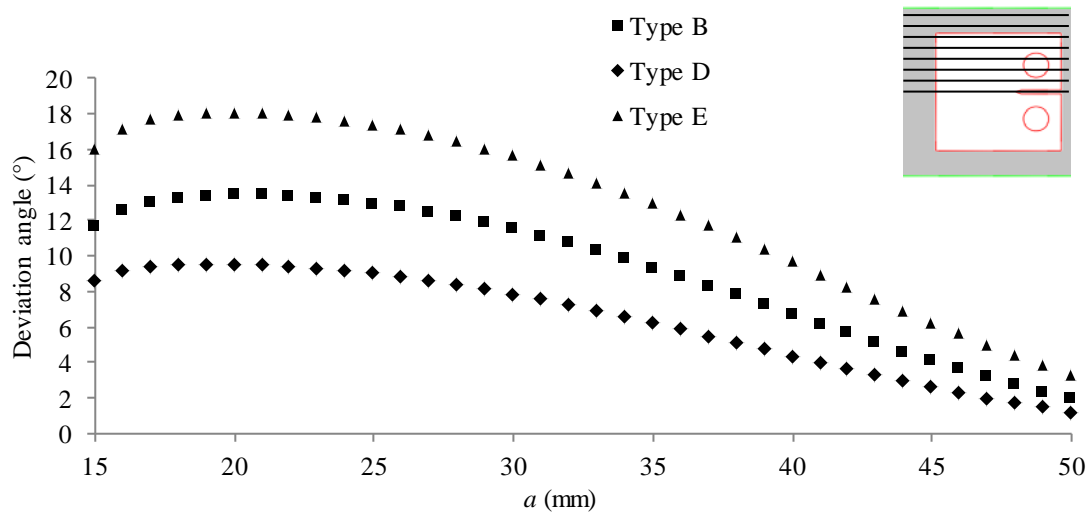


Figure 6-14 Predicted crack deviation angle for C(T) specimens, type B, D and E

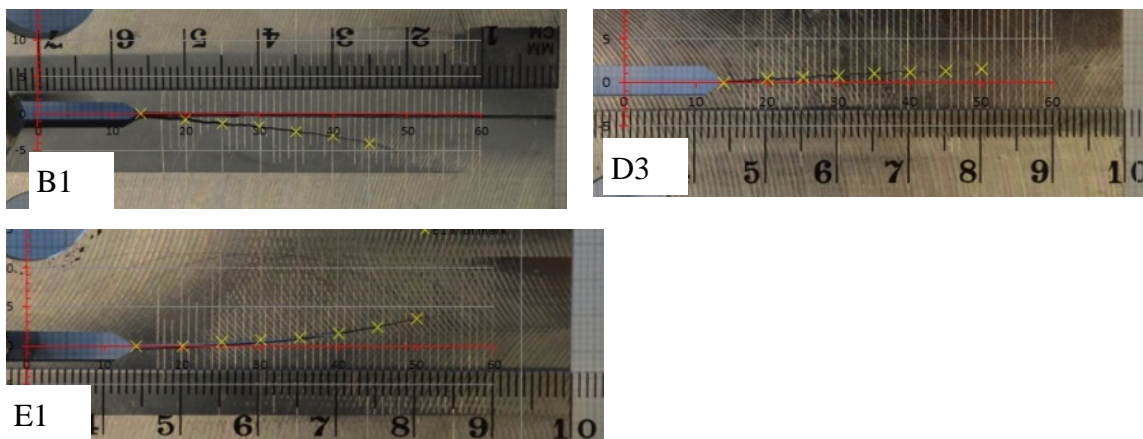


Figure 6-15 Three examples for fatigue crack deviation angles, B1, E1 and D3 specimens.

Predicted deviation angle is consistently larger than the experimental results. Although the calculations are based on a straight crack path, the trend of larger deviation angle is clear.

Such larger predicted deviation angle means that the Mode II stress intensity factor has less effect. The reason may be crack closure. Due to crack closure, crack surfaces get contacted when K_{tot} lower than K_{op} , and the contact between crack surfaces results in friction. The effect of this friction is to reduce the Mode II stress intensity factor.

Chapter 7 Conclusions and Future Work

7.1 Conclusions

This PhD project has developed prediction method for fatigue crack growth life in wire + arc additive manufactured Ti-6Al-4V focusing on cracks near the WAAM-substrate interface. Main tasks are as follows. First, the influence of anisotropic Young's modulus property on the crack growth driving force, the stress intensity factor, was evaluated by a two-dimensional FE model using orthotropic Young's modulus values. Second, the effect of residual stress on the stress intensity factor was evaluated by FE models. Third, the influence of residual stress on fatigue crack growth rate was accounted for by the superposition principle. Finally, the influence of microstructure of WAAM on fatigue crack growth life in bi-material specimens was accounted for by using respective fatigue crack growth rate data from WAAM Ti-6Al-4V or its wrought counterpart. Based on this study, following conclusions can be drawn.

1. Effect of orthotropic Young's modulus on stress intensity factor is found to be small and negligible. To evaluate the worst possible case, the upper and lower limit of the transverse direction Young's modulus were used with an average longitudinal direction Young's modulus. The ratios between the two Young's moduli are 0.94 and 1.10. The difference in calculated stress intensity factors between the orthotropic and isotropic materials are less than 1%. This result indicates that the influence of orthotropic Young's modulus is negligible.
2. Effect of bi-material Young's modulus on stress intensity factor is found to be small and negligible. To evaluate the bi-material effect, the measured Young's moduli were used. The difference in calculated stress intensity factors between bi-material and isotropic material is less than 5% over a 5 mm distance. This result indicates that the influence of bi-material Young's modulus is negligible.
3. The influence of material yield strength on the size of crack tip plastic zone was evaluated by both two-dimensional FE analysis and analytical approach in LEFM. The lower limit of yield strength for WAAM Ti-6Al-4V (800 MPa) and wrought Ti-6Al-4V (860 MPa)

were used for the calculations. The applied load corresponds to the maximum fatigue load in the test cases. The differences in calculated plastic zone size between the two materials (WAAM and wrought Ti-6Al-4V) are around 15%. This difference will affect the degree of crack closure; hence the crack growth rate in the two materials.

4. Residual stress redistribution in C(T) specimens can be evaluated by FE method. To evaluate the retained residual stress in C(T) specimens, residual stress profile from a large WAAM wall (e.g. Wall-Bi120) was inputted into a two-dimensional FE model of C(T) specimen. The retained residual stress in FE model is in good agreement with the experimental measurement by the contour method, which measured the residual stress profile of C(T) specimens that were extracted from the large Wall-Bi120 sample.
5. Assumption of residual stress free FCGR data from pure WAAM Ti-6Al-4V is assessed. Based on an analytical model, residual stress profile in Wall-T145 was estimated. Both K_{res} and R_{eff} were calculated for the across-the-layer crack type specimen. This analysis indicates that the assumption of residual stress free is not correct.
6. Position of WAAM-substrate interface should be defined according to the microstructure difference rather than the geometry border. Fatigue crack growth rates over the whole crack path were calculated by using empirical equations after calculation of K_{res} . A difference of fatigue crack growth rates over a 4 mm distance adjacent to the WAAM-substrate interface was found. And this distance corresponds to the distance between geometry interface and microstructure interface obtained from macrostructure photo of a C(T) specimen. This analysis indicates that microstructure interface should be used for the prediction of fatigue crack growth life.
7. Influence of ends in WAAM part should be considered. By comparing the measured and FE modelled residual stress in Type A specimen, and comparing the predicted FCGRs and experiment results in the Type A specimen, it was found that retained residual stress was higher in the Type A specimen. This indicates that influence of ends on fatigue crack growth rate should be considered.
8. The Harter T-method is a more accurate method and residual stress effect should not be

ignored. By comparing the predicted fatigue crack growth life for the Type C, which is far away from the ends of Wall-Bi120 and has a position to retain higher residual stress, it is found that the Harter T-method is closer to experiments. It is also noted that ignoring the residual stress give rise to overestimated fatigue crack growth life. Although retained residual stress become much less in these specimens, see figures 4-10 and 4-11, in real part, even the size of part is small, residual stress may still be high. As there is no much further machining for AM made part, residual stress introduced during thermal process may not be reduced much by geometry change.

9. The prior- β grain boundary should be considered. FCGR for A3 specimen (third specimen of the type A configuration) and photos of crack surface show that prior- β grain boundary can reduce the FCGR significantly. Although such crack propagation manner was only observed in 1 of 6 specimens, however, it is still an important thing for WAAM made Ti-6Al-4V.

7.2 Future work

Based on analysis, following future work could be done.

1. Fatigue crack growth life prediction using microstructure interface. To improve the accuracy of predicted fatigue crack growth life, this error source should be eliminated.
2. Fatigue crack growth life prediction in Type D specimen. Although the prediction of crack deviation angle is not successful, the fatigue crack growth life still can be calculated using experimental crack growth path.
3. Analytical residual stress model can be used for other samples. Residual stress profile in Wall-Bi120 can be predicted and compared with experiments.

References

- Addison, A., Ding, J., Martina, F., Lockett, H., Williams, S., and Zhang, X. (2015) 'Manufacture of Complex Titanium Parts Using Wire+Arc Additive Manufacture'. In *Titanium Europe 2015*. held 11-13 May 2015 at Birmingham
- Alec (2015) *Mapal Turns to Additive Manufacturing to Create QTD-Series Insert Drills*. [online] available from <<http://www.3ders.org/articles/20150722-mapal-turns-to-additive-manufacturing-to-create-qtd-series-insert-drills.html>> [accessed on 10th September 2015]
- Allen, J. (2006) 'An Investigation into the Comparative Costs of Additive Manufacture vs. Machine from Solid for Aero Engine Parts'. [online] in *Cost Effective Manufacture via Net-Shape Processing* (pp. 17-1 –17-10) Meeting Proceedings RTO-MP-AVT-139, Neuilly-sur-Seine, France: RTO. available from <<http://dtic.mil/dtic/tr/fulltext/u2/a521730.pdf>> [accessed on 4th May 2016]
- AMS 4911J (2003) *Titanium Alloy, Sheet, Strip, and Plate 6Al-4V Annealed*. SAE International
- Anderson, T.L. (2012) *Fracture Mechanics: Fundamentals and Applications*. (3rd ed) London: Taylor & Francis
- Anon. (2015) *Innovation Challenge Uncovers New Approaches to Complex Castings*. [online] available from <http://www.geaviation.com/press/services/services_20150416.html> [accessed on 25th June 2015]
- Antony, A.A. (2012) *Microstructure, Texture and Mechanical Property Evolution during Additive Manufacturing of Ti6Al4V Alloy for Aerospace Applications*. PhD thesis. Manchester: Manchester University
- ASTM Standard E647 (2010) *Standard Test Method for Measurement of Fatigue Crack Growth Rates*. ASTM International
- ASTM Standard F2792 (2012) *Standard Terminology for Additive Manufacturing*

Technologies. ASTM International

ASTM Standard F2924 (2014) *Standard Specification for Additive Manufacturing Titanium-6Aluminium-4Vanadium with Power Bed Fusion*. ASTM International

Bao, R. and Zhang, X. (2010) 'An Inverse Method for Evaluating Weld Residual Stresses via Fatigue Crack Growth Test Data'. *Engineering Fracture Mechanics* 77(16), 3143–3156

Bao, R., Zhang, X., and Yahaya, N.A. (2010) 'Evaluating Stress Intensity Factors due to Weld Residual Stresses by the Weight Function and Finite Element Methods'. *Engineering Fracture Mechanics* 77 (13), 2550–2566

Baufeld, B. and Biest, O.V.D. (2009) 'Mechanical Properties of Ti-6Al-4V Specimens Produced by Shaped Metal Deposition'. *Science and Technology of Advanced Materials* 10, 1–10

Boyce, B.L. and Ritchie, R.O. (2001) 'Effect of Load Ratio and Maximum Stress Intensity on the Fatigue Threshold in Ti-6Al-4V'. *Engineering Fracture Mechanics* 68 (2), 129–147

Boyer, R.R. (1992) 'New Titanium Applications on the Boeing 777 Airplane'. *JOM* 44 (5), 23–25

Brandl, E., Baufeld, B., Leyens, C., and Gault, R. (2010) 'Additive manufactured Ti-6Al-4V using welding wire: comparison of laser and arc beam deposition and evaluation with respect to aerospace material specifications'. *Physics Procedia* 5, 595–606

Bussu, G. and Irving, P.E. (2003) 'The Role of Residual Stress and Heat Affected Zone Properties on Fatigue Crack Propagation in Friction Stir Welded 2024-T351 Aluminium Joints'. *International Journal of Fatigue* 25 (1), 77–88

Cain, V., Thijs, L., Van Humbeeck, J., Hooreweder, B., and Knutsen, R. (2015) 'Crack propagation and fracture toughness of Ti6Al4V alloy produced by selective laser melting'. *Additive Manufacturing* 5, 68–76

Chen, J. (2012) *Hybrid Design Based on Wire and Additive Manufacturing in the Aircraft Industry*. MSc thesis. Cranfield: Cranfield University

- Cheng, W.L. and Finnie, I. (2007) *Residual Stress Measurement and the Slitting Method*. New York: Springer
- Clark, W.G. and Hudak, S.J. (1975) 'Variability in Fatigue Crack Growth Rate Testing'. *Journal of Testing and Evaluation* 3(6), 454–476.
- Colegrove, P.A., Martina, F., Roy, M.J., Szost, B.A., Terzi, S., Williams, S.W., Withers, P.J., and Jarvis, D. (2014) 'High Pressure Interpass Rolling of Wire + Arc Additively Manufactured Titanium Components'. *Advanced Materials Research* 996, 694–700
- Dahlin, P. and Olsson, M. (2002) 'The Effect of Plasticity on Incipient Mixed-Mode Fatigue Crack Growth'. *Fatigue and Fracture of Engineering Materials and Structures* 26, 577–588
- Ding, J. (2012) *Thermo-Mechanical Analysis of Wire and Arc Additive Manufacturing Process*. PhD thesis. Cranfield: Cranfield University
- Donachie, M.J. (2000) *Titanium: A Technical Guide*. [online], 2nd Edn. ASM international. Available from <<http://site.ebrary.com/lib/coventry/reader.action?docID=10320366&ppg=150>> [accessed on 18th May 2016]
- Dubey, S., Soboyejo, A.B.O., and Soboyejo, W.O. (1997) 'An investigation of the effects of stress ratio and crack closure on the micromechanisms of fatigue crack growth in Ti-6Al-4V'. *Acta Materialia* 45(7), 2777–2787
- Edwards, P., O'Conner, A., and Ramulu, M. (2013) 'Electron beam additive manufacturing of titanium components: Properties and performance'. *Journal of Manufacturing Science and Engineering* 135(6), 061016/1-7
- Edwards, P. and Ramulu, M. (2015) 'Effect of Build Direction on the Fracture Toughness and Fatigue Crack Growth in Selective Laser Melted Ti-6Al-4V'. *Fatigue & Fracture of Engineering Materials & Structures* 38 (10), 1228–1236
- Edwards, P. and Ramulu, M. (2014) 'Fatigue performance evaluation of selective laser melted Ti-Al-4V'. *Materials Science and Engineering: A* 598, 327–337

- Elber, W. (1970) 'Fatigue Crack Closure under Cyclic Tension'. *Engineering Fracture Mechanics* 2, 37–45 Cited in Anderson, T.L. (2012) *Fracture Mechanics: Fundamentals and Applications*. (3rd ed) London: Taylor & Francis:458
- Erdogan, F. and Sih, G.C. (1963) 'On the Crack Extension in Plates under Plane Loading and Transverse Shear'. *Journal of Basic Engineering* 85 (4), 519–525 Cited in Plank. R. and Kuhn. G. (1999) 'Fatigue crack propagation under non-proportional mixed mode loading'. *Engineering Fracture Mechanics* 62, 203-229:206
- FAA, T.C. (1993) *Damage Tolerance Assessment Handbook Volume I: Introduction Fracture Mechanics Fatigue Crack Propagation*. [online] report, US Department of Transportation-Federal Aviation Administration, available from < <http://www.tc.faa.gov/its/worldpac/techrpt/ct93-69-1.pdf> > [accessed on 5th August 2015]
- Facchini, L., Magalini, E., Robotti, P., and Molinari, A. (2009) 'Microstructure and Mechanical Properties of Ti-6Al-4V Produced by Electron Beam Melting of Pre-Alloyed Powders'. *Rapid Prototyping Journal* 15 (3), 171–178
- Fedderson, C.E. and Hyler, W.S. (1971) *Fracture and Fatigue-Crack Propagation Characteristics of 1/4-Inch Mill Annealed Ti-6Al-4V Titanium Alloy Plate*. Report No. G9706, Battelle, Columbus, Ohio. Cited in Rice, R.C., Jackson, J.L., Bakuckas, J. and Thompson, S. (2003) *Metallic materials properties development and standardization* (MMPDS-01) Virginia: National Technical Information Service (NTIS): p. 5–74
- Filip, R., Kubiak, K., Ziaja, W., and Sieniawski, J. (2003) 'The Effect of Microstructure on the Mechanical Properties of Two-Phase Titanium Alloys'. *Journal of Materials Processing Technology* 133 (1), 84–89
- Formanoir, C., Michotte, S., Rigo, O., Germain, L., and Godet, S. (2016) 'Electron beam melted Ti-6Al-4V: Microstructure, texture and mechanical behavior of the as-built and heat-treated material'. *Materials Science and Engineering: A* 652, 105–119
- Ganguly, S., Fitzpatrick, M.E., and Edwards, L. (2006) 'Use of neutron and synchrotron X-

- ray diffraction for evaluation of residual stresses in a 2024-T351 aluminum alloy variable-polarity plasma-arc weld'. *Metallurgical and Materials Transactions A* 37(2), 411–420
- Gibson, I., Rosen, D.W., and Stucker, B. (2010) *Additive Manufacturing Technologies*. New York: Springer
- Greitemeier, D., Palm, F., Syassen, F., and Melz, T. (2016) 'Fatigue performance of additive manufactured TiAl6V4 using electron and laser beam melting'. *International Journal of Fatigue* 94, 211-217
- Hale, J. (2006) *Boeing 787 from the Ground Up*. [online] available from <http://www.boeing.com/commercial/aeromagazine/articles/qtr_4_06/AERO_Q406.pdf> [1 Nov 2015]
- Harrington, T.R. (n.d.) *C-17 Material Specimen Tests for Fracture Mechanics Data*. Phase II, Titanium, CRES, Inconel Lot 1. Cited in Forth, S., (2006) *The purpose of generating fatigue crack growth threshold data*. [online] NASA Johnson Space Center. available from <<http://ntrs.nasa.gov/archive/nasa/casi.ntrs.nasa.gov/20080031625.pdf>> [accessed on 10th May 2015]
- Harter, J.A. (2008) *AFGROW Users Guide and Technical Manual*. (AFGROW Version 4.0012.15). U.S. AIR FORCE RESEARCH LAB
- Hills, N. (2014) *Fatigue Crack Propagation Behaviour at the Interface of Additively Manufactured Ti-6Al-4V and the Substrate*. MSc thesis. Cranfield: Cranfield University
- Hooreweder, B. V., Moens, D., Boonen, R., Kruth, J.P., and Sas, P. (2012) 'Analysis of fracture toughness and crack propagation of Ti6Al4V produced by selective laser melting'. *Advanced Engineering Materials* 14(1–2), 92–97
- Hoye, N., Li, H.J., Cuiuri, D., and Paradowska, A.M. (2014) 'Measurement of Residual Stresses in Titanium Aerospace Components Formed via Additive Manufacturing'. *Materials Science Forum* 777, 124–129
- Kandil, F.A., Lord, J.D., Fry, A.T., and Grant, P. V. (2001) *A review of residual stress*

measurement methods – A guide to technique selection. London: National Physical Laboratory

Kartal, M.E., Liljedahl, C.D.M., Gungor, S., Edwards, L., and Fitzpatrick, M.E. (2008) 'Determination of the Profile of the Complete Residual Stress Tensor in a VPPA Weld Using the Multi-Axial Contour Method'. *Acta Materialia* 56 (16), 4417–4428

Katcher, M. and Kaplan, M. (1974) 'Effects of R-Factor and Crack Closure on Fatigue Crack Growth for Aluminium and Titanium Alloys'. in *Fracture Toughness and Slow-Stable Cracking, ASTM STP 559*, American Society for Testing and Materials, 264-282

Kazanas, P. (2011) *Design for Wire and Arc Additive Layer Manufacture*. (unpublished RUAM 8th Industry Day), Cranfield. cited in Chen, J. (2012) *Hybrid design based on wire and additive manufacturing in the aircraft industry*. MSc thesis. Cranfield: Cranfield University

Krueger, R. (2004) 'Virtual Crack Closure Technique: History, Approach, and Applications'. *Applied Mechanics Reviews* 57 (2), 109

Kruth, J.P., Mercelis, P., Vaerenbergh, J., Froyen, L., and Rombouts, M. (2005) 'Binding Mechanisms in Selective Laser Sintering and Selective Laser Melting'. *Rapid Prototyping Journal* 11 (1), 26–36

Law, M., Kirstein, O., and Luzin, V. (2010) 'An Assessment of the Effect of Cutting Welded Samples on Residual Stress Measurements by Chill Modelling'. *The Journal of Strain Analysis for Engineering Design* 45 (8), 567–573

Leggatt, R.H. (2008) 'Residual Stresses in Welded Structures'. *International Journal of Pressure Vessels and Piping* 85 (3), 144–151

Lei, Y., O'dowd, N.P., and Webster, G.A. (2000) 'Fracture Mechanics Analysis of a Crack in a Residual Stress Field'. *International Journal of Fracture* 106(3), 195–216

Leuders, S., Thone, M., Riemer, A., Niendorf, T., Troster, T., and Richard, H.A. (2013) 'On the Mechanical Behavior of Titanium Alloy Ti6Al4V Manufactured by Selective Laser Melting: Fatigue Resistance and Crack Growth Performance'. *International Journal of*

Fatigue 48 (3), 300–317

- Liljedahl, C.D.M., Tan, M.L., Zanellato, O., Ganguly, S., Fitzpatrick, M.E., and Edwards, L. (2008) ‘Evolution of Residual Stresses with Fatigue Loading and Subsequent Crack Growth in a Welded Aluminium Alloy Middle Tension Specimen’. *Engineering Fracture Mechanics* 75 (13), 3881–3894
- Lorant, E. (2010) *Effect of Microstructure on Mechanical Properties of Ti-6Al-4V Structures Made by Additive Layer Manufacturing*. MSc thesis. Cranfield: Cranfield University
- Martina, F. (2014) *Investigation of Methods to Manipulate Geometry, Microstructure and Mechanical Properties in Titanium Large Scale Wire+Arc Additive Manufacturing*. PhD thesis. Cranfield: Cranfield University
- Martina, F., Mehnen, J., Williams, S.W., Colegrove, P., and Wang, F. (2012) ‘INVESTIGATION OF THE BENEFITS OF PLASMA DEPOSITION FOR THE ADDITIVE LAYER MANUFACTURE OF Ti-6Al-4V’. *Journal of Materials Processing Technology* 212 (6), 1377–1386
- Mercelis, P. and Kruth, J. (2006) ‘Residual Stresses in Selective Laser Sintering and Selective Laser Melting’. *Rapid Prototyping Journal* 12 (5), 254–265
- Mok, S.H., Bi, G., Folkes, J., and Pashby, I. (2008) ‘Deposition of Ti-6Al-4V Using a High Power Diode Laser and Wire, Part I: Investigation on the Process Characteristics’. *Surface and Coatings Technology* 202 (16), 3933–3939
- Murr, L.E., Esquivel, E.V., Quinones, S.A., Gaytan, S.M., Lopez, M.I., Martinez, E.Y., Medina, F., and Hernandez, D.H. (2009) ‘Microstructures and Mechanical Properties of Electron Beam-Rapid Manufactured Ti-6Al-4V Biomedical Prototypes Compared to Wrought Ti-6Al-4V’. *Materials Characterization* 60 (2), 96–105
- Murr, L.E., Gaytan, S.M., Ramirez, D.A., Martinez, E., Hernandez, J., and Amato, K.N. (2012) ‘Metal Fabrication by Additive Manufacturing Using Laser and Electron Beam Melting Technologies’. *Journal of Materials Science & Technology* 28 (1), 1–14
- Newman, J. C., J. (1974) ‘Stress Analysis of the Compact Specimen Including the Effects of

- Pin Loading'. *Fracture Analysis, ASTM STP 560* 105–121
- Paddea, S. (2015) *The Open University Report*. Unpublished report. Cranfield: Cranfield University
- Parker, A.P. (1982) 'Stress Intensity Factors, Crack Profiles, and Fatigue Crack Growth Rates in Residual Stress Fields'. *Residual Stress Effects in Fatigue STP 779*, 13–31
- Pasta, S., Reynolds, A.P., and Fratini, L. (2006) 'Residual Stress Effects on Fatigue Crack Growth in Ti-6–4 Friction Stir Welds'. AIAS, Ancona.
- Pike, J. (2016) *F-22 Materials and Processes*. [online] available from < <http://www.globalsecurity.org/military/systems/aircraft/f-22-mp.htm> > [accessed on 25th October 2016]
- Plank, R. and Kuhn, G. (1999) 'Fatigue Crack Propagation under Non-Proportional Mixed Mode Loading'. *Engineering Fracture Mechanics* 62, 203–229
- Prime, M.B. (2001) 'Cross-sectional mapping of residual stresses by measuring the surface contour after a cut'. *Journal of Engineering Materials and Technology* 123(2), 162–168
- Rice, R.C., Jackson, J.L., Bakuckas, J., and Thompson, S. (2003) *Metallic Materials Properties Development and Standardization*. (MMPDS-01) Virginia: National Technical Information Service (NTIS)
- Rybicki, E.F. and Kanninen, M.F. (1977) 'A Finite Element Calculation of Stress Intensity Factors by a Modified Crack Closure Integral'. *Engineering Fracture Mechanics* 9 (4), 931–938 Cited in Valvo, P.S. (2012) 'A revised virtual crack closure technique for physically consistent fracture mode partitioning'. *International journal of fracture* 173(1), 1-20
- Shademan, S., Sinha, V., Soboyejo, A.B.O., and Soboyejo, W.O. (2004) 'An Investigation of the Effects of Microstructure and Stress Ratio on Fatigue Crack Growth in Ti-6Al-4V with Colony A/β Microstructures'. *Mechanics of Materials* 36(1), 161–175
- Shen, C., Pan, Z., Cuiuri, D., Roberts, J., and Li, H. (2016) 'Fabrication of Fe-FeAl

- Functionally Graded Material Using the Wire-Arc Additive Manufacturing Process'. *Metallurgical and Materials Transactions B* 47 (1), 763–772
- Shih, T.T. and Wei, R.P. (1973) *A Study of Crack Closure in Fatigue*. NASA CR-2319 [online] available from < <http://ntrs.nasa.gov/archive/nasa/casi.ntrs.nasa.gov/19730024067.pdf>> [15 Jun 2015]
- Shiomi, M., Osakada, K., Nakamura, K., Yamashita, T., and Abe, F. (2004) 'Residual Stress within Metallic Model Made by Selective Laser Melting Process'. *CIRP Annals - Manufacturing Technology* 53 (1), 195–198
- Sicot, O., Gong, X.L., Cherouat, A., and Lu, J. (2004) 'Influence of experimental parameters on determination of residual stress using the incremental hole-drilling method'. *Composites Science and Technology* 64(2), 171–180
- Sicot, O., Gong, X.L., Cherouat, A., and Lu, J. (2003) 'Determination of residual stress in composite laminates using the incremental hole-drilling method'. *Journal of Composite Materials* 37(9), 831–844
- Sieniawski, J., Ziaja, W., Kubiak, K., and Motyka, M. (2013) 'Microstructure and mechanical properties of high strength two-phase titanium alloys'. [online] in *Titanium Alloys-Advances in Properties Control*, 69-80, available from < <http://www.intechopen.com/books/titanium-alloys-advances-in-properties-control/microstructure-and-mechanical-properties-of-high-strength-two-phase-titanium-alloys>> [accessed on May 2015]
- Simonelli, M., Tse, Y.Y., and Tuck, C. (2014) 'Effect of the build orientation on the Mechanical Properties and Fracture Modes of SLM Ti–6Al–4V'. *Materials Science and Engineering: A* 616, 1-11
- Tada, H., Paris, P., and Irwin, G. (2000) *The Stress Analysis of Cracks Handbook*. 3rd edn. New York: ASME Press
- Thijs, L., Verhaeghe, F., Craeghs, T., Van Humbeeck, J., and Kruth, J.P. (2010) 'A Study of the Microstructural Evolution during Selective Laser Melting of Ti–6Al–4V'. *Acta*

Materialia 58 (9), 3303–3312

Tsui, Y.C. and Clyne, T.W. (1997) ‘An Analytical Model for Predicting Residual Stresses in Progressively Deposited Coatings Part 1: Planar Geometry’. *Thin Solid Films* 306 (1), 23–33

Uriondo, A., Esperon-Miguez, M., and Perinpanayagam, S. (2015) ‘The Present and Future of Additive Manufacturing in the Aerospace Sector: A Review of Important Aspects’. *Proceedings of the Institution of Mechanical Engineers, Part G: Journal of Aerospace Engineering* 229 (11), 2132–2147

Vayre, B., Vignat, F., and Villeneuve, F. (2012) ‘Metallic Additive Manufacturing: State-of-the-Art Review and Prospects’. *Mechanics & Industry* 13 (2), 89–96

Wang, F., Williams, S., Colegrove, P., and Antonysamy, A.A. (2013) ‘Microstructure and Mechanical Properties of Wire and Arc Additive Manufactured Ti-6Al-4V’. *Metallurgical and Materials Transactions A* 44 (2), 968–977

Wang, F., Williams, S., and Rush, M. (2011) ‘Morphology investigation on direct current pulsed gas tungsten arc welded additive layer manufactured Ti6Al4V alloy’. *The international journal of advanced manufacturing technology* 57(5-8), 597-603

Williams, S.W., Martina, F., Addison, A.C., Ding, J., Pardal, G., and Colegrove, P. (2016) ‘Wire + Arc Additive Manufacturing’. *Materials Science and Technology* (7), 641–647

Withers, P.J. and Bhadeshia, H.K.D.H. (2001) ‘Residual stress. Part 1 – Measurement techniques’. *Materials Science and Technology* 17(4), 355–365

Withers, P.J., Turski, M., Edwards, L., Bouchard, P.J., and Buttle, D.J. (2008) ‘Recent Advances in Residual Stress Measurement’. *International Journal of Pressure Vessels and Piping* 85(3), 118–127

Zanin, E. (2012) *Airbus Perspective on Titanium Sourcing*. [online] <
http://c.ymcdn.com/sites/www.titanium.org/resource/resmgr/2010_2014_papers/ZaninEric_2012.pdf> [accessed on 4th May 2016]

- Zarkades, A. and Larson, F.R. (1968) *Sheet Tensile Properties of Titanium Alloys as Affected by Texture*. [online] (No. AMMRC-TR-68-03). ARMY MATERIALS AND MECHANICS RESEARCH CENTER WATERTOWN MA. Available from <http://oai.dtic.mil/oai/oai?verb=getRecord&metadataPrefix=html&identifier=AD0666765> [accessed on 23rd July 2016]
- Zhai, Y., Galarraga, H., and Lados, D.A. (2016) 'Microstructure, Static Properties, and Fatigue Crack Growth Mechanisms in Ti-6Al-4V Fabricated by Additive Manufacturing: LENS and EBM'. *Engineering Failure Analysis* 69, 3–14
- Zhang, J., Wang, X., Paddea, S., and Zhang, X. (2016a) 'Fatigue Crack Propagation Behaviour in Wire+arc Additive Manufactured Ti-6Al-4V: Effects of Microstructure and Residual Stress'. *Materials and Design* 90, 551–561
- Zhang, J., Zhang, X., Wang, X., Ding, J., Traoré, Y., Paddea, S., and Williams, S. (2016b) 'Crack Path Selection at the Interface of Wrought and Wire + Arc Additive Manufactured Ti-6Al-4V'. *Materials and Design* 104, 365–375
- Zhang, X., Martina, F., Ding, J., Wang, X., and Williams, S.W. (2017) 'Fracture Toughness and Fatigue Crack Growth Rate Properties in Wire + Arc Additive Manufactured Ti-6Al-4V'. *Fatigue & Fracture of Engineering Materials & Structures* 40(5), 790–803

Appendix A

Published papers

The work of this PhD project has resulted in the following publication:

Zhang, J., Wang, X., Paddea, S. and Zhang, X. (2016) ‘Fatigue crack propagation behaviour in wire+arc additive manufactured Ti-6Al-4V: Effects of microstructure and residual stress’. *Materials & Design* 90, 551–561

It was led by the first author and contribution of this thesis’ author include all work on FE analysis, part of work on microstructure experiments and all work on FCGR data analysis.

Zhang, J., Zhang, X., Wang, X., Ding, J., Traoré, Y., Paddea, S. and Williams, S. (2016) ‘Crack Path Selection at the Interface of Wrought and Wire+Arc Additive Manufactured Ti-6Al-4V’. *Materials & Design* 104, 365–375

It was led by the first author and contribution of this thesis’ author include part of work on FE analysis, part of work on microstructure experiments and all work on crack path measurement.

Zhang, X., Martina, F., Ding, J., Wang, X., and Williams, S.W. (2017) ‘Fracture Toughness and Fatigue Crack Growth Rate Properties in Wire + Arc Additive Manufactured Ti-6Al-4V’. *Fatigue & Fracture of Engineering Materials & Structures* 40(5), 790–803

It was led by the first author and contribution of this thesis’ author include optical microscope observation and FCGR tests for wrought Ti-6Al-4V.